Title
Fourth-order conservative Vlasov-Maxwell solver for Cartesian and cylindrical phase space coordinates

Author
Vogman, Genia

Publication Date
2016

Peer reviewed|Thesis/dissertation

Fourth-order conservative Vlasov-Maxwell solver for Cartesian and cylindrical phase space coordinates

by

Genia Vogman

A dissertation submitted in partial satisfaction of the

requirements for the degree of

Doctor of Philosophy

in

Engineering — Applied Science and Technology

and the Designated Emphasis

in

Computational Science and Engineering

in the

Graduate Division

of the

University of California, Berkeley

Committee in charge:

Professor Phillip Colella, Chair
Professor Uri Shumlak
Professor Jonathan Wurtele
Professor Per-Olof Persson

Fall 2016

Fourth-order conservative Vlasov-Maxwell solver for Cartesian and cylindrical phase space coordinates

Abstract

Fourth-order conservative Vlasov-Maxwell solver for Cartesian and cylindrical phase space coordinates

by

Genia Vogman

Doctor of Philosophy in Engineering — Applied Science and Technology

and the Designated Emphasis in Computational Science and Engineering

University of California, Berkeley

Professor Phillip Colella, Chair

Plasmas are made up of charged particles whose short-range and long-range interactions give rise to complex behavior that can be difficult to fully characterize experimentally. One of the most complete theoretical descriptions of a plasma is that of kinetic theory, which treats each particle species as a probability distribution function in a six-dimensional position-velocity phase space. Drawing on statistical mechanics, these distribution functions mathematically represent a system of interacting particles without tracking individual ions and electrons. The evolution of the distribution function(s) is governed by the Boltzmann equation coupled to Maxwell's equations, which together describe the dynamics of the plasma and the associated electromagnetic fields. When collisions can be neglected, the Boltzmann equation is reduced to the Vlasov equation. High-fidelity simulation of the rich physics in even a subset of the full six-dimensional phase space calls for low-noise high-accuracy numerical methods. To that end, this dissertation investigates a fourth-order finite-volume discretization of the Vlasov-Maxwell equation system, and addresses some of the fundamental challenges associated with applying these types of computationally intensive enhanced-accuracy numerical methods to phase space simulations.

The governing equations of kinetic theory are described in detail, and their conservation-law weak form is derived for Cartesian and cylindrical phase space coordinates. This formulation is well known when it comes to Cartesian geometries, as it is used in finite-volume and finite-element discretizations to guarantee local conservation for numerical solutions. By contrast, the conservation-law weak form of the Vlasov equation in cylindrical phase space coordinates is largely unexplored, and to the author's knowledge has never previously been solved numerically. Thereby the methods described in this dissertation for simulating plasmas in cylindrical phase space coordinates present a new development in the field of computational plasma physics.

A fourth-order finite-volume method for solving the Vlasov-Maxwell equation system is presented first for Cartesian and then for cylindrical phase space coordinates. Special

attention is given to the treatment of the discrete primary variables and to the quadrature rule for evaluating the surface and line integrals that appear in the governing equations. The finite-volume treatment of conducting wall and axis boundaries is particularly nuanced when it comes to phase space coordinates, and is described in detail. In addition to the mechanics of each part of the finite-volume discretization in the two different coordinate systems, the complete algorithm is also presented.

The Cartesian coordinate discretization is applied to several well-known test problems. Since even linear analysis of kinetic theory governing equations is complicated on account of velocity being an independent coordinate, few analytic or semi-analytic predictions exist. Benchmarks are particularly scarce for configurations that have magnetic fields and involve more than two phase space dimensions. Ensuring that simulations are true to the physics thus presents a difficulty in the development of robust numerical methods. The research described in this dissertation addresses this challenge through the development of more complete physics-based benchmarks based on the Dory-Guest-Harris instability. The instability is a special case of perpendicularly-propagating kinetic electrostatic waves in a warm uniformly magnetized plasma. A complete derivation of the closed-form linear theory dispersion relation for the instability is presented. The electric field growth rates and oscillation frequencies specified by the dispersion relation provide concrete measures against which simulation results can be quantitatively compared. Furthermore, a specialized form of perturbation is shown to strongly excite the fastest growing mode. The fourth-order finite-volume algorithm is benchmarked against the instability, and is demonstrated to have good convergence properties and close agreement with theoretical growth rate and oscillation frequency predictions. The Dory-Guest-Harris instability benchmark extends the scope of standard test problems by providing a substantive means of validating continuum kinetic simulations of warm magnetized plasmas in higher-dimensional 3D (x, v_x, v_y) phase space. The linear theory analysis, initial conditions, algorithm description, and comparisons between theoretical predictions and simulation results are presented.

The cylindrical coordinate finite-volume discretization is applied to model axisymmetric systems. Since mitigating the prohibitive computational cost of simulating six dimensions is another challenge in phase space simulations, the development of a robust means of exploiting symmetry is a major advance when it comes to numerically solving the Vlasov-Maxwell equation system. The discretization is applied to a uniform distribution function to assess the nature of the singularity at the axis, and is demonstrated to converge at fourth-order accuracy. The numerical method is then applied to simulate electrostatic ion confinement in an axisymmetric Z-pinch configuration. To the author's knowledge this presents the first instance of a conservative finite-volume discretization of the cylindrical coordinate Vlasov equation. The computational framework for the Vlasov-Maxwell solver is described, and an outlook for future research is presented.

To my parents and sister

Contents

List of Figures

Acknowledgments

I have had the distinct pleasure of completing my Ph.D. under the tutelage of individuals who are passionate about their line of work, and they have been an invaluable source of guidance and inspiration. In particular, I would like to acknowledge the mentorship of my research advisors – Phillip Colella and Uri Shumlak. I am grateful to them both for making my research possible and for making graduate school such a positive experience.

A big thank you to Phil for giving me tremendous freedom to pursue my interests. Your infectious enthusiasm and zeal for computational research of all types have given me assurance that even the toughest problems are surmountable. Thank you for sharing your deep-seated experience and philosophy on all aspects of research and scientific communication. It has been an honor to be one of your graduate students.

I owe a great deal to Uri. The time and energy you invest in the professional development of your students is unparalleled, and I feel very fortunate to have had the benefit of your thoughtful advice and guidance throughout my undergraduate and graduate education. Thank you for exposing me to research and for introducing me to the field of computational plasma physics. Thank you also for graciously agreeing to co-advise my graduate research and for enabling me to meld my interests in engineering, plasmas, and applied mathematics.

I gratefully acknowledge the financial support I have received from the US Department of Energy Office of Science Graduate Fellowship (SCGF) and the UC Berkeley Chancellor's Fellowship.

I very much appreciate the support of my colleagues at ANAG and UW. Special thanks to Dan Martin and Dan Graves for diligently answering my many questions regarding Chombo and supercomputing. Thank you also to Brian Van Straalen for sharing your insights on all aspects of parallelization and data communication. I am especially grateful to the UW Computational Plasma Dynamics Lab for allowing me to join their meetings remotely and for the many illuminating discussions about plasma physics and numerical methods.

Thank you to those who have been my advocates: to Jonathan Wurtele for always making yourself available, for your constructive criticism, and for exposing me to valuable opportunities; to Karl van Bibber and Sam Burden for your wise counsel and candid career advice; to Sheila Humphreys for enhancing my graduate school experience and for warmly welcoming me into WICSE, where I have the privilege of meeting a number of amazing individuals, some of whom I am lucky to call my friends.

I am grateful for the friends I have made in Berkeley, who through their humor, wit, and sense of irony have made graduate school such a memorable experience.

Finally, to my parents and sister, thank you for planting me in fertile soil.

Chapter 1

Introduction

1.1 Computational modeling of plasmas

Plasma is an ionized gas that consists of charged particles. These constituent particles have long-range interactions through electromagnetic fields and thereby exhibit collective behavior that makes plasmas distinct from other fluids. See Ref [2] for a comprehensive introduction to plasma physics and its core principles. In addition to their unique physical properties, plasmas are studied for their applications to thermonuclear fusion, propulsion, photolithography, hypersonics, material processing, astrophysics, and space weather. Due to the challenges associated with making experimental measurements and the complexity of the physics involved, computational modeling plays a critical role in plasma investigations. The development of robust numerical methods that are able to capture plasma dynamics with high fidelity is therefore a proactive area of research, and is the focus of this dissertation.

Computational modeling of plasmas is made challenging by the fact that plasma dynamics involve spatial and temporal scales that can span many orders of magnitude. For example, electromagnetic waves can propagate through plasma at the speed of light, and can thereby affect dynamics of particles over the course of nanoseconds; whereas bulk motion of the same plasma can evolve over a span of seconds. The different scales are described by a hierarchy of theoretical models. At large scales the state of a plasma is often defined by its macroscopic properties such as density, momentum, and energy. The evolution of these properties is described by fluid theory conservation laws that encode the bulk dynamics of the plasma and by Maxwell's equations, which describe the associated fields. At small scales, the state of a plasma is defined in terms of the statistical distribution and interaction of its particles. In low-density plasmas collisions between particles can be infrequent, and small scale effects like particle-particle and particle-wave interactions can dominate plasma behavior. The generalized mathematical description of plasma dynamics at all scales stems from partial differential equations given by kinetic and electromagnetic theory.

1.2 Kinetic theory description

Kinetic theory offers one of the most complete theoretical descriptions of a plasma. In kinetic theory all particles of a given species (e.g. electrons) are represented by a scalar-valued distribution function $f_s(\boldsymbol{x}, \boldsymbol{v}, t)$ in a six-dimensional phase space. The value of the distribution function encodes the probability that a particle of species s can be found at position $\boldsymbol{x}$, velocity $\boldsymbol{v}$, at time t. In effect, by drawing on statistical mechanics, kinetic theory represents a system of interacting particles without tracking individual ions and electrons. The evolution of the distribution function in phase space is described by the Boltzmann equation coupled to Maxwell's equations. The Boltzmann equation is a six-dimensional (not including time) advection equation with sources to account for collisional effects. In addition to capturing the physics described by fluid theory, the Boltzmann equation includes dynamics associated with particle-particle and particle-wave interactions, and thereby offers a more general plasma description.

The focus of this dissertation is on collisionless plasmas in which the transport of constituent particles is dominated by long-range interactions rather than by collisions. Such plasmas typically have low densities and/or high temperatures – features that are commonly observed in space plasmas, and localized regions within experiments where mean free paths are relatively long. For such plasmas, the collision term in the Boltzmann equation is set to zero, and the resulting governing equation is the Vlasov equation. The Vlasov equation is a purely hyperbolic partial differential equation that represents a conservation law for f_s in six-dimensional phase space. Given an initial condition for a species distribution function, solving the Vlasov equation requires numerical methods that discretize the distribution function in phase space and in time.

1.3 Numerical methods for kinetic theory

The evolution of the distribution function, as described by the Vlasov-Maxwell equation system, can be numerically computed using a variety of methods [3, 4]. These methods all rely on ordinary differential equation solvers to advance the solution in time, but have distinctly different means of discretizing phase space. Generally methods will fall into one of two categories: particle-in-cell (PIC) methods and continuum methods. In PIC methods the phase space distribution function is discretely sampled, whereas in continuum methods it is represented as a smooth function.

Historically, particle-in-cell methods have been the favored approach – they were the first to be developed, and the first to be extended to multiple spatial dimensions [3]. PIC methods sample a species distribution function with superparticles, each of which – through its charge and mass – typically represents many physical-world particles. These methods advance superparticles along trajectories in physical space in response to fields, which are computed on a fixed spatial mesh. Each superparticle has an associated position and velocity, and follows a trajectory given by characteristic curves prescribed by the Vlasov equation.

That is, a superparticle's state changes according to ordinary differential equations: the change in position depends on the velocity, and the change in velocity depends on the acceleration due to long-range forces. See Refs. [5, 6, 7, 8], for a review of PIC methods, their development, and applications. By evolving superparticles, PIC methods can represent a six-dimensional phase space distribution function in three spatial dimensions. As a result they have been successfully applied to model three-dimensional plasma phenomena. The accuracy of PIC methods is limited by the number of particles and the resolution of the spatial grid. Traditional PIC methods, which can be construed as Lagrangian methods in phase space, are typically second-order accurate in space and time [9, 10]. A well-known drawback of these methods is that they suffer from noise [11, 12, 13], such that the error associated with particle positions grows exponentially in time.

Continuum methods define a distribution function on a grid in phase space, and evolve it by solving the Vlasov equation directly. These methods include spectral, semi-Langrangian, and flux-based discretizations, and they evolve the full continuous distribution function in up to six-dimensional phase space. A comparison of these methods is presented in Ref. [4]. Spectral methods represent the distribution function by a finite set of analytic basis functions. The spatial dependence of the distribution function is typically represented by the Fourier basis, and the velocity dependence by either the Fourier basis or Hermite polynomials [14]. Distribution functions associated with colisionless plasmas can become very filamented in velocity space and are difficult to model with spectral methods because a large number of modes is needed to capture the solution, which presents a large computational expense [4]. Semi-Lagrangian methods take advantage of the fact that the distribution function is constant along characteristic curves. Given values of the distribution function at phase space mesh points, updated values are obtained by advecting the points along a characteristic and interpolating them back to the mesh. The viability of these methods was originally demonstrated in the seminal paper by Cheng and Knorr [15], and their applicability was formalized and extended by Sonnendrucker et al. [16]. These methods often employ splitting techniques, which can be computationally expensive in terms of memory [17].

Other continuum grid based methods for directly solving the Vlasov equation include finite-difference, finite-volume, and finite-element methods. These methods have been applied to a wide variety of partial differential equations including hyperbolic advection equations, but were originally considered to be impractical for generalized phase space simulations since the computational cost of these methods scales exponentially with the number of dimensions. Renewed interest in the application of these methods to the Vlasov equation has been facilitated by recent advances in supercomputing, which have enabled four-dimensional [18, 19] and five-dimensional [20, 21] simulations. Finite-volume and finite-element methods have been further enhanced through the use of high-order flux-based discretizations that ensure that the distribution function is locally and globally conserved [22, 23]. High-order methods improve the temporal and spatial accuracy of the solution. Unlike PIC methods, continuum methods are not subject to noise.

1.4 Thesis overview

This dissertation investigates a high-order finite-volume discretization of the Vlasov equation, with the aim of addressing some of the fundamental challenges with these types of grid-based approaches. Unlike fluid simulations in which the variables are physical quantities in a three-dimensional space that can be easily visualized, the value of the distribution function is an abstract quantity in phase space such that position and velocity are independent coordinates. This presents unique challenges in terms of: ensuring results are true to the physics, implementation of boundary conditions, implementation of non-Cartesian geometries, parallelization, and discretization of more than three dimensions. Theoretical analysis of the Vlasov equation – including linear and non-linear analysis – has spanned decades; however, due to the complexity of phase space analysis, many results are not in closed form [24], and benchmarks against which simulations can be quantitatively compared are scarce. Likewise the extensive developments for the treatment of boundaries and non-Cartesian geometries in PIC methods do not, in general, apply to continuum methods. The research described in this dissertation extends the scope of benchmark problems that can be used to assess kinetic simulations, and presents a mathematical and numerical formulation for accurately simulating axisymmetric plasmas in phase space.

Chapter 2 presents the governing equations of plasma kinetic theory. The focus is restricted to collisionless regimes, in which plasma particles collide infrequently. The Vlasov-Maxwell partial differential equation system that describes plasma dynamics in such regimes is cast into an alternative form that makes it conducive to being solved using finite-volume methods. Ultimately a non-dimensionalized weak conservation-law form of the equation system is derived for Cartesian and cylindrical phase space coordinates. A mathematical description of conducting wall and axis boundary conditions is given for phase space distribution functions and for electromagnetic fields. The mass, momentum, and energy diagnostics for phase space coordinates are also presented.

The fourth-order finite-volume discretization used to numerically approximate the solution to the Vlasov-Maxwell equation system is presented in Chapter 3. Convergence properties, temporal discretization, and the general approach to solving systems of hyperbolic partial differential equations are discussed. The spatial discretization, which constitutes the most complicated part of the finite-volume algorithm, is presented in detail. The method relies on a quadrature rule that is based on the integration of Taylor series approximations to analytic functions. This quadrature rule is applied to compute the surface integrals in the weak form of the Vlasov equation, the line integrals in the weak form of Maxwell's equations, and the diagnostics associated with the primary variables. The details of the spatial discretization are presented separately for Cartesian phase space coordinates and for cylindrical phase space coordinates, as the latter require a modified treatment. The complete algorithm is outlined for both coordinate systems.

Chapter 4 presents simulation results from well-known test problems for Cartesian phase space coordinates in electrostatic and electrodynamic regimes. In Chapter 5 a new benchmark is developed [1] based on the Dory-Guest-Harris instability, which is triggered by elec-

trostatic waves propagating through a warm uniformly-magnetized plasma. The closed-form version of the linear theory dispersion relation is derived, and solved to obtain concrete measures against which simulation results can be compared. Since most theoretical predictions for kinetic processes in plasmas involve infinite series and are often treated in limiting cases of delta-function distributions, the derivation of a closed-form expression for characterizing the behavior of warm plasmas presents a significant advance. The benchmark is demonstrated to be well-suited for continuum kinetic Vlasov-Poisson algorithms and demonstrates the value of a fourth-order discretization over a second-order discretization. It addresses one of the fundamental challenges associated with the development of kinetic solvers, which is the paucity of quantitative benchmarks.

Simulation results for cylindrical phase space coordinates are presented in Chapter 6. The discretization of the Poisson equation and Maxwell's equations in cylindrical coordinates are verified to be fourth-order accurate. The cylindrical coordinate Vlasov solver is first applied to model a uniform collisionless neutral gas with the aim of characterizing the singularity at the axis. The numerical solution is shown to converge at fourth-order to the exact solution. The Vlasov-Maxwell solver is then applied to an axisymmetric Z-pinch to model ions being radially confined by current-carrying electrons. To the author's knowledge this presents the first instance in which the cylindrical coordinate Vlasov equation is successfully solved in conservation-law form.

The computational aspects of the finite-volume calculations are presented in Chapter 7. This includes a discussion of the parallelization and the implications of extending the Vlasov-Maxwell solver to four and five phase space dimensions. The mathematical, numerical, and physical developments within this dissertation are summarized in Chapter 8.

Chapter 2

Governing equations of kinetic theory for collisionless plasmas

The kinetic theory description of a plasma stems from statistical mechanics in which a system of interacting particles can be represented by a probability density, in phase space. Instead of following the trajectories of individual charged particles, which would constitute an intractable N-body problem, all particles of a given species (e.g. electrons) are modeled by a scalar-valued distribution function in a position-velocity phase space. Multiple distribution functions are used to represent plasmas with multiple species of particles. Notably, unlike the dynamics of neutral particles in gases, the dynamics of plasma particles depend on long range forces due to electromagnetic fields. The evolution of a plasma is thus described by a coupled system of partial differential equations: the Boltzmann equation for each distribution function and Maxwell's equations for the electromagnetic fields. In cases where collisions between particles can be neglected, the Boltzmann equation reduces to the Vlasov equation.

2.1 Distribution function evolution

Kinetic theory of plasmas treats each constituent particle species as a probability distribution function in a position-velocity phase space. The probability distribution function $f_s(\boldsymbol{x}, \boldsymbol{v}, t)$ for species s depends on the position coordinate $\boldsymbol{x}$, velocity coordinate $\boldsymbol{v}$, and time t. The position and velocity coordinates are independent of each other and the local value of the distribution function indicates the probability, per unit phase space volume, of finding particles in a localized neighborhood of phase space, i.e. at position $\boldsymbol{x}$, moving at velocity $\boldsymbol{v}$. In practice the value of f_s typically represents the probability density rather than a probability, which means that instead of being normalized to one, the distribution function is normalized such that its integral gives the total number of particles in the system of interest.

2.1.1 Boltzmann-Maxwell equation system

The mathematical description for the evolution of each distribution function in phase space, subject to the effects of collisions and forces, is given by the Boltzmann equation,

$$\frac{\partial f_s}{\partial t} + \boldsymbol{v} \cdot \frac{\partial f_s}{\partial \boldsymbol{x}} + \boldsymbol{a} \cdot \frac{\partial f_s}{\partial \boldsymbol{v}} = \left(\frac{\partial f_s}{\partial t} \right)_{collisions} \tag{2.1}$$

where $\boldsymbol{a}$ is the acceleration. If the acceleration of particles in a given system is purely due to electromagnetic fields, then

$$\boldsymbol{a} = \frac{q_s}{m_s} \left(\boldsymbol{E} + \boldsymbol{v} \times \boldsymbol{B} \right) \tag{2.2}$$

where q_s is the charge and m_s is the mass of a species s particle. The term on the righthand side of Eq. (2.1) is shorthand notation for a collision operator that defines how a distribution function changes due to interspecies and intraspecies particle collisions. The specific form of this operator depends on the statistics that the plasma particles obey. Examples of collision operators with varying degrees of sophistication include the BGK operator [25], and various forms of the Fokker-Planck operator [26]. In the limit of no collisions the collision operator term is simply set to zero, and the Boltzmann equation reduces to the collisionless Boltzmann equation, commonly referred to as the Vlasov equation.

Electric field $\boldsymbol{E}$ and magnetic field $\boldsymbol{B}$, which are functions of position $\boldsymbol{x}$ and time t, appear in the Boltzmann equation and their evolution is described by Maxwell's equations,

$$\nabla \cdot \boldsymbol{E} = \frac{1}{\epsilon_0} \sum_s q_s n_s \tag{2.3}$$

$$\nabla \cdot \boldsymbol{B} = 0 \tag{2.4}$$

$$\nabla \times \boldsymbol{E} = -\frac{\partial \boldsymbol{B}}{\partial t} \tag{2.5}$$

$$\nabla \times \boldsymbol{B} = \mu_0 \boldsymbol{J} + \mu_0 \epsilon_0 \frac{\partial \boldsymbol{E}}{\partial t}, \tag{2.6}$$

where ϵ_0 is the vacuum permittivity and μ_0 is the permeability of free space. The species number density n_s is defined in terms of the zeroth velocity moment of the distribution function,

$$n_s(\boldsymbol{x}, t) = \int f_s(\boldsymbol{x}, \boldsymbol{v}, t) d\boldsymbol{v}, \tag{2.7}$$

and the net current $\boldsymbol{J}$ is defined in terms of the first moment of each distribution function, such that

$$\boldsymbol{J}(\boldsymbol{x}, t) = \sum_s q_s \int \boldsymbol{v} f_s(\boldsymbol{x}, \boldsymbol{v}, t) d\boldsymbol{v}, \tag{2.8}$$

where the integrals in Eqs. (2.7) and (2.8) are over the entire velocity space. Faraday's law given by Eq. (2.5) and Ampere's law given by Eq. (2.6) govern the evolution of the fields, whereas Gauss's laws for the electric field (Eq. (2.3)) and magnetic field (Eq. (2.4)) place constraints on their spatial variation. The evolution of the plasma state, defined by variables f_s, $\boldsymbol{E}$ and $\boldsymbol{B}$, is thus governed by non-linearly coupled partial differential equations that describe the self-consistent transport of the particle distribution in phase space and the transport of electromagnetic fields in physical space.

2.1.2 Collisionless plasmas and the Vlasov equation

Since this dissertation is concerned with collisionless plasmas whose transport is dominated by long-range electromagnetic field forces, the Boltzmann equation in the limit of no collisions encapsulates the physics of interest. Nevertheless, it's illustrative to consider both the high collisionality and low collisionality limit, as these have important implications with regard to the physical behavior of a plasma system. In particular, collisionless and semi-collisional plasmas are in some sense more complex than plasmas in which constituent particles collide frequently.

In the limit of high collisionality, plasma particles have small mean free paths relative to the system size and thereby they quickly exchange momentum and energy. This drives the system of particles towards thermodynamic equilibrium, which means that the velocity dependence of the distribution function tends toward a Maxwellian profile. When the velocity dependence of the distribution function can be assumed to be Maxwellian or a profile close to a Maxwellian, the kinetic theory description can be reduced to a simpler fluid theory description. Fluid theory typically preserves information only about the first three velocity moments of the distribution function. Fluid theory variables can be derived by taking velocity moments of the distribution function to obtain species density (see Eq. (2.7)), momentum, and energy. The evolution equations for density, momentum, and energy can be obtained by taking successive velocity moments of the Boltzmann equation. In theory the number of velocity moments can be infinite, but in practice it is typically truncated after three moments – enough to fully describe a Maxwellian profile. Thus in the limit of high collisionality the associated dynamics of the plasma are greatly simplified and the six-dimensional equation system can be reduced to a three-dimensional equation system. By allowing for arbitrary distribution functions, the kinetic theory description is a generalization of fluid theory, and encapsulates physics that is not captured by fluid models.

In the limit in which collisions are negligible, the collision operator on the righthand side of Eq. (2.1) is set to zero. The resulting expression is the collisionless Boltzmann equation, more commonly known as the Vlasov equation,

$$\frac{\partial f_s}{\partial t} + \boldsymbol{v} \cdot \frac{\partial f_s}{\partial \boldsymbol{x}} + \frac{q_s}{m_s} \left(\boldsymbol{E} + \boldsymbol{v} \times \boldsymbol{B} \right) \cdot \frac{\partial f_s}{\partial \boldsymbol{v}} = 0. \tag{2.9}$$

The expression states that the total derivative of f with respect to time is zero, with the rate of change of the position $d\boldsymbol{x}/dt$ given by the velocity coordinate, and the rate of change

of velocity $d\boldsymbol{v}/dt$ given by the acceleration due to the Lorentz force. The Vlasov equation describes the evolution of a distribution function for a plasma in which the mean free path is large relative to the size of the system, and the dominant means of interaction between plasma particles is through electromagnetic forces. The evolution of the fields is governed by Maxwell's equations (Eqs. (2.3) – (2.6)). Collisionless plasmas are typically characterized by having low-density and/or high-temperatures. Without collisions to drive a distribution function toward thermodynamic equilibrium, the behavior of collisionless plasmas can be more complicated than that of collisional plasmas. Being able to capture – with high-fidelity – the rich physics of a collisionless plasma system is one of the primary motivators for the development of robust numerical solvers for the Vlasov equation. Moreover the Vlasov equation forms the foundation for more generalized semi-collisional processes described by the Boltzmann equation, hence numerical advances for the Vlasov equation apply directly to the Boltzmann equation.

2.2 Normalization

It is convenient to express the Vlasov-Maxwell equation system in terms of non-dimensional variables by normalizing each variable to a characteristic value. The motivation for doing this is threefold. Non-dimensionalized form allows for the direct comparison of the magnitudes of terms in the equation and thereby one can make conclusions about their relative importance. The resulting equation system is unit-independent, which is especially advantageous in the field of plasmas in which different unit systems (the Gaussian centimeter-gram-second unit system and the meter-kilogram-second unit system) are often used. From a physics standpoint, non-dimensionalized form ensures self-similar solutions for problems in which parameters are proportionately scaled thereby simplifying the comparison of physical systems that have different scales.

The precise form of the non-dimensionalized equation system depends on the choice of characteristic values chosen to carry out the normalization. Thereby normalizations are not unique. Here one non-dimensionalized form of the Vlasov-Maxwell equation system is derived. For plasmas in which the fields are electrostatic, the non-dimensionalized form of the Vlasov equation with Gauss's law divergence constraint is subsequently derived.

2.2.1 Normalized Vlasov-Maxwell equation system

The normalization of the Vlasov-Maxwell equation system is carried out by first expressing the variables in terms of their normalized counterparts and dimensional characteristic values. Let tildes denote normalized, that is, non-dimensionalized parameters. Then the variables

of interest in terms of normalized quantities are

$$\begin{aligned} t &= \tilde{t}\tau & \boldsymbol{x} &= \tilde{\boldsymbol{x}}L & \boldsymbol{v} &= \tilde{\boldsymbol{v}}v_0 \\ f_s &= \tilde{f}_s n_0 & q_s &= Z_s e & m_s &= M_s m_p \\ \boldsymbol{E} &= \tilde{\boldsymbol{E}}E_0 & \boldsymbol{B} &= \tilde{\boldsymbol{B}}B_0 \end{aligned}$$

where $\tau, L, v_0, n_0, e, m_p, E_0$, and B_0 are characteristic values for time, length, velocity, density, charge, mass, electric field, and magnetic field, respectively. Note that mass m_s and charge q_s are constants, whose characteristic values are chosen to be the proton mass and the proton charge, respectively. Thus for a proton, the normalized mass is $M_s = 1$ and the normalized charge is $Z_s = 1$. Substituting the above definitions into Eq. (2.9) yields the Vlasov equation in terms of normalized variables and characteristic values:

$$\frac{n_0}{\tau}\frac{\partial \tilde{f}_s}{\partial \tilde{t}} + \frac{n_0 v_0}{L}\tilde{\boldsymbol{v}}\cdot\frac{\partial \tilde{f}_s}{\partial \tilde{\boldsymbol{x}}} + \frac{n_0 e E_0}{m_p v_0}\frac{Z_s}{M_s}\left(\tilde{\boldsymbol{E}} + \frac{B_0 v_0}{E_0}\tilde{\boldsymbol{v}}\times\tilde{\boldsymbol{B}}\right)\cdot\frac{\partial \tilde{f}_s}{\partial \tilde{\boldsymbol{v}}} = 0. \tag{2.10}$$

Let the characteristic velocity be the characteristic length divided by the characteristic time, such that

$$v_0 = L/\tau. \tag{2.11}$$

Substituting Eq. (2.11) into Eq. (2.10) and dividing through by n_0/τ, yields a modified expression for the Vlasov equation,

$$\frac{\partial \tilde{f}_s}{\partial \tilde{t}} + \tilde{\boldsymbol{v}}\cdot\frac{\partial \tilde{f}_s}{\partial \tilde{\boldsymbol{x}}} + \frac{eE_0}{m_p L}\tau^2\frac{Z_s}{M_s}\left(\tilde{\boldsymbol{E}} + \frac{B_0 v_0}{E_0}\tilde{\boldsymbol{v}}\times\tilde{\boldsymbol{B}}\right)\cdot\frac{\partial \tilde{f}_s}{\partial \tilde{\boldsymbol{v}}} = 0. \tag{2.12}$$

The variables in Maxwell's equations are likewise replaced with non-dimensionalized variables and characteristic values. Faraday's law (Eq. (2.5)) then becomes

$$\frac{B_0}{\tau}\frac{\partial \tilde{\boldsymbol{B}}}{\partial \tilde{t}} + \frac{E_0}{L}\frac{\partial}{\partial \tilde{\boldsymbol{x}}}\times\tilde{\boldsymbol{E}} = 0, \tag{2.13}$$

which can be rearranged and simplified to yield

$$\frac{\partial \tilde{\boldsymbol{B}}}{\partial \tilde{t}} + \frac{E_0}{B_0 v_0}\frac{\partial}{\partial \tilde{\boldsymbol{x}}}\times\tilde{\boldsymbol{E}} = 0. \tag{2.14}$$

Ampere's law (Eq. (2.6)) in terms of normalized variables is

$$-\frac{\epsilon_0\mu_0 E_0}{\tau}\frac{\partial \tilde{\boldsymbol{E}}}{\partial \tilde{t}} + \frac{B_0}{L}\frac{\partial}{\partial \tilde{\boldsymbol{x}}}\times\tilde{\boldsymbol{B}} = \mu_0 e v_0 n_0 \sum_s Z_s \int \tilde{\boldsymbol{v}}\tilde{f}_s(\tilde{\boldsymbol{x}},\tilde{\boldsymbol{v}},\tilde{t})d\tilde{\boldsymbol{v}}, \tag{2.15}$$

which can be simplified to yield

$$-\frac{\partial \tilde{\boldsymbol{E}}}{\partial \tilde{t}} + \frac{c^2}{v_0^2}\frac{B_0 v_0}{E_0}\frac{\partial}{\partial \tilde{\boldsymbol{x}}}\times\tilde{\boldsymbol{B}} = \frac{e n_0 L}{\epsilon_0 E_0}\sum_s Z_s \int \tilde{\boldsymbol{v}}\tilde{f}_s(\tilde{\boldsymbol{x}},\tilde{\boldsymbol{v}},\tilde{t})d\tilde{\boldsymbol{v}}. \tag{2.16}$$

The speed of light is defined as $c = (\epsilon_0 \mu_0)^{-1/2}$.

The normalized partial differential equations given by Eq. (2.12), Eq. (2.14), and Eq. (2.16) can be further simplified by specifying the relationships between the characteristic values, and using physical quantities of interest. In plasma physics the plasma frequency, defined for species s as

$$\omega_{ps} = \sqrt{\frac{(Z_s e)^2 n_0}{\epsilon_0 m_s}} \tag{2.17}$$

is an important scale length set by physical constants and by the characteristic number density n_0. The cyclotron frequency is likewise an important scale length set by physical constants and the value of the characteristic magnetic field B_0, such that for species s the cyclotron frequency is

$$\omega_{cs} = \frac{Z_s e B_0}{m_s}. \tag{2.18}$$

Thus it is convenient to express the characteristic values for the electric and magnetic fields in terms of these physically-relevant frequencies. In this case, the proton plasma frequency ω_{pp} and proton cyclotron frequency ω_{cp} are chosen as the relevant scales, such that the characteristic fields are defined as

$$E_0 = \frac{e n_0 L}{\epsilon_0} = \frac{m_p L}{e} \omega_{pp}^2 \tag{2.19}$$

$$B_0 = \frac{m_p}{e} \omega_{cp}. \tag{2.20}$$

Note that for the purpose of the investigations conducted here, the ions of interest are protons; however, any particle species can be chosen to define the characteristic values of the fields. Substituting Eq. (2.19) and Eq. (2.20) into Eq. (2.14) and Eq. (2.16) yields the normalized form of Maxwell's equations, such that the normalized form of Faraday's law is

$$\frac{\partial \tilde{\boldsymbol{B}}}{\partial \tilde{t}} + \frac{(\omega_{pp}\tau)^2}{(\omega_{cp}\tau)} \frac{\partial}{\partial \tilde{\boldsymbol{x}}} \times \tilde{\boldsymbol{E}} = 0, \tag{2.21}$$

and the normalized form of Ampere's law is

$$-\frac{\partial \tilde{\boldsymbol{E}}}{\partial \tilde{t}} + \frac{(\omega_{cp}\tau)}{(\omega_{pp}\tau)^2} \left(\frac{c}{v_0}\right)^2 \frac{\partial}{\partial \tilde{\boldsymbol{x}}} \times \tilde{\boldsymbol{B}} = \sum_s Z_s \int \tilde{\boldsymbol{v}} \tilde{f}_s(\tilde{\boldsymbol{x}}, \tilde{\boldsymbol{v}}, \tilde{t}) d\tilde{\boldsymbol{v}}. \tag{2.22}$$

Substituting the characteristic field values given by Eq. (2.19) and Eq. (2.20) into Eq. (2.12) gives the normalized Vlasov equation,

$$\frac{\partial \tilde{f}_s}{\partial \tilde{t}} + \tilde{\boldsymbol{v}} \cdot \frac{\partial \tilde{f}_s}{\partial \tilde{\boldsymbol{x}}} + \frac{Z_s}{M_s} \left[(\omega_{pp}\tau)^2 \tilde{\boldsymbol{E}} + (\omega_{cp}\tau) \tilde{\boldsymbol{v}} \times \tilde{\boldsymbol{B}} \right] \cdot \frac{\partial \tilde{f}_s}{\partial \tilde{\boldsymbol{v}}} = 0. \tag{2.23}$$

Thus the normalized Vlasov-Maxwell equation system is given by Eq. (2.21), Eq. (2.22), and Eq. (2.23). The system is characterized by the species charge state Z_s, species mass ratio M_s, and non-dimensional parameters c/v_0, $\omega_{pp}\tau$, and $\omega_{cp}\tau$. In order to completely specify the system scales, a characteristic time τ and a characteristic velocity v_0 must be set. Note that by setting these two values, the characteristic length L is also specified from the relation given in Eq. (2.11). A logical choice is to set the characteristic time to be the inverse of the proton plasma period, such that $\tau = \omega_{pp}^{-1}$. In this case $\omega_{pp}\tau = 1$, and $\omega_{cp}\tau = \omega_{cp}/\omega_{pp}$. Logical choices for the characteristic velocity are the speed of light c, and the proton thermal speed v_T. If the characteristic velocity is chosen to be the speed of light then $c/v_0 = 1$ and the characteristic length is given by the proton skin depth δ_p,

$$L = \frac{c}{\omega_{pp}} = \delta_p. \tag{2.24}$$

If the characteristic velocity is chosen to be the proton thermal speed then $c/v_0 = c/v_T$ and the characteristic length is in effect the Debye length λ_D,

$$L = \frac{v_T}{\omega_{pp}} = \lambda_D, \tag{2.25}$$

which is another physically-relevant quantity in plasma physics. Thus the characteristic speed defines whether small spatial scales (Eq. (2.24)) or large spatial scales (Eq. (2.25)) are of interest.

For the purposes of numerical investigations conducted here, and unless otherwise specified, the characteristic time is chosen to be the proton plasma frequency, and the characteristic velocity is chosen to be the speed of light, such that the normalized Vlasov-Maxwell equation system takes on the simplified form

$$\frac{\partial f_s}{\partial t} + \boldsymbol{v} \cdot \frac{\partial f_s}{\partial \boldsymbol{x}} + \frac{Z_s}{M_s}\left[\boldsymbol{E} + \left(\frac{\omega_{cp}}{\omega_{pp}}\right)\boldsymbol{v} \times \boldsymbol{B}\right] \cdot \frac{\partial f_s}{\partial \boldsymbol{v}} = 0 \tag{2.26}$$

$$\frac{\partial \boldsymbol{B}}{\partial t} + \frac{\omega_{pp}}{\omega_{cp}}\frac{\partial}{\partial \boldsymbol{x}} \times \boldsymbol{E} = 0 \tag{2.27}$$

$$\frac{\partial \boldsymbol{E}}{\partial t} - \frac{\omega_{cp}}{\omega_{pp}}\frac{\partial}{\partial \boldsymbol{x}} \times \boldsymbol{B} = -\sum_s Z_s \int \boldsymbol{v} f_s(\boldsymbol{x}, \boldsymbol{v}, t) d\boldsymbol{v}, \tag{2.28}$$

where the tildes ($\tilde{}$) denoting normalized variables have been dropped for clarity.

Note that the derived normalized form of the Vlasov-Maxwell equation system does not incorporate the divergence constraint equations given by Gauss's law for the electric field (Eq. (2.3)) and Gauss's law for the magnetic field (Eq. (2.4)). The constraints are not needed to define the normalized system in which the time dependence of the electromagnetic fields is explicitly described by Faraday's law (Eq. (2.5)) and Ampere's law (Eq. (2.6)).

2.2.2 Normalization for Vlasov equation with electrostatic fields

In plasmas in which charges move slowly compared to the speed of light, the fields can be approximated as being electrostatic. In effect the electric field is assumed to be irrotational,

and by Faraday's law the magnetic field does not change in time. If fields are electrostatic then Gauss's law replaces Faraday's law and Ampere's law as the relevant electric field evolution equation. Here the normalized form of the Vlasov equation coupled to Gauss's law for the electric field is derived in two ways: using Gauss's law in its usual form, and using Gauss's law reexpressed as Poisson's equation.

2.2.2.1 Vlasov equation coupled to Gauss's law

Following the same steps as the derivation of the normalized Vlasov-Maxwell system described in Section Section 2.2.1, the normalized form of the electrostatic system described by the Vlasov equation (see Eq. (2.9)) and Gauss's law for electric field (see Eq. (2.3)) is derived. Note that the normalized from of Gauss's law for the magnetic field (see Eq. (2.4)) is trivial. For the electrostatic system, variables are replaced with non-dimensionalized variables and characteristic values, such that the Vlasov equation takes on the form given by Eq. (2.12) and Gauss's law in terms of normalized variables is

$$\frac{\partial}{\partial \tilde{\boldsymbol{x}}} \cdot \tilde{\boldsymbol{E}} = \frac{e n_0 L}{\epsilon_0 E_0} \sum_s Z_s \int \tilde{f}_s(\tilde{\boldsymbol{x}}, \tilde{\boldsymbol{v}}, \tilde{t}) d\tilde{\boldsymbol{v}}. \tag{2.29}$$

The characteristic electric field value E_0 and magnetic field value B_0 are defined in Eq. (2.19) and Eq. (2.20). Substituting these definitions into the above expression yields

$$\frac{\partial}{\partial \tilde{\boldsymbol{x}}} \cdot \tilde{\boldsymbol{E}} = \frac{e n_0 L}{\epsilon_0 \left(\frac{e n_0 L}{\epsilon_0}\right)} \sum_s Z_s \int \tilde{f}_s(\tilde{\boldsymbol{x}}, \tilde{\boldsymbol{v}}, \tilde{t}) d\tilde{\boldsymbol{v}} \tag{2.30}$$

and into the normalized Vlasov equation yields

$$\frac{\partial \tilde{f}_s}{\partial \tilde{t}} + \tilde{\boldsymbol{v}} \cdot \frac{\partial \tilde{f}_s}{\partial \tilde{\boldsymbol{x}}} + \frac{e\left(\frac{e n_0 L}{\epsilon_0}\right)}{m_p L} \tau^2 \frac{Z_\alpha}{A_\alpha} \left(\tilde{\boldsymbol{E}} + \frac{\left(\frac{m_p \omega_{cp}}{e}\right) v_0}{\left(\frac{e n_0 L}{\epsilon_0}\right)} \tilde{\boldsymbol{v}} \times \tilde{\boldsymbol{B}} \right) \cdot \frac{\partial \tilde{f}_s}{\partial \tilde{\boldsymbol{v}}} = 0 \tag{2.31}$$

$$\frac{\partial \tilde{f}_s}{\partial \tilde{t}} + \tilde{\boldsymbol{v}} \cdot \frac{\partial \tilde{f}_s}{\partial \tilde{\boldsymbol{x}}} + \omega_{pp}^2 \tau^2 \frac{Z_s}{M_s} \left(\tilde{\boldsymbol{E}} + \frac{\omega_{cp}}{\omega_{pp}^2 \tau} \tilde{\boldsymbol{v}} \times \tilde{\boldsymbol{B}} \right) \cdot \frac{\partial \tilde{f}_s}{\partial \tilde{\boldsymbol{v}}} = 0, \tag{2.32}$$

where the plasma and cyclotron frequencies are defined for a proton as in Eq. (2.17) and Eq. (2.18). The normalized Vlasov-Gauss system is thus

$$\frac{\partial f_s}{\partial t} + \boldsymbol{v} \cdot \frac{\partial f_s}{\partial \boldsymbol{x}} + \frac{Z_s}{M_s} \Big[(\omega_{pp}\tau)^2 \boldsymbol{E} + (\omega_{cp}\tau) \boldsymbol{v} \times \boldsymbol{B} \Big] \cdot \frac{\partial f_s}{\partial \boldsymbol{v}} = 0 \tag{2.33}$$

$$\frac{\partial}{\partial \boldsymbol{x}} \cdot \boldsymbol{E} = \sum_s Z_s \int f_\alpha(\boldsymbol{v}) d\boldsymbol{v}, \tag{2.34}$$

where the tildes denoting non-dimensional variables have been dropped for clarity. The expression for the Vlasov equation can be further simplified by setting the characteristic

time to be the inverse of the proton plasma frequency, $\tau = \omega_{pp}^{-1}$. Note that unlike in the Vlasov-Maxwell equation system, in which a characteristic velocity v_0 and characteristic time τ together set the characteristic length scale (see Eqs. (2.24) and (2.25)), neither the characteristic velocity nor the characteristic length appear in the normalized form of the Vlasov-Gauss equation system. In effect field information propagates at infinite speed in an electrostatic system.

2.2.2.2 Vlasov-Poisson equation system

In the electrostatic limit, the electric field can be expressed as the gradient of a scalar potential ϕ, such that

$$\boldsymbol{E} = -\nabla\phi. \tag{2.35}$$

Substituting Eq. (2.35) into Eq. (2.3) gives rise to Poisson's equation for the electrostatic potential,

$$-\nabla^2\phi = \frac{1}{\epsilon_0}\sum_s q_s \int f_s(\boldsymbol{x}, \boldsymbol{v}, t) d\boldsymbol{v}. \tag{2.36}$$

It's often more convenient to solve for the electric field by first solving Eq. (2.36) for the potential. For electrostatic physics, the Vlasov-Poisson system is equivalent to the Vlasov-Gauss equation system, and it's important that the two systems have consistent normalized forms. As such, the normalized form of the Vlasov-Poisson system is derived here.

The electrostatic potential can be expressed as a product of a non-dimensional variable $\tilde{\phi}$ and a characteristic value ϕ_0, such that $\phi = \tilde{\phi}\phi_0$. The spatial gradient of the potential is then given by

$$\nabla\phi = \frac{\phi_0}{L}\nabla\tilde{\phi}$$

and the Laplacian operator applied to the potential is

$$\nabla^2\phi = \frac{\phi_0}{L^2}\nabla^2\tilde{\phi}.$$

Substituting the normalization into Eq. (2.36) yields

$$-\frac{\phi_0}{L^2}\nabla^2\tilde{\phi} = \frac{en_0}{\epsilon_0}\sum_s Z_s \int \tilde{f}_s(\tilde{\boldsymbol{x}}, \tilde{\boldsymbol{v}}, \tilde{t}) d\tilde{\boldsymbol{v}}. \tag{2.37}$$

Defining the characteristic electrostatic potential in terms of the other characteristic quantities yields the relation

$$\phi_0 = \frac{en_0L^2}{\epsilon_0}, \tag{2.38}$$

which is consistent with the definition of the characteristic electric field given in Eq. (2.19). The normalized Poisson equation is thus

$$-\nabla^2\tilde{\phi} = \sum_s Z_s \int \tilde{f}_s(\tilde{\boldsymbol{x}}, \tilde{\boldsymbol{v}}, t) d\tilde{\boldsymbol{v}}. \tag{2.39}$$

Substituting the normalized variables including the normalized electrostatic potential defined in Eq. (2.38) into the Vlasov equation and simplifying yields

$$\frac{n_0}{\tau}\frac{\partial \tilde{f}_s}{\partial \tilde{t}} + \frac{n_0 v_0}{L}\tilde{\boldsymbol{v}} \cdot \frac{\partial \tilde{f}_s}{\partial \tilde{\boldsymbol{x}}} + \frac{n_0 e}{m_p v_0}\frac{Z_s}{M_s}\left(-\frac{\phi_0}{L}\nabla\tilde{\phi} + B_0 v_0 \tilde{\boldsymbol{v}} \times \tilde{\boldsymbol{B}}\right) \cdot \frac{\partial \tilde{f}_s}{\partial \tilde{\boldsymbol{v}}} = 0. \tag{2.40}$$

Dividing through by n_0/τ, and using the relationship between characteristic speed and characteristic length given in Eq. (2.11) yields

$$\frac{\partial \tilde{f}_s}{\partial \tilde{t}} + \tilde{\boldsymbol{v}} \cdot \frac{\partial \tilde{f}_s}{\partial \tilde{\boldsymbol{x}}} + \frac{e\phi_0\tau^2}{m_p L^2}\frac{Z_s}{M_s}\left(-\nabla\tilde{\phi} + \frac{B_0 L^2}{\phi_0 \tau}\tilde{\boldsymbol{v}} \times \tilde{\boldsymbol{B}}\right) \cdot \frac{\partial f_s}{\partial \boldsymbol{v}} = 0. \tag{2.41}$$

The definition of the characteristic potential (Eq. (2.38)) and the definition given in Eq. (2.20) for the characteristic magnetic field are substituted into the above expression. Thus the Vlasov equation becomes

$$\frac{\partial \tilde{f}_s}{\partial \tilde{t}} + \tilde{\boldsymbol{v}} \cdot \frac{\partial \tilde{f}_s}{\partial \tilde{\boldsymbol{x}}} + \frac{e\left(en_0L^2/\epsilon_0\right)\tau^2}{m_p L^2}\frac{Z_s}{M_s}\left(-\nabla\tilde{\phi} + \frac{\left(\frac{m_p\omega_{cp}}{e}\right)L^2}{\left(en_0L^2/\epsilon_0\right)\tau}\tilde{\boldsymbol{v}} \times \tilde{\boldsymbol{B}}\right) \cdot \frac{\partial \tilde{f}_s}{\partial \tilde{\boldsymbol{v}}} = 0. \tag{2.42}$$

Using the definitions of plasma and cyclotron frequencies given in Eq. (2.17) and Eq. (2.18), the resulting normalized form of the Vlasov-Poisson equation system is

$$\frac{\partial f_s}{\partial t} + \boldsymbol{v} \cdot \frac{\partial f_s}{\partial \boldsymbol{x}} + \frac{Z_s}{M_s}\left((\omega_{pp}\tau)^2(-\nabla\phi) + (\omega_{cp}\tau)\boldsymbol{v} \times \boldsymbol{B}\right) \cdot \frac{\partial f_s}{\partial \boldsymbol{v}} = 0 \tag{2.43}$$

$$-\nabla^2\phi = \sum_s Z_s \int f_s(\boldsymbol{x}, \boldsymbol{v}, t) d\boldsymbol{v}, \tag{2.44}$$

where the tildes have been dropped for clarity. Note that this normalized equation system is consistent with the Vlasov-Gauss system given by Eq. (2.33) and Eq. (2.34).

2.3 Vlasov equation in conservation-law weak form

The Vlasov equation as it has been presented thus far, with velocity dotted with the spatial gradient and acceleration dotted with the velocity gradient, has been expressed in its Liouville form. This form stems from Hamiltonian mechanics and is the form most often seen in literature. When solving hyperbolic partial differential equations, such as the Vlasov equation, it is often desirable to express them in conservation-law form. Conservation-law

form is a natural formulation in the context of continuum mechanics and in general states that within a given volume the change in time of a quantity q depends on the divergence of the flux (or flow) of q in that volume:

$$\frac{\partial q}{\partial t} + \nabla \cdot \boldsymbol{F}(q) = 0, \tag{2.45}$$

where $\boldsymbol{F}$ is the flux. Integrating this expression over a control volume V and applying the divergence theorem, which equates the volume integral of a divergence to a surface integral over a boundary ∂V, yields the conservation-law weak form

$$\frac{\partial}{\partial t}\int_V q dV + \int_V \nabla \cdot \boldsymbol{F} dV = 0 \tag{2.46}$$

$$\frac{\partial}{\partial t}\int_V q dV + \oint_{\partial V} \boldsymbol{F} \cdot d\boldsymbol{S} = 0, \tag{2.47}$$

which states that in a given volume the change in time of a quantity q depends on the flux of the quantity through the boundaries of the volume. The weak form given by Eq. (2.47) is useful because it can be numerically solved in a way that exactly satisfies the discrete form of the divergence theorem, thereby ensuring that to numerical precision the quantity of interest can be exactly conserved – both locally and globally. The weak form, unlike the strong form, admits solutions that can have local discontinuities, which makes it physically the more relevant form.

For the Vlasov equation the volume of interest is a phase space volume, and the conserved quantity of interest is the volume-integrated distribution function. Mathematically the Liouville and conservation-law forms are equivalent, but numerically the conservation-law form has properties that make it advantageous. Here the conservation-law strong and weak forms of the Vlasov equation are derived for both Cartesian and cylindrical phase space coordinates. The latter present additional complexity on account of the relationship between Cartesian and cylindrical phase space coordinates, and the necessity that strong and weak forms are consistent between coordinate systems.

2.3.1 Cartesian coordinates

In Cartesian phase space coordinates the strong Liouville form of the Vlasov equation can be readily expressed in terms of a divergence of fluxes, i.e. in conservation-law strong form:

$$0 = \frac{\partial f_s}{\partial t} + \frac{\partial}{\partial \boldsymbol{x}} \cdot (\boldsymbol{v} f_s) + \frac{\partial}{\partial \boldsymbol{v}} \cdot \left(\frac{Z_s}{M_s} \left[\boldsymbol{E} + \frac{\omega_{cp}}{\omega_{pp}} \boldsymbol{v} \times \boldsymbol{B} \right] f_s \right). \tag{2.48}$$

This expression is obtained by applying the product rule of differentiation to Eq. (2.26), and noting that the velocity coordinate is independent of the spatial coordinate, that fields are

only a function of position and time, and that

$$\frac{\partial}{\partial \boldsymbol{v}} \cdot (\boldsymbol{v} \times \boldsymbol{B}) = \begin{bmatrix} \frac{\partial}{\partial v_x}(v_y B_z - v_z B_y) \\ \frac{\partial}{\partial v_y}(v_z B_x - v_x B_z) \\ \frac{\partial}{\partial v_z}(v_x B_y - v_y B_x) \end{bmatrix} = \begin{bmatrix} 0 \\ 0 \\ 0 \end{bmatrix}. \tag{2.49}$$

Integrating the conservation-law strong form of the Vlasov equation over a volume V, with differential volume $dV = dxdydydv_xdv_ydv_z$, yields the weak form

$$0 = \frac{\partial}{\partial t}\int f_s dV + \int \frac{\partial}{\partial \boldsymbol{w}} \cdot \boldsymbol{F} dV \tag{2.50}$$

$$0 = \frac{\partial}{\partial t}\int f_s dV + \oint \boldsymbol{F} \cdot d\boldsymbol{S}, \tag{2.51}$$

where the coordinate $\boldsymbol{w}$, the flux $\boldsymbol{F}$, and the differential surface $d\boldsymbol{S}$ in each direction is given by

$$\boldsymbol{w} = \begin{bmatrix} x \\ y \\ z \\ v_x \\ v_y \\ v_z \end{bmatrix}, \quad \boldsymbol{F} = \begin{bmatrix} v_x f_s \\ v_y f_s \\ v_z f_s \\ \frac{Z_s}{M_s}\left(E_x + \frac{\omega_{cp}}{\omega_{pp}}(v_y B_z - v_z B_y)\right) f_s \\ \frac{Z_s}{M_s}\left(E_x + \frac{\omega_{cp}}{\omega_{pp}}(v_z B_x - v_x B_z)\right) f_s \\ \frac{Z_s}{M_s}\left(E_x + \frac{\omega_{cp}}{\omega_{pp}}(v_x B_y - v_y B_x)\right) f_s \end{bmatrix}, \quad d\boldsymbol{S} = \begin{bmatrix} dydzdv_xdv_ydv_z \\ dxdzdv_xdv_ydv_z \\ dxdydv_xdv_ydv_z \\ dxdydzdv_ydv_z \\ dxdydzdv_xdv_z \\ dxdydzdv_xdv_y \end{bmatrix}. \tag{2.52}$$

Thus the change in time of f_s in a given six-dimensional phase space volume depends on the flow of f_s through the five-dimensional surfaces that define the boundaries of the volume. Notably the fluxes along spatial coordinates have a distinctly different form from the fluxes along the velocity coordinates.

2.3.2 Cylindrical coordinates

Deriving the conservation-law form of the Vlasov equation in cylindrical phase space coordinates is not as straightforward as for the case of Cartesian coordinates. This is due to the fact that the divergence operator consists of derivatives with respect to position and velocity, which are independent variables, but are physically related. To illustrate this nuance, a derivation of the strong Liouville form of the cylindrical Vlasov equation is presented. The strong Liouville form can be obtained by using Lamé coefficients as in Ref. [27], by using Christoffel symbols as in Ref. [28], or through a coordinate transformation of the strong Liouville form of the Cartesian coordinate Vlasov equation, as is done here.

The definitions of the phase space coordinates in the two systems are

$$\boldsymbol{x}_{car} = (x, y, z) \tag{2.53}$$
$$\boldsymbol{v}_{car} = (\dot{x}, \dot{y}, \dot{z}) = (v_x, v_y, v_z) \tag{2.54}$$
$$\boldsymbol{x}_{cyl} = (r, \theta, z) \tag{2.55}$$
$$\boldsymbol{v}_{cyl} = (\dot{r}, r\dot{\theta}, z) = (v_r, v_\theta, v_z) \tag{2.56}$$

where $\dot{}$ denotes time derivative. The position, velocity, and acceleration in cylindrical coordinates can be expressed in terms of Cartesian counterparts as follows:

$$\boldsymbol{x}_{cyl} = \begin{bmatrix} r \\ \theta \\ z \end{bmatrix} = \begin{bmatrix} (x^2+y^2)^{1/2} \\ \arctan\left(\frac{y}{x}\right) \\ z \end{bmatrix} \tag{2.57}$$

$$\boldsymbol{v}_{cyl} = \begin{bmatrix} v_r \\ v_\theta \\ v_z \end{bmatrix} = \begin{bmatrix} \frac{v_x x + v_y y}{(x^2+y^2)^{1/2}} \\ \frac{v_y x - v_x y}{(x^2+y^2)^{1/2}} \\ v_z \end{bmatrix} \tag{2.58}$$

$$\boldsymbol{a}_{cyl} = \begin{bmatrix} a_r \\ a_\theta \\ a_z \end{bmatrix} = \begin{bmatrix} \frac{a_x x + a_y y}{(x^2+y^2)^{1/2}} \\ \frac{a_y x - a_x y}{(x^2+y^2)^{1/2}} \\ a_z \end{bmatrix}. \tag{2.59}$$

Note that the radial velocity, like the other velocities, can be positive or negative, which is why it is important that the relations in Eq. (2.58) and Eq. (2.59) accurately denote magnitude and direction. With these definitions, a Jacobian matrix of transformation $\boldsymbol{J}$ can be constructed such that

$$\boldsymbol{J} = \begin{pmatrix} \frac{\partial \boldsymbol{x}_{cyl}}{\partial \boldsymbol{x}_{car}} & \frac{\partial \boldsymbol{x}_{cyl}}{\partial \boldsymbol{v}_{car}} \\ \frac{\partial \boldsymbol{v}_{cyl}}{\partial \boldsymbol{x}_{car}} & \frac{\partial \boldsymbol{v}_{cyl}}{\partial \boldsymbol{v}_{car}} \end{pmatrix} \tag{2.60}$$

$$\frac{\partial \boldsymbol{x}_{cyl}}{\partial \boldsymbol{x}_{car}} = \begin{bmatrix} \frac{\partial r}{\partial x} & \frac{\partial r}{\partial y} & \frac{\partial r}{\partial z} \\ \frac{\partial \theta}{\partial x} & \frac{\partial \theta}{\partial y} & \frac{\partial \theta}{\partial z} \\ \frac{\partial z}{\partial x} & \frac{\partial z}{\partial y} & \frac{\partial z}{\partial z} \end{bmatrix} = \begin{bmatrix} \frac{x}{(x^2+y^2)^{1/2}} & \frac{y}{(x^2+y^2)^{1/2}} & 0 \\ -\frac{y}{x^2+y^2} & \frac{x}{x^2+y^2} & 0 \\ 0 & 0 & 1 \end{bmatrix} \tag{2.61}$$

$$\frac{\partial \boldsymbol{v}_{cyl}}{\partial \boldsymbol{x}_{car}} = \begin{bmatrix} \frac{\partial v_r}{\partial x} & \frac{\partial v_r}{\partial y} & \frac{\partial v_r}{\partial z} \\ \frac{\partial v_\theta}{\partial x} & \frac{\partial v_\theta}{\partial y} & \frac{\partial v_\theta}{\partial z} \\ \frac{\partial v_z}{\partial x} & \frac{\partial v_z}{\partial y} & \frac{\partial v_z}{\partial z} \end{bmatrix} = \begin{bmatrix} \frac{y(v_x y - v_y x)}{(x^2+y^2)^{3/2}} & \frac{x(v_y x - v_x y)}{(x^2+y^2)^{3/2}} & 0 \\ \frac{y(v_x x + v_y y)}{(x^2+y^2)^{3/2}} & -\frac{x(v_x x + v_y y)}{(x^2+y^2)^{3/2}} & 0 \\ 0 & 0 & 0 \end{bmatrix} \tag{2.62}$$

$$\frac{\partial \boldsymbol{v}_{cyl}}{\partial \boldsymbol{v}_{car}} = \begin{bmatrix} \frac{\partial v_r}{\partial v_x} & \frac{\partial v_r}{\partial v_y} & \frac{\partial v_r}{\partial v_z} \\ \frac{\partial v_\theta}{\partial v_x} & \frac{\partial v_\theta}{\partial v_y} & \frac{\partial v_\theta}{\partial v_z} \\ \frac{\partial v_z}{\partial v_x} & \frac{\partial v_z}{\partial v_y} & \frac{\partial v_z}{\partial v_z} \end{bmatrix} = \begin{bmatrix} \frac{x}{(x^2+y^2)^{1/2}} & \frac{y}{(x^2+y^2)^{1/2}} & 0 \\ -\frac{y}{(x^2+y^2)^{1/2}} & \frac{x}{(x^2+y^2)^{1/2}} & 0 \\ 0 & 0 & 1 \end{bmatrix} \tag{2.63}$$

Thus the full Jacobian matrix $\boldsymbol{J}$ and its determinant J is

$$\boldsymbol{J} = \begin{pmatrix} \frac{x}{(x^2+y^2)^{1/2}} & \frac{y}{(x^2+y^2)^{1/2}} & 0 & 0 & 0 & 0 \\ -\frac{y}{x^2+y^2} & \frac{x}{x^2+y^2} & 0 & 0 & 0 & 0 \\ 0 & 0 & 1 & 0 & 0 & 0 \\ \frac{y(v_x y - v_y x)}{(x^2+y^2)^{3/2}} & \frac{x(v_y x - v_x y)}{(x^2+y^2)^{3/2}} & 0 & \frac{x}{(x^2+y^2)^{1/2}} & \frac{y}{(x^2+y^2)^{1/2}} & 0 \\ \frac{y(v_x x + v_y y)}{(x^2+y^2)^{3/2}} & -\frac{x(v_x x + v_y y)}{(x^2+y^2)^{3/2}} & 0 & -\frac{y}{(x^2+y^2)^{1/2}} & \frac{x}{(x^2+y^2)^{1/2}} & 0 \\ 0 & 0 & 0 & 0 & 0 & 1 \end{pmatrix} \tag{2.64}$$

$$J = \det(\boldsymbol{J}) = \frac{1}{r} \tag{2.65}$$

Using the Jacobian matrix, the cylindrical Liouville form of the Vlasov equation is

$$0 = \frac{\partial f}{\partial t} + \begin{bmatrix} \boldsymbol{v}_{car} \\ \\ \boldsymbol{a}_{car} \end{bmatrix} \cdot \left\{ \begin{pmatrix} \frac{\partial \boldsymbol{x}_{cyl}}{\partial \boldsymbol{x}_{car}} & \frac{\partial \boldsymbol{x}_{cyl}}{\partial \boldsymbol{v}_{car}} \\ \\ \frac{\partial \boldsymbol{v}_{cyl}}{\partial \boldsymbol{x}_{car}} & \frac{\partial \boldsymbol{v}_{cyl}}{\partial \boldsymbol{v}_{car}} \end{pmatrix}^T \begin{bmatrix} \frac{\partial f}{\partial \boldsymbol{x}_{cyl}} \\ \\ \frac{\partial f}{\partial \boldsymbol{v}_{cyl}} \end{bmatrix} \right\} \tag{2.66}$$

$$0 = \frac{\partial f}{\partial t} + \begin{bmatrix} v_x \\ v_y \\ v_z \\ a_x \\ a_y \\ a_z \end{bmatrix} \cdot \left\{ \begin{pmatrix} \frac{x}{(x^2+y^2)^{1/2}} & -\frac{y}{x^2+y^2} & 0 & \frac{y(v_x y - v_y x)}{(x^2+y^2)^{3/2}} & \frac{y(v_x x + v_y y)}{(x^2+y^2)^{3/2}} & 0 \\ \frac{y}{(x^2+y^2)^{1/2}} & \frac{x}{x^2+y^2} & 0 & \frac{x(v_y x - v_x y)}{(x^2+y^2)^{3/2}} & -\frac{x(v_x x + v_y y)}{(x^2+y^2)^{3/2}} & 0 \\ 0 & 0 & 1 & 0 & 0 & 0 \\ 0 & 0 & 0 & \frac{x}{(x^2+y^2)^{1/2}} & -\frac{y}{(x^2+y^2)^{1/2}} & 0 \\ 0 & 0 & 0 & \frac{y}{(x^2+y^2)^{1/2}} & \frac{x}{(x^2+y^2)^{1/2}} & 0 \\ 0 & 0 & 0 & 0 & 0 & 1 \end{pmatrix} \begin{bmatrix} \frac{\partial f}{\partial r} \\ \frac{\partial f}{\partial \theta} \\ \frac{\partial f}{\partial z} \\ \frac{\partial f}{\partial v_r} \\ \frac{\partial f}{\partial v_\theta} \\ \frac{\partial f}{\partial v_z} \end{bmatrix} \right\}. \tag{2.67}$$

Using the definitions in Eqs. (2.57) – (2.59), the resulting expression is

$$0 = \frac{\partial f}{\partial t} + v_r \frac{\partial f}{\partial r} + \frac{v_\theta}{r} \frac{\partial f}{\partial \theta} + v_z \frac{\partial f}{\partial z} + \left[a_r + \frac{v_\theta^2}{r} \right] \frac{\partial f}{\partial v_r} + \left[a_\theta - \frac{v_\theta v_r}{r} \right] \frac{\partial f}{\partial v_\theta} + a_z \frac{\partial f}{\partial v_z}, \tag{2.68}$$

which is consistent with the cylindrical Liouville form of the Vlasov equation presented in Refs. [27, 28, 29, 30]. Note that the cylindrical coordinate Vlasov equation includes the acceleration terms v_θ^2/r associated with the centrifugal force and $(-v_\theta v_r)/r$ associated with the Coriolis force. The other forms of acceleration that are of interest are due to the Lorentz force, such that

$$\begin{bmatrix} a_r \\ a_\theta \\ a_z \end{bmatrix} = \begin{bmatrix} \frac{Z_s}{M_s}\left\{E_r + \frac{\omega_{cp}}{\omega_{pp}}\left(v_\theta B_z - v_z B_\theta\right)\right\} \\ \frac{Z_s}{M_s}\left\{E_\theta + \frac{\omega_{cp}}{\omega_{pp}}\left(v_z B_r - v_r B_z\right)\right\} \\ \frac{Z_s}{M_s}\left\{E_z + \frac{\omega_{cp}}{\omega_{pp}}\left(v_r B_\theta - v_\theta B_r\right)\right\} \end{bmatrix}. \tag{2.69}$$

From Eq. (2.68) it is clear that in order to derive the conservation-law form of the Vlasov equation for cylindrical phase space coordinates it is not enough to simply apply the product rule of differentiation as was done in the case of Cartesian coordinates. This is due to the fact that the Coriolis term depends on v_θ, and the gradient in the radial direction does not equate to a radial divergence in cylindrical coordinates. Moreover, it is important to ensure that the cylindrical conservation-law form of the Vlasov equation is physically and mathematically consistent with the Cartesian coordinate expression given in Eq. (2.48). To derive the conservation-law form of the cylindrical coordinate Vlasov equation, a variable transformation of the Cartesian conservation-law form is used.

In the context of conservative finite-volume solvers, it has been shown that the divergence of a vector field in Cartesian coordinates can be rewritten in terms of derivatives in a different coordinate system provided that there is a smooth mapping between the two coordinate systems [31, 32]. Since Cartesian (denoted by x) and cylindrical coordinates (denoted by ξ) are both orthogonal, the divergence of a Cartesian vector field $\boldsymbol{F}$ can be expressed in terms of cylindrical coordinates using the relation

$$\nabla_x \cdot \boldsymbol{F} = J \nabla_\xi \cdot \left(\frac{1}{J}\left(\nabla_x \xi\right)\boldsymbol{F}\right) \tag{2.70}$$

$$J = \det(\nabla_x \xi), \tag{2.71}$$

where $\nabla_x \xi$ is a Jacobian matrix of transformation (given in Eq. (2.64)) that describes how cylindrical coordinates vary with respect to Cartesian coordinates. Note that Eq. (2.70) is a special case of the more general relation given in Ref. [31] for mapped coordinates. For the Vlasov equation, $\boldsymbol{F}$ denotes the six-element flux vector in Cartesian coordinates. Thus the Cartesian divergence of fluxes, $\nabla_x \cdot \boldsymbol{F}$, is given by the last two terms in Eq. (2.48). Evaluating Eq. (2.70) term by term yields an expression for the divergence of fluxes in

cylindrical coordinates that is equivalent to the divergence of fluxes in Cartesian coordinates:

$$\nabla_x \cdot \boldsymbol{F} = \frac{1}{r} \begin{bmatrix} \frac{\partial}{\partial r} \\ \frac{\partial}{\partial \theta} \\ \frac{\partial}{\partial z} \\ \frac{\partial}{\partial v_r} \\ \frac{\partial}{\partial v_\theta} \\ \frac{\partial}{\partial v_z} \end{bmatrix} \cdot \left\{ r \begin{pmatrix} \frac{x}{(x^2+y^2)^{1/2}} & \frac{y}{(x^2+y^2)^{1/2}} & 0 & 0 & 0 & 0 \\ -\frac{y}{x^2+y^2} & \frac{x}{x^2+y^2} & 0 & 0 & 0 & 0 \\ 0 & 0 & 1 & 0 & 0 & 0 \\ \frac{y(v_x y - v_y x)}{(x^2+y^2)^{3/2}} & \frac{x(v_y x - v_x y)}{(x^2+y^2)^{3/2}} & 0 & \frac{x}{(x^2+y^2)^{1/2}} & \frac{y}{(x^2+y^2)^{1/2}} & 0 \\ \frac{y(v_x x + v_y y)}{(x^2+y^2)^{3/2}} & -\frac{x(v_x x + v_y y)}{(x^2+y^2)^{3/2}} & 0 & -\frac{y}{(x^2+y^2)^{1/2}} & \frac{x}{(x^2+y^2)^{1/2}} & 0 \\ 0 & 0 & 0 & 0 & 0 & 1 \end{pmatrix} \begin{bmatrix} v_x f \\ v_y f \\ v_z f \\ a_x f \\ a_y f \\ a_z f \end{bmatrix} \right\} \tag{2.72}$$

$$\nabla_x \cdot \boldsymbol{F} = \frac{1}{r} \begin{bmatrix} \frac{\partial}{\partial r} \\ \frac{\partial}{\partial \theta} \\ \frac{\partial}{\partial z} \\ \frac{\partial}{\partial v_r} \\ \frac{\partial}{\partial v_\theta} \\ \frac{\partial}{\partial v_z} \end{bmatrix} \cdot \left\{ r \begin{bmatrix} \frac{v_x x + v_y y}{(x^2+y^2)^{1/2}} f \\ \frac{v_y x - v_x y}{x^2+y^2} f \\ v_z f \\ \left[\frac{a_x x + a_y y}{(x^2+y^2)^{1/2}} + \frac{(v_x x - v_y y)(v_x x - v_y y)}{(x^2+y^2)^{3/2}} \right] f \\ \left[\frac{a_y x - a_x y}{(x^2+y^2)^{1/2}} - \frac{(v_y x - v_x y)(v_x x + v_y y)}{(x^2+y^2)^{3/2}} \right] f \\ a_z f \end{bmatrix} \right\} \tag{2.73}$$

Noting the definitions given in Eqs. (2.57) – (2.59), the divergence can be expressed in terms of cylindrical coordinate variables, such that

$$\nabla_x \cdot \boldsymbol{F} = \frac{1}{r} \begin{bmatrix} \frac{\partial}{\partial r} \\ \frac{\partial}{\partial \theta} \\ \frac{\partial}{\partial z} \\ \frac{\partial}{\partial v_r} \\ \frac{\partial}{\partial v_\theta} \\ \frac{\partial}{\partial v_z} \end{bmatrix} \cdot \begin{bmatrix} r v_r f \\ v_\theta f \\ r v_z f \\ \left(a_r r + v_\theta^2 \right) f \\ \left(a_\theta r - v_r v_\theta \right) f \\ r a_z f \end{bmatrix}. \tag{2.74}$$

Expanding the dot product yields an expression for the divergence of fluxes in cylindrical phase space coordinates that equates the Cartesian divergence of fluxes. The result can be substituted into the Cartesian conservation-law form of the Vlasov equation in Eq. (2.48) to

obtain

$$0 = \frac{\partial f}{\partial t} + \frac{1}{r}\frac{\partial}{\partial r}\left(r v_r f\right) + \frac{1}{r}\frac{\partial}{\partial \theta}\left(v_\theta f\right) + \frac{1}{r}\frac{\partial}{\partial z}\left(r v_z f\right) + \frac{1}{r}\frac{\partial}{\partial v_r}\left(\left[a_r r + v_\theta^2\right] f\right) + \frac{1}{r}\frac{\partial}{\partial v_\theta}\left(\left[a_\theta r - v_r v_\theta\right] f\right) + \frac{1}{r}\frac{\partial}{\partial v_z}\left(r a_z f\right) \quad (2.75)$$

Noting that the radius r is independent of the other coordinates, the conservation-law form of the Vlasov equation in cylindrical coordinates is

$$0 = \frac{\partial f}{\partial t} + \frac{1}{r}\frac{\partial}{\partial r}\left(r v_r f\right) + \frac{1}{r}\frac{\partial}{\partial \theta}\left(v_\theta f\right) + \frac{\partial}{\partial z}\left(v_z f\right) + \frac{\partial}{\partial v_r}\left(\left[a_r + \frac{v_\theta^2}{r}\right] f\right) + \frac{\partial}{\partial v_\theta}\left(\left[a_\theta - \frac{v_r v_\theta}{r}\right] f\right) + \frac{\partial}{\partial v_z}\left(a_z f\right). \quad (2.76)$$

The Vlasov equation in cylindrical coordinates is hardly ever expressed in conservation-law form – it appears in Ref. [33], but seemingly nowhere else. This speaks to the fact that the Liouville form is much more common in mathematics and plasma physics literature because it is easier to analyze, and to the fact that most continuum kinetic solvers are aimed at Cartesian phase space coordinates, which are readily expressed in conservation-law form and are simpler to discretize.

One can verify that the conservation-law form of the cylindrical coordinate Vlasov equation given by Eq. (2.76) is consistent with Liouville form given in Eq. (2.68) by carrying out the differentiation

$$0 = \frac{\partial f}{\partial t} + \underline{\frac{v_r f}{r}} + v_r\frac{\partial f}{\partial r} + \frac{v_\theta}{r}\frac{\partial f}{\partial \theta} + v_z\frac{\partial f}{\partial z} + \left[a_r + \frac{v_\theta^2}{r}\right]\frac{\partial f}{\partial v_r} - \underline{\frac{v_r f}{r}} + \left[a_\theta - \frac{v_r v_\theta}{r}\right]\frac{\partial f}{\partial v_\theta} + a_z\frac{\partial f}{\partial z}, \quad (2.77)$$

where the underlined terms exactly cancel to yield the Liouville form. In effect, as demonstrated, the cylindrical conservation-law form is mathematically consistent with the cylindrical Liouville form (Eq. (2.68)), the Cartesian conservation-law form (Eq. (2.48)), and the Cartesian Liouville form (Eq. (2.26)).

Much like in the case of Cartesian coordinates, the weak conservation-law form of the cylindrical coordinate Vlasov equation can be obtained by integrating Eq. (2.76) over a phase space volume and applying the divergence theorem. In this case the phase space volume element is $dV = r dr d\theta dz dv_r dv_\theta dv_z$, and the weak form is

$$0 = \frac{\partial}{\partial t}\int f_s dV + \oint \boldsymbol{F}\cdot d\boldsymbol{S}, \quad (2.78)$$

where the flux $\boldsymbol{F}$ and the differential surface $d\boldsymbol{S}$ in each direction is given by

$$\boldsymbol{F} = \begin{bmatrix} v_r f \\ v_\theta f \\ v_z f \\ \left(a_r + \frac{v_\theta^2}{r}\right) f \\ \left(a_\theta - \frac{v_r v_\theta}{r}\right) f \\ a_z f \end{bmatrix}, \qquad d\boldsymbol{S} = \begin{bmatrix} r d\theta dz dv_r dv_\theta dv_z \\ dr dz dv_r dv_\theta dv_z \\ r dr d\theta dv_r dv_\theta dv_z \\ r dr d\theta dz dv_\theta dv_z \\ r dr d\theta dz dv_r dv_z \\ r dr d\theta dz dv_r dv_\theta \end{bmatrix}, \tag{2.79}$$

where acceleration $\{a_r, a_\theta, a_z\}$ due to the Lorentz force is given in Eq. (2.69). Much like in the case of Cartesian coordinates, Eq. (2.78) describes the conservation of the phase-space volume integral of the distribution function: the change in time of the distribution function in a fixed phase space volume depends on the amount of distribution function flowing out (or in) through the boundaries of the volume. Note the distinction between the fluxes and differential areas in Cartesian coordinates (see Eq. (2.52)) and in cylindrical coordinates (Eq. (2.79)). The differential area associated with the radial direction increases with radius.

2.4 Flux-based weak form of Maxwell's equations

Maxwell's equations can be expressed in several ways: using electric scalar potential and magnetic vector potential, as second-order wave equations, and as first-order partial differential equations (as in Eqs. (2.3) – (2.6)). When coupling two sets of partial differential equations – in this case the Vlasov equation for each species is coupled with Maxwell's equations for the electromagnetic fields – it is convenient to express them in the same general form, such that the solutions can be advanced simultaneously using the same algorithm. Since the Vlasov equation is hyperbolic and in the context of a finite-volume discretization it is solved in weak conservation-law form, it is helpful to express Maxwell's equations in the same form.

2.4.1 Weak form of Faraday's law and Ampere's law

Faraday's law and Ampere's law are the primary governing equations for the electric and magnetic fields – they constitute six equations for the six components of the fields. Starting with the normalized form of these field evolution equations, and collecting all spatial derivative operators on the righthand side yields the following expressions

$$\frac{\partial \boldsymbol{B}}{\partial t} = -\frac{\omega_{pp}}{\omega_{cp}} \frac{\partial}{\partial \boldsymbol{x}} \times \boldsymbol{E} \tag{2.80}$$

$$\frac{\partial \boldsymbol{E}}{\partial t} = \frac{\omega_{cp}}{\omega_{pp}} \frac{\partial}{\partial \boldsymbol{x}} \times \boldsymbol{B} - \boldsymbol{J}. \tag{2.81}$$

where the normalized current density $\boldsymbol{J}$ is defined as

$$\boldsymbol{J} = \sum_s Z_s \int \boldsymbol{v} f_s(\boldsymbol{x}, \boldsymbol{v}, t) d\boldsymbol{v}. \tag{2.82}$$

Note that a curl operator in three dimensions can be expressed as a divergence of a rank-2 antisymmetric tensor. Note also that these coupled equations are not strictly hyperbolic due to the presence of current density term on the righthand side of Eq. (2.81), which acts as a source. On account of this term, electric and magnetic fields can be spontaneously created or destroyed, depending on the velocity centroid(s) of the distribution function(s) at any given time and spatial location. To obtain the weak form, Faraday's law and Ampere's law are first integrated over a surface A,

$$\int \frac{\partial \boldsymbol{B}}{\partial t} \cdot d\boldsymbol{A} = -\frac{\omega_{pp}}{\omega_{cp}} \int \frac{\partial}{\partial \boldsymbol{x}} \times \boldsymbol{E} \cdot d\boldsymbol{A} \tag{2.83}$$

$$\int \frac{\partial \boldsymbol{E}}{\partial t} \cdot d\boldsymbol{A} = \frac{\omega_{cp}}{\omega_{pp}} \int \frac{\partial}{\partial \boldsymbol{x}} \times \boldsymbol{B} \cdot d\boldsymbol{A} - \int \boldsymbol{J} \cdot d\boldsymbol{A}. \tag{2.84}$$

Note that the $\boldsymbol{B} \cdot d\boldsymbol{A}$ and $\boldsymbol{E} \cdot d\boldsymbol{A}$ are field fluxes through a differential area $d\boldsymbol{A}$. The curl of a vector field in $\mathbb{R}^3$ integrated over a surface can be expressed in terms of a line integral around the boundary of that surface using Stokes' theorem. Applying Stokes' theorem yields the sought-after weak form of Faraday's law and Ampere's law:

$$\frac{\partial}{\partial t} \int \boldsymbol{B} \cdot d\boldsymbol{A} = -\frac{\omega_{pp}}{\omega_{cp}} \oint \boldsymbol{E} \cdot d\boldsymbol{l} \tag{2.85}$$

$$\frac{\partial}{\partial t} \int \boldsymbol{E} \cdot d\boldsymbol{A} = \frac{\omega_{cp}}{\omega_{pp}} \oint \boldsymbol{B} \cdot d\boldsymbol{l} - \int \boldsymbol{J} \cdot d\boldsymbol{A}. \tag{2.86}$$

In Cartesian coordinates the fields and differential terms are defined as

$$\boldsymbol{E} = \begin{bmatrix} E_x \\ E_y \\ E_z \end{bmatrix} \qquad \boldsymbol{B} = \begin{bmatrix} B_x \\ B_y \\ B_z \end{bmatrix} \qquad d\boldsymbol{A} = \begin{bmatrix} dydz \\ dxdz \\ dxdy \end{bmatrix} \qquad d\boldsymbol{l} = \begin{bmatrix} dx \\ dy \\ dz \end{bmatrix}, \tag{2.87}$$

and in cylindrical coordinates they are

$$\boldsymbol{E} = \begin{bmatrix} E_r \\ E_\theta \\ E_z \end{bmatrix} \qquad \boldsymbol{B} = \begin{bmatrix} B_r \\ B_\theta \\ B_z \end{bmatrix} \qquad d\boldsymbol{A} = \begin{bmatrix} rd\theta dz \\ drdz \\ rdrd\theta \end{bmatrix} \qquad d\boldsymbol{l} = \begin{bmatrix} dr \\ rd\theta \\ dz \end{bmatrix}. \tag{2.88}$$

Equations (2.85) and (2.86) describe the temporal and spatial evolution, i.e. the transport, of the field fluxes. Note that unlike the Vlasov equation, which stipulates that the distribution function cannot be created or destroyed, Faraday's law and Ampere's law are not conservation laws since electric and magnetic fields are not conserved quantities.

2.4.1.1 Incorporation of divergence constraints

The analytical solution for the fields in Faraday's and Ampere's laws will always satisfy the divergence constraints imposed by Gauss's laws (see Eqs. (2.3) and (2.4)), provided the latter are satisfied initially. However, numerical solutions can introduce errors that necessitate explicit enforcement of divergence constraints. To explicitly incorporate these constraints into the field evolution equations requires modifying them. Such modifications are strictly for numerical purposes and are intended to keep the numerical error associated with the divergence constraints bounded, such that errors ε_E and ε_B defined as

$$\varepsilon_E = \nabla \cdot \boldsymbol{E} - \sum_s Z_s n_s \tag{2.89}$$

$$\varepsilon_B = \nabla \cdot \boldsymbol{B} \tag{2.90}$$

stay small. Modified formulations of Ampere's law and Faraday's law typically involve the addition of either a hyperbolic correction [34] or a parabolic correction term [35]. When solving these modified expressions, the error is either propagated to the boundary as in the case of the former, or diffused away as in the case of the latter. A combination of both approaches can also be used. Here the parabolic approach is chosen with the aim of diminishing the amplitude of the error rather than spreading it to other parts of the domain. The resulting modified forms of Faraday's law and Ampere's law are

$$\frac{\partial \boldsymbol{B}}{\partial t} = -\frac{\omega_{pp}}{\omega_{cp}} \frac{\partial}{\partial \boldsymbol{x}} \times \boldsymbol{E} + \lambda \nabla \varepsilon_B \tag{2.91}$$

$$\frac{\partial \boldsymbol{E}}{\partial t} = \frac{\omega_{cp}}{\omega_{pp}} \frac{\partial}{\partial \boldsymbol{x}} \times \boldsymbol{B} - \boldsymbol{J} + \lambda \nabla \varepsilon_E, \tag{2.92}$$

where λ is a constant subject to numerical stability constraints. The associated weak forms are

$$\frac{\partial}{\partial t} \int \boldsymbol{B} \cdot d\boldsymbol{A} = -\frac{\omega_{pp}}{\omega_{cp}} \oint \boldsymbol{E} \cdot d\boldsymbol{l} + \lambda \int (\nabla \varepsilon_B) \cdot d\boldsymbol{A} \tag{2.93}$$

$$\frac{\partial}{\partial t} \int \boldsymbol{E} \cdot d\boldsymbol{A} = \frac{\omega_{cp}}{\omega_{pp}} \oint \boldsymbol{B} \cdot d\boldsymbol{l} - \int \boldsymbol{J} \cdot d\boldsymbol{A} + \lambda \int (\nabla \varepsilon_E) \cdot d\boldsymbol{A}. \tag{2.94}$$

It is important to note that explicit incorporation of the divergence constraints through these modified formulations of the governing equations is not always necessary. In configurations with a reduced number of dimensions the divergence error is exactly zero for certain field components, e.g. in one dimension the dynamics of $E_y(x,t)$ have no associated divergence error. Also, depending on the dynamics of interest, the effect of errors ε_E and ε_B may be negligible.

2.4.2 Weak form of Gauss's law and Poisson's equation

When only electrostatic physics is of interest, the governing equations for the electromagnetic fields are replaced with Gauss's law for the electric field. Gauss's law (see Eq. (2.34) for the

normalized form) is a stipulation on the spatial variation of the electric field and does not involve any time derivatives. Integrating over a volume V and applying the divergence theorem yields the weak form of Gauss's law,

$$\oint \boldsymbol{E} \cdot d\boldsymbol{A} = Z_s \int n_s(\boldsymbol{x}, t) dV, \tag{2.95}$$

where

$$n_s(\boldsymbol{x}, t) = \sum_s \int f_s(\boldsymbol{x}, \boldsymbol{v}, t) d\boldsymbol{v}. \tag{2.96}$$

If the electric field $\boldsymbol{E}$ is expressed in terms of the electrostatic potential, with $\boldsymbol{E} = -\nabla\phi$, then the weak form of the Poisson equation (see Eq. (2.44) for the normalized form) is obtained,

$$-\oint \nabla\phi \cdot d\boldsymbol{A} = Z_s \int n_s(\boldsymbol{x}, t) dV. \tag{2.97}$$

Note that in the case of electrostatics, the electric field depends only on the zeroth moment of the distribution function, which means that unlike the case of Ampere's law, the temporal evolution of the electric field is strictly a function of f_s. In electrostatic and magnetostatic configurations the magnetic field can be non-zero, but does not have an associated evolution equation, and thereby must be fixed for all time.

2.5 Boundary conditions

Solutions to the Vlasov-Maxwell equation system are subject to initial conditions and boundary conditions. Generalized boundary conditions for the Vlasov equation are a topic of research in their own right. For the numerical investigations conducted here, the scope of physical boundary conditions is limited to periodic, perfectly conducting wall, and an axis boundary for axisymmetric configurations.

2.5.1 Distribution function boundary conditions

Periodic boundary conditions in phase space coordinates are straightforward extensions of periodic boundary conditions in physical coordinates in that the velocity dependence is not affected. In a periodic domain $x \in [0, L]$, the boundary condition on the distribution function is

$$f(0, \boldsymbol{v}, t) = f(L, \boldsymbol{v}, t). \tag{2.98}$$

Note that the subscript s denoting species has been dropped for clarity.

Non-periodic boundary conditions for the Vlasov equation are non-trivial, and the associated existence and stability properties of the solution – even from an analytical perspective

– are the subject of mathematics research [36, 37, 38]. The complexity stems from the fact that conditions on the net velocity at a physical boundary require non-local information about the velocity dependence of the distribution function. Notably, boundary conditions for kinetic theory governing equations are even more nuanced for systems in which collisions are present, and in systems where particles can interact with (e.g. be absorbed by) a boundary [39].

Since collisions are not in any way modeled by the Vlasov-Maxwell system, a pure specular reflection boundary condition can be applied in the case of both a conducting wall [37] and an axis of symmetry [38]. For a point $\boldsymbol{x}$ on a boundary $\partial\Omega$ of an arbitrary region Ω, the specular reflection condition on the distribution function is

$$f(\boldsymbol{x}, \boldsymbol{v}, t) = f(\boldsymbol{x}, \boldsymbol{v} - 2(\boldsymbol{v} \cdot \hat{\boldsymbol{n}})\hat{\boldsymbol{n}}, t), \qquad \hat{\boldsymbol{n}} \cdot \boldsymbol{v} < 0, \qquad \boldsymbol{x} \in \partial\Omega, \tag{2.99}$$

where $\hat{\boldsymbol{n}}$ is the outward normal vector of $\partial\Omega$ (pointing out of Ω) at point $\boldsymbol{x}$. Physically this means that any plasma particles that impinge upon an axis or a wall boundary are reflected, with the original normal component of velocity becoming negative. In effect the normal velocity of particles at the axis or at a wall must be zero. In phase space, only a portion of the distribution function (in one dimension either the $v_x > 0$ or the $v_x < 0$ portion) can be moving toward a given boundary due to the fact that the direction and magnitude of advection along a position coordinate (e.g. x) depends only on the local value of the corresponding velocity coordinate (v_x). Consequently the specular reflection boundary condition must take into account the appropriate velocity half-plane when setting a condition on f.

In addition to physical boundary conditions, it is important to consider velocity-space boundaries. Analytically, the velocity domain is infinite such that $\boldsymbol{v} \in \mathbb{R}^3$ since there is nothing in the non-relativistic equation system to ensure velocities are smaller than the speed of light. For the purposes of numerical simulations, a finite velocity domain is assumed such that $\boldsymbol{v} \in [-v_{\max}, v_{\max}] \times [-v_{\max}, v_{\max}] \times [-v_{\max}, v_{\max}]$. This assumption can be physically justified by the fact that physical particles cannot move faster than the speed of light, and consequently the velocity dependence of the distribution function must – in principle – have compact support. The choice of the value of $v_{\max}$ is important because velocity boundaries should be far enough away so as not to affect the evolution of f. Numerically this can be guaranteed if $f(v_{\max})$ is zero to machine precision for all simulated time. If $f(v_{\max})$ is non-zero, then in flux-based simulations the distribution function can "leak" through the velocity boundaries. At the same time, $v_{\max}$ dictates the magnitude of the maximum advection speed in the system, which for numerical simulations places a constraint on the time step size. Consequently $v_{\max}$ should be small enough to ensure that simulations are feasible. To prevent any loss/gain of the distribution function through the velocity boundaries, i.e. to ensure conservation of the distribution function in a finite velocity domain, it is sufficient to set the flux at velocity boundaries to zero.

2.5.2 Electromagnetic field boundary conditions

For each of the field components in Maxwell's equations, non-periodic boundary conditions are either Neumann or Dirichlet. Conducting wall boundary conditions stem from physical considerations, and axis boundary conditions stem from symmetry analysis.

2.5.2.1 Conducting wall boundary

Conducting wall boundary conditions stipulate that the electric field tangent to the conductor is zero, and that the magnetic field normal to the conductor is zero. If $\hat{\boldsymbol{n}}$ denotes the unit normal vector pointing out of the domain Ω, then the constraints on the electric and magnetic fields for a conducting wall boundary $\partial\Omega$ are

$$\hat{\boldsymbol{n}} \times \boldsymbol{E}\Big|_{\partial\Omega} = 0 \tag{2.100}$$

$$\hat{\boldsymbol{n}} \cdot \boldsymbol{B}\Big|_{\partial\Omega} = 0. \tag{2.101}$$

In order for Eq. (2.100) to hold for all time, the steady-state Ampere's law must be satisfied at the conducting wall, such that

$$0 = \frac{\partial}{\partial t}\left(\hat{\boldsymbol{n}} \times \boldsymbol{E}\right) = \left[\frac{\omega_{cp}}{\omega_{pp}}\hat{\boldsymbol{n}} \times \left(\nabla \times \boldsymbol{B}\right) - \hat{\boldsymbol{n}} \times \boldsymbol{J}\right]_{\partial\Omega}. \tag{2.102}$$

See Eq. (2.82) for the definition of current density $\boldsymbol{J}$.

2.5.2.2 Axis boundary

Axis boundary conditions for the fields in an axisymmetric configuration are obtained by using the mapping between Cartesian and cylindrical coordinates, and taking the limit as $r \to 0$. This analysis relies on the fact that a vector field configuration is axisymmetric if certain symmetry conditions hold in both a Cartesian and cylindrical coordinate system. The mapping between Cartesian coordinates and cylindrical coordinates is

$$x = r\cos\theta \tag{2.103}$$

$$y = r\sin\theta. \tag{2.104}$$

The Cartesian components of the electric field can likewise be expressed in terms of cylindrical coordinates, such that

$$E_x = E_r\cos\theta - E_\theta\sin\theta \tag{2.105}$$

$$E_y = E_r\sin\theta + E_\theta\cos\theta. \tag{2.106}$$

In an axisymmetric system, all variables are independent of the angle θ. This means that for the purposes of this analysis, θ is arbitrary and for convenience is chosen to have a fixed value

of zero. Substituting $\theta = 0$ into Eq. (2.104) gives $y = 0$. In an axisymmetric configuration, given a continuous vector field, the limits $x \to 0^+$ and $x \to 0^-$ should be equal, such that

$$\lim_{x\to 0^+} E_x(x,0) = \lim_{x\to 0^-} E_x(x,0) \tag{2.107}$$

$$\lim_{x\to 0^+} E_y(x,0) = \lim_{x\to 0^-} E_y(x,0) \tag{2.108}$$

$$\lim_{x\to 0^+} E_z(x,0) = \lim_{x\to 0^-} E_z(x,0). \tag{2.109}$$

Moreover for y fixed at zero, the limit $x \to 0^+$ is the same as taking the limit of $r \to 0$ for $\theta = 0$, and the limit $x \to 0^-$ is the same as taking the limit of $r \to 0$ for $\theta = \pi$. Using Eq. (2.105) to evaluate the limits in Eq. (2.107) yields

$$\lim_{x\to 0^+} E_x(x,0) = \lim_{r\to 0} E_r \cos 0 = \lim_{r\to 0} (E_r) \tag{2.110}$$

$$\lim_{x\to 0^-} E_x(x,0) = \lim_{r\to 0} E_r \cos \pi = \lim_{r\to 0} (-E_r) \tag{2.111}$$

The only way that the limits in Eq. (2.110) and Eq. (2.111) can be equal is if $E_r = 0$ at the origin. In a similar manner, using Eq. (2.106) to evaluate the limits in Eq. (2.108) yields

$$\lim_{x\to 0^+} E_y(x,0) = \lim_{r\to 0} (E_\theta \cos 0) = \lim_{r\to 0} (E_\theta) \tag{2.112}$$

$$\lim_{x\to 0^-} E_y(x,0) = \lim_{r\to 0} (E_\theta \cos \pi) = \lim_{r\to 0} (-E_\theta) \tag{2.113}$$

For the limits in Eq. (2.112) and Eq. (2.113) to be equal, as per Eq. (2.108), E_θ must be zero at the origin.

In order to evaluate the one sided limits of E_z, a Taylor series expansion is used. For y fixed at zero, the Taylor series is

$$\lim_{x\to 0^+} E_z(x,0) = \lim_{r\to 0} \left(E_z(0,0) + r\cos 0 \left[\frac{\partial E_z}{\partial r}\right]_{(0,0)} + \frac{(r\cos 0)^2}{2} \left[\frac{\partial^2 E_z}{\partial r^2}\right]_{(0,0)} + \cdots \right) \tag{2.114}$$

$$\lim_{x\to 0^-} E_z(x,0) = \lim_{r\to 0} \left(E_z(0,0) + r\cos \pi \left[\frac{\partial E_z}{\partial r}\right]_{(0,0)} + \frac{(r\cos \pi)^2}{2} \left[\frac{\partial^2 E_z}{\partial r^2}\right]_{(0,0)} + \cdots \right) \tag{2.115}$$

Note that for an axisymmetric system $\partial/\partial x = \partial/\partial r$. According to Eq. (2.109) the limit expressions in Eq. (2.114) and Eq. (2.115) must be equal for the configuration to be axisymmetric. The only way for the equality in Eq. (2.109) to be satisfied is if $\frac{\partial E_z}{\partial r} = 0$.

The boundary conditions for the magnetic field in an axisymmetric configuration can be derived in the same way. Thus the complete set of axis boundary conditions for the

electromagnetic fields in an axisymmetric configuration are

$$E_r|_{r=0} = 0 \tag{2.116}$$
$$E_\theta|_{r=0} = 0 \tag{2.117}$$
$$\left.\frac{\partial E_z}{\partial r}\right|_{r=0} = 0 \tag{2.118}$$
$$B_r|_{r=0} = 0 \tag{2.119}$$
$$B_\theta|_{r=0} = 0 \tag{2.120}$$
$$\left.\frac{\partial B_z}{\partial r}\right|_{r=0} = 0 \tag{2.121}$$

It is important to note that depending on the number of physical dimensions in a simulation, not all of these boundary conditions are needed. For example, in a one-dimensional configuration where fields are only a function of radius, the axis boundary condition for E_r is superfluous in that it is never needed to advance the fields in Maxwell's equations.

2.5.2.3 Boundary condition for a charge-neutral domain

The net electric field in a system has to be consistent with the total charge in the system, as stipulated by Gauss's law (see Eq. (2.95)) applied to the entire domain Ω. Thus an additional constraint at boundaries is that

$$\oint_{\partial\Omega} \boldsymbol{E} \cdot d\boldsymbol{A} = Z_s \int_\Omega n_s(\boldsymbol{x}, t) dV. \tag{2.122}$$

This boundary condition does not play a role at the axis in cylindrical coordinates, where $d\boldsymbol{A}$ is zero; however, it is important at other non-periodic boundaries. In a closed charge-neutral system, the righthand side of Eq. (2.122) is simply zero.

2.6 Local and global diagnostics for the Vlasov-Maxwell system

A set of distribution functions encodes a lot of information about the state of a plasma, and the state of each species in the plasma. It can be difficult, however, to interpret the distribution function itself since it can occupy a space of dimension greater than three. Thereby to make deductions about the plasma state, it is convenient to take velocity moments of the distribution function. Velocity moments reduce the dimensionality of the distribution function, and – more importantly – yield fluid variables, which lend themselves to direct physical interpretation. It is worth noting that in plasma experiments it is generally the bulk fluid quantities like density and temperature that are measured, rather than velocities and positions of individual particles, although there are exceptions [40, 41]. A finite number

of velocity moments is not enough to capture all kinetic behavior, but the first three moments serve as useful diagnostics for numerical simulations. These first three moments, combined with electromagnetic fields, yield insights into the local and global behavior of the plasma.

A detailed discussion of the relationship between distribution functions and associated fluid variables can be found in textbooks, see for example Ref. [2]. The local number density for a given species, relative to a characteristic value (see Section 2.2.1 on normalization), is obtained by taking the zeroth velocity moment of the distribution function

$$n_s(\boldsymbol{x}, t) = \int f_s(\boldsymbol{x}, \boldsymbol{v}, t) d\boldsymbol{v}, \tag{2.123}$$

where the integral is over all velocity coordinates. The number density can be used to compute the charge density $Z_s n_s$ and mass density $M_s n_s$. These quantities can be summed over species to obtain the net number density, net charge density, and net mass in a given physical volume or in the entire system. The local momentum density $\boldsymbol{p}_s$ of a given species, relative to a characteristic value, is given by the first velocity moment

$$\boldsymbol{p}_s(\boldsymbol{x}, t) = M_s \int \boldsymbol{v} f_s(\boldsymbol{x}, \boldsymbol{v}, t) d\boldsymbol{v}. \tag{2.124}$$

From number density and momentum density, the bulk species velocity $\boldsymbol{u}_s$ can be obtained such that

$$\boldsymbol{u}_s(\boldsymbol{x}, t) = \frac{\boldsymbol{p}_s}{M_s n_s} = \frac{\int \boldsymbol{v} f_s(\boldsymbol{x}, \boldsymbol{v}, t) d\boldsymbol{v}}{\int f_s(\boldsymbol{x}, \boldsymbol{v}, t) d\boldsymbol{v}}. \tag{2.125}$$

The scalar-valued kinetic energy density W_s for a given species, that is the sum of the energies associated with directed motion and random motion, is obtained from the second velocity moment, such that

$$W_s(\boldsymbol{x}, t) = \frac{1}{2} M_s \int \boldsymbol{v} \cdot \boldsymbol{v} f_s(\boldsymbol{x}, \boldsymbol{v}, t) d\boldsymbol{v}. \tag{2.126}$$

The thermal speed $\boldsymbol{v}_{Ts}$ for a species, which in plasmas can have a different value along each direction, is obtained using the zeroth, first, and second moments of the distribution function, such that

$$\boldsymbol{v}_{Ts}^2 = \frac{1}{n_s} \int \boldsymbol{v}^2 f_s(\boldsymbol{x}, \boldsymbol{v}, t) d\boldsymbol{v} - \boldsymbol{u}_s^2, \tag{2.127}$$

where $\boldsymbol{v}^2$ in this case is defined to be a vector consisting of the terms in the main diagonal of the dyadic product $\boldsymbol{v}\boldsymbol{v}$ (likewise for $\boldsymbol{u}_s^2$). Thermal speed along a given direction j is related to temperature along that direction by

$$T_{s,j} = \frac{1}{2} M_s v_{Ts,j}^2. \tag{2.128}$$

Thermal speed and temperature are physically meaningful only for a distribution function that is in thermal equilibrium, i.e. one that has a Maxwellian profile in velocity space. While distribution functions modeled by the Vlasov equation will not in general be Maxwellian, comparing their velocity dependence to an equivalent (in terms of density, bulk velocity, and thermal speed) Maxwellian profile can serve as a useful measure of the departure away from thermal equilibrium. Such a Maxwellian can be constructed using the above definitions, such that

$$\mathcal{M}_s = n_s \prod_{j=1}^{D} \left(\frac{1}{\pi v_{Ts,j}^2} \right)^{1/2} \exp\left(-\frac{(v_j - u_{s,j})^2}{v_{Ts,j}^2} \right), \tag{2.129}$$

where j denotes a given velocity direction and D is the number of velocity dimensions that are of interest.

Another useful diagnostic for the Vlasov-Maxwell equation system is the total energy, defined as the sum of electric field energy, magnetic field energy, and kinetic energy. The total energy $\mathcal{E}$ in a given physical volume V is

$$\mathcal{E} = \int_V U dV + \int_V \sum_s W_s dV, \tag{2.130}$$

where W_s is the kinetic energy for species s, defined in Eq. (2.126), and U is the field energy defined as

$$U = \frac{1}{2}\big(\boldsymbol{E} \cdot \boldsymbol{E} + \boldsymbol{B} \cdot \boldsymbol{B}\big). \tag{2.131}$$

Combined these diagnostics provide a means to interpret the physics associated with the evolution of a distribution function, and also constitute metrics by which numerical solvers can be evaluated. For example, for a given numerical method the degree to which total mass, momentum, and energy can be conserved in a closed system is important to assess.

Chapter 3

Fourth-order finite-volume discretization

Finite-volume methods are often used for the discretization of partial differential equations involving conservation laws because they ensure that the discrete form of the divergence theorem is satisfied to machine precision. In effect they guarantee local conservation, such that for two volumes that share a surface the flux leaving one volume exactly matches the flux entering the other volume. Beyond their conservation properties, finite-volume methods offer additional features that make them well-suited for the Vlasov-Maxwell system of interest. Compared to finite-difference methods, finite-volume methods are more robust when it comes to handling solutions with steep gradients. While there are no shocks in a collisionless plasmas, large gradients can arise in Vlasov simulations due to the tendency of the distribution function to filament in phase space. Much like high-order finite-difference and high-order finite-element methods, high-order finite-volume methods can achieve a desired accuracy using a smaller number of degrees of freedom than their low-order counterparts.

In finite-volume methods the domain of interest is decomposed into control volumes, and the change in time of a quantity in the control volume is dictated by the surface integral of the fluxes through the boundaries of the volume, as described by the weak conservation-law form of the governing equations. The fluxes are computed using a quadrature rule, and the accuracy of the flux calculation determines the spatial accuracy of the method. State-of-the-art high-order finite-volume methods include weighted essentially non-oscillatory (WENO) methods [42, 43] and arbitrary derivative Riemann problem (ADER) methods [44, 45]. The fourth-order finite-volume method implemented here is based on the approach presented in Refs. [31, 46], and does not fall into either of these two categories. The approach is geared toward structured-mesh calculations and, like ADER methods, it incorporates a systematic means of computing quadratures in more than one dimension. This latter feature is especially critical for phase space distribution functions, as they can occupy a space of more than three dimensions. In addition, the finite-volume method used here anticipates the need for adaptive mesh refinement, and thereby is designed to have a robust means of evaluating fluxes at non-trivial interfaces, e.g. interfaces between coarse and fine grids, or interfaces

that involve coupling fluxes from different models.

This chapter describes the fourth-order finite-volume implementation used to solve Vlasov-Maxwell equation system for the distribution function and the electromagnetic fields. This constitutes a new application of the method described in Refs. [31, 46]. The Cartesian coordinate and cylindrical coordinate implementations are discussed separately so as to facilitate comprehensive treatment of both. An overview of the finite-volume approach to the Vlasov-Maxwell system is given in Section 3.1 followed by a discussion of convergence in Section 3.2 and a description of the temporal discretization in Section 3.3. The spatial discretization of the Vlasov equation and Maxwell's equations in Cartesian coordinates is presented in Section 3.4 and Section 3.5, respectively. Section 3.6 describes the associated diagnostics, and Section 3.7 outlines the mechanics of the numerical algorithm. A description of the spatial discretization for cylindrical coordinates is given in Section 3.8 for the Vlasov equation and Section 3.9 for Maxwell's equations, and is contrasted with the spatial discretization in Cartesian coordinates. The diagnostics and algorithm for cylindrical coordinates are described in Section 3.10 and Section 3.11, respectively.

3.1 Finite-volume overview

Computationally solving the Vlasov-Maxwell system requires a discretization of the governing equations with the aim of ultimately representing all integrals in terms of arithmetic operators. In the context of finite-volume methods this discretization is achieved by decomposing the domain into indexed control volumes, with each volume subject to the weak form of the governing equations. The distribution function in each control volume (or "cell") is subject to the weak conservation-law form of the Vlasov equation, which analytically states that

$$\frac{\partial}{\partial t}\int_V f dV = -\oint_{\partial V} \boldsymbol{F}\cdot d\boldsymbol{S}, \tag{3.1}$$

where flux $\boldsymbol{F}$ is defined at the differential surface on the boundary of the phase space control volume. The fluxes and differential surfaces for phase space coordinates are defined in Eq. (2.52) for Cartesian coordinates and in Eq. (2.79) for cylindrical coordinates. Analogously, the fields are subject to the weak form of Faraday's law and Ampere's law defined locally in a cell as

$$\frac{\partial}{\partial t}\int_A \boldsymbol{B}\cdot d\boldsymbol{A} = -\frac{\omega_{pp}}{\omega_{cp}}\oint_{\partial A}\boldsymbol{E}\cdot d\boldsymbol{l} \tag{3.2}$$

$$\frac{\partial}{\partial t}\int_A \boldsymbol{E}\cdot d\boldsymbol{A} = \frac{\omega_{cp}}{\omega_{pp}}\oint_{\partial A}\boldsymbol{B}\cdot d\boldsymbol{l} - \int_A \boldsymbol{J}\cdot d\boldsymbol{A}, \tag{3.3}$$

where fields are defined through a cross section A of a physical space control volume, and the closed-loop integral is evaluated along the boundary of the cross section.

To facilitate consistent spatial and temporal discretization of these governing equations, they are cast into a generic form, such that each phase space control volume has an associated set of equations,

$$\frac{\partial \boldsymbol{q}}{\partial t} = \boldsymbol{L}\boldsymbol{q} + \boldsymbol{Y}, \tag{3.4}$$

where $\boldsymbol{q}$ is a vector of primary variables, $\boldsymbol{L}$ is some integro-differential operator associated with spatial (as opposed to temporal) variations, and $\boldsymbol{Y}$ is a source term that can be a function of $\boldsymbol{q}$. For the Vlasov-Maxwell system $\boldsymbol{q}$, $\boldsymbol{L}\boldsymbol{q}$, and $\boldsymbol{Y}$ are analytically defined as

$$\boldsymbol{q} = \begin{bmatrix} \int_V f_s dV \\ \int_A \boldsymbol{E} \cdot d\boldsymbol{A} \\ \int_A \boldsymbol{B} \cdot d\boldsymbol{A} \end{bmatrix}, \qquad \boldsymbol{L}\boldsymbol{q} = \begin{bmatrix} -\oint_{\partial V} \boldsymbol{F} \cdot d\boldsymbol{S} \\ \frac{\omega_{cp}}{\omega_{pp}} \oint_{\partial A} \boldsymbol{B} \cdot d\boldsymbol{l} \\ -\frac{\omega_{pp}}{\omega_{cp}} \oint_{\partial A} \boldsymbol{E} \cdot d\boldsymbol{l} \end{bmatrix}, \qquad \boldsymbol{Y} = \begin{bmatrix} 0 \\ -\int_A \boldsymbol{J} \cdot d\boldsymbol{A} \\ 0 \end{bmatrix}. \tag{3.5}$$

Note that since electromagnetic fields are independent of the velocity coordinates the field equations are applied to a subspace of a given phase-space control volume. For the Vlasov-Poisson system, the terms $\boldsymbol{q}$, $\boldsymbol{L}\boldsymbol{q}$, and $\boldsymbol{Y}$ are simply

$$\boldsymbol{q} = \int_V f_s dV, \qquad \boldsymbol{L}\boldsymbol{q} = -\oint_{\partial V} \boldsymbol{F} \cdot d\boldsymbol{S}, \qquad \boldsymbol{Y} = 0, \tag{3.6}$$

and Poisson's equation provides an equation of state, such that the electric field can – at any given time – be computed from the distribution function.

The objective is to be able to solve for $\boldsymbol{q}$ in Eq. (3.4) within every control volume as a function of time. Provided that there is a way to evaluate the righthand side of Eq. (3.4), then the solution can be integrated in time using a standard ordinary differential equation solver. The rest of the finite-volume discretization consists of a formalism for evaluating the righthand side of Eq. (3.4) for each control volume. This formalism prescribes quadrature rules, by which to evaluate the integrals in $\boldsymbol{L}\boldsymbol{q}$ and $\boldsymbol{Y}$.

One of the fundamental aims of this research is obtaining a solution that is fourth-order accurate in space and time. To that end a fourth-order explicit Runge-Kutta method is used for the time advance, and a fourth-order spatial discretization is used to evaluate the integrals on the righthand side of Eq. (3.4). The finite-volume method thus consists of a temporal discretization and a spatial discretization that together are used to advance the solution.

3.2 Convergence

Much of the emphasis here is on fourth-order accuracy, which adds considerable complexity when it comes to the finite-volume discretization. It is important to understand why this

complexity is worthwhile and how the convergence rate is evaluated. Ultimately any discretization method results in an approximation to the true solution of a partial differential equation system. The objective is to have high accuracy, meaning have an approximation as good as reasonably possible, and in the limit of infinite resolution arrive at the true solution of the analytic equations.

For an p-th order accurate method, the norm of the difference between the exact solution u^{exact} and simulated solution u^{sim} is

$$\|u^{\text{exact}} - u^{\text{sim}}\| = Ch^p, \tag{3.7}$$

where C is a constant, h is the cell spacing, and $\|\cdot\|$ typically denotes the max-norm, L1-norm, or the L2-norm. This is in effect the error associated with the simulation. For a second-order accurate method, doubling the resolution results in a factor of four decrease in the error. For a fourth-order accurate method, doubling the resolution decreases the error by a factor of sixteen. For a parallel implementation of a finite-volume method on modern computer architectures, the cost of an h-resolution calculation is effectively independent of the order of accuracy. This is because communication costs are independent of p, and because floating point operations, of which there are more in higher order methods, are cheap in terms of compute time. This means that for computational cost measured in terms of compute time (as opposed to, for example, processor energy consumption), high-order methods achieve higher accuracy per unit of computational cost. In effect, increasing order of accuracy is a more efficient way to minimize the error associated with the discrete solution than increasing resolution. Computational cost considerations and efficiency are particularly important when the number of dimensions is greater than three, as it can be in phase space simulations.

If the exact solution is known, then the order of accuracy p can be evaluated by using Eq. (3.7) and discrete solutions at two different resolution. Let u^h be the discrete solution with cell width h, and u^{2h} be the discrete with cell width $2h$, then according to Eq. (3.7),

$$\|u^{\text{exact}} - u^h\| = Ch^p \tag{3.8}$$

$$\|u^{\text{exact}} - u^{2h}\| = C(2h)^p \tag{3.9}$$

Taking the ratio of Eq. (3.8) and Eq. (3.9) and solving for p yields

$$p = \frac{1}{\log 2} \log\left(\frac{\|u^{\text{exact}} - u^{2h}\|}{\|u^{\text{exact}} - u^h\|}\right). \tag{3.10}$$

If the exact solution is not known then the order of accuracy can be evaluated using the Richardson extrapolation formula, applied to the solution at three different resolutions, such that

$$p = \frac{1}{\log 2} \log\left(\frac{\|u^{4h} - u^{2h}\|}{\|u^{2h} - u^h\|}\right). \tag{3.11}$$

It is important to note that a discrete solution may not converge exactly to the true solution due to errors that are not related to the discretization. For example, truncating the velocity boundaries at a small value of $v_{\max}$ can introduce physics-based errors that are independent of discretization error. Thereby to test the accuracy of the discretization alone, Eq. (3.11) is often the more useful expression.

3.3 Temporal discretization using explicit fourth-order Runge-Kutta method

With the aim of achieving fourth-order accuracy overall, a fourth-order explicit Runge-Kutta (RK4) method is used for the temporal discretization. RK4 is a common multi-stage ordinary differential equation solver, and can be applied to any partial differential equation system that can be expressed as

$$\frac{\partial \boldsymbol{q}}{\partial t} = \Gamma(\boldsymbol{q}, t), \tag{3.12}$$

where $\boldsymbol{q}$ is a vector of primary variables that are to be solved for, and Γ is a combination of operators and functions acting on the known solution. In the context of the Vlasov-Maxwell equation system, Γ is any term that does not involve a time derivative, and encapsulates the integro-differential operator $\boldsymbol{L}$ and the source term $\boldsymbol{Y}$ defined in Section 3.1, such that

$$\Gamma(\boldsymbol{q}, t) = \boldsymbol{L}\boldsymbol{q} + \boldsymbol{Y}. \tag{3.13}$$

The RK4 method consists of stages each of which is based on the first-order accurate forward Euler method,

$$\boldsymbol{q}^{n+1} = \boldsymbol{q}^n + \Delta t \cdot \Gamma(\boldsymbol{q}^n, t^n), \tag{3.14}$$

which expresses the solution $\boldsymbol{q}^{n+1}$ at t^{n+1} in terms of the solution $\boldsymbol{q}^n$ at time t^n, Γ, and the time step size $\Delta t = (t^{n+1} - t^n)$. In RK4 the solution vector is advanced from time t^n to time t^{n+1} as follows:

$$k_1 = \Delta t \cdot \Gamma\left(\boldsymbol{q}^n, t^n\right) \tag{3.15}$$

$$k_2 = \Delta t \cdot \Gamma\left(\boldsymbol{q}^n + \frac{1}{2}k_1, t^n + \frac{1}{2}\Delta t\right) \tag{3.16}$$

$$k_3 = \Delta t \cdot \Gamma\left(\boldsymbol{q}^n + \frac{1}{2}k_2, t^n + \frac{1}{2}\Delta t\right) \tag{3.17}$$

$$k_4 = \Delta t \cdot \Gamma\big(\boldsymbol{q}^n + k_3, t^n + \Delta t\big) \tag{3.18}$$

$$\boldsymbol{q}^{n+1} = \boldsymbol{q}^n + \frac{1}{6}k_1 + \frac{1}{3}k_2 + \frac{1}{3}k_3 + \frac{1}{6}k_4. \tag{3.19}$$

The method has a simple iterative structure, which relies on evaluating the operator Γ for each stage of the solution. The bulk of the numerical effort is thus in the evaluation of Γ, i.e. in the spatial discretization.

3.3.1 CFL stability condition on time step size

Discrete solvers for hyperbolic partial differential equations are subject to the Courant-Friedrichs-Lewy (CFL) condition, which is a necessary condition for convergence. The condition stipulates an upper bound on the time step size, such that in one dimension

$$\Delta t \leq \frac{\sigma h}{a}, \tag{3.20}$$

where σ is the dimensionless Courant number, h is the cell spacing, and a is the maximum advection speed in the system. For explicit time advance methods like RK4, the maximum value of σ is one; however, the details of the spatial discretization can place additional constraints on the Courant number. In multiple dimensions, the CFL constraint on the time step size is

$$\Delta t \leq \sigma \left[\sum_{d=1}^{D} \frac{a_d}{h_d} \right]^{-1}, \tag{3.21}$$

where a_d is the maximum advection speed in the d-th direction, h_d is the cell spacing along the d-th direction, and D is the number of dimensions. Note that the upper bound on Δt given by Eq. (3.21) is a necessary, but not sufficient condition for stability.

In the normalized form of Maxwell's equations (see Eqs. (2.27) and (2.28)), the advection speed is the normalized speed of light; whereas in the Vlasov equation the advection speeds along each direction in Cartesian and cylindrical phase space coordinates are

$$a^{car} = \begin{bmatrix} v_x \\ v_y \\ v_z \\ \frac{Z_s}{M_s}\left(E_x + \frac{\omega_{cp}}{\omega_{pp}}\left[v_y B_z - v_z B_y\right]\right) \\ \frac{Z_s}{M_s}\left(E_y + \frac{\omega_{cp}}{\omega_{pp}}\left[v_z B_x - v_x B_z\right]\right) \\ \frac{Z_s}{M_s}\left(E_z + \frac{\omega_{cp}}{\omega_{pp}}\left[v_x B_y - v_y B_x\right]\right) \end{bmatrix} \tag{3.22}$$

$$a^{cyl} = \begin{bmatrix} v_r \\ v_\theta \\ v_z \\ \frac{Z_s}{M_s}\left(E_r + \frac{\omega_{cp}}{\omega_{pp}}\left[v_\theta B_z - v_z B_\theta\right]\right) + \frac{v_\theta^2}{r} \\ \frac{Z_s}{M_s}\left(E_\theta + \frac{\omega_{cp}}{\omega_{pp}}\left[v_z B_r - v_r B_z\right]\right) - \frac{v_r v_\theta}{r} \\ \frac{Z_s}{M_s}\left(E_z + \frac{\omega_{cp}}{\omega_{pp}}\left[v_r B_\theta - v_\theta B_r\right]\right) \end{bmatrix}. \tag{3.23}$$

Since velocities are coordinates in phase space, the maximum values of $\{v_x, v_y, v_z\}$, and $\{v_r, v_\theta, v_z\}$ are set by the location of velocity domain boundaries, which can depend on the species. If the velocity domain has the same bounds, $\pm v_{\max}$, along each velocity direction, then

$$\max\{|v_x|, |v_y|, |v_z|\} = v_{\max} \tag{3.24}$$
$$\max\{|v_r|, |v_\theta|, |v_z|\} = v_{\max}. \tag{3.25}$$

Thus the maximum advection speed along the spatial coordinate directions is determined by the maximum of the $v_{\max}$ value and the speed of light. In Cartesian coordinates the maximum advection speed along the velocity coordinate directions is dictated by the Lorentz force term. Notably when evolving two distribution functions associated with species with disparate masses (e.g. electrons and protons) the constraint on the time step size is set by the fastest species (e.g. electrons). In the case of cylindrical coordinates the Lorentz force term and the centrifugal force (v_θ^2/r) and the Coriolis force ($v_r v_\theta/r$) terms dictate the maximum advection speed along the velocity coordinates. The latter two present particularly stringent constraints on the time step size. Since the minimum value of the radius in the finite-volume discretization is $h_r/2$, then both the centrifugal and Coriolis terms can have a value as high as $2v_{\max}^2/h_r$. The higher the resolution along the radial direction the higher the advection speed along v_r and v_θ directions. Consequently the time step size associated with cylindrical coordinate simulations is typically very small even when no electromagnetic fields are present.

3.4 Cartesian coordinates: spatial discretization of the Vlasov equation

3.4.1 Taylor series based approach to fourth-order quadratures

For the spatial discretization of the Vlasov equation the phase space domain is decomposed into control volumes defined by a structured grid. The governing equation for the integral of the distribution function in each control volume is

$$\frac{\partial}{\partial t}\int_V f dV = -\oint_{\partial V} \boldsymbol{F}\cdot d\boldsymbol{S}, \tag{3.26}$$

which is an exact statement without approximations. The spatial discretization of the Vlasov equation involves approximating the closed surface integral of fluxes in Eq. (3.26) for each control volume, or "cell", within a domain.

Note that each component of the flux $\boldsymbol{F}$ is a product of the distribution function f with another term g (see Eq. (2.52) for the definition of fluxes in Cartesian phase space coordinates). In practice g is the advection speed and can be a function of position, velocity, and/or time, but for the purposes of this discussion g can be considered to be an arbitrary function. Given the volume integral of the distribution function, the goal is to compute the

surface integral of the product $F = fg$ on each face of a cell. This is done through a two-step process. The first step is a one-dimensional polynomial interpolation of volume-integrated values of the distribution function to a cell face. The second step uses a relationship, derived from Taylor series expansion, between point values and surface integral values in order to compute the surface integral of the product fg (i.e. the flux) to fourth-order accuracy on each face.

To illustrate where this two-step procedure comes from, it is helpful to consider the discrete math associated with the flux calculation. Let each control volume be defined by its cell-center multi-index $\boldsymbol{i} = (i_1, i_2, i_3, \cdots, i_D)$, where D is the number of phase space dimensions being modeled. Then the face of a cell, with normal in the d-th coordinate direction can be designated by multi-index $\boldsymbol{i} + \frac{1}{2}\boldsymbol{e}^d$, where $\boldsymbol{e}^d$ denotes the unit vector in the d-th direction. For convenience, let $\langle\cdot\rangle_{\boldsymbol{i}}$ denote the volume integral, and let $\langle\cdot\rangle_{\boldsymbol{i}+\frac{1}{2}\boldsymbol{e}^d}$ denote the surface integral value over a face whose normal points in the d-th direction. Equation (3.26) can thus be reexpressed using this structured grid indexing notation,

$$\frac{\partial}{\partial t}\langle f\rangle_{\boldsymbol{i}} = -\sum_{d=1}^{D}\left(\langle F\rangle_{\boldsymbol{i}+\frac{1}{2}\boldsymbol{e}^d} - \langle F\rangle_{\boldsymbol{i}-\frac{1}{2}\boldsymbol{e}^d}\right), \tag{3.27}$$

where the surface integral has been replaced by cell-face integrals summed over all orthogonal directions. The primary variable here, i.e. the variable that is initialized and that is to be evolved forward in time, is the volume-integrated distribution function, $\langle f\rangle_{\boldsymbol{i}}$. Typically in finite-volume methods, Eq. (3.27) would be divided through by the volume of the cell, such that the primary variable would be a volume-averaged quantity. This is not done here because the conserved quantity is the volume-integrated (as opposed to the volume-averaged) distribution function, a distinction that is particularly consequential in flux calculations in cylindrical coordinates where cell volumes depend on the radius. Note that the general mechanics of a finite-volume method are not affected by whether a volume-integrated or volume-average primary variable is used, provided that there is a systematic means to compute the face-integrated fluxes $\langle F\rangle_{\boldsymbol{i}+\frac{1}{2}\boldsymbol{e}^d}$.

Computing $\langle F\rangle_{\boldsymbol{i}+\frac{1}{2}\boldsymbol{e}^d}$ to fourth-order accuracy requires a means of computing a surface integral of a product of two (or more) terms to fourth-order accuracy. Let $f(x_{\boldsymbol{i}+\frac{1}{2}\boldsymbol{e}^d})$ denote the point value of the analytic distribution function f at the center of the $(\boldsymbol{i} + \frac{1}{2}\boldsymbol{e}^d)$ face and let $g(x_{\boldsymbol{i}+\frac{1}{2}\boldsymbol{e}^d})$ denote the point value of the arbitrary analytic function g at the center of the $(\boldsymbol{i} + \frac{1}{2}\boldsymbol{e}^d)$ face . Let f_T and g_T be Taylor series expansions of f and g about the center of the $(\boldsymbol{i} + \frac{1}{2}\boldsymbol{e}^d)$ face. Keeping terms up to fourth-order accuracy, the surface integrals of the

Taylor expansions f_T, g_T, and $f_T g_T$ are

$$\langle f_T \rangle_{\boldsymbol{i}+\frac{1}{2}\boldsymbol{e}^d} = \int_{A_{\boldsymbol{i}+\frac{1}{2}\boldsymbol{e}^d}} f_T dA = \left[f(x_{\boldsymbol{i}+\frac{1}{2}\boldsymbol{e}^d}) + \frac{1}{24} \sum_{d' \neq d} h_{d'}^2 \frac{\partial^2 f}{\partial x_{d'}^2} + \mathcal{O}(h^4) \right] \prod_{d' \neq d} h_{d'} \tag{3.28}$$

$$\langle g_T \rangle_{\boldsymbol{i}+\frac{1}{2}\boldsymbol{e}^d} = \int_{A_{\boldsymbol{i}+\frac{1}{2}\boldsymbol{e}^d}} g_T dA = \left[g(x_{\boldsymbol{i}+\frac{1}{2}\boldsymbol{e}^d}) + \frac{1}{24} \sum_{d' \neq d} h_{d'}^2 \frac{\partial^2 g}{\partial x_{d'}^2} + \mathcal{O}(h^4) \right] \prod_{d' \neq d} h_{d'} \tag{3.29}$$

$$\langle f_T g_T \rangle_{\boldsymbol{i}+\frac{1}{2}\boldsymbol{e}^d} = \int_{A_{\boldsymbol{i}+\frac{1}{2}\boldsymbol{e}^d}} f_T g_T dA = \left[f(x_{\boldsymbol{i}+\frac{1}{2}\boldsymbol{e}^d}) g(x_{\boldsymbol{i}+\frac{1}{2}\boldsymbol{e}^d}) + \frac{1}{24} \sum_{d' \neq d} h_{d'}^2 \frac{\partial^2 (fg)}{\partial x_{d'}^2} + \mathcal{O}(h^4) \right] \prod_{d' \neq d} h_{d'} \tag{3.30}$$

where $h_{d'}$ denotes the cell width along the d'-th coordinate direction. All derivative terms in Eqs. (3.28) – (3.30) are evaluated in the plane of the $\boldsymbol{i} + \frac{1}{2}\boldsymbol{e}^d$ face. Equations (3.28) and (3.29) give the relationship between a surface-integrated value and a point value for a single function, whereas Eq. (3.30) gives the relationship for a product of two functions. Note that if the differential surface dA depends on the coordinate (as it does in a cylindrical coordinate system), then that dependence can be absorbed into the function g. This means that the relationship between point values and integral values given by Eq. (3.30) holds independent of whether the coordinate system is Cartesian or cylindrical. Note also that in Cartesian coordinates the surface integral of the product, $\langle f_T g_T \rangle_{\boldsymbol{i}+\frac{1}{2}\boldsymbol{e}^d}$, can be expressed in terms of the surface integral of f_T and the surface integral of g_T such that

$$\langle f_T g_T \rangle_{\boldsymbol{i}+\frac{1}{2}\boldsymbol{e}^d} = \frac{1}{\prod_{d' \neq d} h_{d'}} \left(\langle f_T \rangle_{\boldsymbol{i}+\frac{1}{2}\boldsymbol{e}^d} \langle g_T \rangle_{\boldsymbol{i}+\frac{1}{2}\boldsymbol{e}^d} \right) + \left(\frac{1}{12} \sum_{d' \neq d} h_{d'}^2 \frac{\partial f}{\partial x_{d'}} \frac{\partial g}{\partial x_{d'}} + \mathcal{O}(h^4) \right) \prod_{d' \neq d} h_{d'}. \tag{3.31}$$

Equations (3.30) and (3.31) form the backbone of the finite-volume implementation pursued here, and it is worth highlighting some of the implications of these expressions, both for second-order and fourth-order accurate flux evaluations. The relation given by Eq. (3.30) states that to evaluate the face integral of a product fg to second-order accuracy, it is sufficient to know the point values $f(x_{\boldsymbol{i}+\frac{1}{2}\boldsymbol{e}^d})$ and $g(x_{\boldsymbol{i}+\frac{1}{2}\boldsymbol{e}^d})$ at the center of the cell face. Evaluating the face integral of the product fg to fourth-order accuracy requires point values as well as the second derivatives of fg along every direction in the plane of the face. In essence, fourth-order accuracy requires information about the transverse variation of the flux along a cell face. For a fourth-order accurate flux the derivative terms need only be evaluated to second-order accuracy.

Equation (3.31) gives an alternative means of evaluating the surface integral of a product fg by using the face integral of f and the face integral of g to either second-order accuracy (without first derivative terms) or to fourth-order accuracy (with first derivative terms). In a sense Eq. (3.31) states that the product of integrals and the integral of products are equivalent (to within a scale factor) in second-order flux calculations, but are not equivalent when it

comes to fourth-order flux calculations. In practice Eq. (3.30) constitutes a more useful relation because it can be applied to evaluate the surface integral of a product of more than two terms. Note that because all derivative terms need only be second-order accurate, they can be evaluated using simple finite-difference stencils. Note also that the distinction between volume-integrals, face-integrals, and point values is important, particularly for finite-volume methods whose accuracy is greater than second order.

Since second-order accurate derivatives can be readily evaluated using volume-integrated, face-integrated, or point values, then based on Eq. (3.30) the face-integrated flux over face can be computed to fourth-order accuracy provided that the face-centered point values of the quantities that constitute the flux are known. Point values $f(x_{\boldsymbol{i}+\frac{1}{2}\boldsymbol{e}^d})$ and $g(x_{\boldsymbol{i}+\frac{1}{2}\boldsymbol{e}^d})$ can be obtained from face-integrated values $\langle f \rangle_{\boldsymbol{i}+\frac{1}{2}\boldsymbol{e}^d}$ and $\langle g \rangle_{\boldsymbol{i}+\frac{1}{2}\boldsymbol{e}^d}$ using the relations in Eq. (3.28) and Eq. (3.29). Consequently the only additional piece of information needed to compute the flux is a means by which to obtain a face-integrated value of the distribution function $\langle f \rangle_{\boldsymbol{i}+\frac{1}{2}\boldsymbol{e}^d}$ from a volume-integrated value $\langle f \rangle_{\boldsymbol{i}}$. This is done using a one-dimensional polynomial reconstruction of the volume-integrated values

$$\left\{ \langle f \rangle_{\boldsymbol{i}-2\boldsymbol{e}^d}, \langle f \rangle_{\boldsymbol{i}-\boldsymbol{e}^d}, \langle f \rangle_{\boldsymbol{i}}, \langle f \rangle_{\boldsymbol{i}+\boldsymbol{e}^d}, \langle f \rangle_{\boldsymbol{i}+2\boldsymbol{e}^d}, \langle f \rangle_{\boldsymbol{i}+3\boldsymbol{e}^d} \right\} \tag{3.32}$$

along the d-th coordinate direction. The order of the polynomial used for the reconstruction is important. For a fourth-order accurate finite-volume method, the polynomial should be at least of degree three. A third degree polynomial calls for a four-point stencil, using two cells one either side of the $(\boldsymbol{i}+\frac{1}{2}\boldsymbol{e}^d)$ face. Such "centered" reconstructions lead to an accumulation of dispersive errors, which can be diminished by instead using an upwind reconstruction that accounts for the direction of the flux. Thus a polynomial of degree four, which requires a five-point stencil for reconstruction, is preferred. Upwinding improves numerical stability without affecting the accuracy. Upwinding can be used in equations like the Vlasov equation where the wave speeds in the system are simply the advection speeds along each of the coordinate directions, such that the direction of the flux at any given cell face is well defined.

3.4.2 Fourth-order flux calculation for the Vlasov equation

For a six-dimensional phase space volume the surface integral of fluxes in the weak form of the Vlasov equation (see Eq. (3.26)), is performed over five-dimensional surfaces, which are defined in Eq. (2.52). For the purpose of illustrating how the finite-volume flux calculation works in practice, a two-dimensional phase space volume with one-dimensional surfaces is considered. The procedure described extends directly to more phase space dimensions.

Consider a distribution function $f(\eta, \xi)$ in two dimensions defined by coordinates η and ξ. In this two-dimensional system, the volume integral is an integral over η and ξ, whereas a surface integral is an integral along one of the coordinates. Let i denote the cell index along the η direction, and j denote the cell index along the ξ direction, such that the center of the cell (i, j) has coordinates (η_i, ξ_j) and the cell spans the volume $\left[\eta_{i-\frac{1}{2}}, \eta_{i+\frac{1}{2}}\right] \times \left[\xi_{j-\frac{1}{2}}, \xi_{j+\frac{1}{2}}\right]$,

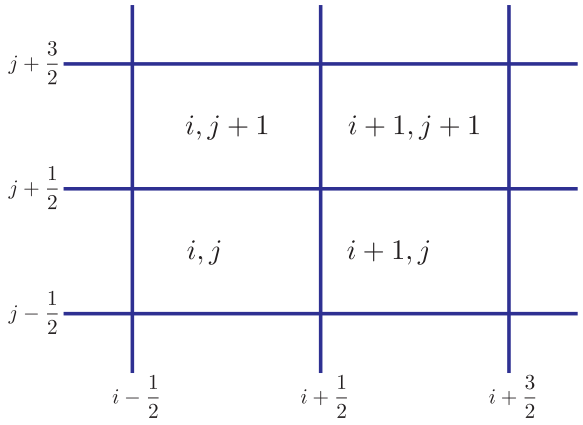

Figure 3.1: Index notation for a regular grid in two dimensions with a generic cell (i, j), its faces at $i \pm \frac{1}{2}$ and $j \pm \frac{1}{2}$, and its neighboring cells.

where

$$\eta_{i\pm\frac{1}{2}} = \eta_i \pm \frac{h_\eta}{2} \tag{3.33}$$

$$\xi_{j\pm\frac{1}{2}} = \xi_j \pm \frac{h_\xi}{2} \tag{3.34}$$

and h_η and h_ξ denote the cell widths along each direction. The indexing of cells and their associated faces is illustrated in Fig. 3.1. Let the primary variable in this finite-volume discretization be the volume integral of f, such that the local volume-integrated value in this Cartesian coordinate system is

$$\langle f \rangle_{i,j} = \int_{\eta_{i-\frac{1}{2}}}^{\eta_{i+\frac{1}{2}}} \int_{\xi_{j-\frac{1}{2}}}^{\xi_{j+\frac{1}{2}}} f(\eta, \xi) d\eta d\xi. \tag{3.35}$$

Note that the differential areas for this Cartesian coordinate system are $\{d\xi, d\eta\}$, such that analytically the cell-face integrals of f are defined as

$$\langle f \rangle_{i+\frac{1}{2},j} = \int_{\xi_{j-\frac{1}{2}}}^{\xi_{j+\frac{1}{2}}} f\left(\eta_{i+\frac{1}{2}}, \xi\right) d\xi \tag{3.36}$$

$$\langle f \rangle_{i,j+\frac{1}{2}} = \int_{\eta_{i-\frac{1}{2}}}^{\eta_{i+\frac{1}{2}}} f\left(\eta, \xi_{j+\frac{1}{2}}\right) d\eta. \tag{3.37}$$

Let the evolution of the primary variable $\langle f \rangle_{i,j}$ be described according to Eq. (3.27) such that the change in time of the primary variable is expressed in terms of cell-face integrated fluxes:

$$\frac{\partial}{\partial t} \langle f \rangle_{i,j} = -\left(\left[\langle F \rangle_{i+\frac{1}{2},j} - \langle F \rangle_{i-\frac{1}{2},j} \right] + \left[\langle F \rangle_{i,j+\frac{1}{2}} - \langle F \rangle_{i,j-\frac{1}{2}} \right] \right). \tag{3.38}$$

By way of example, suppose the fluxes along the η and ξ directions are defined to be $\boldsymbol{F} = \{\alpha f, \beta f\}$, where α defines the advection speed along the η direction and β defines the advection speed along the ξ-direction. Suppose α and β are known analytic functions. Then the goal is to be able to use $\langle f \rangle_{i,j}$ to compute the surface-integrated fluxes in this two-dimensional system,

$$\langle F \rangle_{i+\frac{1}{2},j} = \int_{\xi_{j-\frac{1}{2}}}^{\xi_{j+\frac{1}{2}}} \alpha\left(\eta_{i+\frac{1}{2}}, \xi\right) f\left(\eta_{i+\frac{1}{2}}, \xi\right) d\xi \tag{3.39}$$

$$\langle F \rangle_{i,j+\frac{1}{2}} = \int_{\eta_{i-\frac{1}{2}}}^{\eta_{i+\frac{1}{2}}} \beta\left(\eta, \xi_{j+\frac{1}{2}}\right) f\left(\eta, \xi_{j+\frac{1}{2}}\right) d\eta, \tag{3.40}$$

to fourth-order accuracy so as to evaluate the righthand side of Eq. (3.38). This is accomplished through the following steps.

3.4.2.1 One-dimensional polynomial interpolation

The first step in computing a flux involves interpolation: the primary variable is interpolated to cell faces using one-dimensional polynomial reconstructions. If advection speeds α and β were not analytically defined, as they are in this example, they too would be interpolated. Note that f needs to be evaluated at $i + \frac{1}{2}$ and $j + \frac{1}{2}$ faces. See Fig. 3.1 for reference. To obtain a cell-face integrated value $\langle f \rangle_{i+\frac{1}{2},j}$ from volume-integrated values $\langle f \rangle_{i,j}$, a third degree polynomial P_3 is used to reconstruct the solution, where

$$P_3(\eta) = p_3\eta^3 + p_2\eta^2 + p_1\eta + p_0. \tag{3.41}$$

Solving for the constant coefficients $\{p_3, p_2, p_1, p_0\}$ requires four volume-integrated values $\langle f \rangle_{i,j}$ around the face $(i + \frac{1}{2}, j)$. Constructing a linear system with four equations and four unknowns yields

$$\langle f \rangle_{i-1,j} = \int_{\eta_{i-\frac{3}{2}}}^{\eta_{i-\frac{1}{2}}} P_3(\eta) d\eta \tag{3.42}$$

$$\langle f \rangle_{i,j} = \int_{\eta_{i-\frac{1}{2}}}^{\eta_{i+\frac{1}{2}}} P_3(\eta) d\eta \tag{3.43}$$

$$\langle f \rangle_{i+1,j} = \int_{\eta_{i+\frac{1}{2}}}^{\eta_{i+\frac{3}{2}}} P_3(\eta) d\eta \tag{3.44}$$

$$\langle f \rangle_{i+2,j} = \int_{\eta_{i+\frac{3}{2}}}^{\eta_{i+\frac{5}{2}}} P_3(\eta) d\eta. \tag{3.45}$$

This linear system is solved for the coefficients of P_3 in terms of the volume-integrated values of f. Note that information about the variation of f along the ξ-direction (i.e. the direction

transverse to the $i + \frac{1}{2}$ face) is already embedded into the volume integral $\langle f \rangle_{i,j}$, which is why the polynomial reconstruction can be one-dimensional. The polynomial can then be evaluated at $\eta_{i+\frac{1}{2}}$ to determine the face-integrated value $\langle f \rangle_{i+\frac{1}{2},j}$ to fourth-order accuracy. The resulting stencil is

$$\langle f \rangle_{i+\frac{1}{2},j} = P_3\left(\eta_{i+\frac{1}{2}}\right) = \frac{1}{h_\eta}\left[\frac{7}{12}\left(\langle f \rangle_{i,j} + \langle f \rangle_{i+1,j}\right) - \frac{1}{12}\left(\langle f \rangle_{i+2,j} + \langle f \rangle_{i-1,j}\right)\right]. \tag{3.46}$$

In the same manner $\langle f \rangle_{i,j}$ can be interpolated to the $(i, j+\frac{1}{2})$ face, such that the face integral value is

$$\langle f \rangle_{i,j+\frac{1}{2}} = \frac{1}{h_\xi}\left[\frac{7}{12}\left(\langle f \rangle_{i,j} + \langle f \rangle_{i,j+1}\right) - \frac{1}{12}\left(\langle f \rangle_{i,j+2} + \langle f \rangle_{i,j-1}\right)\right]. \tag{3.47}$$

Note that this stencil for computing a face-integrated solution value is the same one that appears in Ref. [46]. As a point of comparison, note that a second-order accurate interpolation would use a first degree polynomial reconstruction, in which case the face value would be the average of neighboring volume-integrated values, scaled by a factor of cell width: $\langle f \rangle_{i+\frac{1}{2},j} = (\langle f \rangle_i + \langle f \rangle_{i+1})/(2h_\eta)$.

3.4.2.2 Upwinded one-dimensional polynomial interpolation

The procedure outlined above in Section 3.4.2.1 is sufficient to compute a fourth-order accurate face-integrated value from a volume-integrated value $\langle f \rangle_{i,j}$. The resulting stencils are centered about a given face, and use two cells on either side of the cell face to perform the interpolation. For stability purposes, however, it is advantageous to use an upwinded stencil for the primary variable. Upwinding adds dissipation that damps dispersive numerical errors – particularly those that have wavelengths $2h_\eta$ and $2h_\xi$. In order to incorporate upwinding and retain overall fourth-order accuracy, a fourth degree fifth-order accurate polynomial is used to reconstruct f. This means that to evaluate the surface integral of f at a particular cell face, an upwinded interpolation requires five volume-integrated values. Exactly which five cells are used for the reconstruction is determined by the direction of the advection speed.

Consider a one-dimensional polynomial reconstruction of f along the η direction. Let P_4 be a fourth-degree polynomial, such that

$$P_4(\eta) = p_4\eta^4 + p_3\eta^3 + p_2\eta^2 + p_1\eta + p_0. \tag{3.48}$$

The values of the constant coefficients $\{p_4, p_3, p_2, p_1, p_0\}$ are determined by solving a linear system of equations that relate values of the volume-integrated distribution function, which are known, to the polynomial reconstruction within the same cell. To reconstruct the solution at the $(i + \frac{1}{2}, j)$ cell face, a linear system made up of five of the following six relations is

solved:

$$\langle f \rangle_{i-2,j} = \int_{\eta_{i-\frac{5}{2}}}^{\eta_{i-\frac{3}{2}}} P_4(\eta) d\eta \tag{3.49}$$

$$\langle f \rangle_{i-1,j} = \int_{\eta_{i-\frac{3}{2}}}^{\eta_{i-\frac{1}{2}}} P_4(\eta) d\eta \tag{3.50}$$

$$\langle f \rangle_{i,j} = \int_{\eta_{i-\frac{1}{2}}}^{\eta_{i+\frac{1}{2}}} P_4(\eta) d\eta \tag{3.51}$$

$$\langle f \rangle_{i+1,j} = \int_{\eta_{i+\frac{1}{2}}}^{\eta_{i+\frac{3}{2}}} P_4(\eta) d\eta \tag{3.52}$$

$$\langle f \rangle_{i+2,j} = \int_{\eta_{i+\frac{3}{2}}}^{\eta_{i+\frac{5}{2}}} P_4(\eta) d\eta \tag{3.53}$$

$$\langle f \rangle_{i+3,j} = \int_{\eta_{i+\frac{5}{2}}}^{\eta_{i+\frac{7}{2}}} P_4(\eta) d\eta. \tag{3.54}$$

Which five equations are used to solve for the coefficients of P_4 is determined by the sign of the advection speed. If the advection speed $\alpha_{i+\frac{1}{2},j}$ is positive, then three volume-integrated values to the left and two volume-integrated values to the right of the $(i+\frac{1}{2}, j)$ face are used for the polynomial reconstruction, i.e. Eqs. (3.49) – (3.53). If, on the other hand, the advection speed is negative, then two volume-integrated values to the left and three volume-integrated values to the right of the $(i+\frac{1}{2}, j)$ face are used for the polynomial reconstruction, i.e. Eqs. (3.50) – (3.54). Note that independent of the sign of the advection speed, there are five equations and five unknown coefficients $\{p_4, p_3, p_2, p_1, p_0\}$. Solving the linear system for the coefficients in terms of volume integrated values and evaluating P_4 at the $(i+\frac{1}{2}, j)$ cell face, yields a stencil that depends on the advection speed:

$$\langle f \rangle_{i+\frac{1}{2},j} = \begin{cases} \frac{1}{60h_\eta} \left(2\langle f \rangle_{i-2,j} - 13\langle f \rangle_{i-1,j} + 47\langle f \rangle_{i,j} + 27\langle f \rangle_{i+1,j} - 3\langle f \rangle_{i+2,j} \right) & \text{if } \alpha_{i+\frac{1}{2},j} > 0 \\ \frac{1}{60h_\eta} \left(-3\langle f \rangle_{i-1,j} + 27\langle f \rangle_{i,j} + 47\langle f \rangle_{i+1,j} - 13\langle f \rangle_{i+2,j} + 2\langle f \rangle_{i+3,j} \right) & \text{if } \alpha_{i+\frac{1}{2},j} < 0 \end{cases} \tag{3.55}$$

where $\alpha_{i+\frac{1}{2},j} = \alpha(\eta_{i+\frac{1}{2}}, \xi_j)$. If the advection speed is zero then either stencil, or the average of the two stencils in Eq. (3.55) can be used. A similar polynomial reconstruction can be performed along the ξ direction, taking into account that the advection speed along the ξ direction is β. The resulting stencil to compute the face-integrated value of f at face $(i, j+\frac{1}{2})$ is

$$\langle f \rangle_{i,j+\frac{1}{2}} = \begin{cases} \frac{1}{60h_\xi} \left(2\langle f \rangle_{i,j-2} - 13\langle f \rangle_{i,j-1} + 47\langle f \rangle_{i,j} + 27\langle f \rangle_{i,j+1} - 3\langle f \rangle_{i,j+2} \right) & \text{if } \beta_{i,j+\frac{1}{2}} > 0 \\ \frac{1}{60h_\xi} \left(-3\langle f \rangle_{i,j-1} + 27\langle f \rangle_{i,j} + 47\langle f \rangle_{i,j+1} - 13\langle f \rangle_{i,j+2} + 2\langle f \rangle_{i,j+3} \right) & \text{if } \beta_{i,j+\frac{1}{2}} < 0 \end{cases} \tag{3.56}$$

Just as in the case of η-directed advection, if the ξ-directed advection speed is zero then either stencil, or the average of the two stencils in Eq. (3.56) can be used. Since α and β have been assumed to be analytically defined, the advection speeds in Eq. (3.55) and Eq. (3.56) can be readily evaluated as point values. Ultimately, whether the analytic/discrete advection speed is evaluated as a point value or as a face-integrated value is immaterial, since upwinding affects stability and not accuracy. It is worth pointing out that the emphasis here is on computing fourth-order fluxes, which is why polynomials of degree three (for centered stencils) and four (for upwinded stencils) are used. It is also important to note that the upwinded reconstruction used here is applicable as long as the direction of transport is well defined, as it is in this case. For second-order accurate fluxes, a three-cell stencil is sufficient for an upwinded interpolation and can be derived using the same procedure.

3.4.2.3 Fourth-order quadrature for surface-integrated flux

After interpolating the primary variable to cell faces, the second step in the flux calculation involves computing fourth-order accurate cell-face integrated products $\langle \alpha f \rangle_{i+\frac{1}{2},j}$ and $\langle \beta f \rangle_{i,j+\frac{1}{2}}$ using face-integrated values $\langle f \rangle_{i+\frac{1}{2},j}$ and $\langle f \rangle_{i,j+\frac{1}{2}}$. This step relies on the Taylor series relations given by Eqs. (3.28) – (3.30).

Using the relation given by Eq. (3.28), the point values of the primary variable at the center of each face are obtained from face-integrated values. For the $(i+\frac{1}{2},j)$ face, the point value to fourth-order accuracy is

$$f_{i+\frac{1}{2},j} = f(\eta_{i+\frac{1}{2}},\xi_j) = \frac{1}{h_\xi}\langle f \rangle_{i+\frac{1}{2},j} - \frac{1}{24}h_\xi^2 \left[\frac{\partial^2 f}{\partial \xi^2}\right]_{\eta_{i+\frac{1}{2}}} \tag{3.57}$$

The second derivative transverse to the $(i+\frac{1}{2},j)$ face is evaluated as a second-order accurate finite difference using face-integrated values. Accounting for factors of h_ξ both in the finite-difference stencil and in the face-integrated values yields the discrete form for the second derivative,

$$\left[\frac{\partial^2 f}{\partial \xi^2}\right]_{\eta_{i+\frac{1}{2}}} = \frac{1}{h_\xi^3}\left(\langle f \rangle_{i+\frac{1}{2},j+1} - 2\langle f \rangle_{i+\frac{1}{2},j} + \langle f \rangle_{i+\frac{1}{2},j-1}\right). \tag{3.58}$$

Note that for the purposes of computing a fourth-order accurate flux, it is critical that the face-integrated value in Eq. (3.57) is high-order accurate. In the second derivative expression given by Eq. (3.58), the face-integrated values need only be second-order accurate. Substituting Eq. (3.58) into Eq. (3.57) yields the complete expression for the point value of f at the $(i+\frac{1}{2},j)$ face:

$$f_{i+\frac{1}{2},j} = \frac{1}{h_\xi}\langle f \rangle_{i+\frac{1}{2},j} - \frac{1}{24h_\xi}\left(\langle f \rangle_{i+\frac{1}{2},j+1} - 2\langle f \rangle_{i+\frac{1}{2},j} + \langle f \rangle_{i+\frac{1}{2},j-1}\right). \tag{3.59}$$

The face-integrated fourth-order flux $\langle F\rangle_{i+\frac{1}{2},j} = \langle \alpha f\rangle_{i+\frac{1}{2},j}$ is evaluated using Eq. (3.30) and the point values derived above, such that

$$\langle \alpha f\rangle_{i+\frac{1}{2},j} = \left(\alpha_{i+\frac{1}{2},j} f_{i+\frac{1}{2},j} + \frac{1}{24} h_\xi^2 \left[\frac{\partial^2}{\partial \xi^2} (\alpha f) \right]_{\eta_{i+\frac{1}{2}}} \right) h_\xi. \tag{3.60}$$

The second derivative term in the square brackets is evaluated to second-order accuracy using finite differences of known discrete values. Again factors of h_ξ have to be carefully accounted for within the finite-difference stencil (which has a factor of h_ξ^2) as well as within the face-integrated values (which have a factor of h_ξ), such that the second derivative in terms of known discrete values is

$$\left[\frac{\partial^2}{\partial \xi^2} (\alpha f) \right]_{\eta_{i+\frac{1}{2}}} = \frac{1}{h_\xi^3} \left(\alpha_{i+\frac{1}{2},j+1} \langle f\rangle_{i+\frac{1}{2},j+1} - 2\alpha_{i+\frac{1}{2},j} \langle f\rangle_{i+\frac{1}{2},j} + \alpha_{i+\frac{1}{2},j-1} \langle f\rangle_{i+\frac{1}{2},j-1} \right). \tag{3.61}$$

Substituting Eq. (3.61) into Eq. (3.60) results in the complete expression for the fourth-order flux at the $(i+\frac{1}{2}, j)$ face

$$\begin{aligned} \langle F\rangle_{i+\frac{1}{2},j} = {} & \alpha_{i+\frac{1}{2},j} f_{i+\frac{1}{2},j} h_\xi \\ & + \frac{1}{24} \left(\alpha_{i+\frac{1}{2},j+1} \langle f\rangle_{i+\frac{1}{2},j+1} - 2\alpha_{i+\frac{1}{2},j} \langle f\rangle_{i+\frac{1}{2},j} + \alpha_{i+\frac{1}{2},j-1} \langle f\rangle_{i+\frac{1}{2},j-1} \right). \end{aligned} \tag{3.62}$$

Using the same procedure, the point value of f can be obtained at the center of the $(i, j+\frac{1}{2})$ face,

$$f_{i,j+\frac{1}{2}} = f(\eta_i, \xi_{j+\frac{1}{2}}) = \frac{1}{h_\eta} \langle f\rangle_{i,j+\frac{1}{2}} - \frac{1}{24} h_\eta^2 \left[\frac{\partial^2 f}{\partial \eta^2} \right]_{\xi_{j+\frac{1}{2}}} \tag{3.63}$$

$$= \frac{1}{h_\eta} \left(\langle f\rangle_{i,j+\frac{1}{2}} - \frac{1}{24} \left(\langle f\rangle_{i+1,j+\frac{1}{2}} - 2\langle f\rangle_{i,j+\frac{1}{2}} + \langle f\rangle_{i-1,j+\frac{1}{2}} \right) \right) \tag{3.64}$$

and the fourth-order accurate flux along the ξ direction at the $(i, j+\frac{1}{2})$ face is thus

$$\langle F\rangle_{i,j+\frac{1}{2}} = \left(\beta_{i,j+\frac{1}{2}} f_{i,j+\frac{1}{2}} + \frac{1}{24} h_\eta^2 \left[\frac{\partial^2}{\partial \eta^2} (\beta f) \right]_{\xi_{j+\frac{1}{2}}} \right) h_\eta, \tag{3.65}$$

which in terms of known discrete values is

$$\begin{aligned} \langle F\rangle_{i,j+\frac{1}{2}} = {} & \beta_{i,j+\frac{1}{2}} f_{i,j+\frac{1}{2}} h_\eta \\ & + \frac{1}{24} \left(\beta_{i+1,j+\frac{1}{2}} \langle f\rangle_{i+1,j+\frac{1}{2}} - 2\beta_{i,j+\frac{1}{2}} \langle f\rangle_{i,j+\frac{1}{2}} + \beta_{i-1,j+\frac{1}{2}} \langle f\rangle_{i-1,j+\frac{1}{2}} \right). \end{aligned} \tag{3.66}$$

Computing fourth-order accurate fluxes in effect relies on deconvolving (i.e. undoing the integral associated with) face-integrated values to obtain point values of the primary variable, and then integrating products of point values to obtain fluxes. These deconvolution and integration steps involve subtracting (or adding) second derivative terms that account for the variation of a variable (or product of variables) across a cell face. There is some flexibility in the way that these second derivatives are evaluated since they need only be second-order accurate, but it is important to account for factors of cell width along the direction of integration. In combination, the interpolation step and the expressions given by Eq. (3.62) and Eq. (3.66) prescribe a means of computing fourth-order accurate face-integrated fluxes from the discrete volume-integrated primary variable.

3.4.3 Boundary condition implementation for the Vlasov equation

The finite-volume method described here consists of an interpolation stage and a quadrature evaluation stage, both of which are affected by the presence of boundaries. The one-dimensional polynomial interpolation uses multiple cells and is typically centered (or close to centered) about the cell face at which a flux is being evaluated. Boundaries and boundary conditions require an alternate means of reconstructing the solution, such that fluxes at or near the domain boundary can be computed in the absence of neighboring cells i.e. without using information outside of the domain. This is typically achieved either by modifying the one-dimensional polynomial reconstruction stencil to be one-sided and subject to the boundary condition, or by adding an auxiliary domain consisting of a layer of "ghost cells". Ghost cells are in effect a surrogate for a one-sided polynomial reconstruction, but they can simplify the boundary condition implementation by allowing the same interpolation stencil to be used throughout the domain. Ghost cells are especially convenient for Cartesian geometries, in which the stencils are independent of the coordinates. If ghost cells are used, then neither the interpolation stage, nor the quadrature evaluation stage is affected by the boundaries.

If ghost cells are incorporated into the finite-volume implementation, then the interpolation stencils given in Sections 3.4.2.1 and 3.4.2.2 for the domain interior can be used in the exact same way for cells near boundaries. Boundary conditions handled through one-sided reconstructions require modifying the interpolation procedure for cells near domain boundaries. This is done by using one-sided polynomial reconstructions, as opposed to a centered or a slightly-upwinded reconstruction, in order to interpolate volume-integrated quantities to cell faces. As a consequence, the linear system of equations set up to perform the polynomial reconstruction would depend on volume-integrated values, as well as constraints specified by boundary conditions.

The flux calculation step described in Section 3.4.2.3 can also require modification for cells near a domain boundary. For boundary conditions that are handled through one-sided reconstructions, the finite-difference stencil used in the evaluation of second derivative terms

(see for example Eq. (3.58) and Eq. (3.61)) has to be one-sided. A one-sided second-order accurate second derivative finite-difference stencil equivalent (in accuracy) to the centered-difference stencil presented in Eq. (3.58) is

$$\left[\frac{\partial^2 f}{\partial \xi^2}\right]_{\eta_{i+\frac{1}{2}}} = \frac{1}{h_\xi^3}\left(2\left\langle f\right\rangle_{i+\frac{1}{2},j} - 5\left\langle f\right\rangle_{i+\frac{1}{2},j+1} + 4\left\langle f\right\rangle_{i+\frac{1}{2},j+2} - \left\langle f\right\rangle_{i+\frac{1}{2},j+3}\right). \tag{3.67}$$

Note that $\left\langle f\right\rangle_{i+\frac{1}{2},j}$ is an integrated value, as defined in Eq. (3.36), which is why there is an extra factor of h_ξ in the denominator.

3.4.3.1 Periodic boundary via ghost cells

Periodic boundary conditions are straightforward to implement in a structured grid finite-volume discretization. This is done by appending ghost cells to the domain, which are used purely for the calculation of fluxes near domain boundaries, but are not a part of the solution. Suppose the x direction is the direction of periodicity, and suppose there are N_x number of cells along the x direction, such that cells are indexed by $i = \{0, 1, \cdots, N_x - 2, N_x - 1\}$. Then for the fourth order implementation with upwinded interpolation, three ghost cells are appended to either side of the domain, such that with ghost cells the cell indices are $i = \{-3, -2, -1, 0, 1, \cdots, N_x - 2, N_x - 1, N_x, N_x + 1, N_x + 2\}$. If j is the index for a direction orthogonal to x, then the ghost cells are filled using values inside the domain, such that for the periodic case the ghost cell values are

$$\left\langle f\right\rangle_{-3,j} = \left\langle f\right\rangle_{N_x-3,j} \tag{3.68}$$
$$\left\langle f\right\rangle_{-2,j} = \left\langle f\right\rangle_{N_x-2,j} \tag{3.69}$$
$$\left\langle f\right\rangle_{-1,j} = \left\langle f\right\rangle_{N_x-1,j} \tag{3.70}$$
$$\left\langle f\right\rangle_{N_x,j} = \left\langle f\right\rangle_{0,j} \tag{3.71}$$
$$\left\langle f\right\rangle_{N_x+1,j} = \left\langle f\right\rangle_{1,j} \tag{3.72}$$
$$\left\langle f\right\rangle_{N_x+2,j} = \left\langle f\right\rangle_{2,j}. \tag{3.73}$$

The same ghost cell filling procedure can be applied to the fields. Since a centered interpolation is used for the fields, they only need two ghost cells. With ghost cells there is no need to modify interpolation stencils near boundaries.

3.4.3.2 Zero-flux velocity boundary conditions for distribution function

For the purposes of numerical simulations, the velocity domain is assumed to be finite. For simplicity the velocity domain is also set to have the same range along every velocity direction, such that $\boldsymbol{v} \in [-v_{\max}, v_{\max}] \times [-v_{\max}, v_{\max}] \times [-v_{\max}, v_{\max}]$. The value of $v_{\max}$ is dictated in part by time-step constraints, and consequently $f_s(v_{\max})$ can be non-zero. Also note that the value of $v_{\max}$ can depend on the species. To ensure that the total integral of the

distribution function is conserved to numerical precision, velocity-direction ghost cells are set to have zero values, and the flux at velocity boundaries is set to zero. Through the use of ghost cells, the interpolation stencil near velocity boundaries is unmodified. At velocity boundaries fluxes are reset to zero before the divergence of fluxes is evaluated. This amounts to setting a velocity limit, which is unphysical, but has no noticeable effect on the solution as long as $f(v_{\max})$ is zero to machine precision for all simulated time.

3.4.3.3 Specular reflection boundary condition via ghost cells

For Cartesian phase space coordinates the specular reflection boundary condition on the distribution function is applied at solid wall boundaries. Unlike typical Neumann and Dirichlet boundary conditions, the specular reflection boundary condition on the distribution function requires non-local information. For example, for a conducting wall boundary at $x = 0$ in (x, v_x, v_y) phase space coordinates, the specular reflection condition is

$$f(x, v_x, v_y)|_{x=0} = f(x, -v_x, v_y)|_{x=0} \qquad \text{for } v_x > 0, \tag{3.74}$$

which requires information from $v_x < 0$ to set the boundary condition for $v_x > 0$. Velocity components that are parallel to a specular-reflection boundary do not play a role when it comes to setting the boundary condition. Consequently the implementation discussion is limited to the two-dimensional (x, v_x) position-velocity plane.

In Cartesian coordinates, specular reflection boundary conditions at conducting walls can be implemented through a one-dimensional extrapolation, followed by a copy step. This approach is discussed in Section 3.8.3.1 for cylindrical coordinates. However, the procedure can also be dramatically simplified by using ghost cells and setting their values in a special way. In an (x, v_x) phase space domain, with the x coordinate indexed by $i = \{0, 1, 2, \cdots, N_x - 1\}$, and the v_x coordinate indexed by $j = \{0, 1, 2, \cdots, N_{v_x} - 1\}$, at the $i = -\frac{1}{2}$ boundary, the ghost cells $i = \{-3, -2, -1\}$ are filled as follows:

- For $j = \{0, 1, \cdots, N_{v_x} - 1\}$ fill ghost cells using reflected interior domain values

$$\langle f \rangle_{-3,j} = \langle f \rangle_{2,N_{v_x}-1-j} \tag{3.75}$$
$$\langle f \rangle_{-2,j} = \langle f \rangle_{1,N_{v_x}-1-j} \tag{3.76}$$
$$\langle f \rangle_{-1,j} = \langle f \rangle_{0,N_{v_x}-1-j}\,. \tag{3.77}$$

Likewise at the righthand boundary, the ghost cells values for specular reflection are set as follows:

- For $j = \{0, 1, \cdots, N_{v_x} - 1\}$ fill ghost cells using reflected interior domain values

$$\langle f \rangle_{N_x,j} = \langle f \rangle_{N_x-1,N_{v_x}-1-j} \tag{3.78}$$
$$\langle f \rangle_{N_x+1,j} = \langle f \rangle_{N_x-2,N_{v_x}-1-j} \tag{3.79}$$
$$\langle f \rangle_{N_x+2,j} = \langle f \rangle_{N_x-3,N_{v_x}-1-j}\,. \tag{3.80}$$

See Fig. 3.2 for an illustration of how the ghost cells are filled for a x domain bounded by conducting walls. By using ghost cells to set the boundary conditions, the one-dimensional interpolation stencil used throughout the domain can be left unmodified near boundaries. Thus in Cartesian coordinates Eq. (3.55) can be used to compute the values of the distribution function at the boundaries: $\langle f \rangle_{-\frac{1}{2},j}$ and $\langle f \rangle_{N_x-\frac{1}{2},j}$. Note that the entire distribution function $f(v_x)$ is reflected near the boundary in order to fill the ghost cells. This is to ensure that the flux at $\left(-\frac{1}{2}, j\right)$ is exactly equal to the flux at $\left(-\frac{1}{2}, N_{v_x} - j - 1\right)$, and likewise that flux at $\left(N_x - \frac{1}{2}, j\right)$ is exactly equal to the flux at $\left(N_x - \frac{1}{2}, N_{v_x} - j - 1\right)$.

It is important to note that while this approach to filling ghost cells simplifies the implementation of the specular reflection condition, it also imposes an additional constraint in that the number density gradient is forced to be zero at a conducting wall boundary. This additional constraint can be seen in Fig. 3.2, in that the zeroth velocity moment of the distribution function in the $i = -1$ ghost cell is exactly equal to the zeroth velocity moment of the distribution function in the $i = 0$ cell. The additional constraint on number density is not expected to play a significant role in simulation results because the gradient of the number density for the problems of interest is effectively zero near conducting walls. For problems that do not have a zero density gradient at conducting wall boundaries, the boundary condition should be handled by setting the values of the distribution function directly (i.e. through the extrapolation and copy procedure described in Section 3.8.3.1).

3.4.4 Fourth-order accurate initialization

It is important to initialize primary variables in the Vlasov-Maxwell solver to the correct order of accuracy. For fourth-order accurate finite-volume simulations it is important that the initial condition is at least fourth-order accurate. A second-order accurate initial condition does not result in fourth-order convergence as the solution is evolved in time because a second-order variable does not encapsulate the variation of the solution within a cell.

Initial conditions for the analytic Vlasov-Maxwell system of equations are typically given by prescribed analytic functions for the distribution function(s) and the fields. Notably the primary variables in the finite-volume discretization are volume- and area-integrated quantities, and initializing them to fourth-order accuracy can be done using one of two approaches. If the prescribed initial conditions have a closed-form analytic expression for the integrals (which is not always guaranteed), then the initial values of the primary variables can be evaluated exactly by computing the appropriate definite integral in each cell. The second approach does not rely on having closed-form expressions for the integrals of the primary variables and instead uses a quadrature rule based on evaluations of derivatives. The quadrature rule is the same one used throughout the discretization and uses point values and point-value second-derivatives to compute fourth-order accurate integrals.

Consider an example. Let $G(x, v_x, v_y)$ be the analytic function that defines the distribution function at initial time. If G has an analytic antiderivative, then the discrete cell-volume-integrated distribution function can be initialized in terms of a well-defined def-

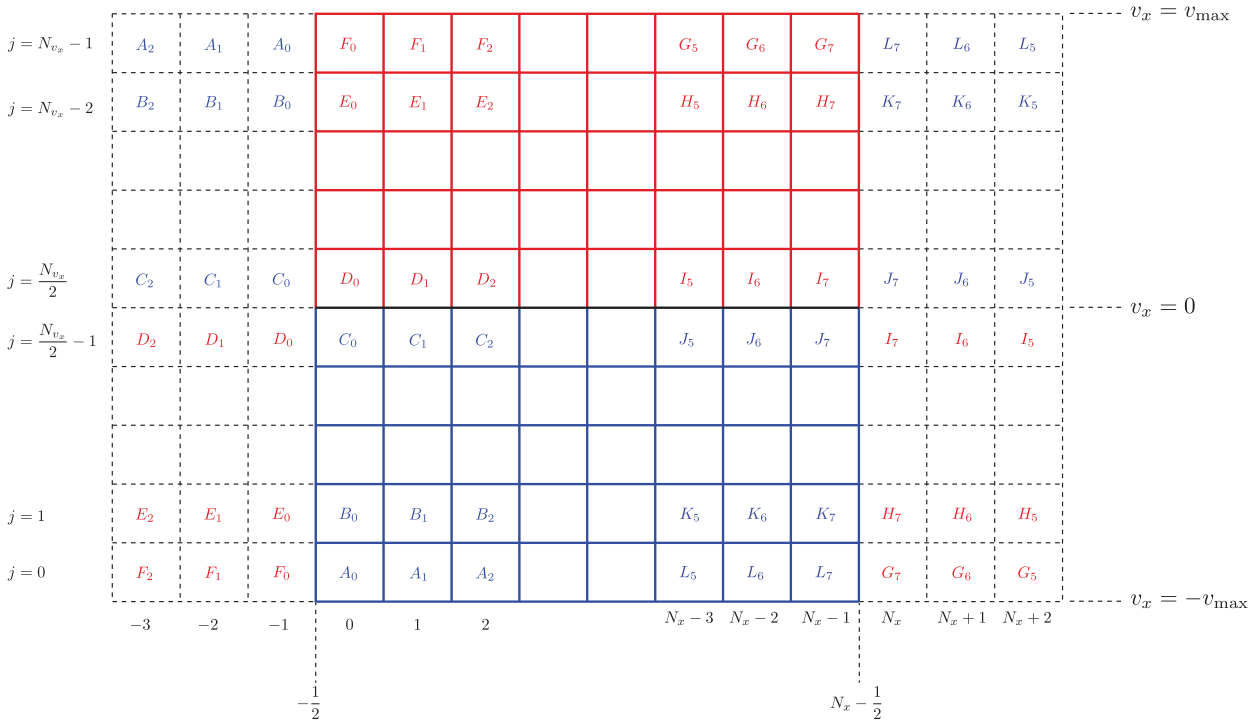

Figure 3.2: Illustration of specular reflection boundary condition implementation for Cartesian (x, v_x) phase space coordinates both at the lefthand and righthand boundaries. The red grid denotes $v_x > 0$, and the blue grid denotes $v_x < 0$. A subset of the distribution function values in the interior domain are denoted by capital letters. Ghost cells, denoted by dashed grid, are filled with domain values from the opposite half-plane. Note that this ghost cells implementation combined with the upwind interpolation in Eq. (3.55) will result in the same flux being computed at faces $\left(-\frac{1}{2}, j\right)$ and $\left(-\frac{1}{2}, N_{v_x} - j - 1\right)$. Likewise at the righthand boundary, the upwind interpolation will yield equal values of the distribution function at cell faces $\left(N_x - \frac{1}{2}, j\right)$ and $\left(N_x - \frac{1}{2}, N_{v_x} - j - 1\right)$. Implementation of the specular reflection boundary condition through ghost cells imposes the additional constraint that the density gradient is zero at the boundaries.

inite integral. If G does not have an analytic antiderivative, then the distribution function is initialized using a fourth order approximation to the cell-volume integral. In Cartesian coordinates this approximation is

$$\langle f \rangle_{i,l,m} = h_x h_{v_x} h_{v_y} \Bigg(G(x_i, (v_x)_l, (v_y)_m) + \frac{1}{24} \left[h_x^2 \frac{\partial^2 G}{\partial x^2} + h_{v_x}^2 \frac{\partial^2 G}{\partial v_x^2} + h_{v_y}^2 \frac{\partial^2 G}{\partial v_y^2} \right]_{(x_i,(v_x)_l,(v_y)_m)} \Bigg), \quad (3.81)$$

where the second-derivative terms can either be evaluated analytically or as point-value finite-differences, such that

$$\left[\frac{\partial^2 G}{\partial x^2} \right]_{(x_i,(v_x)_l,(v_y)_m)} = \frac{1}{h_x^2} \Big[G\big(x_{i+1}, (v_x)_l, (v_y)_m\big) - 2G\big(x_i, (v_x)_l, (v_y)_m\big) + G\big(x_{i-1}, (v_x)_l, (v_y)_m\big) \Big]. \quad (3.82)$$

The quadrature expressions given by Eq. (3.81) is convenient because it can be used to initialize a distribution function to fourth-order accuracy without relying on the existence of a closed-form antiderivative. More practically, even if a closed-form antiderivative does exist, it is not always easy to evaluate it using available software libraries. It is worth noting that the quadrature expressions require some level of smoothness for the analytic function G, otherwise the second derivative terms hold little meaning.

3.5 Cartesian coordinates: spatial discretization of Maxwell's equations

3.5.1 Fourth-order line integrals for Maxwell's equations

The fourth-order finite-volume flux calculations described in Section 3.4.2 apply to primary variables that are volume integrals, such as the volume-integrated distribution function in the Vlasov equation. In the weak form of Faraday's law (see Eq. (2.85)) and Ampere's law (see Eq. (2.86)), however, the primary variables are area-integrated quantities. The evolution of the area-integrated fields depends not on fluxes integrated over a cell face, but rather on closed-loop line integrals. As such, a means of evaluating the closed-loop integrals in Faraday's law and Ampere's law in terms of discrete area-integrated primary variables is needed. To that end, a two-step finite-volume procedure involving an interpolation step and a quadrature evaluation step is applied. The procedure is described for Ampere's law,

$$\frac{\partial}{\partial t} \int \boldsymbol{E} \cdot d\boldsymbol{A} = \frac{\omega_{cp}}{\omega_{pp}} \oint \boldsymbol{B} \cdot d\boldsymbol{l} - \int \boldsymbol{J} \cdot d\boldsymbol{A}, \quad (3.83)$$

and extends directly to Faraday's law since the latter has the same mathematical formulation as the former, but without a source term.

Let i denote the cell index along the x direction, j denote the index along the y direction, and k denote the index along the z direction, such that the center of the cell (i, j, k) has coordinates (x_i, y_j, z_k) and the cell spans the volume $\left[x_{i-\frac{1}{2}}, x_{i+\frac{1}{2}}\right] \times \left[y_{j-\frac{1}{2}}, y_{j+\frac{1}{2}}\right] \times \left[z_{i-\frac{1}{2}}, z_{i+\frac{1}{2}}\right]$, where

$$x_{i\pm\frac{1}{2}} = x_i \pm \frac{h_x}{2} \tag{3.84}$$

$$y_{j\pm\frac{1}{2}} = y_j \pm \frac{h_y}{2} \tag{3.85}$$

$$z_{k\pm\frac{1}{2}} = z_k \pm \frac{h_z}{2} \tag{3.86}$$

and h_x, h_y, and h_z denote the cell widths along each direction. The primary variable in the weak form of Ampere's law (see Eq. (3.83)) is the area-integrated electric field, which in this Cartesian coordinate system has three components:

$$\lfloor E_x \rfloor_{i_0,j,k} = \int_{z_{k-\frac{1}{2}}}^{z_{k+\frac{1}{2}}} \int_{y_{j-\frac{1}{2}}}^{y_{j+\frac{1}{2}}} E_x(x_i, y, z) dy dz \tag{3.87}$$

$$\lfloor E_y \rfloor_{i,j_0,k} = \int_{z_{k-\frac{1}{2}}}^{z_{k+\frac{1}{2}}} \int_{x_{i-\frac{1}{2}}}^{x_{i+\frac{1}{2}}} E_y(x, y_j, z) dx dz \tag{3.88}$$

$$\lfloor E_z \rfloor_{i,j,k_0} = \int_{y_{j-\frac{1}{2}}}^{y_{j+\frac{1}{2}}} \int_{x_{i-\frac{1}{2}}}^{x_{i+\frac{1}{2}}} E_z(x, y, z_k) dx dy, \tag{3.89}$$

where the notation $\lfloor E_x \rfloor_{i_0,j,k}$ denotes an area integral of the E_x component of the electric field over the fixed central $x = x_i$ plane of the cell (i, j, k). The plane over which the field is defined is illustrated in Fig. 3.3. The area-integrated current in Eq. (3.83) can be evaluated in the same way. Likewise the area-integrated magnetic field components, which appear in Faraday's law, are defined in the same manner,

$$\lfloor B_x \rfloor_{i_0,j,k} = \int_{z_{k-\frac{1}{2}}}^{z_{k+\frac{1}{2}}} \int_{y_{j-\frac{1}{2}}}^{y_{j+\frac{1}{2}}} B_x(x_i, y, z) dy dz \tag{3.90}$$

$$\lfloor B_y \rfloor_{i,j_0,k} = \int_{z_{k-\frac{1}{2}}}^{z_{k+\frac{1}{2}}} \int_{x_{i-\frac{1}{2}}}^{x_{i+\frac{1}{2}}} B_y(x, y_j, z) dx dz \tag{3.91}$$

$$\lfloor B_z \rfloor_{i,j,k_0} = \int_{y_{j-\frac{1}{2}}}^{y_{j+\frac{1}{2}}} \int_{x_{i-\frac{1}{2}}}^{x_{i+\frac{1}{2}}} B_z(x, y, z_k) dx dy. \tag{3.92}$$

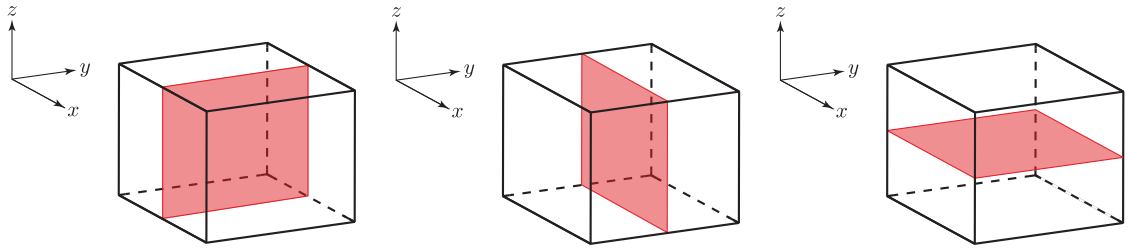

(a) E_x, B_x **(b)** E_y, B_y **(c)** E_z, B_z

Figure 3.3: Cross sections of a cell on which the area-integrated electric and magnetic field primary variables are defined in Cartesian coordinates. The current is also computed as an area-integrated value on these cross-sections.

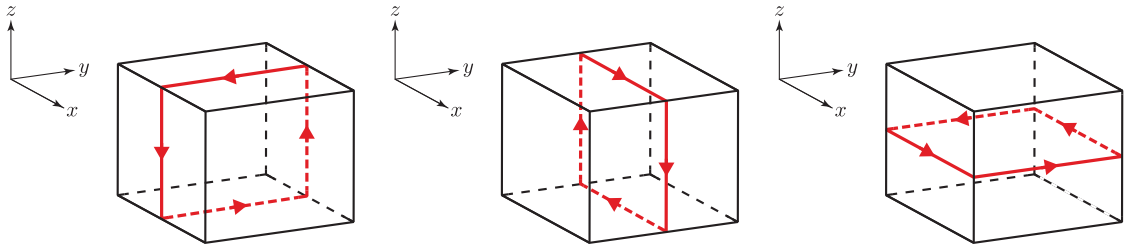

(a) $\int \boldsymbol{B} \cdot d\boldsymbol{l}$ for E_x **(b)** $\int \boldsymbol{B} \cdot d\boldsymbol{l}$ for E_y **(c)** $\int \boldsymbol{B} \cdot d\boldsymbol{l}$ for E_z

Figure 3.4: Line integrals of the magnetic field that are needed to update components of the electric field. Note that the direction of integration, indicated by the arrows, is associated with the sign on the $\oint \boldsymbol{B} \cdot d\boldsymbol{l}$ term in Ampere's law (see Eq. (3.83)).

The closed-loop line-integral in Ampere's law (Eq. (3.83)) for a single cell in this Cartesian coordinate system can be expressed in terms of one-dimensional line integrals

$$\oint \boldsymbol{B} \cdot d\boldsymbol{l} = \begin{bmatrix} -\left[\int B_y(x_i, y, z)dy\right]_{z_{k-\frac{1}{2}}}^{z_{k+\frac{1}{2}}} + \left[\int B_z(x_i, y, z)dz\right]_{y_{j-\frac{1}{2}}}^{y_{j+\frac{1}{2}}} \\ \left[\int B_x(x, y_j, z)dx\right]_{z_{k-\frac{1}{2}}}^{z_{k+\frac{1}{2}}} - \left[\int B_z(x, y_j, z)dz\right]_{x_{i-\frac{1}{2}}}^{x_{i+\frac{1}{2}}} \\ -\left[\int B_x(x, y, z_k)dx\right]_{y_{j-\frac{1}{2}}}^{y_{j+\frac{1}{2}}} + \left[\int B_y(x, y, z_k)dy\right]_{x_{i-\frac{1}{2}}}^{x_{i+\frac{1}{2}}} \end{bmatrix}. \tag{3.93}$$

These line integrals are shown in Fig. 3.4. Thus each component of the magnetic field must be evaluated as a one-dimensional integral, with the remaining coordinates fixed either at a cell center or at a cell face. The objective for a finite-volume discretization is to use the

area-integrated magnetic field components given by Eqs. (3.90) – (3.92) (shown in Fig. 3.3) to compute the one-dimensional integrals in Eq. (3.93) (shown in Fig. 3.4). Much like in the case of volume-integrated primary variables, the finite-volume approach for line integrals is based on an interpolation, followed by an evaluation of a quadrature based on the Taylor series relation given by Eq. (3.28).

3.5.1.1 One-dimensional polynomial interpolation

From Eq. (3.93) note that the B_x line integrals need to be evaluated at $j \pm \frac{1}{2}$ and $k \pm \frac{1}{2}$ faces, the B_y line integrals need to be evaluated at $i \pm \frac{1}{2}$ and $k \pm \frac{1}{2}$ faces, and the B_z line integrals need to be evaluated at $i \pm \frac{1}{2}$, and $j \pm \frac{1}{2}$ faces (see Fig. 3.4). To achieve this, each area-integrated component of the magnetic field is first interpolated to a cell face using a one-dimensional fourth-order accurate polynomial reconstruction (see Section 3.4.2.1). For example, the resulting stencils for the interpolation of $\lfloor B_x \rfloor_{i_0,j,k}$ to the $(i, j + \frac{1}{2}, k)$ face and the $(i, j, k + \frac{1}{2})$ face are

$$\lfloor B_x \rfloor_{i_0,j+\frac{1}{2},k} = \frac{7}{12h_y}\left(\lfloor B_x \rfloor_{i_0,j,k} + \lfloor B_x \rfloor_{i_0,j+1,k}\right) - \frac{1}{12h_y}\left(\lfloor B_x \rfloor_{i_0,j-1,k} + \lfloor B_x \rfloor_{i_0,j+2,k}\right) \quad (3.94)$$

$$\lfloor B_x \rfloor_{i_0,j,k+\frac{1}{2}} = \frac{7}{12h_z}\left(\lfloor B_x \rfloor_{i_0,j,k} + \lfloor B_x \rfloor_{i_0,j,k+1}\right) - \frac{1}{12h_z}\left(\lfloor B_x \rfloor_{i_0,j,k-1} + \lfloor B_x \rfloor_{i_0,j,k+2}\right), \quad (3.95)$$

where $\lfloor B_x \rfloor_{i_0,j+\frac{1}{2},k}$ is the integral of B_x over the z direction at fixed coordinates $(x_i, y_{j+\frac{1}{2}})$ and $\lfloor B_x \rfloor_{i_0,j,k+\frac{1}{2}}$ is the integral of B_x over the y direction at fixed coordinates $(x_i, z_{k+\frac{1}{2}})$. Analogous stencils can be derived for $\lfloor B_y \rfloor_{i+\frac{1}{2},j_0,k}$, $\lfloor B_y \rfloor_{i,j_0,k+\frac{1}{2}}$, $\lfloor B_z \rfloor_{i+\frac{1}{2},j,k_0}$, and $\lfloor B_z \rfloor_{i+\frac{1}{2},j,k_0}$. The interpolation stencils above thus give fourth-order accurate values of the analytic integrals

$$\lfloor B_x \rfloor_{i_0,j+\frac{1}{2},k} = \int B_x(x_i, y_{j+\frac{1}{2}}, z)dz \quad (3.96)$$

$$\lfloor B_x \rfloor_{i_0,j,k+\frac{1}{2}} = \int B_x(x_i, y, z_{k+\frac{1}{2}})dy \quad (3.97)$$

in terms of known discrete quantities. For simplicity, the interpolation uses a centered stencil because at any given cell face, the direction of light wave propagation is not unique, which means that, in the absence of a Riemann solver, an upwinded stencil is not appropriate. As a result of using a centered stencil, the finite-volume discretization of the fields is subject to dispersive errors.

3.5.1.2 Quadrature rule for evaluating line integrals

The integrals obtained from the interpolation (given analytically by Eqs. (3.96) and (3.97) and discretely by Eqs. (3.94) and (3.95)) are not the integrals that appear in the closed loop integral expression in the governing differential equation (see Eq. (3.93)). To obtain fourth-order accurate expressions for the line integrals in Eq. (3.93) using discrete values requires

the use of the Taylor series relation in Eq. (3.28). First fourth-order accurate point-values of the fields are obtained by deconvolving the integrals in Eq. (3.96) and Eq. (3.97):

$$B_x(x_i, y_{j+\frac{1}{2}}, z_k) = \frac{1}{h_z} \lfloor B_x \rfloor_{i_0,j+\frac{1}{2},k} - \frac{1}{24} h_z^2 \left[\frac{\partial^2 B_x}{\partial z^2} \right]_{(x_i, y_{j+\frac{1}{2}}, z_k)} \tag{3.98}$$

$$B_x(x_i, y_j, z_{k+\frac{1}{2}}) = \frac{1}{h_y} \lfloor B_x \rfloor_{i_0,j,k+\frac{1}{2}} - \frac{1}{24} h_y^2 \left[\frac{\partial^2 B_x}{\partial y^2} \right]_{(x_i, y_j, z_{k+\frac{1}{2}})} \tag{3.99}$$

where the second derivative terms can be evaluated using second-order finite-difference stencils. One option for evaluating the second derivative is to use the known interpolated discrete values of the field, such that

$$\left[\frac{\partial^2 B_x}{\partial z^2} \right]_{(x_i, y_{j+\frac{1}{2}}, z_k)} = \frac{1}{h_z^3} \left(\lfloor B_x \rfloor_{i_0,j+\frac{1}{2},k+1} - 2 \lfloor B_x \rfloor_{i_0,j+\frac{1}{2},k} - \lfloor B_x \rfloor_{i_0,j+\frac{1}{2},k-1} \right) \tag{3.100}$$

$$\left[\frac{\partial^2 B_x}{\partial y^2} \right]_{(x_i, y_j, z_{k+\frac{1}{2}})} = \frac{1}{h_y^3} \left(\lfloor B_x \rfloor_{i_0,j+1,k+\frac{1}{2}} - 2 \lfloor B_x \rfloor_{i_0,j,k+\frac{1}{2}} - \lfloor B_x \rfloor_{i_0,j-1,k+\frac{1}{2}} \right), \tag{3.101}$$

where the extra factor of spacing is due to the fact that $\lfloor B_x \rfloor$ is an integral value. Using the point values given by Eqs. (3.98) and (3.99) and the relation in Eq. (3.28), the one-dimensional line-integrals for B_x to fourth-order accuracy are

$$\lfloor B_x \rfloor_{i,j+\frac{1}{2},k_0} = \int B_x(x, y_{j+\frac{1}{2}}, z_k) dx = \left(B_x(x_i, y_{j+\frac{1}{2}}, z_k) + \frac{1}{24} h_x^2 \left[\frac{\partial^2 B_x}{\partial x^2} \right]_{(x_i, y_{j+\frac{1}{2}}, z_k)} \right) h_x \tag{3.102}$$

$$\lfloor B_x \rfloor_{i,j_0,k+\frac{1}{2}} = \int B_x(x, y_j, z_{k+\frac{1}{2}}) dx = \left(B_x(x_i, y_j, z_{k+\frac{1}{2}}) + \frac{1}{24} h_x^2 \left[\frac{\partial^2 B_x}{\partial x^2} \right]_{(x_i, y_j, z_{k+\frac{1}{2}})} \right) h_x. \tag{3.103}$$

Note that these are the line integrals that appear in the weak form of Ampere's law (see Eq. (3.93)). The second derivatives are evaluated using known discrete values, such that

$$\left[\frac{\partial^2 B_x}{\partial x^2} \right]_{(x_i, y_{j+\frac{1}{2}}, z_k)} = \frac{1}{h_x^2} \left(\lfloor B_x \rfloor_{i_0+1,j+\frac{1}{2},k} - 2 \lfloor B_x \rfloor_{i_0,j+\frac{1}{2},k} - \lfloor B_x \rfloor_{i_0-1,j+\frac{1}{2},k} \right) \tag{3.104}$$

$$\left[\frac{\partial^2 B_x}{\partial x^2} \right]_{(x_i, y_j, z_{k+\frac{1}{2}})} = \frac{1}{h_x^2} \left(\lfloor B_x \rfloor_{i_0+1,j,k+\frac{1}{2}} - 2 \lfloor B_x \rfloor_{i_0,j,k+\frac{1}{2}} - \lfloor B_x \rfloor_{i_0-1,j,k+\frac{1}{2}} \right) \tag{3.105}$$

Note that $\lfloor B_x \rfloor_{i_0,j+\frac{1}{2},k}$ represents an integral over the z direction, but not the x direction, which is why the denominator in Eq. (3.104) is h_x^2, and the denominator in Eq. (3.100) is h_z^3.

As illustrated here for the case of B_x, each of the line integrals that appears in Eq. (3.93) can be evaluated to fourth-order accuracy using known discrete values and applying the procedure above. Thus the analytic form of Ampere's law given in Eq. (3.83) can be expressed in fourth-order discrete form. The main difficulty is in keeping track of coordinates that are fixed, and accounting for second-derivatives in the appropriate directions. Because most of the integrals involved in obtaining point values and line-integrated values are one-dimensional, the procedure simplifies considerably if the number of coordinates is reduced from three down to two, or to one.

3.5.2 Current source term in Ampere's law

A complete discretization of Ampere's law in electrodynamic simulations involves the evaluation of the area-integrated current density source term (see righthand side of Eq. (3.83)). The current density is computed from the first velocity moment of the distribution function(s), as prescribed by the analytic relation given by Eq. (2.82). Unlike number density which can be computed through a direct summation, the calculation of the first moment of the distribution function involves the integration of a product of two terms, namely a component of velocity and the distribution function. As a consequence, computing an area-integrated current density (i.e. the current) to fourth-order accuracy requires a quadrature rule. A quadrature rule based on the Taylor series relations in Eqs. (3.28) and (3.30), which are the basis for the overall finite-volume discretization, is used.

To compute the first velocity moment of the distribution function, the cell-volume-integrated distribution function is deconvolved to obtain a point value, the point value is multiplied by a velocity component point value, and then the product is integrated over an area using the relation in Eq. (3.30). In Cartesian coordinates the local point value of the species distribution function is

$$
\begin{aligned}
(f_s)_{i,j,k,l,m,n} = \frac{1}{h_x h_y h_z h_{v_x} h_{v_y} h_{v_z}} \Bigg(\langle f_s \rangle_{i,j,k,l,m,n} - \frac{1}{24} \Bigg[& h_x^2 \frac{\partial^2}{\partial x^2} \langle f_s \rangle \\
& + h_y^2 \frac{\partial^2}{\partial y^2} \langle f_s \rangle + h_z^2 \frac{\partial^2}{\partial z^2} \langle f_s \rangle + h_{v_x}^2 \frac{\partial^2}{\partial v_x^2} \langle f_s \rangle \\
& + h_{v_y}^2 \frac{\partial^2}{\partial v_y^2} \langle f_s \rangle + h_{v_z}^2 \frac{\partial^2}{\partial v_z^2} \langle f_s \rangle \Bigg]_{i,j,k,l,m,n} \Bigg)
\end{aligned}
\tag{3.106}
$$

where the second derivative terms are evaluated to second-order accuracy using a centered finite difference stencil or a one-sided finite difference stencil for cells near boundaries (see

Eq. (3.67)), such that

$$\left[\frac{\partial^2}{\partial x^2}\langle f_s\rangle\right]_{i,j,k,l,m,n} = \frac{1}{h_x^2}\left(\langle f_s\rangle_{i+1,j,k,l,m,n} - 2\langle f_s\rangle_{i,j,k,l,m,n} + \langle f_s\rangle_{i-1,j,k,l,m,n}\right) \tag{3.107}$$

$$\left[\frac{\partial^2}{\partial y^2}\langle f_s\rangle\right]_{i,j,k,l,m,n} = \frac{1}{h_y^2}\left(\langle f_s\rangle_{i,j+1,k,l,m,n} - 2\langle f_s\rangle_{i,j,k,l,m,n} + \langle f_s\rangle_{i,j-1,k,l,m,n}\right) \tag{3.108}$$

$$\vdots$$

$$\left[\frac{\partial^2}{\partial v_z^2}\langle f_s\rangle\right]_{i,j,k,l,m,n} = \frac{1}{h_{v_z}^2}\left(\langle f_s\rangle_{i,j,k,l,m,n+1} - 2\langle f_s\rangle_{i,j,k,l,m,n} + \langle f_s\rangle_{i,j,k,l,m,n-1}\right). \tag{3.109}$$

Much like the area-integrated fields in Ampere's law and Faraday's law, the current is defined to be the area-integrated quantity through the central cross section (see Fig. 3.3) of a given cell. To illustrate the reintegration step, consider the v_x velocity moment for the distribution function f_s. The local area-integrated value of $(v_x f_s)$ to fourth order accuracy is computed using Eq. (3.30), such that

$$\begin{aligned}\langle v_x f_s\rangle_{i,j,k,l,m,n} = (v_x)_l(f_s)_{i,j,k,l,m,n}h_y h_z h_{v_x} h_{v_y} h_{v_z} + \frac{1}{24h_x}\Bigg[&h_y^2\frac{\partial^2}{\partial y^2}(v_x\langle f_s\rangle)\\ &+ h_z^2\frac{\partial^2}{\partial z^2}(v_x\langle f_s\rangle) + h_{v_x}^2\frac{\partial^2}{\partial v_x^2}(v_x\langle f_s\rangle)\\ &+ h_{v_y}^2\frac{\partial^2}{\partial v_y^2}(v_x\langle f_s\rangle) + h_{v_z}^2\frac{\partial^2}{\partial v_z^2}(v_x\langle f_s\rangle)\Bigg]_{i,j,k,l,m,n}.\end{aligned} \tag{3.110}$$

Note that in Eq. (3.110) all terms are evaluated at the x-midpoint of the cell. It is important that the integration in Eq. (3.110) is performed locally before summing over velocity coordinates, such that all variations of the product $(v_x f_s)$ in coordinates orthogonal to x are accounted for to fourth-order accuracy. Note that the integration is being performed over all directions except for x, since the current density in Ampere's law is integrated over a cell cross section. With respect to the x coordinate, the integral given by Eq. (3.110) is being evaluated at the center of the cell. The second derivative terms are computed using

second-order accurate finite-difference stencils,

$$\left[\frac{\partial^2}{\partial y^2}(v_x \langle f\rangle_s)\right]_{i,j,k,l,m,n} = \frac{(v_x)_l}{h_y^2}\left(\langle f_s\rangle_{i,j+1,k,l,m,n} - 2\langle f_s\rangle_{i,j,k,l,m,n} + \langle f_s\rangle_{i,j-1,k,l,m,n}\right) \tag{3.111}$$

$$\left[\frac{\partial^2}{\partial z^2}(v_x \langle f\rangle_s)\right]_{i,j,k,l,m,n} = \frac{(v_x)_l}{h_z^2}\left(\langle f_s\rangle_{i,j,k+1,l,m,n} - 2\langle f_s\rangle_{i,j,k,l,m,n} + \langle f_s\rangle_{i,j,k-1,l,m,n}\right) \tag{3.112}$$

$$\left[\frac{\partial^2}{\partial v_x^2}(v_x \langle f\rangle_s)\right]_{i,j,k,l,m,n} = \frac{1}{h_{v_x}^2}\Big((v_x)_{l+1}\langle f_s\rangle_{i,j,k,l+1,m,n} - 2(v_x)_l\langle f_s\rangle_{i,j,k,l,m,n} + (v_x)_{l-1}\langle f_s\rangle_{i,j,k,l-1,m,n}\Big) \tag{3.113}$$

$$\left[\frac{\partial^2}{\partial v_y^2}(v_x \langle f\rangle_s)\right]_{i,j,k,l,m,n} = \frac{(v_x)_l}{h_{v_y}^2}\left(\langle f_s\rangle_{i,j,k,l,m+1,n} - 2\langle f_s\rangle_{i,j,k,l,m,n} + \langle f_s\rangle_{i,j,k,l,m-1,n}\right) \tag{3.114}$$

$$\left[\frac{\partial^2}{\partial v_z^2}(v_x \langle f\rangle_s)\right]_{i,j,k,l,m,n} = \frac{(v_x)_l}{h_{v_z}^2}\left(\langle f_s\rangle_{i,j,k,l,m,n+1} - 2\langle f_s\rangle_{i,j,k,l,m,n} + \langle f_s\rangle_{i,j,k,l,m,n-1}\right) \tag{3.115}$$

The species current is then a summation of $\langle v_x f_s\rangle_{i,j,k,l,m,n}$ over all velocity directions, such that

$$\langle J_{sx}\rangle_{i,j,k} = Z_s \sum_{l=0}^{N_{v_x}-1}\sum_{m=0}^{N_{v_y}-1}\sum_{n=0}^{N_{v_z}-1}\langle v_x f_s\rangle_{i,j,k,l,m,n} \tag{3.116}$$

and the total x-directed current is computed by summing over species, such that

$$\langle J_x\rangle_{i,j,k} = \sum_s \langle J_{sx}\rangle_{i,j,k}\,. \tag{3.117}$$

The current along the other directions can be computed by following the same procedure; using the point value to reintegrate and compute local values of $\langle v_y f_s\rangle_{i,j,k,l,m,n}$ and $\langle v_z f_s\rangle_{i,j,k,l,m,n}$, multiplying by the charge of species s, summing over velocity coordinates, and summing over species. Through this formalism the current source term in Ampere's law can be evaluated to fourth-order accuracy.

3.5.3 Implementation of conducting wall boundary conditions for fields

Analytic expressions for conducting wall boundary conditions for the fields are given in Section 2.5.2, Eq. (2.100) through Eq. (2.102). For a subset of the Cartesian coordinate simulations carried out here the domain along the x direction, with $x \in [0, L]$, is assumed to be bounded by perfectly conducting walls. Thus at the $x = 0$ and $x = L$ boundaries the

fields are subject to the conditions

$$E_y|_{x=0,L} = 0 \tag{3.118}$$

$$E_z|_{x=0,L} = 0 \tag{3.119}$$

$$B_x|_{x=0,L} = 0 \tag{3.120}$$

$$\left[\frac{\partial B_x}{\partial z} - \frac{\partial B_z}{\partial x} - J_y\right]_{x=0,L} = 0 \tag{3.121}$$

$$\left[\frac{\partial B_y}{\partial x} - \frac{\partial B_x}{\partial y} - J_z\right]_{x=0,L} = 0. \tag{3.122}$$

Note that since B_x is specified along the boundary by Eq. (3.120), then $\partial B_x/\partial z$ and $\partial B_x/\partial y$ are zero along the $x = 0, L$ boundaries, and consequently Eq. (3.121) is a boundary condition only on B_z and Eq. (3.122) is a boundary condition only on B_y. For a bounded charge-neutral system, an additional boundary constraint arises from Gauss's law (see Eq. (2.122)), such that

$$[E_x]_{x=L} - [E_x]_{x=0} = 0. \tag{3.123}$$

The simplest way to implement field boundary conditions is through ghost cells. When using ghost cells stencils can be left unmodified near boundaries, and thereby boundary conditions can easily be incorporated both into the interpolation step as well as the quadrature evaluation step. Ghost cells are ultimately a proxy for a one-sided reconstruction and their usage can impose additional constraints unrelated to the boundary condition (e.g. see discussion at the end of Section 3.4.3.3). As such, ghost cells are not a generalized means of boundary condition implementation. Without ghost cells, the incorporation of boundary conditions is made more complicated, requiring one-sided reconstructions of the field variables subject to boundary constraints.

While boundary conditions for the Cartesian coordinate Vlasov-Maxwell solver can be handled through ghost cells, this is not the case for the cylindrical coordinate Vlasov-Maxwell discretization. In anticipation of the need for one-sided reconstructions, and in effort to have consistent boundary condition treatment in both coordinate systems, a simplifying design choice is made for the finite-volume algorithm: all boundary conditions are implemented exclusively through the interpolation step. As a consequence, not all of the boundary conditions given by Eqs. (3.118) – (3.123) are needed. The boundary condition on B_x given by Eq. (3.120) is never used in the interpolation stage since for the purposes of line-integral calculations the x component of the magnetic field need never be evaluated at an $x = 0$ or $x = L$ boundary. Since E_x is never evaluated at an x-directed face, then Eq. (3.123) likewise constitutes an unnecessary boundary condition in the context of the interpolation stage. Note that if quadrature evaluation required boundary condition information, then the constraints given by Eq. (3.120) and Eq. (3.123) would be necessary. For the chosen discretization, the boundary conditions that are needed in order to numerically solve for the

area-integrated field variables are

$$E_y|_{x=0,L} = 0 \tag{3.124}$$

$$E_z|_{x=0,L} = 0 \tag{3.125}$$

$$\left[\frac{\partial B_z}{\partial x} + J_y\right]_{x=0,L} = 0 \tag{3.126}$$

$$\left[\frac{\partial B_y}{\partial x} - J_z\right]_{x=0,L} = 0. \tag{3.127}$$

A ghost cell implementation is used for the homogeneous Dirichlet boundary conditions, and thereby the polynomial reconstruction stencil can be left unmodified for E_y and E_z near boundaries. At the lefthand boundary E_y and E_z ghost cells, indexed by $i = \{-2, -1\}$, are filled with data from interior domain cells $i = \{0, 1\}$, such that

$$\lfloor E_y \rfloor_{-1,j,k} = -\lfloor E_y \rfloor_{0,j,k} \tag{3.128}$$

$$\lfloor E_y \rfloor_{-2,j,k} = -\lfloor E_y \rfloor_{1,j,k} \tag{3.129}$$

$$\lfloor E_z \rfloor_{-1,j,k} = -\lfloor E_z \rfloor_{0,j,k} \tag{3.130}$$

$$\lfloor E_z \rfloor_{-2,j,k} = -\lfloor E_z \rfloor_{1,j,k}\,. \tag{3.131}$$

Likewise at the righthand boundary E_y and E_z ghost cells, indexed by $i = \{N_x, N_x + 1\}$, are filled with data from interior domain cells $i = \{N_x - 1, N_x - 2\}$, such that

$$\lfloor E_y \rfloor_{N_x,j,k} = -\lfloor E_y \rfloor_{N_x-1,j,k} \tag{3.132}$$

$$\lfloor E_y \rfloor_{N_x+1,j,k} = -\lfloor E_y \rfloor_{N_x-2,j,k} \tag{3.133}$$

$$\lfloor E_z \rfloor_{N_x,j,k} = -\lfloor E_z \rfloor_{N_x-1,j,k} \tag{3.134}$$

$$\lfloor E_z \rfloor_{N_x+1,j,k} = -\lfloor E_z \rfloor_{N_x-2,j,k}\,. \tag{3.135}$$

Magnetic field B_z is evaluated at $x = 0$, $x = h_x$, $x = L$, and $x = L - h_x$ faces using a fourth-order accurate one-sided one-dimensional polynomial reconstruction subject to the constraint in Eq. (3.126), such that

$$\lfloor B_z \rfloor|_{x=0} = \frac{1}{66h_x}\left(85\lfloor B_z \rfloor_0 - 23\lfloor B_z \rfloor_1 + 4\lfloor B_z \rfloor_2 + 18J_y(0)h_x^2\right) \tag{3.136}$$

$$\lfloor B_z \rfloor|_{x=h_x} = \frac{1}{66h_x}\left(34\lfloor B_z \rfloor_0 + 37\lfloor B_z \rfloor_1 - 5\lfloor B_z \rfloor_2 - 6J_y(0)h_x^2\right) \tag{3.137}$$

$$\lfloor B_z \rfloor|_{x=L} = \frac{1}{66h_x}\left(4\lfloor B_z \rfloor_{N_x-3} - 23\lfloor B_z \rfloor_{N_x-2} + 85\lfloor B_z \rfloor_{N_x-1} - 18J_y(L)h_x^2\right) \tag{3.138}$$

$$\lfloor B_z \rfloor|_{x=L-h_x} = \frac{1}{66h_x}\left(-5\lfloor B_z \rfloor_{N_x-3} + 37\lfloor B_z \rfloor_{N_x-2} + 34\lfloor B_z \rfloor_{N_x-1} + 6J_y(L)h_x^2\right). \tag{3.139}$$

Likewise B_y is evaluated at $x = 0$, $x = h_x$, $x = L$, and $x = L - h_x$ faces using a fourth-order accurate one-sided one-dimensional polynomial reconstruction subject to the constraint in Eq. (3.127), such that

$$\lfloor B_y \rfloor|_{x=0} = \frac{1}{66h_x}\left(85\lfloor B_y\rfloor_0 - 23\lfloor B_y\rfloor_1 + 4\lfloor B_y\rfloor_2 - 18J_z(0)h_x^2\right) \tag{3.140}$$

$$\lfloor B_y \rfloor|_{x=h_x} = \frac{1}{66h_x}\left(34\lfloor B_y\rfloor_0 + 37\lfloor B_y\rfloor_1 - 5\lfloor B_y\rfloor_2 + 6J_z(0)h_x^2\right) \tag{3.141}$$

$$\lfloor B_y \rfloor|_{x=L} = \frac{1}{66h_x}\left(4\lfloor B_y\rfloor_{N_x-3} - 23\lfloor B_y\rfloor_{N_x-2} + 85\lfloor B_y\rfloor_{N_x-1} + 18J_z(L)h_x^2\right) \tag{3.142}$$

$$\lfloor B_y \rfloor|_{x=L-h_x} = \frac{1}{66h_x}\left(-5\lfloor B_y\rfloor_{N_x-3} + 37\lfloor B_y\rfloor_{N_x-2} + 34\lfloor B_y\rfloor_{N_x-1} - 6J_z(L)h_x^2\right). \tag{3.143}$$

Note that the interpolation stencils for B_y and B_z are modified for cells near $x = 0, L$ boundaries, whereas the interpolation stencils for E_y and E_z are not modified since the boundary conditions for the latter are implemented through ghost cells. The boundary conditions for the magnetic field components can also be implemented through ghost cells; however, since filling ghost cells for an inhomogeneous Neumann boundary condition requires the same amount of arithmetic as a one-sided reconstruction, the latter – more general – approach is used here.

3.5.4 Dispersive error and artificial diffusion in Maxwell's equations

All numerical methods used to approximate solutions to partial differential equations are subject to a combination of amplitude error and phase error, and control of these errors is an important objective for any spatial discretization method. In terms of the effect on the solution, amplitude errors are diffusive and phase errors are dispersive, and the latter present a more significant challenge for high-order methods.

The fourth-order accurate finite-volume method used for the distribution function relies on upwinding to combat dispersive errors. Upwinding is introduced by using a five-point polynomial reconstruction, with three cells on the upwind side and two cells on the downwind side, to interpolate the distribution function to a cell face. Upwinding electromagnetic fields would require solving a Riemann problem since the direction of electromagnetic wave propagation is not unique (e.g. counter-propagating light waves are possible). To avoid the associated complexity, the discretization for electromagnetic fields does not incorporate upwinding. As a result, the numerical solution for the electromagnetic fields is dominated by dispersive errors. In order to damp the spurious oscillations associated with dispersive errors, an artificial high-order dissipation is introduced. The degree to which dispersive errors can be dissipated is subject to numerical stability constraints, which for the case of Cartesian coordinates are described below.

The stability properties of the Maxwell solver with artificial dissipation are assessed by casting the equation system in the form

$$\frac{\partial \boldsymbol{q}}{\partial t} = L\boldsymbol{q}, \tag{3.144}$$

where $\boldsymbol{q}$ is a vector of electromagnetic field variables, and L is the linear spatial discretization operator. The eigenvalues of L combined with the properties of the characteristic polynomial of the RK4 time discretization provide a criteria for stability. Note that current source terms are ignored in this analysis.

Consider Ampere's law and Faraday's law in the absence of currents for fields in one dimension. The associated system of equations has a form that is consistent with Eq. (3.144):

$$\begin{bmatrix} B_y \\ B_z \\ E_y \\ E_z \end{bmatrix} = \begin{bmatrix} 0 & 0 & 0 & -\partial_x \\ 0 & 0 & \partial_x & 0 \\ 0 & -\partial_x & 0 & 0 \\ \partial_x & 0 & 0 & 0 \end{bmatrix} \begin{bmatrix} B_y \\ B_z \\ E_y \\ E_z \end{bmatrix}. \tag{3.145}$$

Adding artificial dissipation to a fourth-order discretization involves adding a sixth-derivative term $\alpha h_x^6 (d^6 q/dx^6)$ to the spatial discretization, where α is a scalar parameter. The associated operator matrix is then modified, such that

$$L = \begin{bmatrix} \alpha\partial_x^6 & 0 & 0 & -\partial_x \\ 0 & \alpha\partial_x^6 & \partial_x & 0 \\ 0 & -\partial_x & \alpha\partial_x^6 & 0 \\ \partial_x & 0 & 0 & \alpha\partial_x^6 \end{bmatrix}. \tag{3.146}$$

The derivative operators in discrete undivided finite-difference form are

$$\partial_x q_i = \frac{8}{12}\left(q_{i+1} - q_{i-1}\right) - \frac{1}{12}\left(q_{i+2} - q_{i-2}\right) \tag{3.147}$$

$$\partial_x^6 q_i = q_{i-3} - 6q_{i-2} + 15q_{i-1} - 20q_i + 15q_{i+1} - 6q_{i+2} + q_{i+3}, \tag{3.148}$$

where the first derivative is fourth-order accurate, and the sixth derivative is second-order accurate. Applying Von Neumann analysis, let each field component q be defined as $q = \hat{q}e^{ikx}$, where $\hat{q}$ depends on time. Noting that $q_{i+1} = \hat{q}e^{ik(x+h_x)}$ and letting $\beta = kh_x$, the transformed equation system operator matrix in terms of β is

$$\begin{bmatrix} -64\alpha\sin\left(\frac{\beta}{2}\right)^6 & 0 & 0 & -\frac{1}{6h_x}i(8\sin\beta - \sin(2\beta)) \\ 0 & -64\alpha\sin\left(\frac{\beta}{2}\right)^6 & \frac{1}{6h_x}i(8\sin\beta - \sin(2\beta)) & 0 \\ 0 & -\frac{1}{6h_x}i(8\sin\beta - \sin(2\beta)) & -64\alpha\sin\left(\frac{\beta}{2}\right)^6 & 0 \\ \frac{1}{6h_x}i(8\sin\beta - \sin(2\beta)) & 0 & 0 & -64\alpha\sin\left(\frac{\beta}{2}\right)^6 \end{bmatrix} \tag{3.149}$$

The unique eigenvalues w_1 and w_2 of the operator matrix are functions of β, such that

$$w_1 = \frac{1}{6}\left[-120\alpha - 180\alpha\cos\beta + 72\alpha\cos(2\beta) - 12\alpha\cos(3\beta) + \frac{1}{h_x}\left(\sin(2\beta) - 8\sin\beta\right)\right] \tag{3.150}$$

$$w_2 = \frac{1}{6}\left[-120\alpha + 180\alpha\cos\beta - 72\alpha\cos(2\beta) - 12\alpha\cos(3\beta) + \frac{1}{h_x}\left(\sin(2\beta) - 8\sin\beta\right)\right]. \tag{3.151}$$

These eigenvalues contain information about the stability properties of the algorithm. Completing the stability analysis involves accounting for the fact that a fourth-order Runge-Kutta method is used for the temporal discretization. The characteristic polynomial for RK4 is

$$P(z) = 1 + z + \frac{z^2}{2} + \frac{z^3}{6} + \frac{z^4}{24}. \tag{3.152}$$

For numerical stability the polynomial has to satisfy

$$|P(w\Delta t)| \leq 1 \tag{3.153}$$

for all eigenvalues $\{w\}$ of the spatial operator.

Let $\tilde{\alpha} = \alpha\Delta t$ and with the understanding that the advection speed is one, let $\sigma = \Delta t/h_x$ be the CFL number. Expressing the eigenvalues in terms of the parameter $\tilde{\alpha}$ and the CFL number yields

$$w_1\Delta t = \frac{1}{6}\left[\tilde{\alpha}\big(-120 - 180\cos\beta + 72\cos(2\beta) - 12\cos(3\beta)\big) + \sigma\left(\sin(2\beta) - 8\sin\beta\right)\right] \tag{3.154}$$

$$w_2\Delta t = \frac{1}{6}\left[\tilde{\alpha}\big(-120 + 180\cos\beta - 72\cos(2\beta) - 12\cos(3\beta)\big) + \sigma\left(\sin(2\beta) - 8\sin\beta\right)\right]. \tag{3.155}$$

Evaluating the characteristic polynomial in Eq. (3.152) for arguments $z = w_1\Delta t$ and $z = w_2\Delta t$, and determining where this polynomial satisfies Eq. (3.153) yields stability conditions on the values of the diffusion parameter $\tilde{\alpha}$ and CFL number. Through this analysis it is found that for stability the dissipation parameter $\tilde{\alpha}$ cannot exceed 0.0435.

3.5.5 Parabolic cleaning of divergence error in Maxwell's equations

When solving Faraday's law and Ampere's law for the electromagnetic fields, numerical errors can cause the discrete solution for the fields to violate the divergence constraints given by Gauss's laws. In order to explicitly enforce divergence constraints modified formulations of Faraday's law and Ampere's law are used, see discussion in Section 2.4.1.1. These

modified formulations, based on the method in Ref. [35], involve a parabolic term that is implemented as a filtering step: after the solution is advanced through all the stages of RK4 using the standard formulation of Faraday's law and Ampere's law, the solution is subsequently filtered to minimize divergence error. The reason for implementing this "parabolic cleaning" of the error as a filter is largely associated with order of accuracy considerations; the parabolic cleaning should be fourth-order accurate and act on a fourth-order accurate solution. Consequently the parabolic cleaner is not implemented within each stage of RK4, since the solution within each stage is not fourth-order accurate, but rather as a filtering step after the time advance.

3.5.5.1 Von Neumann stability analysis

The degree to which the divergence error associated with the electric and magnetic field (see Eq. (2.89) and Eq. (2.90)) can be filtered is limited on account of numerical stability constraints. To understand the scope of these constraints, Von Neumann numerical stability analysis is applied to a finite-difference formulation of the filtering step. The divergence error associated with the magnetic field is considered first, although the same analysis can be applied to the divergence error associated with the electric field in the absence of charges.

For the magnetic field in two dimension, this filtering step can be expressed as the differential equation system

$$\frac{\partial \boldsymbol{B}}{\partial t} = \lambda \nabla (\nabla \cdot \boldsymbol{B}) \tag{3.156}$$

$$\frac{\partial}{\partial t} \begin{bmatrix} B_x \\ B_y \end{bmatrix} = \lambda \begin{bmatrix} \frac{\partial^2}{\partial x^2} & \frac{\partial^2}{\partial x \partial y} \\ \frac{\partial^2}{\partial x \partial y} & \frac{\partial^2}{\partial y^2} \end{bmatrix} \begin{bmatrix} B_x \\ B_y \end{bmatrix}, \tag{3.157}$$

where $\lambda = ah^2/\Delta t$ is a constant that sets the rate which divergence error is diminished. Note that a is a constant, h is the cell width which for convenience is assumed to be the same along the x and y directions, and Δt is the time step size. Von Neumann stability analysis is used to determine a range for the value a, such that the numerical method remains stable. The analysis calls for the temporal and spatial discretization of the differential equation system in Eq. (3.157). Note that two is the minimum number of dimensions in which this analysis can be applied due to the presence of mixed derivative terms.

To simplify the analysis, the fields are treated as volume-average quantities, as opposed to the area-integrated quantities used in the field solver. Here the notation $\langle B_x \rangle_{i,j}$ denotes a volume average of the x-component of the magnetic field over the (i, j) cell. Using volume-averaged fields yields discretization stencils that are independent of direction. In effect the Von Neumann analysis is applied to a somewhat simpler system of equations, but can still be used to shed light on the stability properties of the discrete system. Although it would require modification, the analysis can be extended to apply to area-integrated fields. Replacing the analytic fields in Eq. (3.157) with discrete analogs, and replacing the time derivative by a

forward difference, such that

$$\frac{\partial \langle B \rangle_{i,j}}{\partial t} = \frac{1}{\Delta t}\left(\langle B \rangle_{i,j}^{n+1} - \langle B \rangle_{i,j}^{n} \right), \tag{3.158}$$

allows the solution at time t^{n+1} to be expressed, through a linear operator relation, in terms of the solution at time t^n:

$$\begin{bmatrix} \langle B_x \rangle \\ \langle B_y \rangle \end{bmatrix}^{n+1} = \begin{bmatrix} \left(1 + \Delta t \lambda \frac{\partial^2}{\partial x^2}\right) & \Delta t \lambda \frac{\partial^2}{\partial x \partial y} \\ \Delta t \lambda \frac{\partial^2}{\partial x \partial y} & \left(1 + \Delta t \lambda \frac{\partial^2}{\partial y^2}\right) \end{bmatrix} \begin{bmatrix} \langle B_x \rangle \\ \langle B_y \rangle \end{bmatrix}^{n}. \tag{3.159}$$

3.5.5.2 Stability constraint for fourth-order parabolic cleaning

For the spatial discretization, the spatial derivative terms in Eq. (3.159) are replaced with their discrete representations. Fourth-order accurate finite-difference representations of these derivatives are

$$\frac{\partial^2}{\partial x^2} \langle B \rangle_{i,j} = \frac{1}{12h^2}\left[- \langle B \rangle_{i-2,j} + 16 \langle B \rangle_{i-1,j} - 30 \langle B \rangle_{i,j} + 16 \langle B \rangle_{i+1,j} - \langle B \rangle_{i+2,j} \right] \tag{3.160}$$

$$\frac{\partial^2}{\partial y^2} \langle B \rangle_{i,j} = \frac{1}{12h^2}\left[- \langle B \rangle_{i,j-2} + 16 \langle B \rangle_{i,j-1} - 30 \langle B \rangle_{i,j} + 16 \langle B \rangle_{i,j+1} - \langle B \rangle_{i,j+2} \right] \tag{3.161}$$

$$\begin{aligned} \frac{\partial^2}{\partial x \partial y} \langle B \rangle_{i,j} = \frac{1}{144h^2}\Big[& \langle B \rangle_{i-2,j-2} + \langle B \rangle_{i+2,j+2} - \langle B \rangle_{i-2,j+2} - \langle B \rangle_{i+2,j-2} \\ & + 8\Big(\langle B \rangle_{i-2,j+1} + \langle B \rangle_{i-1,j+2} + \langle B \rangle_{i+1,j-2} + \langle B \rangle_{i+2,j-1} \\ & - \langle B \rangle_{i-2,j-1} - \langle B \rangle_{i-1,j-2} - \langle B \rangle_{i+1,j+2} - \langle B \rangle_{i+2,j+1} \Big) \\ & + 64\left(\langle B \rangle_{i-1,j-1} + \langle B \rangle_{i+1,j+1} - \langle B \rangle_{i-1,j+1} - \langle B \rangle_{i+1,j-1} \right) \Big] \end{aligned} \tag{3.162}$$

where i and j are indices denoting the spatial location. The stencils in Eq. (3.160) can be derived by performing a one-dimensional fourth-order accurate polynomial reconstruction. The large stencil given by Eq. (3.162) can be derived by applying the stencil in Eq. (3.94) along each direction to obtain corner point values of the field, $\langle B \rangle_{i+\frac{1}{2},j+\frac{1}{2}}$, which can be used to evaluate the mixed derivative term

$$\frac{\partial^2}{\partial x \partial y} \langle B \rangle_{i,j} = \left(\langle B \rangle_{i+\frac{1}{2},j+\frac{1}{2}} - \langle B \rangle_{i-\frac{1}{2},j+\frac{1}{2}} \right) - \left(\langle B \rangle_{i+\frac{1}{2},j-\frac{1}{2}} - \langle B \rangle_{i-\frac{1}{2},j-\frac{1}{2}} \right). \tag{3.163}$$

It is assumed that the cell spacing in the x and y directions are equal such that $h = h_x = h_y$. Consistent with the Von Neumann analysis procedure, a single Fourier mode is analyzed, such that the solution is assumed to have the form

$$\boldsymbol{B} = \hat{\boldsymbol{B}} e^{\iota k x + \iota m y} \tag{3.164}$$

where ι is the unit imaginary number, k denotes the wavenumber of a mode along the x-direction, and m is the wavenumber of a mode along the y-direction. This means that each of the discrete terms that appear in Eqs. (3.160) – (3.162) can be represented by a shift away from the cell (i, j) and an amplitude g^n at time n, such that

$$\left\langle \hat{B} \right\rangle_{i,j}^{n} = g^n e^{\iota k x + \iota m y} \tag{3.165}$$

$$\left\langle \hat{B} \right\rangle_{i+1,j}^{n} = \left\langle \hat{B} \right\rangle_{i,j}^{n} e^{\iota k h} \tag{3.166}$$

$$\left\langle \hat{B} \right\rangle_{i,j-1}^{n} = \left\langle \hat{B} \right\rangle_{i,j}^{n} e^{-\iota m h} \tag{3.167}$$

$$\left\langle \hat{B} \right\rangle_{i,j}^{n+1} = \left\langle \hat{B} \right\rangle_{i,j}^{n} g. \tag{3.168}$$

Let $\beta = kh$ and $\gamma = mh$. Then the discrete derivatives given by Eqs. (3.160) – (3.162) can be expressed in terms of $\langle B \rangle_{i,j}^{n}$ through the relations given by Eqs. (3.165) – (3.168). Since each term is expressed in terms of an exponential function of β or γ the resulting discrete operators simplify to

$$\frac{\partial^2}{\partial x^2} = \frac{2}{3h^2}\left(-7 + \cos\beta\right)\sin\left(\frac{\beta}{2}\right)^2 \tag{3.169}$$

$$\frac{\partial^2}{\partial y^2} = \frac{2}{3h^2}\left(-7 + \cos\gamma\right)\sin\left(\frac{\gamma}{2}\right)^2 \tag{3.170}$$

$$\frac{\partial^2}{\partial x \partial y} = -\frac{1}{36h^2}\left(-8\sin\beta + \sin(2\beta)\right)\left(-8\sin\gamma + \sin(2\gamma)\right). \tag{3.171}$$

Having applied a Fourier transform to the magnetic field variable, Eq. (3.159) in terms of Fourier-transformed variables is

$$\begin{bmatrix} \left\langle \hat{B}_x \right\rangle \\ \left\langle \hat{B}_y \right\rangle \end{bmatrix}^{n+1} = \begin{bmatrix} \left(1 + \Delta t \lambda \frac{\partial^2}{\partial x}\right) & \Delta t \frac{\partial^2}{\partial x \partial y} \\ \Delta t \lambda \frac{\partial^2}{\partial x \partial y} & \left(1 + \Delta t \lambda \frac{\partial^2}{\partial y^2}\right) \end{bmatrix} \begin{bmatrix} \left\langle \hat{B}_x \right\rangle \\ \left\langle \hat{B}_y \right\rangle \end{bmatrix}^{n}. \tag{3.172}$$

Substituting the derivative expressions in Eqs. (3.169) – (3.171) into Eq. (3.172) yields a modified linear system that lends itself to stability analysis. In particular, the matrix in Eq. (3.172) becomes

$$\begin{bmatrix} 1 + \frac{2}{3}a\left(\cos\beta - 7\right)\sin\left(\frac{\beta}{2}\right)^2 & -\frac{1}{36}a\left(\sin(2\beta) - 8\sin\beta\right)\left(\sin(2\gamma) - 8\sin\gamma\right) \\ -\frac{1}{36}a\left(\sin(2\beta) - 8\sin\beta\right)\left(\sin(2\gamma) - 8\sin\gamma\right) & 1 + \frac{2}{3}a\left(\cos\gamma - 7\right)\sin\left(\frac{\gamma}{2}\right)^2 \end{bmatrix}, \tag{3.173}$$

where factors of $\lambda = ah^2/\Delta t$ have cancelled with factors of Δt from the temporal discretization and factors of h^2 from the derivatives. This matrix is referred to as the amplification

matrix (see for example Refs. [47, 48]). For numerical stability the eigenvalues of the amplification matrix must be less than or equal to one for all values of $\beta, \gamma \in [-\pi, \pi] \times [-\pi, \pi]$. Since the expressions for the eigenvalues can be complicated, they can analyzed in terms of Taylor series expansions in the variables β and γ or they can be plotted. In terms of Taylor series expansions, the eigenvalues w_1 and w_2 of the amplification matrix in Eq. (3.173) are

$$\begin{aligned} w_1 = &\left(1 + \left[-\frac{a}{2} - \frac{\sqrt{a^2}}{2}\right]\gamma^2 + \mathcal{O}(\gamma^6)\right) + \left(\left[-\frac{a}{2} - \frac{\sqrt{a^2}}{2}\right] + \frac{1}{18}\sqrt{a^2}\gamma^4 + \mathcal{O}(\gamma^6)\right)\beta^2 \\ &+ \left(-\frac{\sqrt{a^2}\gamma^2}{18} + \frac{1}{144}\sqrt{a^2}\gamma^4 + \mathcal{O}(\gamma^6)\right)\beta^4 + \mathcal{O}(\beta^6) \end{aligned} \tag{3.174}$$

$$\begin{aligned} w_2 = &\left(1 + \left[-\frac{a}{2} + \frac{\sqrt{a^2}}{2}\right]\gamma^2 + \mathcal{O}(\gamma^6)\right) + \left(\left[-\frac{a}{2} + \frac{\sqrt{a^2}}{2}\right] - \frac{1}{18}\sqrt{a^2}\gamma^4 + \mathcal{O}(\gamma^6)\right)\beta^2 \\ &+ \left(\frac{1}{18}\sqrt{a^2}\gamma^2 - \frac{1}{144}\sqrt{a^2}\gamma^4 + \mathcal{O}(\gamma^6)\right)\beta^4 + \mathcal{O}(\beta^6). \end{aligned} \tag{3.175}$$

To determine whether the eigenvalues are less than one, the analytic expressions for w_1 and w_2 can be plotted. Regions of β and γ values for which $|w_1| < 1$ and $|w_2| < 1$ are shown in Fig. 3.5 for different values of constant a. For both eigenvalues to be less than one, the value of a must be less than or equal to approximately 0.35. This means that the maximum rate that divergence error can be diminished by is set by $a = 0.35$. Higher values of a would result in numerical instability.

Since the eigenvalues appear to be symmetric along the line $\beta = \gamma$, then setting $\gamma = \beta$ in the amplification matrix in Eq. (3.173) results in simpler analytic expressions for the eigenvalues, such that

$$w_1 = \frac{1}{72}\left(72 - 115a + 176a\cos\beta - 76a\cos(2\beta) + 16a\cos(3\beta) - a\cos(4\beta)\right) \tag{3.176}$$

$$w_2 = \frac{1}{72}\left(72 - 245a + 208a\cos\beta + 52a\cos(2\beta) - 16a\cos(3\beta) + a\cos(4\beta)\right) \tag{3.177}$$

Plots of these eigenvalues are shown in Fig. 3.6 for different values of parameter a. These plots likewise indicate that $a \lesssim 0.35$ is a requirement for numerical stability.

3.5.5.3 Stability constraint for second-order parabolic cleaning

To determine whether the stability constraint for the fourth-order discretization derived above is reasonable, Von Neumann stability analysis is performed for a second-order spatial discretization of the grad-div parabolic cleaning operator. The constraint on the constant a should be less stringent in a second-order discretization. Second-order discrete derivative

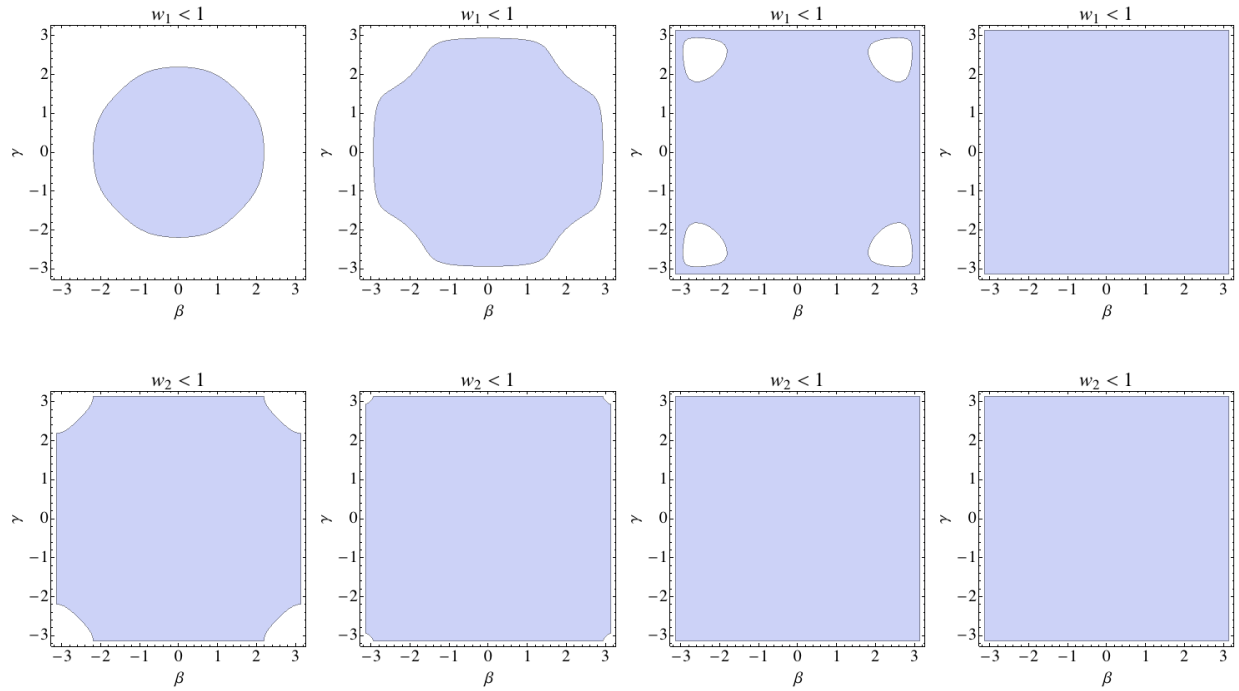

(a) $a = 0.4$ **(b)** $a = 0.38$ **(c)** $a = 0.37$ **(d)** $a = 0.35$

Figure 3.5: The eigenvalues $w_1(\beta, \gamma)$ and $w_2(\beta, \gamma)$ of the amplification matrix given by Eq. (3.173) must be less than one for all values of β and γ in order for the parabolic cleaning discretization to be numerically stable. Shaded regions indicate where in the (β, γ) plane the inequalities $w_1 < 1$ and $w_2 < 1$ are satisfied for different values of the parabolic cleaning constant a. These plots indicate that a must be less than approximately 0.35 for the fourth-order accurate parabolic cleaning implementation to be stable.

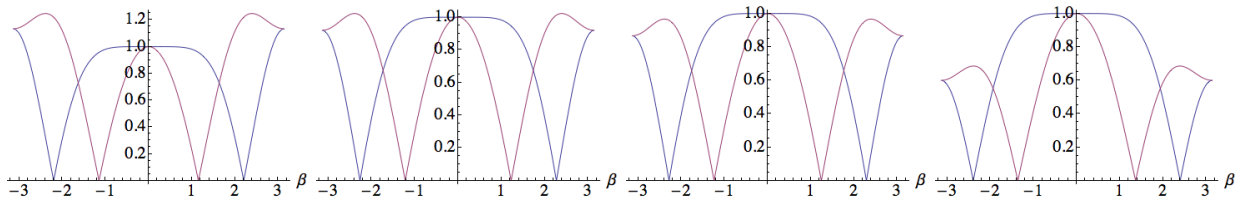

(a) $a = 0.4$ **(b)** $a = 0.36$ **(c)** $a = 0.35$ **(d)** $a = 0.3$

Figure 3.6: Eigenvalues w_1 (blue) and w_2 (pink) given by Eq. (3.176) and Eq. (3.177) are plotted as a function of β for different values of divergence cleaning parameter a. Both eigenvalues must be less than one for numerical stability. In this case the wavenumber k along the x-direction is assumed to be equal to the wavenumber m along the y-direction, such that $\beta = \gamma$. This simplification yields the same upper bound on the parameter a, such that $a \lesssim 0.35$ is needed for numerical stability of fourth-order parabolic divergence cleaning.

terms expressed in terms of discrete volume-averages are

$$\frac{\partial^2}{\partial x^2}\left\langle B\right\rangle_{i,j} = \frac{1}{h^2}\left(\left\langle B\right\rangle_{i+1,j} - 2\left\langle B\right\rangle_{i,j} + \left\langle B\right\rangle_{i-1,j}\right) \tag{3.178}$$

$$h^2\frac{\partial^2}{\partial y^2}\left\langle B\right\rangle_{i,j} = \left(\left\langle B\right\rangle_{i,j+1} - 2\left\langle B\right\rangle_{i,j} + \left\langle B\right\rangle_{i,j+1}\right) \tag{3.179}$$

$$h^2\frac{\partial^2}{\partial x\partial y}\left\langle B\right\rangle_{i,j} = B_{i+\frac{1}{2},j+\frac{1}{2}} + B_{i-\frac{1}{2},j-\frac{1}{2}} - B_{i-\frac{1}{2},j+\frac{1}{2}} - B_{i+\frac{1}{2},j-\frac{1}{2}} \tag{3.180}$$

where

$$B_{i+\frac{1}{2},j+\frac{1}{2}} = \frac{1}{4}\left(\left\langle B\right\rangle_{i,j} + \left\langle B\right\rangle_{i+1,j} + \left\langle B\right\rangle_{i+1,j+1} + \left\langle B\right\rangle_{i,j+1}\right). \tag{3.181}$$

A single Fourier mode is analyzed, such that the solution is assumed to have the form in Eq. (3.164). The derivatives in Eq. (3.178), Eq. (3.179), and Eq. (3.180) can be expressed in terms of $\left\langle \hat{B}\right\rangle_{i,j}^{n}$, using the relations given by Eq. (3.165) through Eq. (3.168), such that

$$\frac{\partial^2}{\partial x^2} = 2(\cos\beta - 1) \tag{3.182}$$

$$h^2\frac{\partial^2}{\partial y^2} = 2(\cos\gamma - 1) \tag{3.183}$$

$$h^2\frac{\partial^2}{\partial x\partial y} = -\sin\beta\sin\gamma \tag{3.184}$$

The amplification matrix is obtained by substituting Eq. (3.182), Eq. (3.183), and Eq. (3.184) into the matrix in Eq. (3.172). The eigenvalues of the resulting amplification matrix are

$$w_1 = 1 - a + a\cos\gamma + \cos\beta(a - a\cos\gamma) \tag{3.185}$$

$$w_2 = 1 - 3a + a\cos\gamma + a\cos\beta(1 + \cos\gamma). \tag{3.186}$$

These eigenvalues can be plotted as a function of $\beta = kh$ and $\gamma = mh$ to determine the upper bound on the value of a. Regions of β and γ values for which $|w_1| < 1$ and $|w_2| < 1$ are shown in Fig. 3.7 for different values of constant a. For both eigenvalues to be less than one, the value of a must be less than or equal to approximately 0.5. Note that the maximum rate at which divergence error can be diminished by is set by $a = 0.35$ for a fourth-order discretization and by $a = 0.5$ for a second-order spatial discretization.

3.5.5.4 Limitations of stability analysis and parabolic cleaning approach

Von Neumann stability analysis yields an upper bound on the parameter a, which determines the maximum rate of parabolic divergence error cleaning. It is important to note that this upper bound is an approximation to the true upper bound since the approach relies

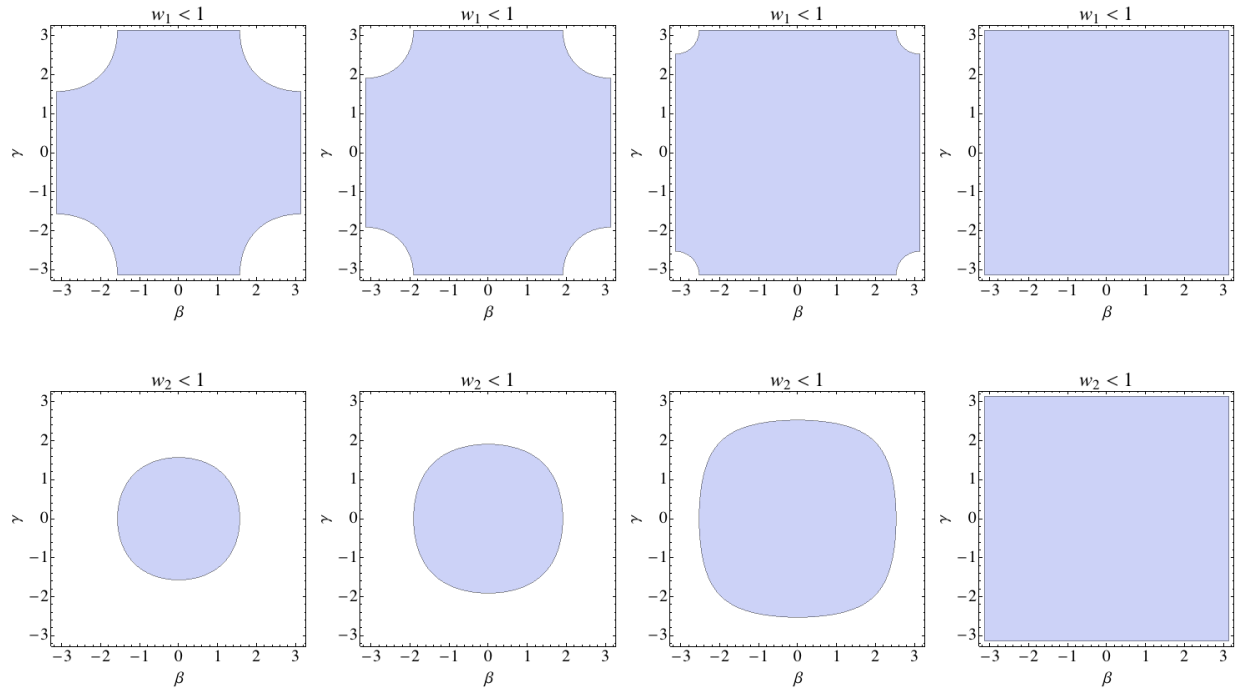

(a) $a = 1.0$ **(b)** $a = 0.75$ **(c)** $a = 0.55$ **(d)** $a = 0.5$

Figure 3.7: For different values of the parabolic cleaning constant a, the shaded regions indicate where in the (β, γ) plane the eigenvalues w_1 and w_2 are less than or equal to one. These plots indicate that a must be less than approximately 0.5 for the second-order accurate parabolic cleaning implementation to be numerically stable.

on linear Fourier analysis and ignores boundaries. Moreover, additional assumptions were introduced to simplify the analysis, including the assumption that cell spacings are equal along each direction, and that the variables of interest are volume-average quantities. In order to generalize the analysis to area-integrated quantities (recall that the field variables are area-integrals), the discretization stencils for the grad-div operator would need to be modified.

Von Neumann stability analysis can be reproduced for the electric field constraint, which involves a gradient-of-charge-density term (see Eq. (2.89)). Likewise the analysis can be extended to three dimensions. Note that Von Neumann stability analysis would not be appropriate in the context of cylindrical coordinates that involve the radius since Fourier transforms are not applicable in that case.

It is also important to note some of the limitations associated with parabolic cleaning itself, even in the context of Cartesian coordinates, in which the procedure is relatively straightforward to implement. One limitation is that the stencil required to evaluate the grad-div operator to fourth-order accuracy is large. This presents issues near boundaries of the domain, and specifically corners of the domain, where ghost cells may not be well-defined.

Modifying the parabolic cleaning stencil near boundaries presents additional complexity that is not explored here. Another limitation is the rate of cleaning, which is more restricted for higher-order discretizations, such that divergence errors are diffused away quite slowly. Ultimately, the difficulties associated with the implementation of a generalized parabolic cleaner should be weighed against the benefits of the procedure. If divergence errors are small relative to the values of the fields, then parabolic cleaning may not be necessary.

3.5.6 Fourth-order finite-volume discretization for electrostatic field

The Vlasov equation, Faraday's law, and Ampere's law can all be cast in hyperbolic form, and thereby have similar spatial discretizations. The governing equation for electrostatic fields is the Poisson equation, which is an elliptic partial differential equation and requires a slightly different finite-volume treatment. In particular, unlike hyperbolic equations for which only local information is needed to update the solution, the Poisson equation requires a global solve in order to update local values of the fields. Another distinction is that electrostatic field discretization involves interpolation, but does not involve quadratures. Consequently the Taylor series relations used in Section 3.4.2.3 and Section 3.5.1.2 do not play a role in the discretization of the electrostatic field.

In general, solving for the electrostatic field using a finite-volume approach involves constructing a linear operator for the weak form of Poisson's equation and solving the resulting discrete linear system. In certain special cases, alternative means can be used. These include the use of the strong form of Gauss's law in one dimensional configurations, and the use the strong form of Poisson's equation in combination with Fourier transforms in periodic domains.

3.5.6.1 Charge density for electrostatic field calculations

The finite-volume solution to the electric field in the context of electrostatic calculations relies on knowing the cell-integrated charge density (i.e. the charge) to fourth order accuracy. Charge density is computed by way of number density, which is analytically defined to be the zeroth velocity moment of the distribution function (see Eq. (2.96)). In a finite-volume calculation, the discretized distribution function is defined to be a cell-volume-integrated quantity (see discussion in Section 3.4.1). Since a fourth-order accurate cell-integrated quantity incorporates information about the distribution function variation along each direction, then computing the zeroth velocity moment to fourth-order accuracy amounts to a simple sum. For a six-dimensional discrete volume-integrated distribution function, whose spatial coordinates are indexed by (i, j, k) and whose velocity coordinates are indexed by (l, m, n), the

volume-integrated number density $\langle n_s \rangle$ in cell (i, j, k) for species s is

$$\langle n_s \rangle_{i,j,k} = \sum_{l=0}^{N_{v_1}-1} \sum_{m=0}^{N_{v_2}-1} \sum_{n=0}^{N_{v_3}-1} \langle f_s \rangle_{i,j,k,l,m,n} \,, \tag{3.187}$$

where the integral over a cell volume, denoted by $\langle \cdot \rangle$, has different definitions in Cartesian and cylindrical coordinates. In essence, the volume-integrated number density is the number of particles in a cell, relative to a global characteristic value. The actual number density can be computed by dividing Eq. (3.187) by the volume of each cell. The summations in Eq. (3.187) are performed over all velocity coordinate directions. Note that the discrete volume-integrated distribution function occupies a six-dimensional phase space volume, whereas the volume-integrated density occupies a physical space volume. While Eq. (3.187) states the general case, in practice the number of discretized phase space dimensions is typically less than six.

The volume-integrated charge density is computed by multiplying the volume-integrated number density by the relative species charge, and summing over species,

$$\langle \rho \rangle_{i,j,k} = \sum_s Z_s \langle n_s \rangle_{i,j,k} \,. \tag{3.188}$$

With charge density known to fourth-order accuracy, the electrostatic potential, and by extension the electric field can be computed as well.

3.5.6.2 One-dimensional electric field solver using Gauss's law

In a one-dimensional electrostatic system, the strong form of Gauss's law (see Eq. (2.34)) can be solved directly for the electric field without using Poisson's equation. This is because the divergence term reduces to a derivative of a scalar. In one dimension, Gauss's law states that

$$\frac{\partial E_x}{\partial x} = \sum_s Z_s n_s. \tag{3.189}$$

Integrating both sides yields an expression for the electric field as a function of the coordinate x,

$$E_x(x) = E_x(x_0) + \sum_s Z_s \int_{x_0}^{x} n_s(x') dx', \tag{3.190}$$

where $E_x(x_0)$ is a known value of the electric field at a reference point x_0. In practice the reference point is typically chosen to be at a boundary. For a finite-volume formulation, Eq. (3.190) is recast in terms of discrete quantities. Let $\langle n_s \rangle_i$ be the cell-integrated number

density and let $\langle\rho\rangle_i$ be the cell-integrated charge density (i.e. the charge) in cell i, such that

$$\langle n_s\rangle_i = \int_{x_{i-\frac{1}{2}}}^{x_{i+\frac{1}{2}}} n_s(x')dx' \tag{3.191}$$

$$\langle\rho\rangle_i = \sum_s Z_s \langle n_s\rangle_i . \tag{3.192}$$

Note that $\langle n_s\rangle_i$, as defined in Eq. (3.191), is computed from the distribution function using the relation in Eq. (3.188). Then the electric field at the $i+\frac{1}{2}$ cell face can be expressed in terms of known discrete quantities:

$$\langle E_x\rangle_{i+\frac{1}{2}} = \langle E_x\rangle_{-\frac{1}{2}} + \sum_{k=0}^{i} \langle\rho\rangle_k \qquad \text{for } i \in \{0, 1, \cdots, N-1\}, \tag{3.193}$$

where $\langle E_x\rangle_{-\frac{1}{2}}$ is the reference value of the electric field, in this case defined to be at the left end of the domain. The choice of reference value for the field is important, particularly in cases where the electric field value is not constrained at boundaries. For example, in a periodic domain that contains zero net charge, setting $\langle E_x\rangle_{-\frac{1}{2}}$ to a fixed value can be problematic since numerical errors can lead to the development of a net electric field, which is a violation of Gauss's law. A better choice of reference value for a charge-neutral periodic domain is to set $\langle E_x\rangle_{-\frac{1}{2}}$ to be the negative of the domain-average electric field. This ensures that the net electric field is consistent with the net charge in the system for all time.

The cell-face value of the electric field can be interpolated using a polynomial reconstruction to compute the cell-center point value. Let P_4 be a fourth-order accurate polynomial,

$$P_4(x) = p_3x^3 + p_2x^2 + p_1x + p_0. \tag{3.194}$$

Setting up a linear system of equations,

$$\langle E_x\rangle_{i-\frac{3}{2}} = P_4(x_{i-\frac{3}{2}}) \tag{3.195}$$

$$\langle E_x\rangle_{i-\frac{1}{2}} = P_4(x_{i-\frac{1}{2}}) \tag{3.196}$$

$$\langle E_x\rangle_{i+\frac{1}{2}} = P_4(x_{i+\frac{1}{2}}) \tag{3.197}$$

$$\langle E_x\rangle_{i+\frac{3}{2}} = P_4(x_{i+\frac{3}{2}}), \tag{3.198}$$

solving the system for the coefficients $\{p_3, p_2, p_1, p_0\}$, and evaluating P_4 at the center of the cell $x = x_i$, yields the stencil for computing the cell-center point value,

$$(E_x)_i = P_4(x_i) = \frac{9}{16}\left(\langle E_x\rangle_{i+\frac{1}{2}} + \langle E_x\rangle_{i-\frac{1}{2}}\right) - \frac{1}{16}\left(\langle E_x\rangle_{i+\frac{3}{2}} + \langle E_x\rangle_{i-\frac{3}{2}}\right). \tag{3.199}$$

Likewise a cell-integrated value $\langle E_x\rangle_i$ can be computed by using the same reconstructed polynomial P_4, such that

$$\langle E_x\rangle_i = \int_{x_{i-\frac{1}{2}}}^{x_{i+\frac{1}{2}}} P_4(x)dx = \frac{13h_x}{24}\left(\langle E_x\rangle_{i+\frac{1}{2}} + \langle E_x\rangle_{i-\frac{1}{2}}\right) - \frac{h_x}{24}\left(\langle E_x\rangle_{i+\frac{3}{2}} + \langle E_x\rangle_{i-\frac{3}{2}}\right). \tag{3.200}$$

3.5.6.3 Poisson solve using FFTs on periodic domain

The Fourier transform, cosine transform, and sine transform can be used to solve the Poisson equation, provided that the boundary conditions are periodic, homogeneous Neumann, and homogeneous Dirichlet, respectively. FFTs are not well suited for inhomogeneous boundary conditions and for calculations involving adaptive mesh refinement. Here only the periodic case for a uniform structured grid is considered.

Consider a one-dimensional periodic domain. Applying a Fourier transform to the strong form of the Poisson equation yields

$$\mathcal{F}\left(-\frac{d^2\phi}{dx^2}\right) = \mathcal{F}(\rho) \tag{3.201}$$

$$k^2\mathcal{F}(\phi) = \mathcal{F}(\rho) \tag{3.202}$$

where $\mathcal{F}$ is the Fourier transform operator and $k = \frac{2\pi}{x}$ is the wavenumber. Solving for ϕ then yields

$$\phi = \mathcal{F}^{-1}\left(\frac{\mathcal{F}(\rho)}{k^2}\right), \tag{3.203}$$

where $\mathcal{F}^{-1}$ is the inverse Fourier transform operator.

The same procedure can be applied using discrete fast Fourier transforms (FFT) and a discrete formulation of the one-dimensional Poisson equation. Discrete FFTs are implemented as operators (much like in Eq. (3.203)) using commercial or open-source software library packages (see Appendix A). Thus to implement a discrete FFT solver for the Poisson equation it is sufficient to define a discrete charge density and a discrete wave number. Suppose that ρ is discretely defined, such that ρ_i is the cell-center charge density for cells indexed by $i \in \{0, \cdots, N-1\}$ on domain $x \in [0, L]$. Then the wave number in this discretized domain is defined as

$$k = \frac{2\pi}{L}\left\{0, 1, 2, \cdots, \frac{N}{2} - 1,\right\} \cup \left\{-\frac{N}{2}, -\frac{N}{2} + 1, -\frac{N}{2} + 2, \cdots, -1\right\}, \tag{3.204}$$

where the ordering of terms is due to conventions used in typical FFT software implementations. Note that the smallest wavenumber k that can be captured in a finite domain is $k = 2\pi/L$. Then the solution given by Eq. (3.203) would yield the cell-centered value of the electrostatic potential which can be interpolated to solve for the gradient of ϕ, and thereby for the electric field. The procedure can be applied in much the same way to two- and three-dimensional periodic domains. See Appendix A for examples of using FFTs to solve the Poisson equation in two dimensions using Matlab and FFTW library in C++ implementations.

3.5.6.4 Poisson solve based on global linear system of equations

For a system that involves a multidimensional domain with inhomogeneous boundary conditions and multiple components of the electric field, solving for the electric field requires first

solving for the electrostatic potential. In finite-volume implementations solving the Poisson equation calls for the construction of a linear operator.

Consider the one-dimensional weak form of the Poisson equation (see Eq. (2.97)). Let $\langle\rho\rangle_i$ denote the cell volume integrated charge density, defined in Eq. (3.192). Then for a given cell i, the Poisson equation in weak form states that

$$-\left[\frac{d\phi}{dx}\right]_{i-\frac{1}{2}}^{i+\frac{1}{2}} = \langle\rho\rangle_i \,. \tag{3.205}$$

Note that the differential area along the x direction is arbitrary and for convenience is assumed to be one for this one-dimensional system. Eq. (3.205) is an analytic expression that relates the cell face derivatives of the electrostatic potential to the cell-integrated charge density, or the charge in a cell. In anticipation of 2D and 3D domains, the objective is to solve for ϕ, rather than the gradient of ϕ. Thus the derivative term on the lefthand side of Eq. (3.205) needs to be recast as a discrete linear operator acting on ϕ. Since one of the objectives in this discretization is to have a fourth-order accurate electric field, the derivative operator in Eq. (3.205) should be fourth-order accurate.

The stencil for a fourth-order accurate face value of the derivative of ϕ is given by

$$\left\langle\frac{d\phi}{dx}\right\rangle_{i+\frac{1}{2}} = \frac{15}{12h_x^2}\left(\langle\phi\rangle_{i+1} - \langle\phi\rangle_i\right) - \frac{1}{12h_x^2}\left(\langle\phi\rangle_{i+2} - \langle\phi\rangle_{i-1}\right). \tag{3.206}$$

This expression for the derivative in terms of volume-integrated values is analogous to the expression derived in Ref. [49] in terms of volume-average values. Note that the fourth-order stencil and fifth-order stencil for evaluating the derivative of ϕ at a cell face are identical. Using this stencil, the discrete version of the lefthand side term in Eq. (3.205) is

$$-\left[\frac{d\phi}{dx}\right]_{i-\frac{1}{2}}^{i+\frac{1}{2}} = -\left(\left\langle\frac{d\phi}{dx}\right\rangle_{i+\frac{1}{2}} - \left\langle\frac{d\phi}{dx}\right\rangle_{i-\frac{1}{2}}\right) \tag{3.207}$$

$$= -\frac{1}{h_x^2}\left(\frac{1}{12}\langle\phi\rangle_{i+2} + \frac{4}{3}\langle\phi\rangle_{i+1} - \frac{5}{2}\langle\phi\rangle_i + \frac{4}{3}\langle\phi\rangle_{i-1} - \frac{1}{12}\langle\phi\rangle_{i-2}\right). \tag{3.208}$$

Using the stencil in Eq. (3.208) for each cell in the domain, a global matrix operator L can be constructed, such that the local analytic expression given by Eq. (3.205) is recast as a global linear system:

$$L\underline{\phi} = \underline{\rho} \tag{3.209}$$

where $\underline{\phi}$ is a vector of N unknowns, and $\underline{\rho}$ is a vector of cell-integrated charge density values in each cell in the domain. The main diagonals of the matrix L are given by the coefficients in the stencil in Eq. (3.208), and the first two rows and last two rows are modified to account for changes in the stencil near boundaries. See Ref. [49] for high-order boundary condition

stencils. As an example, the operator matrix for periodic boundary conditions in an eight-cell system is

$$\frac{1}{h_x^2}\begin{bmatrix} -\frac{5}{2} & \frac{4}{3} & -\frac{1}{12} & 0 & 0 & 0 & -\frac{1}{12} & \frac{4}{3} \\ \frac{4}{3} & -\frac{5}{2} & \frac{4}{3} & -\frac{1}{12} & 0 & 0 & 0 & -\frac{1}{12} \\ -\frac{1}{12} & \frac{4}{3} & -\frac{5}{2} & \frac{4}{3} & -\frac{1}{12} & 0 & 0 & 0 \\ 0 & -\frac{1}{12} & \frac{4}{3} & -\frac{5}{2} & \frac{4}{3} & -\frac{1}{12} & 0 & 0 \\ 0 & 0 & -\frac{1}{12} & \frac{4}{3} & -\frac{5}{2} & \frac{4}{3} & -\frac{1}{12} & 0 \\ 0 & 0 & 0 & -\frac{1}{12} & \frac{4}{3} & -\frac{5}{2} & \frac{4}{3} & -\frac{1}{12} \\ -\frac{1}{12} & 0 & 0 & 0 & -\frac{1}{12} & \frac{4}{3} & -\frac{5}{2} & \frac{4}{3} \\ \frac{4}{3} & -\frac{1}{12} & 0 & 0 & 0 & -\frac{1}{12} & \frac{4}{3} & -\frac{5}{2} \end{bmatrix}. \tag{3.210}$$

This matrix is singular, and thereby requires further modification. To implement periodic boundaries, an additional constraint, stipulating that the average value of the potential is zero ($\sum_i \phi_i = 0$), is incorporated, such that the resulting linear system is

$$\frac{1}{h_x^2}\begin{bmatrix} -\frac{5}{2} & \frac{4}{3} & -\frac{1}{12} & 0 & 0 & 0 & -\frac{1}{12} & \frac{4}{3} \\ \frac{4}{3} & -\frac{5}{2} & \frac{4}{3} & -\frac{1}{12} & 0 & 0 & 0 & -\frac{1}{12} \\ -\frac{1}{12} & \frac{4}{3} & -\frac{5}{2} & \frac{4}{3} & -\frac{1}{12} & 0 & 0 & 0 \\ 0 & -\frac{1}{12} & \frac{4}{3} & -\frac{5}{2} & \frac{4}{3} & -\frac{1}{12} & 0 & 0 \\ 0 & 0 & -\frac{1}{12} & \frac{4}{3} & -\frac{5}{2} & \frac{4}{3} & -\frac{1}{12} & 0 \\ 0 & 0 & 0 & -\frac{1}{12} & \frac{4}{3} & -\frac{5}{2} & \frac{4}{3} & -\frac{1}{12} \\ -\frac{1}{12} & 0 & 0 & 0 & -\frac{1}{12} & \frac{4}{3} & -\frac{5}{2} & \frac{4}{3} \\ \frac{4}{3} & -\frac{1}{12} & 0 & 0 & 0 & -\frac{1}{12} & \frac{4}{3} & -\frac{5}{2} \\ 1 & 1 & 1 & 1 & 1 & 1 & 1 & 1 \end{bmatrix} \begin{bmatrix} \langle\phi\rangle_0 \\ \langle\phi\rangle_1 \\ \langle\phi\rangle_2 \\ \langle\phi\rangle_3 \\ \langle\phi\rangle_4 \\ \langle\phi\rangle_5 \\ \langle\phi\rangle_6 \\ \langle\phi\rangle_7 \end{bmatrix} = \begin{bmatrix} \langle\rho\rangle_0 \\ \langle\rho\rangle_1 \\ \langle\rho\rangle_2 \\ \langle\rho\rangle_3 \\ \langle\rho\rangle_4 \\ \langle\rho\rangle_5 \\ \langle\rho\rangle_6 \\ \langle\rho\rangle_7 \\ 0 \end{bmatrix}. \tag{3.211}$$

Whether the global operator matrix is square or not, the resulting linear system is solved for the electrostatic potential using standard linear algebra techniques and software packages. Using a polynomial reconstruction of the resulting volume-integrated values of $\langle\phi\rangle_i$ the cell-center value of the electric field is computed to fourth-order accuracy:

$$(E_x)_i = -\left\langle \frac{d\phi}{dx} \right\rangle_i = \frac{8}{12h_x^2}\left(\langle\phi\rangle_{i+1} - \langle\phi\rangle_{i-1}\right) - \frac{1}{12h_x^2}\left(\langle\phi\rangle_{i+2} - \langle\phi\rangle_{i-2}\right). \tag{3.212}$$

3.6 Cartesian coordinates: fourth-order accurate diagnostics

The Vlasov-Maxwell system encapsulates a considerable amount of information, and assessing the physical and numerical accuracy of a given simulation typically relies on computing reduced quantities such as velocity moments of the distribution function and field energy. See discussion of diagnostics in Section 2.6. When it comes to gauging whether simulation results are true to the physics, it is often sufficient to compute these reduced quantities to second-order accuracy. When it comes to tracking numerical convergence, however, diagnostics like momentum and energy must be computed to fourth-order accuracy. Computing integrals of products to fourth-order accuracy relies on the Taylor series relation in Eq. (3.30), which underpins each step of the finite-volume method implementation.

3.6.1 Mass and charge

The calculation of species particle inventory to fourth-order accuracy involves a simple summation, and is described in Section 3.5.6.1. Note that the particle inventory is simply the volume-integrated number density. The local number density is one of the fundamental quantities that is tracked in electrostatic and electrodynamic Vlasov simulations (see discussion in Section 2.6) since it is a much simpler indicator of the transport of plasma species in physical coordinates than the full phase space distribution function. By extension, the species charge density and species mass density are readily computed by multiplying the species number density by the appropriate scalar factor. The total charge in a cell can be computed by summing over species (see Eq. (3.188)). The total mass of a given species within the domain is often of interest, and can be obtained by summing the distribution function along all directions and multiplying by the relative species mass M_s. Finite-volume discretization of the Vlasov equation in a system with closed boundaries should result in zero (to machine precision) net change in mass.

3.6.2 Momentum

The calculation of the fourth-order accurate momentum along each direction relies on the steps outlined in Section 3.5.2 for computing the current. The main distinction is that for the purpose of diagnostics, there is no reason to evaluate momentum as an area-integrated quantity. Whether a quantity is area-integrated, volume-integrated, or a point value is consequential in high-order finite-volume methods, but since the value of momentum is not used anywhere in the discretization, the choice of what type of integral to evaluate is somewhat arbitrary. Here momentum is computed as a volume-integrated quantity. Thus when evaluating local cell-volume-integrated products like $(v_x f_s)$ to fourth-order accuracy, the integration is performed over all directions, not just a subset. The following steps are used to compute the species momentum

1. The point value of the distribution function is computed at the center of a cell. See Eq. (3.106).

2. The local cell-volume-integrated product vf is computed to fourth-order accuracy using point values and the quadrature rule given by Eq. (3.30). Note that the quadrature rule in Eq. (3.30) is for area integrals, not volume integrals, but the extension to volume integrals is straightforward in that transverse derivative terms are included for each direction of integration.

3. The local fourth-order accurate product $\langle vf \rangle_{i,j,k,l,m,n}$ is summed over velocity directions l, m, n to compute momentum.

For Cartesian coordinates the local products of the velocity coordinate and the distribution function are

$$\begin{aligned}\langle v_x f_s \rangle_{i,j,k,l,m,n} = (v_x)_l (f_s)_{i,j,k,l,m,n} h_x h_y h_z h_{v_x} h_{v_y} h_{v_z} + \frac{1}{24} \Bigg[& h_x^2 \frac{\partial^2}{\partial x^2} (v_x \langle f_s \rangle) \\ & + h_y^2 \frac{\partial^2}{\partial y^2} (v_x \langle f_s \rangle) + h_z^2 \frac{\partial^2}{\partial z^2} (v_x \langle f_s \rangle) + h_{v_x}^2 \frac{\partial^2}{\partial v_x^2} (v_x \langle f_s \rangle) \\ & + h_{v_y}^2 \frac{\partial^2}{\partial v_y^2} (v_x \langle f_s \rangle) + h_{v_z}^2 \frac{\partial^2}{\partial v_z^2} (v_x \langle f_s \rangle) \Bigg]_{i,j,k,l,m,n}\end{aligned} \tag{3.213}$$

$$\begin{aligned}\langle v_y f_s \rangle_{i,j,k,l,m,n} = (v_y)_m (f_s)_{i,j,k,l,m,n} h_x h_y h_z h_{v_x} h_{v_y} h_{v_z} + \frac{1}{24} \Bigg[& h_x^2 \frac{\partial^2}{\partial x^2} (v_y \langle f_s \rangle) \\ & + h_y^2 \frac{\partial^2}{\partial y^2} (v_y \langle f_s \rangle) + h_z^2 \frac{\partial^2}{\partial z^2} (v_y \langle f_s \rangle) + h_{v_x}^2 \frac{\partial^2}{\partial v_x^2} (v_y \langle f_s \rangle) \\ & + h_{v_y}^2 \frac{\partial^2}{\partial v_y^2} (v_y \langle f_s \rangle) + h_{v_z}^2 \frac{\partial^2}{\partial v_z^2} (v_y \langle f_s \rangle) \Bigg]_{i,j,k,l,m,n}\end{aligned} \tag{3.214}$$

$$\begin{aligned}\langle v_z f_s \rangle_{i,j,k,l,m,n} = (v_z)_n (f_s)_{i,j,k,l,m,n} h_x h_y h_z h_{v_x} h_{v_y} h_{v_z} + \frac{1}{24} \Bigg[& h_x^2 \frac{\partial^2}{\partial x^2} (v_z \langle f_s \rangle) \\ & + h_y^2 \frac{\partial^2}{\partial y^2} (v_z \langle f_s \rangle) + h_z^2 \frac{\partial^2}{\partial z^2} (v_z \langle f_s \rangle) + h_{v_x}^2 \frac{\partial^2}{\partial v_x^2} (v_z \langle f_s \rangle) \\ & + h_{v_y}^2 \frac{\partial^2}{\partial v_y^2} (v_z \langle f_s \rangle) + h_{v_z}^2 \frac{\partial^2}{\partial v_z^2} (v_z \langle f_s \rangle) \Bigg]_{i,j,k,l,m,n}\end{aligned} . \tag{3.215}$$

Summing these local cell-integrated values over velocity space, the discrete cell-volume-integrated momentum (see Eq. (2.124) for the analytic definition) is obtained, such that

$$\langle p_{sx} \rangle_{i,j,k} = \sum_{l=0}^{N_{v_x}-1} \sum_{m=0}^{N_{v_y}-1} \sum_{n=0}^{N_{v_z}-1} \langle v_x f_s \rangle_{i,j,k,l,m,n} \tag{3.216}$$

$$\langle p_{sy} \rangle_{i,j,k} = \sum_{l=0}^{N_{v_x}-1} \sum_{m=0}^{N_{v_y}-1} \sum_{n=0}^{N_{v_z}-1} \langle v_y f_s \rangle_{i,j,k,l,m,n} \tag{3.217}$$

$$\langle p_{sz} \rangle_{i,j,k} = \sum_{l=0}^{N_{v_x}-1} \sum_{m=0}^{N_{v_y}-1} \sum_{n=0}^{N_{v_z}-1} \langle v_z f_s \rangle_{i,j,k,l,m,n} \,. \tag{3.218}$$

The momentum is used as an indicator of the local velocity of each species. The components of momentum given by Eqs. (3.216) – (3.218) can also be integrated over the spatial coordinate to obtain a global value of the net momentum along a given direction. The global value of momentum along each direction serves as an indicator of how well the total momentum is conserved.

3.6.3 Energy

Energy is another diagnostic that serves as a metric for the physical and numerical accuracy of the finite-volume discretization of the Vlasov-Maxwell system. Kinetic energy is defined analytically in Eq. (2.126), and is computed discretely using the same procedure as the momentum calculation; first the point value of the distribution function is computed at the center of a cell, then the local cell-volume-integrated product $\langle v^2 f \rangle$ is computed to fourth-order accuracy for each velocity component using the quadrature rule in Eq. (3.30), after which the local fourth-order accurate product is summed over velocity directions.

For Cartesian coordinates the local products of the square of the velocity and the distribution function are

$$\begin{aligned} \left\langle v_x^2 f_s \right\rangle_{i,j,k,l,m,n} = (v_x)_l^2 (f_s)_{i,j,k,l,m,n} h_x h_y h_z h_{v_x} h_{v_y} h_{v_z} + \frac{1}{24} \Bigg[& h_x^2 \frac{\partial^2}{\partial x^2} (v_x^2 \langle f_s \rangle) \\ & + h_y^2 \frac{\partial^2}{\partial y^2} (v_x^2 \langle f_s \rangle) + h_z^2 \frac{\partial^2}{\partial z^2} (v_x^2 \langle f_s \rangle) + h_{v_x}^2 \frac{\partial^2}{\partial v_x^2} (v_x^2 \langle f_s \rangle) \\ & + h_{v_y}^2 \frac{\partial^2}{\partial v_y^2} (v_x^2 \langle f_s \rangle) + h_{v_z}^2 \frac{\partial^2}{\partial v_z^2} (v_x^2 \langle f_s \rangle) \Bigg]_{i,j,k,l,m,n} \end{aligned} \tag{3.219}$$

$$\left\langle v_y^2 f_s \right\rangle_{i,j,k,l,m,n} = (v_y)_m^2 (f_s)_{i,j,k,l,m,n} h_x h_y h_z h_{v_x} h_{v_y} h_{v_z} + \frac{1}{24} \Bigg[h_x^2 \frac{\partial^2}{\partial x^2} (v_y^2 \langle f_s \rangle) + h_y^2 \frac{\partial^2}{\partial y^2} (v_y^2 \langle f_s \rangle) + h_z^2 \frac{\partial^2}{\partial z^2} (v_y^2 \langle f_s \rangle) + h_{v_x}^2 \frac{\partial^2}{\partial v_x^2} (v_y^2 \langle f_s \rangle) + h_{v_y}^2 \frac{\partial^2}{\partial v_y^2} (v_y^2 \langle f_s \rangle) + h_{v_z}^2 \frac{\partial^2}{\partial v_z^2} (v_y^2 \langle f_s \rangle) \Bigg]_{i,j,k,l,m,n} \quad (3.220)$$

$$\left\langle v_z^2 f_s \right\rangle_{i,j,k,l,m,n} = (v_z)_n^2 (f_s)_{i,j,k,l,m,n} h_x h_y h_z h_{v_x} h_{v_y} h_{v_z} + \frac{1}{24} \Bigg[h_x^2 \frac{\partial^2}{\partial x^2} (v_z^2 \langle f_s \rangle) + h_y^2 \frac{\partial^2}{\partial y^2} (v_z^2 \langle f_s \rangle) + h_z^2 \frac{\partial^2}{\partial z^2} (v_z^2 \langle f_s \rangle) + h_{v_x}^2 \frac{\partial^2}{\partial v_x^2} (v_z^2 \langle f_s \rangle) + h_{v_y}^2 \frac{\partial^2}{\partial v_y^2} (v_z^2 \langle f_s \rangle) + h_{v_z}^2 \frac{\partial^2}{\partial v_z^2} (v_z^2 \langle f_s \rangle) \Bigg]_{i,j,k,l,m,n} . \quad (3.221)$$

These expressions for local fourth-order accurate products for kinetic energy evaluation very closely resemble those in Eqs. (3.213) – (3.215) for momentum. This illustrates the flexibility of the quadrature rule, in that the same general form can be used to compute fourth-order accurate products independent of the number of variables being multiplied.

The values of $\langle v_x^2 f_s \rangle$, $\left\langle v_y^2 f_s \right\rangle$, and $\langle v_z^2 f_s \rangle$ given by Eqs. (3.219) – (3.221) can each be summed over velocity space, and combined with local values of momentum and density to compute thermal speed and temperature (see Eqs. (2.127) and (2.128)). Summing these local cell-integrated products over all of velocity space and over direction components, yields the discrete fourth-order accurate cell-volume-integrated kinetic energy,

$$\langle W_s \rangle_{i,j,k} = \frac{1}{2} \sum_{l=0}^{N_{v_x}-1} \sum_{m=0}^{N_{v_y}-1} \sum_{n=0}^{N_{v_z}-1} \left(\left\langle v_x^2 f_s \right\rangle_{i,j,k,l,m,n} + \left\langle v_y^2 f_s \right\rangle_{i,j,k,l,m,n} + \left\langle v_z^2 f_s \right\rangle_{i,j,k,l,m,n} \right) . \quad (3.222)$$

In addition to the kinetic energy of the plasma, which is encoded by the distribution function, it is also important to account for the field energy. See Eq. (2.130) for the analytic definition of total energy. Since the fields exist in a subspace of the full phase space domain, the local cell-volume integrals of $\lfloor E^2 \rfloor$ and $\lfloor B^2 \rfloor$ are simpler to evaluate than the terms contributing to the kinetic energy. Moreover, the calculation of field energy does not involve velocity moments. The quadrature rule given by Eq. (3.30) is still needed, however, in order to compute the squares of the field components to fourth-order accuracy.

Computing a fourth-order accurate cell-volume-integrated value of B^2 in Cartesian coordinates requires using the area-integrated field variables. First the point value of each component of the field is computed. For Cartesian coordinates, the point values of the

magnetic field components are

$$(B_x)_{i,j,k} = \frac{1}{h_y h_z}\left(\lfloor B_x \rfloor_{i_0,j,k} - \frac{1}{24}\left[h_y^2 \frac{\partial^2}{\partial y^2}\lfloor B_x \rfloor + h_z^2 \frac{\partial^2}{\partial z^2}\lfloor B_x \rfloor\right]_{i_0,j,k}\right) \tag{3.223}$$

$$(B_y)_{i,j,k} = \frac{1}{h_x h_z}\left(\lfloor B_y \rfloor_{i,j_0,k} - \frac{1}{24}\left(h_x^2 \frac{\partial^2}{\partial x^2}\lfloor B_y \rfloor + h_z^2 \frac{\partial^2}{\partial z^2}\lfloor B_y \rfloor\right]_{i,j_0,k}\right) \tag{3.224}$$

$$(B_z)_{i,j,k} = \frac{1}{h_x h_z}\left(\lfloor B_y \rfloor_{i,j,k_0} - \frac{1}{24}\left(h_x^2 \frac{\partial^2}{\partial x^2}\lfloor B_z \rfloor + h_y^2 \frac{\partial^2}{\partial y^2}\lfloor B_z \rfloor\right]_{i,j,k_0}\right). \tag{3.225}$$

See Section 3.5.1 for the definitions of $\lfloor B_x \rfloor_{i_0,j,k}$, $\lfloor B_y \rfloor_{i,j_0,k}$, and $\lfloor B_z \rfloor_{i,j,k_0}$. Much as in the case of integrals involving the distribution function, the second derivatives are evaluated using a second-order accurate finite-difference stencil. The point values are then used to compute the volume-integrated squared values of each component of the magnetic field. In Cartesian coordinates these are:

$$\left\langle B_x^2 \right\rangle_{i,j,k} = (B_x)_{i,j,k}^2 h_x h_y h_z + \frac{h_x}{24 h_y h_z}\left(h_x^2 \frac{\partial^2}{\partial x^2}\lfloor B_x \rfloor_{i_0,j,k}^2 + h_y^2 \frac{\partial^2}{\partial y^2}\lfloor B_x \rfloor_{i_0,j,k}^2 + h_z^2 \frac{\partial^2}{\partial z^2}\lfloor B_x \rfloor_{i_0,j,k}^2\right) \tag{3.226}$$

$$\left\langle B_y^2 \right\rangle_{i,j,k} = (B_y)_{i,j,k}^2 h_x h_y h_z + \frac{h_y}{24 h_x h_z}\left(h_x^2 \frac{\partial^2}{\partial x^2}\langle B_y \rangle_{i,j_0,k}^2 + h_y^2 \frac{\partial^2}{\partial y^2}\lfloor B_x \rfloor_{i,j_0,k}^2 + h_z^2 \frac{\partial^2}{\partial z^2}\lfloor B_y \rfloor_{i,j_0,k}^2\right) \tag{3.227}$$

$$\left\langle B_z^2 \right\rangle_{i,j,k} = (B_z)_{i,j,k}^2 h_x h_y h_z + \frac{h_z}{24 h_x h_y}\left(h_x^2 \frac{\partial^2}{\partial x^2}\langle B_z \rangle_{i,j,k_0}^2 + h_y^2 \frac{\partial^2}{\partial y^2}\lfloor B_z \rfloor_{i,j,k_0}^2 + h_z^2 \frac{\partial^2}{\partial z^2}\lfloor B_z \rfloor_{i,j,k_0}^2\right). \tag{3.228}$$

Note that the cell-volume-integrated squared values of each component of the electric field can be computed in the exact same manner. The total volume-integrated field energy is defined analytically in Eq. (2.131), and is computed discretely to fourth-order accuracy as

$$\langle U \rangle_{i,j,k} = \frac{1}{2}\left(\left\langle B_x^2 \right\rangle_{i,j,k} + \left\langle B_y^2 \right\rangle_{i,j,k} + \left\langle B_z^2 \right\rangle_{i,j,k} + \left\langle E_x^2 \right\rangle_{i,j,k} + \left\langle E_y^2 \right\rangle_{i,j,k} + \left\langle E_z^2 \right\rangle_{i,j,k}\right). \tag{3.229}$$

Local values of kinetic energy and field energy give an indication of how energy is transported, specifically when and where it is converted into a different form. Tracking the global integral of the sum of $\langle W \rangle_{i,j,k}$ and $\langle U \rangle_{i,j,k}$ gives an indicator of how well the discretization method is able to conserve energy.

3.7 Cartesian coordinates: algorithm outline

The spatial discretization of the Vlasov equation and Maxwell's equations combined with the temporal discretization of the entire system allows the analytic governing differential

equations to be approximated with discrete analogs. As such the Vlasov-Maxwell system can be expressed in the generic form given in Eq. (3.12), i.e.

$$\frac{\partial \boldsymbol{q}}{\partial t} = \boldsymbol{L}\boldsymbol{q} + \boldsymbol{Y}. \tag{3.230}$$

In effect the primary variable $\boldsymbol{q}$, source $\boldsymbol{Y}$, and flux terms $\boldsymbol{L}\boldsymbol{q}$ can all be evaluated in terms of arithmetic operations that can be processed on a computer. The terms in this discrete system of equations are

$$\boldsymbol{q} = \begin{bmatrix} \langle f_s \rangle_{i,j,k,l,m,n} \\ \lfloor E_x \rfloor_{i_0,j,k} \\ \lfloor E_y \rfloor_{i,j_0,k} \\ \lfloor E_z \rfloor_{i,j,k_0} \\ \lfloor B_x \rfloor_{i_0,j,k} \\ \lfloor B_y \rfloor_{i,j_0,k} \\ \lfloor B_z \rfloor_{i,j,k_0} \end{bmatrix}, \qquad \boldsymbol{Y} = \begin{bmatrix} 0 \\ -\lfloor J_x \rfloor_{i_0,j,k} \\ -\lfloor J_y \rfloor_{i,j_0,k} \\ -\lfloor J_z \rfloor_{i,j,k_0} \\ 0 \\ 0 \\ 0 \end{bmatrix} \tag{3.231}$$

$$\boldsymbol{L}\boldsymbol{q} = \begin{bmatrix} L(F_x) + L(F_y) + L(F_z) + L(F_{v_x}) + L(F_{v_y}) + L(F_{v_z}) \\ \frac{\omega_{cp}}{\omega_{pp}} \left(-\lfloor B_y \rfloor \Big|_{i_0,j,k-\frac{1}{2}}^{i_0,j,k+\frac{1}{2}} + \lfloor B_z \rfloor \Big|_{i_0,j-\frac{1}{2},k}^{i_0,j+\frac{1}{2},k} \right) \\ \frac{\omega_{cp}}{\omega_{pp}} \left(\lfloor B_x \rfloor \Big|_{i,j_0,k-\frac{1}{2}}^{i,j_0,k+\frac{1}{2}} - \lfloor B_z \rfloor \Big|_{i-\frac{1}{2},j_0,k}^{i+\frac{1}{2},j_0,k} \right) \\ \frac{\omega_{cp}}{\omega_{pp}} \left(-\lfloor B_x \rfloor \Big|_{i,j-\frac{1}{2},k_0}^{i,j+\frac{1}{2},k_0} + \lfloor B_y \rfloor \Big|_{i-\frac{1}{2},j,k_0}^{i+\frac{1}{2},j,k_0} \right) \\ \frac{\omega_{pp}}{\omega_{cp}} \left(\lfloor E_y \rfloor \Big|_{i_0,j,k-\frac{1}{2}}^{i_0,j,k+\frac{1}{2}} - \lfloor E_z \rfloor \Big|_{i_0,j-\frac{1}{2},k}^{i_0,j+\frac{1}{2},k} \right) \\ \frac{\omega_{pp}}{\omega_{cp}} \left(-\lfloor E_x \rfloor \Big|_{i,j_0,k-\frac{1}{2}}^{i,j_0,k+\frac{1}{2}} + \lfloor E_z \rfloor \Big|_{i-\frac{1}{2},j_0,k}^{i+\frac{1}{2},j_0,k} \right) \\ \frac{\omega_{pp}}{\omega_{cp}} \left(\lfloor E_x \rfloor \Big|_{i,j-\frac{1}{2},k_0}^{i,j+\frac{1}{2},k_0} - \lfloor E_y \rfloor \Big|_{i-\frac{1}{2},j,k_0}^{i+\frac{1}{2},j,k_0} \right) \end{bmatrix}, \tag{3.232}$$

where the flux terms associated with the distribution function are

$$L(F_x) = - \left\langle v_x f_s \right\rangle \Big|_{i-\frac{1}{2},j,k,l,m,n}^{i+\frac{1}{2},j,k,l,m,n} \tag{3.233}$$

$$L(F_y) = - \left\langle v_y f_s \right\rangle \Big|_{i,j-\frac{1}{2},k,l,m,n}^{i,j+\frac{1}{2},k,l,m,n} \tag{3.234}$$

$$L(F_z) = - \left\langle v_z f_s \right\rangle \Big|_{i,j,k-\frac{1}{2},l,m,n}^{i,j,k+\frac{1}{2},l,m,n} \tag{3.235}$$

$$L(F_{v_x}) = - \left\langle \frac{Z_s}{M_s} \left\{ E_x + \frac{\omega_{cp}}{\omega_{pp}} \left[v_y B_z - v_z B_y \right] \right\} f_s \right\rangle \Big|_{i,j,k,l-\frac{1}{2},m,n}^{i,j,k,l+\frac{1}{2},m,n} \tag{3.236}$$

$$L(F_{v_y}) = - \left\langle \frac{Z_s}{M_s} \left\{ E_y + \frac{\omega_{cp}}{\omega_{pp}} \left[v_z B_x - v_x B_z \right] \right\} f_s \right\rangle \Big|_{i,j,k,l,m+\frac{1}{2}n}^{i,j,k,l,m-\frac{1}{2},n} \tag{3.237}$$

$$L(F_{v_z}) = - \left\langle \frac{Z_s}{M_s} \left\{ E_z + \frac{\omega_{cp}}{\omega_{pp}} \left[v_x B_y - v_y B_x \right] \right\} f_s \right\rangle \Big|_{i,j,k,l,m,n-\frac{1}{2}}^{i,j,k,l,m,n+\frac{1}{2}}. \tag{3.238}$$

Note the distinction between a phase space volume-integrated quantity $\langle f \rangle_{i,j,k,l,m,n}$, a phase space surface-integrated quantity $\langle f \rangle_{i+\frac{1}{2},j,k,l,m,n}$, a physical space center-of-cell area-integrated quantity $\lfloor E_x \rfloor_{i_0,j,k}$, and a physical space line-integrated quantity along a face $\lfloor E_x \rfloor_{i,j_0,k+\frac{1}{2}}$. Note that the angular brackets denote surface integrals with Cartesian coordinate phase space surfaces defined in Eq. (2.52).

The outline of the Cartesian coordinate Vlasov-Maxwell algorithm for solving Eq. (3.230) is as follows. First the primary variables are initialized to fourth-order accuracy, using either analytic definite integrals or quadrature rules. The distribution function is initialized as a fourth-order volume integrated value in each phase space cell, and the electromagnetic fields are initialized as fourth-order area integrals through the mid-planes of each cell in physical space. For each time step the algorithm for advancing the primary variables performs the following steps.

1. For each stage in RK4

    a) Compute the distribution function flux terms in $\boldsymbol{Lq}$.

        i. Deconvolve the electric and magnetic field so as to compute point-values in the center of a cell to fourth-order accuracy.

        ii. Interpolate the volume-integrated distribution function to cell faces using an upwinded stencil (see Section 3.4.2.2). Upwinding direction is based on advection speeds – either the velocity coordinates or the local point-value of the Lorentz force.

iii. Compute the distribution function fluxes given in Eqs. (3.233) – (3.238), using the fourth-order quadrature rule described in Section 3.4.2.3.

iv. Compute the divergence of fluxes, i.e. the sum of the terms in Eqs. (3.233) – (3.238) to obtain the distribution function increment associated with the k-th stage of RK4 (see Eqs. (3.15) – (3.18)).

b) Compute the line-integral and source terms in $\boldsymbol{Lq} + \boldsymbol{Y}$ associated with the electromagnetic fields.

i. Interpolate the area-integrated electromagnetic field variables to cell faces, using the centered stencil described in Section 3.5.1.1.

ii. Evaluate the local line integrals needed to update each field component as described in Section 3.5.1.2.

iii. Compute the area-integrated current density from the distribution function, as described in Section 3.5.2.

iv. Compute the closed-loop line-integrals given in the term $\boldsymbol{Lq}$ in Eq. (3.232) to obtain the electromagnetic field increment associated with the k-th stage of RK4.

2. Update distribution function and electromagnetic field solution using the k_1, k_2, k_3, k_4 increments obtained from each stage of RK4 (see Eq. (3.19)).

3. Apply divergence cleaning, if applicable.

4. Compute diagnostics, as described in Section 3.6.

The Vlasov-Poisson algorithm for solving the system $\frac{\partial \boldsymbol{q}}{\partial t} = \boldsymbol{Lq}$ with electrostatic fields requires only the distribution function to be initialized. The distribution function is initialized as a fourth-order volume integrated value in each phase space cell, and the following steps are performed to update the solution.

1. For each stage in RK4

a) Compute the charge density from the distribution function (see Section 3.5.6.1).

b) Solve the Poisson equation for the discrete potential (see Section 3.5.6).

c) Compute the electric field from the discrete values of the potential using a fourth-order interpolation.

d) Interpolate the volume-integrated distribution function to cell faces using an upwinded stencil (see Section 3.4.2.2). Upwinding direction is based on advection speeds – either the velocity coordinates or the local point-value of the Lorentz force.

e) Compute the distribution function fluxes given in Eqs. (3.233) – (3.238), using the fourth-order quadrature rule described in Section 3.4.2.3.

f) Compute the divergence of fluxes, i.e. the sum of the terms in Eqs. (3.233) – (3.238) to obtain the RK4 distribution function increment associated with the k-th stage of RK4 (see Eqs. (3.15) – (3.18)).

2. Update distribution function using the k_1, k_2, k_3, k_4 increments obtained from each stage of RK4. See Eq. (3.19).

3. Compute diagnostics, as described in Section 3.6.

Both algorithms rely on evaluating the terms $\boldsymbol{Lq} + \boldsymbol{Y}$ for each stage of the RK4 time integrator, using the interpolation and quadrature evaluation procedure detailed in this chapter.

3.8 Cylindrical coordinates: spatial discretization of the Vlasov equation

3.8.1 Taylor series based approach to fourth-order quadratures

Taylor series based approach to evaluating quadratures to fourth-order accuracy is largely unchanged for cylindrical phase space coordinates. The approach is described in Section 3.4.1. The main distinction is that the fluxes in the cylindrical coordinate Vlasov equation (see Eq. (2.79)) are often products of three terms (instead of two terms) and involve radius multipliers for evaluation of surface integrals. The Taylor series relation given in Eq. (3.30) for evaluating the product of two or more functions still holds and is applied to evaluate quadratures in cylindrical phase space coordinates.

3.8.2 Fourth-order flux calculation for the Vlasov equation

The general approach for a finite-volume flux calculation for cylindrical coordinates is the same as that for Cartesian coordinates (see Section 3.4.2); however, the details are sufficiently different that they warrant a separate discussion. The surface integral of fluxes in the weak form of the Vlasov equation is given in Eq. (2.78) and the associated five-dimensional differential surfaces for cylindrical phase space coordinates are defined in Eq. (2.79). In the interest of clarity, the mechanics of the finite-volume discretization are described in detail for two phase space dimensions rather than the full six dimensions. The discretization extends directly to $(r, z, v_r, v_\theta, v_z)$ coordinates. The procedure can be further extended to include the discretization of the azimuthal coordinate θ; however, since the objective here is to model axisymmetric plasmas, variation along the azimuthal direction is not taken into account.

Consider the distribution function $f(r, \xi)$ in two dimensions defined by the radius r and a coordinate ξ, where ξ can be either the z, v_r, v_θ, or v_z coordinate. The distribution function is assumed to be axisymmetric, such that it is independent of the azimuthal coordinate θ. Note that even in axisymmetric configurations it is very important to account for the

azimuthal direction, as it affects the form of the integrals along the r and ξ directions. Let i denote the cell index along the r direction, and j denote the cell index along the ξ direction, such that the center of the cell (i,j) has coordinates (r_i, ξ_j) and the cell spans the volume $\left[r_{i-\frac{1}{2}}, r_{i+\frac{1}{2}}\right] \times [0, h_\theta] \times \left[\xi_{j-\frac{1}{2}}, \xi_{j+\frac{1}{2}}\right]$, where

$$r_{i\pm\frac{1}{2}} = r_i \pm \frac{h_r}{2} \tag{3.239}$$

$$\xi_{j\pm\frac{1}{2}} = \xi_j \pm \frac{h_\xi}{2} \tag{3.240}$$

and h_r, h_θ, and h_ξ are the cell spacings along each direction. Note that the azimuthal coordinate is not discretized, and the associated cell spacing h_θ is arbitrary as long as $h_\theta \neq 0$. The spacing must be non-zero so as to properly account for cell volume variation with radius. For convenience h_θ can be chosen to be one radian or 2π radians for the axisymmetric system of interest. For the simulations in this dissertation h_θ is chosen to have a value of one.

Let the primary variable in this finite-volume discretization be the volume integral of f, such that the local volume-integrated value in this cylindrical coordinate system is

$$\langle f \rangle_{i,j,k} = \int_{r_{i-\frac{1}{2}}}^{r_{i+\frac{1}{2}}} \int_0^{h_\theta} \int_{\xi_{k-\frac{1}{2}}}^{\xi_{k+\frac{1}{2}}} f(r,\xi) r dr d\theta d\xi, \tag{3.241}$$

where the differential volume of a cell is $r dr d\theta d\xi$. Note that even though the distribution function is independent of θ, the distribution function must still be integrated over a finite azimuthal extent to properly account for the fact that in cylindrical coordinates volume varies with radius. The differential areas for this cylindrical coordinate system are $d\boldsymbol{A} = \{r d\theta d\xi, dr d\xi, r dr d\theta\}$, such that analytically the cell-face integrals of f are defined as

$$\langle f \rangle_{i+\frac{1}{2},j} = \int_0^{h_\theta} \int_{\xi_{j-\frac{1}{2}}}^{\xi_{j+\frac{1}{2}}} f\left(r_{i+\frac{1}{2}}, \xi\right) r_{i+\frac{1}{2}} d\theta d\xi \tag{3.242}$$

$$\langle f \rangle_{i,j}\Big|_{\theta=0} = \int_{r_{i-\frac{1}{2}}}^{r_{i+\frac{1}{2}}} \int_{\xi_{k-\frac{1}{2}}}^{\xi_{k+\frac{1}{2}}} f\left(r,\xi\right) dr d\xi \tag{3.243}$$

$$\langle f \rangle_{i,j+\frac{1}{2}} = \int_{r_{i-\frac{1}{2}}}^{r_{i+\frac{1}{2}}} \int_0^{h_\theta} f\left(r, \xi_{j+\frac{1}{2}}\right) r d\theta dr \tag{3.244}$$

Note that the Jacobian of integration, r, only appears when integrating over the azimuthal direction, which is why it is present in Eq. (3.242) and Eq. (3.244), but not in Eq. (3.243). The value of the integral on the righthand side of Eq. (3.243) is completely independent of the azimuthal location θ, since f is assumed to be axisymmetric, and consequently Eq. (3.243) is never used in the discretization, and is included here only for the sake of completion. Let the evolution of the volume-integrated primary variable $\langle f \rangle_{i,j}$ be described according

to Eq. (3.27) such that the change in time of the primary variable is expressed in terms of cell-face integrated fluxes:

$$\frac{\partial}{\partial t}\langle f\rangle_{i,j} = -\Big(\Big[\langle F\rangle_{i+\frac{1}{2},j} - \langle F\rangle_{i-\frac{1}{2},j}\Big] + \Big[\langle F\rangle_{i,j+\frac{1}{2}} - \langle F\rangle_{i,j-\frac{1}{2}}\Big] \Big). \tag{3.245}$$

See Fig. 3.1 for an illustration of the cell and cell-face indexes in a structured grid.

Suppose the fluxes along the r and ξ direction are defined analytically to be $\boldsymbol{F} = \{\alpha f, \beta f\}$, where α defines the advection speed along the r direction and β defines the advection speed along the ξ direction. For the purposes of this discussion, let α and β be analytic functions. Then the goal is to use the volume-integrated values $\langle f\rangle_{i,j}$ to compute the surface-integrated fluxes,

$$\langle F\rangle_{i+\frac{1}{2},j} = \int_{\xi_{j-\frac{1}{2}}}^{\xi_{j+\frac{1}{2}}} \int_0^{h_\theta} \alpha\left(r_{i+\frac{1}{2}}, \xi\right) f\left(r_{i+\frac{1}{2}}, \xi\right) r_{i+\frac{1}{2}} d\theta d\xi \tag{3.246}$$

$$\langle F\rangle_{i,j+\frac{1}{2}} = \int_{r_{i-\frac{1}{2}}}^{r_{i+\frac{1}{2}}} \int_0^{h_\theta} \beta\left(r, \xi_{j+\frac{1}{2}}\right) f\left(r, \xi_{j+\frac{1}{2}}\right) r d\theta dr, \tag{3.247}$$

to fourth-order accuracy so as to evaluate the righthand side of Eq. (3.245). The interpolation and quadrature procedure for evaluating these flux terms are described below. Note the distinction between these cylindrical coordinate fluxes and the fluxes for a Cartesian coordinate system (see Eqs. (3.39) and (3.40)). For cylindrical coordinates, depending on the direction of the flux, integration over a surface area requires accounting for the variations of cell face area with the radius. Note also that in an axisymmetric system in which α, β, and f are independent of the angle θ, the integrals in Eq. (3.246) and Eq. (3.247) must still include integration over the θ direction and the associated Jacobian r. The azimuthal flux in an axisymmetric system is zero and consequently an expression for it is not included.

3.8.2.1 One-dimensional polynomial interpolation

Much like in the case of Cartesian coordinates, the first step in computing the flux for a cylindrical coordinate system involves interpolation. Variables associated with a given flux are interpolated to cell faces using a one-dimensional polynomial reconstruction. In this case, since advection speeds α and β are assumed to be analytically defined, then only the primary variable f needs to be interpolated to a face. To obtain a cell-face integrated value $\langle f\rangle_{i+\frac{1}{2},j}$ from the volume-integrated value $\langle f\rangle_{i,j}$, a third degree polynomial P_3 is used to reconstruct the solution, where

$$P_3(r) = p_3 r^3 + p_2 r^2 + p_1 r + p_0. \tag{3.248}$$

Even though the variables of interest exist in three dimensions, the polynomial is one-dimensional because variation along the ξ direction, i.e. the direction transverse to the $(i+\frac{1}{2}, j)$ face, is already embedded into the volume integral $\langle f\rangle_{i,j}$. Solving for the constant

coefficients of P_3 requires four volume-integrated values of $\langle f \rangle_{i,j}$ around the face $(i+\frac{1}{2}, j)$. Constructing a linear system with four equations and four unknowns yields

$$\langle f \rangle_{i-1,j} = \int_{r_{i-\frac{3}{2}}}^{r_{i-\frac{1}{2}}} P_3(r) r dr \tag{3.249}$$

$$\langle f \rangle_{i,j} = \int_{r_{i-\frac{1}{2}}}^{r_{i+\frac{1}{2}}} P_3(r) r dr \tag{3.250}$$

$$\langle f \rangle_{i+1,j} = \int_{r_{i+\frac{1}{2}}}^{r_{i+\frac{3}{2}}} P_3(r) r dr \tag{3.251}$$

$$\langle f \rangle_{i+2,j} = \int_{r_{i+\frac{3}{2}}}^{r_{i+\frac{5}{2}}} P_3(r) r dr. \tag{3.252}$$

Solving this linear system for the coefficients $\{p_3, p_2, p_1, p_0\}$ in terms of volume-integrated values and evaluating the polynomial at $r_{i+\frac{1}{2}}$ yields a stencil for the face-integrated value $\langle f \rangle_{i+\frac{1}{2},j}$ to fourth-order accuracy:

$$\langle f \rangle_{i+\frac{1}{2},j} = P_3\left(r_{i+\frac{1}{2}}\right) \tag{3.253}$$

$$\begin{aligned} = \frac{1}{12 h_r^2 (4 - 15\ell^2 + 5\ell^4)} \Big\{ & \\ & \left(\quad 4 + \quad 3\ell - \quad 8\ell^2 - \quad 5\ell^3 \right) \langle f \rangle_{i-1,j} \\ & + \left(-60 - 93\ell + 24\ell^2 + 35\ell^3 \right) \langle f \rangle_{i,j} \\ & + \left(\quad 60 - 93\ell - 24\ell^2 + 35\ell^3 \right) \langle f \rangle_{i+1,j} \\ & + \left(\quad -4 + \quad 3\ell + \quad 8\ell^2 - \quad 5\ell^3 \right) \langle f \rangle_{i+2,j} \Big\} \end{aligned} , \tag{3.254}$$

where the index ℓ is defined as

$$\ell = \frac{r_{i+\frac{1}{2}}}{h_r} \tag{3.255}$$

and denotes the number of h_r lengths between the axis at $r = 0$ and the cell face $(i+\frac{1}{2}, j)$. The stencil for interpolating the primary variable to a $(i+\frac{1}{2}, j)$ cell face in cylindrical coordinates involves coefficients that depend on the distance from the axis, whereas in Cartesian coordinates the stencil coefficients are coordinate independent.

When it comes to interpolating the volume-integrated values of f to cell face $(i, j+\frac{1}{2})$, the procedure is the same as in the case of Cartesian coordinates because the volume of a cell does not vary with ξ and the reconstruction is one-dimensional. Thus the fourth-order accurate centered stencil for computing the cell face value $\langle f \rangle_{i,j+\frac{1}{2}}$ is given by

$$\langle f \rangle_{i,j+\frac{1}{2}} = \frac{1}{h_\xi} \left[\frac{7}{12} \left(\langle f \rangle_{i,j} + \langle f \rangle_{i,j+1} \right) - \frac{1}{12} \left(\langle f \rangle_{i,j+2} + \langle f \rangle_{i,j-1} \right) \right]. \tag{3.256}$$

This stencil is analogous to the expression in Eq. (3.47) for Cartesian coordinates. It is worth noting that in cylindrical coordinates the stencil for reconstructing variables along the radial direction is decidedly different from the reconstruction along the other orthogonal directions, and this difference is due to the fact that cell volumes increase with radius, but do not vary as a function of the other coordinates.

3.8.2.2 Upwinded one-dimensional polynomial interpolation

As in Cartesian coordinates, for stability purposes it is advantageous to use an upwinded stencil for the primary variable. See discussion in Section 3.4.2.2. To incorporate upwinding and retain overall order of accuracy in the flux calculation, the third degree polynomial reconstruction used above is replaced with a fourth degree fifth-order accurate polynomial reconstruction. For the ξ direction the reconstruction is analogous to that of Cartesian coordinates, such that the upwind interpolation stencil for evaluating f at face $(i, j+\frac{1}{2})$ is given by

$$\langle f \rangle_{i,j+\frac{1}{2}} = \begin{cases} \frac{1}{60h_\xi}\Big(\quad 2\langle f \rangle_{i,j-2} - 13\langle f \rangle_{i,j-1} + 47\langle f \rangle_{i,j} & \\ \qquad\qquad + 27\langle f \rangle_{i,j+1} - 3\langle f \rangle_{i,j+2} \Big) & \text{if } \beta_{i,j+\frac{1}{2}} > 0 \\ \frac{1}{60h_\xi}\Big(-3\langle f \rangle_{i,j-1} + 27\langle f \rangle_{i,j} + 47\langle f \rangle_{i,j+1} & \\ \qquad\qquad - 13\langle f \rangle_{i,j+2} + 2\langle f \rangle_{i,j+3} \Big) & \text{if } \beta_{i,j+\frac{1}{2}} < 0 \end{cases} \tag{3.257}$$

where $\beta_{i,j+\frac{1}{2}}$ is the advection speed at the $(i, j+\frac{1}{2})$ cell face, and where $\langle f \rangle_{i,j}$ is defined in Eq. (3.241). If the ξ-directed advection speed is zero then either stencil, or the average of the two stencils in Eq. (3.257) can be used. For the radial direction, the upwind reconstruction of f at cell face $(i+\frac{1}{2}, j)$ is derived as follows.

Consider a one-dimensional local polynomial reconstruction of the solution f along the radial direction. Define a fourth degree polynomial

$$P_4(r) = p_4 r^4 + p_3 r^3 + p_2 r^2 + p_1 r + p_0, \tag{3.258}$$

with constant coefficients $\{p_4, p_3, p_2, p_1, p_0\}$. The values of the coefficients are determined by solving a linear system of equations in which the volume-integrated distribution function

values are known. The linear system is made up of five of the following six relations:

$$\langle f \rangle_{i-2,j} = \int_{r_{i-\frac{5}{2}}}^{r_{i-\frac{3}{2}}} P_4(r) r dr \tag{3.259}$$

$$\langle f \rangle_{i-1,j} = \int_{r_{i-\frac{3}{2}}}^{r_{i-\frac{1}{2}}} P_4(r) r dr \tag{3.260}$$

$$\langle f \rangle_{i,j} = \int_{r_{i-\frac{1}{2}}}^{r_{i+\frac{1}{2}}} P_4(r) r dr \tag{3.261}$$

$$\langle f \rangle_{i+1,j} = \int_{r_{i+\frac{1}{2}}}^{r_{i+\frac{3}{2}}} P_4(r) r dr \tag{3.262}$$

$$\langle f \rangle_{i+2,j} = \int_{r_{i+\frac{3}{2}}}^{r_{i+\frac{5}{2}}} P_4(r) r dr \tag{3.263}$$

$$\langle f \rangle_{i+3,j} = \int_{r_{i+\frac{5}{2}}}^{r_{i+\frac{7}{2}}} P_4(r) r dr. \tag{3.264}$$

Which five equations are used to solve for the coefficients of P_4 is determined by the sign of the advection speed. If the local value of the advection speed $\alpha_{i+\frac{1}{2},j}$ is positive, then three volume-integrated values to the left and two volume-integrated values to the right of the $(i+\frac{1}{2}, j)$ face are used for the polynomial reconstruction (Eqs. (3.259) – (3.263)). Solving for the coefficients of P_4 and evaluating the polynomial at the $(i+\frac{1}{2}, j)$ cell face yields the stencil for $\alpha_{i+\frac{1}{2},j} > 0$:

$$\begin{aligned}
\langle f \rangle_{i+\frac{1}{2},j} = & \frac{1}{60 h_r^2 (-12 + 8\ell + 45\ell^2 - 20\ell^3 - 15\ell^4 + 6\ell^5)} \Big\{ \\
& \left(\quad 16 \quad - \quad 40\ell^2 \quad + \quad 12\ell^4 \right) \langle f \rangle_{i-2,j} \\
& + \left(-164 \; - \quad 45\ell \; + \quad 380\ell^2 \; + \quad 75\ell^3 \; - \quad 78\ell^4 \right) \langle f \rangle_{i-1,j} \\
& + \left(\; 1276 \; + \; 1395\ell \; - \; 1300\ell^2 \; - \; 525\ell^3 \; + \; 282\ell^4 \right) \langle f \rangle_{i,j} \\
& + \left(-684 \; + \; 1395\ell \; - \quad 180\ell^2 \; - \; 525\ell^3 \; + \; 162\ell^4 \right) \langle f \rangle_{i+1,j} \\
& + \left(\quad 36 \; - \quad 45\ell \; - \quad 60\ell^2 \; + \quad 75\ell^3 \; - \quad 18\ell^4 \right) \langle f \rangle_{i+2,j} \Big\}
\end{aligned} . \tag{3.265}$$

If, on the other hand, the advection speed is negative, then the set of volume integrals used for the reconstruction is shifted by one index, such that the linear system of equations used to solve for coefficients of P_4 is made up of Eqs. (3.260) – (3.264). Solving the linear system for the polynomial coefficients in terms of volume integrated distribution function values,

and evaluating P_4 at the $(i+\frac{1}{2},j)$ cell face yields the stencil for $\alpha_{i+\frac{1}{2},j}<0$:

$$\begin{aligned}\langle f\rangle_{i+\frac{1}{2},j} =& \frac{1}{60h_r^2(12+8\ell-45\ell^2-20\ell^3+15\ell^4+6\ell^5)}\Big\{ \\ &\big(\quad 36 \;+\quad 45\ell - \quad 60\ell^2 \;-\; 75\ell^3 \;-\quad 18\ell^4\big)\langle f\rangle_{i-1,j} \\ &+\big(-684 \;-\; 1395\ell - \quad 180\ell^2 +525\ell^3 \;+\; 162\ell^4\big)\langle f\rangle_{i,j} \\ &+\big(\;1276 \;-\; 1395\ell - \; 1300\ell^2 +525\ell^3 \;+\; 282\ell^4\big)\langle f\rangle_{i+1,j} \\ &+\big(-164 \;-\quad 45\ell + \quad 380\ell^2 \;+\; 75\ell^3 \;-\quad 78\ell^4\big)\langle f\rangle_{i+2,j} \\ &+\big(\quad 16 \qquad\quad -\quad 40\ell^2 \qquad\quad +\quad 12\ell^4\big)\langle f\rangle_{i+3,j}\Big\}\end{aligned} \tag{3.266}$$

where ℓ is defined as in Eq. (3.255). Thus depending on the direction of advection, either the stencil in Eq. (3.265) or the stencil in Eq. (3.266) is used to interpolate the distribution function to a cell face along the radial direction.

3.8.2.3 Fourth-order quadrature for surface-integrated flux

The second step in the flux calculation involves computing fourth-order accurate cell-face integrated products $\langle \alpha f\rangle_{i+\frac{1}{2},j}$, and $\langle \beta f\rangle_{i,j+\frac{1}{2}}$ using face-integrated values of the primary variable, derived in the interpolation step. Much as in the case of Cartesian coordinates, the flux calculation relies on the Taylor series relation given by Eq. (3.30).

Using the relation given by Eq. (3.30), the point values of the primary variable at the center of each face are obtained from face-integrated values. For the $(i+\frac{1}{2},j)$ face, the point value $f_{i+\frac{1}{2},j}$ to fourth-order accuracy is

$$f_{i+\frac{1}{2},j} = \frac{1}{r_{i+\frac{1}{2}}}\left(\frac{1}{h_\theta h_\xi}\langle f\rangle_{i+\frac{1}{2},j} - \frac{1}{24}h_\xi^2\left[\frac{\partial^2(fr)}{\partial\xi^2}\right]_{r_{i+\frac{1}{2}}}\right). \tag{3.267}$$

Note that h_θ is chosen to have a value of one, but is explicitly included in Eq. (3.267) for the sake of completion. Note also that the factor of radius comes about from the fact that the volume integral $\langle f\rangle_{i,j}$ (see definition in Eq. (3.241)) contains the Jacobian r. Obtaining a point value thus requires undoing the integration with respect to θ and ξ, and dividing through by r. In effect the cylindrical volume integral of f is treated as a Cartesian volume integral of the product of two terms. Note the distinction between the point value evaluation for cylindrical coordinates given in Eq. (3.267) and for Cartesian coordinates given in Eq. (3.57).

In Eq. (3.267), the second derivative transverse to the $(i+\frac{1}{2},j)$ face is evaluated as a second-order accurate finite differences using face-integrated values. Accounting for factors of cell spacing both in the finite-difference stencil and in the face-integrated values yields the

discrete form for the second derivative,

$$\left[\frac{\partial^2(fr)}{\partial\xi^2}\right]_{r_{i+\frac{1}{2}}} = \frac{1}{h_\xi^3}\left(\langle f\rangle_{i+\frac{1}{2},j+1} - 2\langle f\rangle_{i+\frac{1}{2},j} + \langle f\rangle_{i+\frac{1}{2},j-1}\right). \tag{3.268}$$

Just as in Cartesian coordinates, it is important that the face-integrated value on the righthand side of Eq. (3.267) is high-order accurate, whereas the face-integrated values in Eq. (3.268) need only be second-order accurate. Substituting Eq. (3.268) into Eq. (3.267) yields the complete expression for the point value of f at the center of the $(i+\frac{1}{2},j)$ face,

$$f_{i+\frac{1}{2},j} = \frac{1}{r_{i+\frac{1}{2}}h_\theta h_\xi}\left(\langle f\rangle_{i+\frac{1}{2},j} - \frac{1}{24}\left(\langle f\rangle_{i+\frac{1}{2},j+1} - 2\langle f\rangle_{i+\frac{1}{2},j} + \langle f\rangle_{i+\frac{1}{2},j-1}\right)\right) \tag{3.269}$$

The face-integrated fourth-order flux $\langle F\rangle_{i+\frac{1}{2},j} = \langle \alpha f\rangle_{i+\frac{1}{2},j}$ is evaluated to fourth-order accuracy using Eq. (3.30) and using the expression for the point value given in Eq. (3.269), such that

$$\langle \alpha f\rangle_{i+\frac{1}{2},j} = r_{i+\frac{1}{2}}\left(\alpha_{i+\frac{1}{2},j}f_{i+\frac{1}{2},j} + \frac{1}{24}h_\xi^2\left[\frac{\partial^2}{\partial\xi^2}(\alpha f)\right]_{r_{i+\frac{1}{2}}}\right)h_\theta h_\xi, \tag{3.270}$$

where the multiplier $r_{i+\frac{1}{2}}$ stems from the flux definition in Eq. (3.246). The second derivative term is evaluated to second-order accuracy using finite differences of known discrete values, such that

$$\left[\frac{\partial^2}{\partial\xi^2}(\alpha f)\right]_{r_{i+\frac{1}{2}}} = \frac{1}{h_\xi^3}\left(\alpha_{i+\frac{1}{2},j+1}\frac{\langle f\rangle_{i+\frac{1}{2},j+1}}{r_{i+\frac{1}{2}}} - 2\alpha_{i+\frac{1}{2},j}\frac{\langle f\rangle_{i+\frac{1}{2},j}}{r_{i+\frac{1}{2}}} + \alpha_{i+\frac{1}{2},j-1}\frac{\langle f\rangle_{i+\frac{1}{2},j-1}}{r_{i+\frac{1}{2}}}\right). \tag{3.271}$$

Substituting Eq. (3.271) into Eq. (3.270) results in the complete expression for the fourth-order flux at the $(i+\frac{1}{2},j)$ face:

$$\begin{aligned}\langle F\rangle_{i+\frac{1}{2},j} = {}& r_{i+\frac{1}{2}}\alpha_{i+\frac{1}{2},j}f_{i+\frac{1}{2},j}h_\theta h_\xi \\ & + \frac{1}{24}\left(\alpha_{i+\frac{1}{2},j+1}\langle f\rangle_{i+\frac{1}{2},j+1} - 2\alpha_{i+\frac{1}{2},j}\langle f\rangle_{i+\frac{1}{2},j} + \alpha_{i+\frac{1}{2},j-1}\langle f\rangle_{i+\frac{1}{2},j-1}\right).\end{aligned} \tag{3.272}$$

Using the same procedure based on the relation in Eq. (3.30), the point value of f can be obtained at the center of the $(i,j+\frac{1}{2})$ face,

$$f_{i,j+\frac{1}{2}} = \frac{1}{r_i}\left(\frac{1}{h_r h_\theta}\langle f\rangle_{i,j+\frac{1}{2}} - \frac{1}{24}h_r^2\left[\frac{\partial^2(rf)}{\partial r^2}\right]_{\xi_{j+\frac{1}{2}}}\right) \tag{3.273}$$

$$= \frac{1}{r_i h_r h_\theta}\left(\langle f\rangle_{i,j+\frac{1}{2}} - \frac{1}{24}\left[\langle f\rangle_{i+1,j+\frac{1}{2}} - 2\langle f\rangle_{i,j+\frac{1}{2}} + \langle f\rangle_{i-1,j+\frac{1}{2}}\right]\right) \tag{3.274}$$

where the terms in the square brackets can be evaluated to second-order accuracy. The flux associated with the ξ-direction is

$$\langle F\rangle_{i,j+\frac{1}{2}} = r_i\beta_{i,j+\frac{1}{2}} f_{i,j+\frac{1}{2}} h_r h_\theta + \frac{1}{24}\left(\beta_{i+1,j+\frac{1}{2}}\langle f\rangle_{i+1,j+\frac{1}{2}} - 2\beta_{i,j+\frac{1}{2}}\langle f\rangle_{i,j+\frac{1}{2}} + \beta_{i-1,j+\frac{1}{2}}\langle f\rangle_{i-1,j+\frac{1}{2}}\right) \quad (3.275)$$

It is important to note that the Jacobian r appears in the definitions of the volume integral $\langle f\rangle_{i,j}$ and the face integrals $\langle f\rangle_{i+\frac{1}{2},j}$ and $\langle f\rangle_{i,j+\frac{1}{2}}$. See Eqs. (3.241), (3.242), and (3.244), respectively, for these definitions. Combined with the interpolation step, Eqs. (3.272) and (3.275) prescribe a means of computing fourth-order fluxes from discrete volume-integrated values of the distribution function.

3.8.3 Boundary condition implementation for the Vlasov equation

The interpolation and fourth-order evaluation steps outlined in Sections 3.8.2.2 and 3.8.2.3 for computing fluxes apply for cells that have neighbors. For cells near domain boundaries this procedure has to be modified. As discussed in Section 3.4.3, boundary conditions in finite-volume implementations can be handled through ghost cells or through one-sided reconstructions. Note that the use of ghost cells constitutes a proxy for using one-sided reconstructions. While ghost cells simplify boundary treatment in Cartesian coordinates, they are not well suited for the radial direction in the cylindrical coordinate Vlasov equation because stencil coefficients depend on the distance from the axis. Consequently boundary conditions for the cylindrical coordinate Vlasov equation are implemented using one-sided reconstructions of the solution.

Generalized one-sided reconstructions near boundaries call for a modified quadrature evaluation, such that transverse second-derivative terms are evaluated in a way that is consistent with the boundary condition. Such an implementation would require special-case treatment of each variable, near each boundary, along each direction. To avoid the complexity associated with such a treatment, the quadrature evaluation is modified in a very limited way near boundaries. Instead of using a centered finite-difference stencil for evaluating the second-derivative terms as is done throughout the interior of the domain, a one-sided finite difference stencil (see Eq. (3.67)) is used for cells at boundaries. Thus, in the absence of ghost cells, the quadrature rule near boundaries does not account for any specific boundary conditions, but still computes transverse second derivatives to second-order accuracy using a one-sided stencil. By using one-sided stencil for second derivative evaluation, some accuracy is lost near boundaries, but the overall method remains globally fourth-order accurate. In effect, boundary conditions for cylindrical phase space coordinates are enforced exclusively through the one-dimensional interpolation stage of the discretization.

3.8.3.1 Specular reflection boundary condition

The specular reflection boundary condition on the distribution function is applied at conducting wall boundaries and at the axis boundary in cylindrical coordinates. The analytical expression that describes the boundary condition is given in Eq. (2.99). Unlike typical Neumann and Dirichlet boundary conditions, the specular reflection boundary condition on the distribution function requires non-local information. For example, for the axis boundary condition in (r, v_r, v_θ) cylindrical phase space coordinates, the specular reflection condition is

$$f(r, v_r, v_\theta)|_{r=0} = f(r, -v_r, v_\theta)|_{r=0} \qquad \text{for } v_r > 0, \tag{3.276}$$

which requires information from $v_r < 0$ to set the boundary condition for $v_r > 0$. Note that Eq. (3.276) is consistent with the specular reflection description given in Ref. [29]. Velocity components that are parallel to a specular-reflection boundary do not play a role when it comes to setting the boundary condition. Consequently the implementation discussion is limited to the two-dimensional (r, v_r) plane.

Unlike in Cartesian coordinates, in cylindrical (r, v_r) coordinates, specular reflection is implemented through an extrapolation procedure and a copy operation. Let the radius be indexed by $i = \{0, 1, 2, \cdots, N_r - 1\}$ and let the velocity coordinate be indexed by $j = \{0, 1, 2, \cdots, N_{v_r} - 1\}$, such that indices $j = \left\{0, 1, 2, \frac{N_{v_r}}{2} - 1\right\}$ denote the cells for which $v_r < 0$. See Fig. 3.8 for an illustration of the (r, v_r) plane and the associated indexing. Then specular reflection involves an extrapolation step, and a copy step so as to have well-defined values of the distribution function at the $r = 0$ boundary (denoted by index $i = -\frac{1}{2}$) and at the $r = r_{\max}$ boundary (denoted by index $i = N_r - \frac{1}{2}$). At the axis, these steps are:

1. for $j = \left\{0, 1, \cdots, \frac{N_{v-r}}{2} - 1\right\}$, corresponding to $v_r < 0$

   a) Use cells $i = \{0, 1, 2, 3, 4\}$ to perform a one-dimensional extrapolation, using a fifth-order accurate polynomial reconstruction to obtain the boundary value $\langle f \rangle_{-\frac{1}{2},j}$ in terms of $\left\{\langle f \rangle_{0,j}, \langle f \rangle_{1,j}, \langle f \rangle_{2,j}, \langle f \rangle_{3,j}, \langle f \rangle_{4,j}\right\}$, such that

$$\langle f \rangle_{-\frac{1}{2},j} = \frac{1}{1800 h_r^2}\Big(12019 \langle f \rangle_{0,j} - 5981 \langle f \rangle_{1,j} + 3019 \langle f \rangle_{2,j} - 981 \langle f \rangle_{3,j} + 144 \langle f \rangle_{4,j}\Big) \tag{3.277}$$

   b) Copy value of $\langle f \rangle_{-\frac{1}{2},j}$ to $\langle f \rangle_{-\frac{1}{2},N_{v_r}-j-1}$.

At the $r = r_{\max}$ conducting wall boundary, the extrapolation and copy steps are:

1. for $j = \left\{\frac{N_{v_r}}{2}, \frac{N_{v_r}}{2} + 1, \cdots, N_{v_r} - 1\right\}$, corresponding to $v_r > 0$

a) use cells $i = \{N_r - 5, N_r - 4, N_r - 3, N_r - 2, N_r - 1\}$ to perform a one-dimensional extrapolation using fifth-order accurate polynomial reconstruction to obtain the boundary value $\langle f \rangle_{N_r - \frac{1}{2}, j}$, such that

$$\begin{aligned}\langle f \rangle_{N_r-\frac{1}{2},j} = \frac{1}{60h_r^2(2N_r-5)(24+(N_r-5)N_r(20+3(N_r-5)N_r))}\Big(\\ \Big(\quad 576 - 1800N_r + 1680N_r^2 - 600N_r^3 + 72N_r^4\Big)\langle f \rangle_{N_r-5,j} \\ +\Big(-3924 + 11925N_r - 10620N_r^2 + 3525N_r^3 - 378N_r^4\Big)\langle f \rangle_{N_r-4,j} \\ +\Big(12076 - 34875N_r + 28580N_r^2 - 8475N_r^3 + 822N_r^4\Big)\langle f \rangle_{N_r-3,j} \\ +\Big(-23924 + 61425N_r - 42220N_r^2 + 11025N_r^3 - 978N_r^4\Big)\langle f \rangle_{N_r-2,j} \\ +\Big(48076 - 77175N_r + 42980N_r^2 - 9975N_r^3 + 822N_r^4\Big)\langle f \rangle_{N_r-1,j}\Big)\end{aligned} \tag{3.278}$$

b) Copy value of $\langle f \rangle_{N_r-\frac{1}{2},j}$ to $\langle f \rangle_{N_r-\frac{1}{2},N_{v_r}-j-1}$.

This procedure is illustrated in Fig. 3.8. The resulting values of $\langle f \rangle_{-\frac{1}{2},j}$ and $\langle f \rangle_{N_r-\frac{1}{2},j}$ for all j at the radial boundaries can then be used to evaluate fluxes. Note that at $r = 0$ the radially-directed face-integrated flux is zero since the area associated with this cell face is zero. As a consequence the values of the distribution function at the axis boundary only play a role in high-order (i.e. greater than second-order) methods. For the fourth-order discretization used here the values $\langle f \rangle_{-\frac{1}{2},j}$ obtained from the extrapolation-and-copy procedure are needed to compute high-order fluxes at the $(\frac{1}{2}, j)$ faces. At $r = r_{\max}$ the radially-directed flux is non-zero, consequently the values $\langle f \rangle_{N_r-\frac{1}{2},j}$ play a role in both the flux at index $(N_r - \frac{1}{2}, j)$ and also in the interpolation of the distribution function to index $(N_r - \frac{3}{2}, j)$.

3.8.4 Fourth-order accurate initialization

Just as in Cartesian coordinates, it is important that the initialization of the primary variables is fourth-order accurate (see discussion in Section 3.4.4). Since initial conditions are typically prescribed by analytic functions, a fourth-order initialization of volume-integrated quantities can be achieved in one of two ways: by using closed-form definite integrals of analytic functions; or by using the quadrature rule given by Eq. (3.30), with integration along all (instead of a subset) of the directions. To demonstrate the quadrature approach for cylindrical coordinates, let $G(r, v_r, v_\theta)$ be the prescribed analytic function in cylindrical phase space coordinates that sets the distribution function value at initial time. The cell-volume-integrated distribution function can then be evaluated to fourth-order accuracy

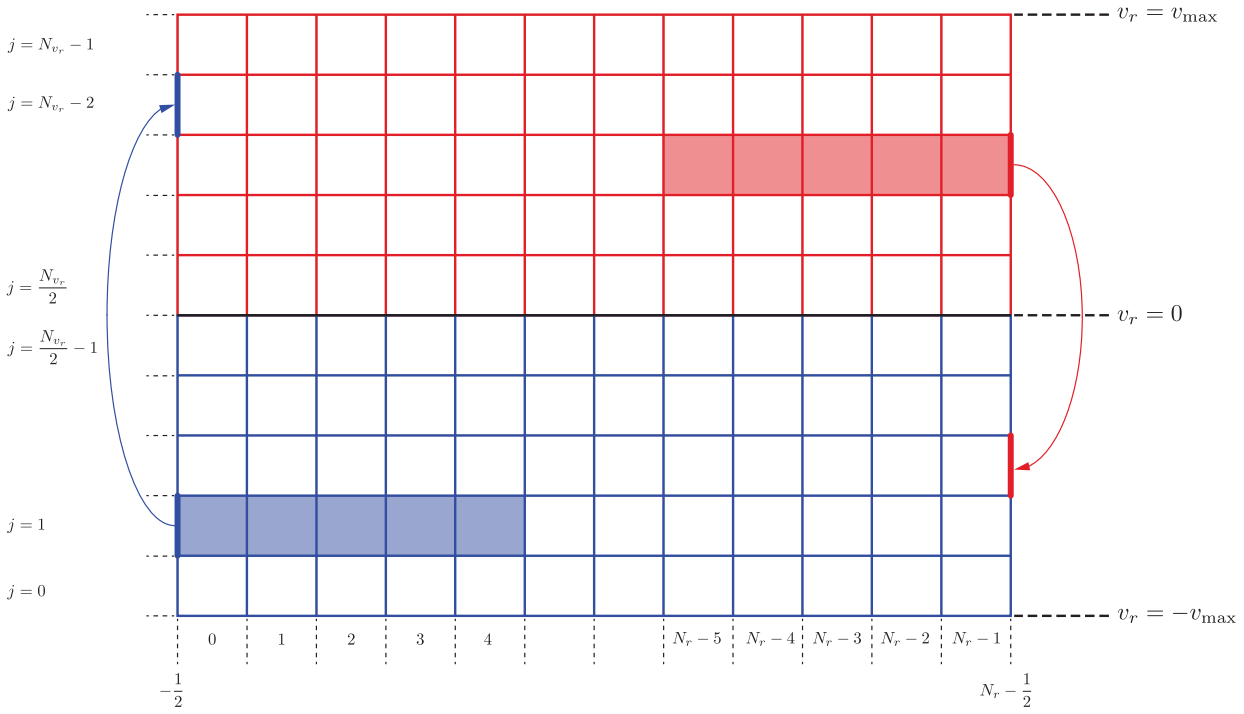

Figure 3.8: Illustration of specular reflection boundary condition implementation for cylindrical (r, v_r) phase space coordinates at the lefthand $(r = 0)$ axis boundary and at the righthand conducting wall boundary. The red grid denotes $v_r > 0$, and the blue grid denotes $v_r < 0$. At the lefthand axis boundary, for each $j \in \left\{0, 1, \cdots, \frac{N_{v_r}}{2} - 1\right\}$ corresponding to $v_r < 0$ a fifth-order accurate one-dimensional polynomial reconstruction is performed using five cells to extrapolate the distribution function value to the $i = -\frac{1}{2}$ face (thick blue line). This extrapolated value is then copied (blue arrow) to the cell face $\left(-\frac{1}{2}, N_{v_r} - j - 1\right)$. At the righthand conducting wall boundary, for each $j \in \left\{\frac{N_{v_r}}{2}, \cdots, N_{v_r} - 1\right\}$ corresponding to $v_r > 0$, a fifth-order accurate one-dimensional polynomial reconstruction is performed using five cells to extrapolate the distribution function value to the $i = N_r - \frac{1}{2}$ face (thick red line). This extrapolated value is then copied (red arrow) from the $\left(N_r - \frac{1}{2}, j\right)$ cell face to the $\left(N_r - \frac{1}{2}, N_{v_r} - j - 1\right)$ cell face. In this case $N_r = 12$ and $N_{v_r} = 10$. Note that to set the axis boundary condition only $f(v_r)$ for $v_r < 0$ is used, and to set the righthand boundary condition only $f(v_r)$ for $v_r > 0$ is used.

as

$$\langle f\rangle_{i,l,m} = h_r h_{v_r} h_{v_\theta}\Bigg(G\big(r_i,(v_r)_l,(v_\theta)_m\big)r_i + \frac{1}{24}\left[h_r^2\frac{\partial^2}{\partial r^2}(rG) + h_{v_r}^2\frac{\partial^2}{\partial v_r^2}(rG) + h_{v_\theta}^2\frac{\partial^2}{\partial v_\theta^2}(rG)\right]_{(r_i,(v_r)_l,(v_\theta)_m)}\Bigg). \quad (3.279)$$

The second-derivative terms can be evaluated either analytically or as point-value finite-differences, such that

$$\left[\frac{\partial^2}{\partial r^2}(rG)\right]_{(r_i,(v_r)_l,(v_\theta)_m)} = \frac{1}{h_r^2}\Big[r_{i+1}G\big(r_{i+1},(v_r)_l,(v_\theta)_m\big) - 2r_iG\big(r_i,(v_r)_l,(v_\theta)_m\big) + r_{i-1}G\big(r_{i-1},(v_r)_l,(v_\theta)_m\big)\Big]. \quad (3.280)$$

The use of Eq. (3.279) allows the distribution function to be initialized to fourth-order accuracy even in cases where a definite integral over a cell volume cannot be readily evaluated.

3.8.5 Pitfalls of treating cylindrical phase space coordinates as Cartesian

The finite-volume discretization of the distribution function and fields in cylindrical phase space coordinates requires considerable care on account of cell volumes varying with radius. One can make a compelling argument that much of the complexity associated with the cylindrical coordinate flux evaluations can be eliminated by evolving a volume-integral of the quantity rf with volume defined as in Cartesian coordinates ($dV = drd\theta dzdv_rdv_\theta dv_z$) rather than evolving the volume-integral of the distribution function f with volume defined as in cylindrical coordinates ($dV = rdrd\theta dzdv_rdv_\theta dv_z$). Analytically the two formulations for the primary variable are equivalent, but numerically they amount to very different discretizations.

Evolving an auxiliary variable $\check{f} = rf$ is problematic because it conflates the coordinate r, the value of which is known everywhere in the domain for all time, with the variable of interest, f. As a consequence, boundary conditions that require non-local information about the velocity dependence of the distribution function (see Section 2.5.1) are largely ambiguous for the auxiliary variable $\check{f}$. This is especially true of fourth-order boundary conditions, which require more cells to reconstruct the solution than second-order boundary conditions. Ensuring fourth-order accuracy of the spatial discretization is also difficult when evolving the auxiliary quantity $\check{f}$ since the distinction between area-integrated quantities and volume-integrated quantities is blurred. This lack of distinction is acceptable in second-order calculations, but is less forgiving if fourth-order accuracy is sought.

3.9 Cylindrical coordinates: spatial discretization of Maxwell's equations

3.9.1 Fourth-order line integrals for Maxwell's equations

The general approach for computing fourth-order accurate line-integrals in cylindrical coordinates is the same as that for Cartesian coordinates. There are, however, important differences in the details of the interpolation and the evaluation of quadratures that call for a separate discussion of line-integrated fluxes for cylindrical coordinates. The procedure for evaluating line integrals to fourth-order accuracy is presented for the case of Ampere's law, and extends directly to Faraday's law.

First a regular grid in cylindrical coordinates is defined. Let i denote the cell index along the r direction, j denote the index along the θ direction, and k denote the index along the z direction, such that the center of the cell (i,j,k) has coordinates (r_i, θ_j, z_k) and the cell spans the volume $\left[r_{i-\frac{1}{2}}, r_{i+\frac{1}{2}}\right] \times \left[\theta_{j-\frac{1}{2}}, \theta_{j+\frac{1}{2}}\right] \times \left[z_{k-\frac{1}{2}}, z_{k+\frac{1}{2}}\right]$, where

$$r_{i\pm\frac{1}{2}} = r_i \pm \frac{h_r}{2} \tag{3.281}$$

$$\theta_{j\pm\frac{1}{2}} = \theta_j \pm \frac{h_\theta}{2} \tag{3.282}$$

$$z_{k\pm\frac{1}{2}} = z_k \pm \frac{h_z}{2} \tag{3.283}$$

where h_r, h_θ, and h_z denote the cell widths along each direction. The primary variable in the weak form of Ampere's law (see Eq. (3.83)) is the area-integrated electric field with $d\boldsymbol{A} = \{rd\theta dz, drdz, rdrd\theta\}$. For convenience this area integral is assumed to be evaluated in the middle of the cell. In this cylindrical coordinate system the electric field has three components:

$$\lfloor E_r \rfloor_{i_0,j,k} = r_i \int_{z_{k-\frac{1}{2}}}^{z_{k+\frac{1}{2}}} \int_{\theta_{j-\frac{1}{2}}}^{\theta_{j+\frac{1}{2}}} E_r(r_i, \theta, z) d\theta dz \tag{3.284}$$

$$\lfloor E_\theta \rfloor_{i,j_0,k} = \int_{z_{k-\frac{1}{2}}}^{z_{k+\frac{1}{2}}} \int_{r_{i-\frac{1}{2}}}^{r_{i+\frac{1}{2}}} E_\theta(r, \theta_j, z) dr dz \tag{3.285}$$

$$\lfloor E_z \rfloor_{i,j,k_0} = \int_{\theta_{j-\frac{1}{2}}}^{\theta_{j+\frac{1}{2}}} \int_{r_{i-\frac{1}{2}}}^{r_{i+\frac{1}{2}}} E_z(r, \theta_j, z) r dr d\theta. \tag{3.286}$$

The notation $\lfloor E_r \rfloor_{i_0,j,k}$ denotes an area integral of the E_r component of the electric field over the fixed central $r = r_i$ plane of the cell (i,j,k). The area integrated current that appears in Eq. (3.83) can be evaluated in the same way. Likewise the area-integrated magnetic field

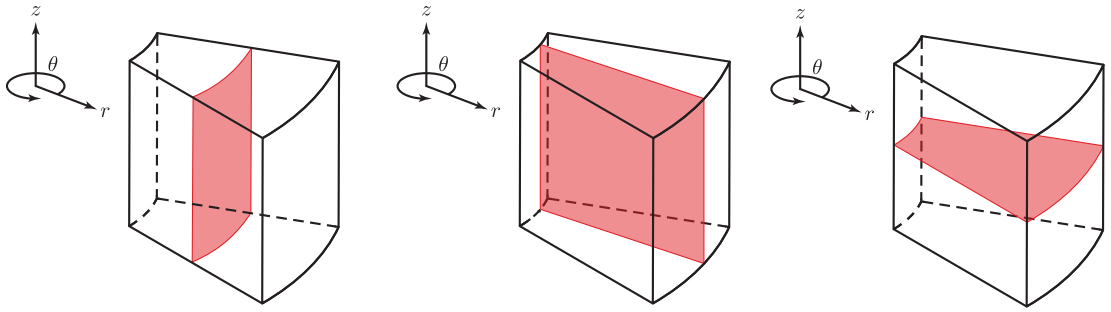

(a) E_r, B_r **(b)** E_θ, B_θ **(c)** E_z, B_z

Figure 3.9: Cross sections of a cell on which the area-integrated electric and magnetic field primary variables are defined. The current is also computed as an area-integrated value on these cross sections.

components, which appear in Faraday's law, are

$$\lfloor B_r \rfloor_{i_0,j,k} = r_i \int_{z_{k-\frac{1}{2}}}^{z_{k+\frac{1}{2}}} \int_{\theta_{j-\frac{1}{2}}}^{\theta_{j+\frac{1}{2}}} B_r(r_i, \theta, z) d\theta dz \tag{3.287}$$

$$\lfloor B_\theta \rfloor_{i,j_0,k} = \int_{z_{k-\frac{1}{2}}}^{z_{k+\frac{1}{2}}} \int_{r_{i-\frac{1}{2}}}^{r_{i+\frac{1}{2}}} B_\theta(r, \theta_j, z) dr dz \tag{3.288}$$

$$\lfloor B_z \rfloor_{i,j,k_0} = \int_{\theta_{j-\frac{1}{2}}}^{\theta_{j+\frac{1}{2}}} \int_{r_{i-\frac{1}{2}}}^{r_{i+\frac{1}{2}}} B_z(r, \theta_j, z) r dr d\theta. \tag{3.289}$$

The area integrals given by Eqs. (3.284) – (3.289) are illustrated in Fig. 3.9.

The closed-loop line integrals in Ampere's law (Eq. (3.83)) for a single cell in this cylindrical coordinate system can be expressed in terms of one-dimensional line integrals,

$$\oint \boldsymbol{B} \cdot d\boldsymbol{l} = \begin{bmatrix} -\left[r_i \int B_\theta(r_i, \theta, z) d\theta\right]_{z_{k-\frac{1}{2}}}^{z_{k+\frac{1}{2}}} + \left[\int B_z(r_i, \theta, z) dz\right]_{\theta_{j-\frac{1}{2}}}^{\theta_{j+\frac{1}{2}}} \\ \left[\int B_r(r, \theta_j, z) dr\right]_{z_{k-\frac{1}{2}}}^{z_{k+\frac{1}{2}}} - \left[\int B_z(r, \theta_j, z) dz\right]_{r_{i-\frac{1}{2}}}^{r_{i+\frac{1}{2}}} \\ -\left[\int B_r(r, \theta, z_k) dr\right]_{\theta_{j-\frac{1}{2}}}^{\theta_{j+\frac{1}{2}}} + \left[r \int B_\theta(r, \theta, z_k) d\theta\right]_{r_{i-\frac{1}{2}}}^{r_{i+\frac{1}{2}}} \end{bmatrix}. \tag{3.290}$$

These line integrals are illustrated in Fig. 3.10.

The objective of the finite-volume discretization for Ampere's law is to be able to express the line integrals in Eq. (3.290) in terms of the known discrete quantities given by the area integrals in Eqs. (3.287) – (3.289). As in the finite-volume implementation for Cartesian coordinates, this is achieved by first interpolating the area-integrated fields to cell faces, and then evaluating the integrals in Eq. (3.290) using a quadrature rule based on the Taylor series relation given by Eq. (3.28).

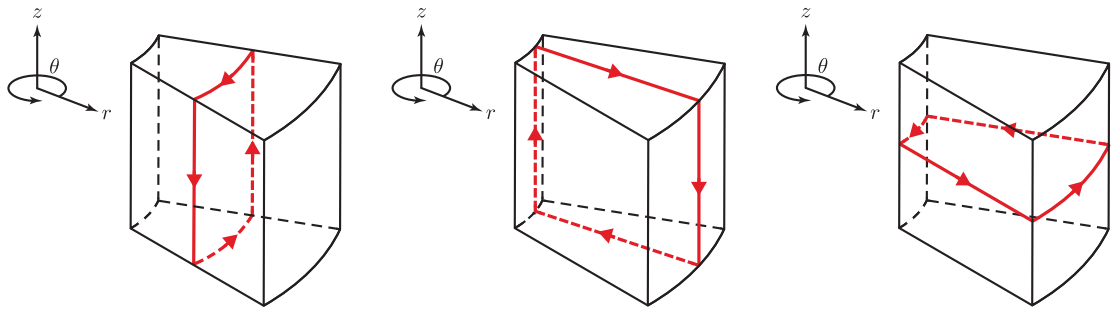

(a) $\int \boldsymbol{B} \cdot d\boldsymbol{l}$ for E_r **(b)** $\int \boldsymbol{B} \cdot d\boldsymbol{l}$ for E_θ **(c)** $\int \boldsymbol{B} \cdot d\boldsymbol{l}$ for E_z

Figure 3.10: Line integrals of the magnetic field that are needed to update components of the electric field. Note that the direction of integration, indicated by the arrows, is associated with the sign on the $\oint \boldsymbol{B} \cdot d\boldsymbol{l}$ term in Ampere's law (see Eq. (3.83)).

3.9.1.1 One-dimensional polynomial interpolation

The primary variables in Ampere's law and Faraday's law are area-integrated quantities defined over cell cross sections, whereas the sought-after line integrals in Eq. (3.290) are evaluated at the centers of cell faces, denoted by half-indices $i \pm \frac{1}{2}$, $j \pm \frac{1}{2}$, and $k \pm \frac{1}{2}$. To convert center-of-cell area-integrated quantities to center-of-face one-dimensional-integral quantities, a one-dimensional fourth-order accurate polynomial reconstruction (see Section 3.4.2.1 and Section 3.8.2.1) is used.

The one-dimensional polynomial interpolations of $\lfloor B_r \rfloor_{i_0,j,k}$ to cell face $(i_0, j+\frac{1}{2}, k)$ and to cell face $(i_0, j, k+\frac{1}{2})$ occur in the same radius plane. This can be seen from the center-of-face integral definitions,

$$\lfloor B_r \rfloor_{i_0,j+\frac{1}{2},k} = r_i \int B_r(r_i, \theta_{j+\frac{1}{2}}, z) dz \tag{3.291}$$

$$\lfloor B_r \rfloor_{i_0,j,k+\frac{1}{2}} = r_i \int B_r(r_i, \theta, z_{k+\frac{1}{2}}) d\theta. \tag{3.292}$$

Note that while the radius r_i does appear in the analytic definitions of center-of-cell integral $\lfloor B_r \rfloor_{i_0,j,k}$ and center-of-face one-dimensional integrals $\lfloor B_r \rfloor_{i_0,j+\frac{1}{2},k}$ and $\lfloor B_r \rfloor_{i_0,j,k+\frac{1}{2}}$, the radius is fixed, and is thereby factored out of the integrals. Thus the interpolation stencils for $\lfloor B_r \rfloor_{i_0,j+\frac{1}{2},k}$ and $\lfloor B_r \rfloor_{i_0,j,k+\frac{1}{2}}$ are analogous to the stencils for Cartesian coordinates (see Section 3.4.2.1 and Section 3.5.1.1), such that center-of-face integral values of B_r are

$$\lfloor B_r \rfloor_{i_0,j+\frac{1}{2},k} = \frac{7}{12h_\theta}\left(\lfloor B_r \rfloor_{i_0,j,k} + \lfloor B_r \rfloor_{i_0,j+1,k}\right) - \frac{1}{12h_\theta}\left(\lfloor B_r \rfloor_{i_0,j-1,k} + \lfloor B_r \rfloor_{i_0,j+2,k}\right) \tag{3.293}$$

$$\lfloor B_r \rfloor_{i_0,j,k+\frac{1}{2}} = \frac{7}{12h_z}\left(\lfloor B_r \rfloor_{i_0,j,k} + \lfloor B_r \rfloor_{i_0,j,k+1}\right) - \frac{1}{12h_z}\left(\lfloor B_r \rfloor_{i_0,j,k-1} + \lfloor B_r \rfloor_{i_0,j,k+2}\right), \tag{3.294}$$

where $\lfloor B_r \rfloor_{i_0,j+\frac{1}{2},k}$ is the one-dimensional integral of B_r over the z direction at fixed coordinates $(r_i, \theta_{j+\frac{1}{2}})$, and $\lfloor B_r \rfloor_{i_0,j,k+\frac{1}{2}}$ is a one-dimensional integral of B_r over the θ direction at fixed coordinates $(r_i, z_{k+\frac{1}{2}})$. Equations (3.293) and (3.294) are fourth-order accurate evaluations of the analytic expressions given in Eq. (3.291) and Eq. (3.292), respectively.

One-dimensional polynomial interpolations of $\lfloor B_\theta \rfloor_{i,j_0,k}$ to cell face $i+\frac{1}{2}$ and to cell face $k+\frac{1}{2}$ are used to evaluate approximations to the analytic center-of-face integral definitions

$$\lfloor B_\theta \rfloor_{i+\frac{1}{2},j_0,k} = \int_{z_{k-\frac{1}{2}}}^{z_{k+\frac{1}{2}}} B_\theta(r_{i+\frac{1}{2}}, \theta_j, z) dz \tag{3.295}$$

$$\lfloor B_\theta \rfloor_{i,j_0,k+\frac{1}{2}} = \int_{r_{i-\frac{1}{2}}}^{r_{i+\frac{1}{2}}} B_\theta(r, \theta_j, z_{k+\frac{1}{2}}) dr. \tag{3.296}$$

The associated reconstruction stencils are analogous to the stencils for Cartesian coordinates, such that the center-of-face integral values of B_θ to fourth-order accuracy are

$$\lfloor B_\theta \rfloor_{i+\frac{1}{2},j_0,k} = \frac{7}{12h_r}\left(\lfloor B_\theta \rfloor_{i,j_0,k} + \lfloor B_\theta \rfloor_{i+1,j_0,k}\right) - \frac{1}{12h_r}\left(\lfloor B_\theta \rfloor_{i-1,j_0,k} + \lfloor B_\theta \rfloor_{i+2,j_0,k}\right) \tag{3.297}$$

$$\lfloor B_\theta \rfloor_{i,j_0,k+\frac{1}{2}} = \frac{7}{12h_z}\left(\lfloor B_\theta \rfloor_{i_0,j,k} + \lfloor B_\theta \rfloor_{i,j_0,k+1}\right) - \frac{1}{12h_z}\left(\lfloor B_\theta \rfloor_{i,j_0,k-1} + \lfloor B_\theta \rfloor_{i,j_0,k+2}\right), \tag{3.298}$$

where $\lfloor B_\theta \rfloor_{i+\frac{1}{2},j_0,k}$ is the one-dimensional integral of B_θ over the z direction at fixed coordinates $(r_{i+\frac{1}{2}}, \theta_j)$, and $\lfloor B_\theta \rfloor_{i,j_0,k+\frac{1}{2}}$ is the one-dimensional integral of B_θ over the r direction at fixed coordinates $(\theta_j, z_{k+\frac{1}{2}})$.

The one-dimensional polynomial interpolation of $\lfloor B_z \rfloor_{i,j,k_0}$ to cell face $j+\frac{1}{2}$ likewise results in an analogous stencil, such that the analytic definition

$$\lfloor B_z \rfloor_{i,j+\frac{1}{2},k_0} = \int_{r_{i-\frac{1}{2}}}^{r_{i+\frac{1}{2}}} B_z(r, \theta_{j+\frac{1}{2}}, z_k) r dr, \tag{3.299}$$

is approximated to fourth-order accuracy by an expression that uses known discrete quantities,

$$\lfloor B_z \rfloor_{i,j+\frac{1}{2},k_0} = \frac{7}{12h_\theta}\left(\lfloor B_z \rfloor_{i,j,k_0} + \lfloor B_z \rfloor_{i,j+1,k_0}\right) - \frac{1}{12h_\theta}\left(\lfloor B_z \rfloor_{i,j-1,k_0} + \lfloor B_z \rfloor_{i,j+2,k_0}\right). \tag{3.300}$$

The one-dimensional polynomial interpolation of $\lfloor B_z \rfloor_{i,j,k_0}$ to cell face $i+\frac{1}{2}$ requires accounting for the fact that in cylindrical coordinates the size of the differential area element in the z direction increases with radius. This means that the polynomial reconstruction needs to include the Jacobian r (see Section 3.8.2.1). Thus in order to obtain the fourth-order accurate value of center-of-face integral

$$\lfloor B_z \rfloor_{i+\frac{1}{2},j,k_0} = \int_{\theta_{j-\frac{1}{2}}}^{\theta_{j+\frac{1}{2}}} B_z(r_{i+\frac{1}{2}}, \theta_j, z) r_{i+\frac{1}{2}} d\theta \tag{3.301}$$

the following stencil is used:

$$\begin{aligned}\lfloor B_z \rfloor_{i+\frac{1}{2},j,k_0} =& \frac{1}{12h_r^2(4-15\ell^2+5\ell^4)}\Big\{ \\ &\Big(\quad 4 \;+\; 3\ell \;-\; 8\ell^2 \;-\; 5\ell^3\Big)\lfloor B_z \rfloor_{i-1,j,k_0} \\ &+\Big(-60 \;-\; 93\ell \;+\; 24\ell^2 \;+\; 35\ell^3\Big)\lfloor B_z \rfloor_{i,j,k_0} \\ &+\Big(\quad 60 \;-\; 93\ell \;-\; 24\ell^2 \;+\; 35\ell^3\Big)\lfloor B_z \rfloor_{i+1,j,k_0} \\ &+\Big(\;-4 \;+\; 3\ell \;+\; 8\ell^2 \;-\; 5\ell^3\Big)\lfloor B_z \rfloor_{i+2,j,k_0}\Big\},\end{aligned} \tag{3.302}$$

where the index ℓ is defined in Eq. (3.255). Thus to interpolate center-of-cell integrated values to center-of-face integrals in cylindrical coordinates requires careful consideration of the differential line elements and their dependence on the coordinate r.

3.9.1.2 Quadrature rule for evaluating line integrals to fourth-order accuracy

The center-of-face integrals obtained from the interpolation step (given analytically by Eqs. (3.291), (3.292), (3.295), (3.296), (3.299), and (3.301) and discretely by Eqs. (3.293), (3.294), (3.297), (3.298), (3.300), and (3.302)) are not the integrals that appear in the closed-loop integrals of the weak form of Ampere's law (see Eq. (3.290)). A quadrature rule is needed in order to derive fourth-order accurate approximations to the line integrals that appear in Eq. (3.290), using the interpolated values derived above. Just as in other integral evaluations, the quadrature rule relies on the Taylor series relations given in Eq. (3.28) and Eq. (3.30).

The first step in the quadrature evaluation involves computing the fourth-order accurate point-values of the fields by undoing the integrals in Eqs. (3.293), (3.294), (3.297), (3.298), (3.300), and (3.302). The point values are evaluated using Eq. (3.28), such that

$$\begin{aligned}&B_r(r_i,\theta_{j+\frac{1}{2}},z_k) \\ &\quad= \frac{1}{h_z r_i}\lfloor B_r \rfloor_{i_0,j+\frac{1}{2},k} - \frac{1}{24}h_z^2\left[\frac{\partial^2 B_r}{\partial z^2}\right]_{(r_i,\theta_{j+\frac{1}{2}},z_k)} \\ &\quad= \frac{1}{r_i h_z}\left[\lfloor B_r \rfloor_{i_0,j+\frac{1}{2},k} - \frac{1}{24}\left(\lfloor B_r \rfloor_{i_0,j+\frac{1}{2},k+1} - 2\lfloor B_r \rfloor_{i_0,j+\frac{1}{2},k} + \lfloor B_r \rfloor_{i_0,j+\frac{1}{2},k-1}\right)\right] \qquad (3.303) \\ &B_r(r_i,\theta_j,z_{k+\frac{1}{2}}) \\ &\quad= \frac{1}{h_\theta r_i}\lfloor B_r \rfloor_{i_0,j,k+\frac{1}{2}} - \frac{1}{24}h_\theta^2\left[\frac{\partial^2 B_r}{\partial \theta^2}\right]_{r_i,\theta_j,z_{k+\frac{1}{2}}} \\ &\quad= \frac{1}{h_\theta r_i}\left[\lfloor B_r \rfloor_{i_0,j,k+\frac{1}{2}} - \frac{1}{24}\left(\lfloor B_r \rfloor_{i_0,j+1,k+\frac{1}{2}} - 2\lfloor B_r \rfloor_{i_0,j,k+\frac{1}{2}} + \lfloor B_r \rfloor_{i_0,j-1,k+\frac{1}{2}}\right)\right] \qquad (3.304)\end{aligned}$$

$$
\begin{aligned}
&B_\theta(r_{i+\frac{1}{2}}, \theta_j, z_k) \\
&\quad = \frac{1}{h_z} \lfloor B_\theta \rfloor_{i+\frac{1}{2},j_0,k} - \frac{1}{24} h_z^2 \left[\frac{\partial^2 B_\theta}{\partial z^2} \right]_{r_{i+\frac{1}{2}},\theta_j,z_k} \\
&\quad = \frac{1}{h_z} \left[\lfloor B_\theta \rfloor_{i+\frac{1}{2},j_0,k} - \frac{1}{24} \left(\lfloor B_\theta \rfloor_{i+\frac{1}{2},j_0,k+1} - 2 \lfloor B_\theta \rfloor_{i+\frac{1}{2},j_0,k} + \lfloor B_\theta \rfloor_{i+\frac{1}{2},j_0,k-1} \right) \right] \qquad (3.305) \\
&B_\theta(r_i, \theta_j, z_{k+\frac{1}{2}}) \\
&\quad = \frac{1}{h_r} \lfloor B_\theta \rfloor_{i,j_0,k+\frac{1}{2}} - \frac{1}{24} h_z^2 \left[\frac{\partial^2 B_\theta}{\partial z^2} \right]_{r_i,\theta_j,z_{k+\frac{1}{2}}} \\
&\quad = \frac{1}{h_z} \left[\lfloor B_\theta \rfloor_{i,j_0,k+\frac{1}{2}} - \frac{1}{24} \left(\lfloor B_\theta \rfloor_{i+1,j_0,k+\frac{1}{2}} - 2 \lfloor B_\theta \rfloor_{i,j_0,k+\frac{1}{2}} + \lfloor B_\theta \rfloor_{i-1,j_0,k+\frac{1}{2}} \right) \right] \qquad (3.306) \\
&B_z(r_i, \theta_{j+\frac{1}{2}}, z_k) \\
&\quad = \frac{1}{h_r r_i} \lfloor B_z \rfloor_{i,j+\frac{1}{2},k_0} - \frac{1}{24} h_r^2 \left[\frac{\partial^2 (r B_z)}{\partial r^2} \right]_{r_i,\theta_{j+\frac{1}{2}},z_k} \qquad (3.307) \\
&\quad = \frac{1}{h_r r_i} \left[\lfloor B_z \rfloor_{i,j+\frac{1}{2},k_0} - \frac{1}{24} \left(\lfloor B_z \rfloor_{i+1,j+\frac{1}{2},k_0} - 2 \lfloor B_z \rfloor_{i,j+\frac{1}{2},k_0} + \lfloor B_z \rfloor_{i-1,j+\frac{1}{2},k_0} \right) \right] \qquad (3.308) \\
&B_z(r_{i+\frac{1}{2}}, \theta_j, z_k) \\
&\quad = \frac{1}{h_\theta r_{i+\frac{1}{2}}} \lfloor B_z \rfloor_{i+\frac{1}{2},j,k_0} - \frac{1}{24} h_\theta^2 \left[\frac{\partial^2 B_z}{\partial \theta^2} \right]_{r_{i+\frac{1}{2}},\theta_j,z_k} \qquad (3.309) \\
&\quad = \frac{1}{h_\theta r_{i+\frac{1}{2}}} \left[\lfloor B_z \rfloor_{i+\frac{1}{2},j,k_0} - \frac{1}{24} \left(\lfloor B_z \rfloor_{i+\frac{1}{2},j+1,k_0} - 2 \lfloor B_z \rfloor_{i+\frac{1}{2},j,k_0} + \lfloor B_z \rfloor_{i+\frac{1}{2},j-1,k_0} \right) \right]. \qquad (3.310)
\end{aligned}
$$

As in the case of Cartesian coordinates, centered second-order accurate finite-difference stencils are used to evaluate the second derivative terms in the expressions for point values. The physical problem of interest determines which of the point value expressions given by Eq. (3.303) – Eq. (3.310) are needed. Some of these expressions are simplified under certain assumptions. For example, if axisymmetry is assumed then all variables are assumed to be independent of the θ coordinate, and thereby the second derivative term in Eq. (3.304) and Eq. (3.310) are set to zero.

The final step in evaluating the fourth-order line integrals is to use the point values derived above to compute the line integrals of interest. To fourth-order accuracy, the line integrals that appear in Ampere's law (see Eq. (3.290)) in terms of known discrete values

are

$$\begin{aligned}
&\int B_r(r,\theta_{j+\frac{1}{2}},z_k)dr \\
&\quad= \left[B_r(r_i,\theta_{j+\frac{1}{2}},z_k)+\frac{1}{24}h_r^2\frac{\partial^2 B_r}{\partial r^2}\right]h_r \\
&\quad= \left[B_r(r_i,\theta_{j+\frac{1}{2}},z_k)+\frac{1}{24h_z}\left(\lfloor B_r\rfloor_{i_0+1,j+\frac{1}{2},k}-2\lfloor B_r\rfloor_{i_0,j+\frac{1}{2},k}+\lfloor B_r\rfloor_{i_0-1,j+\frac{1}{2},k}\right)\right]h_r \qquad (3.311)\\
&\int B_r(r,\theta_j,z_{k+\frac{1}{2}})dr \\
&\quad= \left[B_r(r_i,\theta_j,z_{k+\frac{1}{2}})+\frac{1}{24}h_r^2\frac{\partial^2 B_r}{\partial r^2}\right]h_r \\
&\quad= \left[B_r(r_i,\theta_j,z_{k+\frac{1}{2}})+\frac{1}{24h_\theta}\left(\lfloor B_r\rfloor_{i_0+1,j,k+\frac{1}{2}}-2\lfloor B_r\rfloor_{i_0,j,k+\frac{1}{2}}+\lfloor B_r\rfloor_{i_0-1,j,k+\frac{1}{2}}\right)\right]h_r \qquad (3.312)\\
&r_i\int B_\theta(r_i,\theta,z_{k+\frac{1}{2}})d\theta \\
&\quad= r_i\left[B_\theta(r_i,\theta_j,z_{k+\frac{1}{2}})+\frac{1}{24}h_\theta^2\frac{\partial^2 B_\theta}{\partial\theta^2}\right]h_\theta \\
&\quad= r_i\left[B_\theta(r_i,\theta_j,z_{k+\frac{1}{2}})+\frac{1}{24h_r}\left(\lfloor B_\theta\rfloor_{i,j_0+1,k+\frac{1}{2}}-2\lfloor B_\theta\rfloor_{i,j_0,k+\frac{1}{2}}+\lfloor B_\theta\rfloor_{i,j_0-1,k+\frac{1}{2}}\right)\right]h_\theta \qquad (3.313)\\
&r_{i+\frac{1}{2}}\int B_\theta(r_{i+\frac{1}{2}},\theta,z_k)d\theta \\
&\quad= r_{i+\frac{1}{2}}\left[B_\theta(r_{i+\frac{1}{2}},\theta_j,z_k)+\frac{1}{24h_z}h_\theta^2\frac{\partial^2 B_\theta}{\partial\theta^2}\right]h_\theta \\
&\quad= r_{i+\frac{1}{2}}\left[B_\theta(r_{i+\frac{1}{2}},\theta_j,z_k)+\frac{1}{24}\left(\lfloor B_\theta\rfloor_{i+\frac{1}{2},j_0+1,k}-2\lfloor B_\theta\rfloor_{i,j_0,k}+\lfloor B_\theta\rfloor_{i,j_0-1,k}\right)\right]h_\theta \qquad (3.314)\\
&\int B_z(r_i,\theta_{j+\frac{1}{2}},z)dz \\
&\quad= \left[B_z(r_i,\theta_{j+\frac{1}{2}},z_k)+\frac{1}{24}h_z^2\frac{\partial^2 B_z}{\partial z^2}\right]h_z \\
&\quad= \left[B_z(r_i,\theta_{j+\frac{1}{2}},z_k)+\frac{1}{24r_ih_r}\left(\lfloor B_z\rfloor_{i,j+\frac{1}{2},k_0+1}-2\lfloor B_z\rfloor_{i,j+\frac{1}{2},k_0}+\lfloor B_z\rfloor_{i,j+\frac{1}{2},k_0-1}\right)\right]h_z \qquad (3.315)
\end{aligned}$$

$$\begin{aligned}
&\int B_z(r_{i+\frac{1}{2}},\theta_j,z)dz \\
&\quad= \left[B_z(r_{i+\frac{1}{2}},\theta_j,z_k) + \frac{1}{24}h_z^2\frac{\partial^2 B_z}{\partial z^2}\right]h_z \\
&\quad= \left[B_z(r_{i+\frac{1}{2}},\theta_j,z_k) + \frac{1}{24h_\theta r_{i+\frac{1}{2}}}\left(\lfloor B_z\rfloor_{i+\frac{1}{2},j,k_0+1} - 2\lfloor B_z\rfloor_{i+\frac{1}{2},j,k_0} + \lfloor B_z\rfloor_{i+\frac{1}{2},j,k_0-1}\right)\right]h_z
\end{aligned} \tag{3.316}$$

where the Taylor series relation given by Eq. (3.30) has been invoked, and second derivatives are evaluated using a second-order finite-difference stencil. Expressions for the electric field line integrals that appear in Faraday's law can be obtained by replacing the magnetic field variable with the electric field in Eqs. (3.311) – (3.316). For cells near boundaries, the centered finite-difference stencil for the second derivative is replaced by a one-sided finite difference stencil, as described in Section 3.4.3.

For completion and to illustrate the direction-dependence in cylindrical coordinates, fourth-order accurate expressions for all of the line integrals that appear in Eq. (3.290) are given. Depending which field components are of interest in a simulation, however, not all of the fourth-order line integrals given by Eqs. (3.311) – (3.316) are needed. And depending on the number of spatial coordinates in a simulation, some of the second derivatives may simply be zero, meaning that a field cannot vary along a coordinate direction that is not being simulated. For example, in an axisymmetric configuration, the second derivative of B_θ with respect to θ, which appears in Eqs. (3.313) and (3.314), is zero.

3.9.2 Current density source term in Maxwell's equations

A complete discretization of Maxwell's equations requires evaluating the current source term in Ampere's law. Computing the area-integrated current density, i.e. the current, in cylindrical coordinates to fourth-order accuracy requires accounting for the fact that certain cell cross sections depend on the coordinate r. Following the same general procedure as in Cartesian coordinates, the first step in the calculation of current is obtaining the local point value of the species distribution function, such that

$$\begin{aligned}
r_i(f_s)_{i,j,k,l,m,n} = \frac{1}{h_r h_\theta h_z h_{v_r} h_{v_\theta} h_{v_z}}\Bigg(&\langle f_s\rangle_{i,j,k,l,m,n} - \frac{1}{24}\Bigg[h_r^2\frac{\partial^2}{\partial r^2}\langle f_s\rangle \\
&+ h_\theta^2\frac{\partial^2}{\partial\theta^2}\langle f_s\rangle + h_z^2\frac{\partial^2}{\partial z^2}\langle f_s\rangle + h_{v_r}^2\frac{\partial^2}{\partial v_r^2}\langle f_s\rangle \\
&+ h_{v_\theta}^2\frac{\partial^2}{\partial v_\theta^2}\langle f_s\rangle + h_{v_z}^2\frac{\partial^2}{\partial v_z^2}\langle f_s\rangle\Bigg]_{i,j,k,l,m,n}\Bigg)
\end{aligned} \tag{3.317}$$

Note that the point value of the radius appears on the lefthand side since the cell volume integral $\langle f_s\rangle_{i,j,k,l,m,n}$ contains the Jacobian r. Instead of moving r_i to the righthand side, the

radius is left as a multiplier on the point value of the distribution function in anticipation of the reintegration step. The second derivative terms are defined in the usual way, such that

$$\left[\frac{\partial^2}{\partial r^2}\left\langle f_s\right\rangle\right]_{i,j,k,l,m,n} = \frac{1}{h_r^2}\left(\left\langle f_s\right\rangle_{i+1,j,k,l,m,n} - 2\left\langle f_s\right\rangle_{i,j,k,l,m,n} + \left\langle f_s\right\rangle_{i-1,j,k,l,m,n}\right) \tag{3.318}$$

$$\left[\frac{\partial^2}{\partial \theta^2}\left\langle f_s\right\rangle\right]_{i,j,k,l,m,n} = \frac{1}{h_\theta^2}\left(\left\langle f_s\right\rangle_{i,j+1,k,l,m,n} - 2\left\langle f_s\right\rangle_{i,j,k,l,m,n} + \left\langle f_s\right\rangle_{i,j-1,k,l,m,n}\right) \tag{3.319}$$

$$\vdots$$

$$\left[\frac{\partial^2}{\partial v_z^2}\left\langle f_s\right\rangle\right]_{i,j,k,l,m,n} = \frac{1}{h_{v_z}^2}\left(\left\langle f_s\right\rangle_{i,j,k,l,m,n+1} - 2\left\langle f_s\right\rangle_{i,j,k,l,m,n} + \left\langle f_s\right\rangle_{i,j,k,l,m,n-1}\right). \tag{3.320}$$

The reintegration step involves computing the local area-integrated values of $(v_r f_s)$, $(v_\theta f_s)$, and $(v_z f_s)$. These are computed to fourth-order accuracy using the Taylor series relation given in Eq. (3.30), such that

$$\begin{aligned}\left\langle v_r f_s\right\rangle_{i,j,k,l,m,n} = (v_r)_l r_i (f_s)_{i,j,k,l,m,n} h_\theta h_z h_{v_r} h_{v_\theta} h_{v_z} + \frac{1}{24 h_r}\Bigg[& h_\theta^2 \frac{\partial^2}{\partial \theta^2}\left(v_r\left\langle f_s\right\rangle\right) \\ & + h_z^2 \frac{\partial^2}{\partial z^2}\left(v_r\left\langle f_s\right\rangle\right) + h_{v_r}^2 \frac{\partial^2}{\partial v_r^2}\left(v_r\left\langle f_s\right\rangle\right) \\ & + h_{v_\theta}^2 \frac{\partial^2}{\partial v_\theta^2}\left(v_r\left\langle f_s\right\rangle\right) + h_{v_z}^2 \frac{\partial^2}{\partial v_z^2}\left(v_r\left\langle f_s\right\rangle\right)\Bigg]_{i,j,k,l,m,n}.\end{aligned} \tag{3.321}$$

$$\begin{aligned}\left\langle v_\theta f_s\right\rangle_{i,j,k,l,m,n} = (v_\theta)_m (f_s)_{i,j,k,l,m,n} h_r h_z h_{v_r} h_{v_\theta} h_{v_z} + \frac{1}{24 h_\theta}\Bigg[& h_r^2 \frac{\partial^2}{\partial r^2}\left(v_\theta \frac{\left\langle f_s\right\rangle}{r}\right) \\ & + h_z^2 \frac{\partial^2}{\partial z^2}\left(v_\theta \frac{\left\langle f_s\right\rangle}{r}\right) + h_{v_r}^2 \frac{\partial^2}{\partial v_r^2}\left(v_\theta \frac{\left\langle f_s\right\rangle}{r}\right) \\ & + h_{v_\theta}^2 \frac{\partial^2}{\partial v_\theta^2}\left(v_\theta \frac{\left\langle f_s\right\rangle}{r}\right) + h_{v_z}^2 \frac{\partial^2}{\partial v_z^2}\left(v_\theta \frac{\left\langle f_s\right\rangle}{r}\right)\Bigg]_{i,j,k,l,m,n}.\end{aligned} \tag{3.322}$$

$$\begin{aligned}\left\langle v_z f_s\right\rangle_{i,j,k,l,m,n} = (v_z)_n r_i (f_s)_{i,j,k,l,m,n} h_r h_\theta h_{v_r} h_{v_\theta} h_{v_z} + \frac{1}{24 h_z}\Bigg[& h_r^2 \frac{\partial^2}{\partial r^2}\left(v_z\left\langle f_s\right\rangle\right) \\ & + h_\theta^2 \frac{\partial^2}{\partial \theta^2}\left(v_z\left\langle f_s\right\rangle\right) + h_{v_r}^2 \frac{\partial^2}{\partial v_r^2}\left(v_z\left\langle f_s\right\rangle\right) \\ & + h_{v_\theta}^2 \frac{\partial^2}{\partial v_\theta^2}\left(v_z\left\langle f_s\right\rangle\right) + h_{v_z}^2 \frac{\partial^2}{\partial v_z^2}\left(v_z\left\langle f_s\right\rangle\right)\Bigg]_{i,j,k,l,m,n}.\end{aligned} \tag{3.323}$$

In Eq. (3.321), note that the integration is being performed over all directions except for r, since the current density in Ampere's law is integrated over a cell cross section. Likewise in Eq. (3.322) and Eq. (3.323) the local integration is being performed over five of the six phase space coordinate directions. Note also that the radius multiplier is left in place in Eq. (3.321) and Eq. (3.323) since the r-directed and z-directed cell cross sections depend on the radius. The second derivatives are computed using second-order accurate finite difference-stencils, much like in Cartesian coordinates (see Eqs. (3.111) – (3.115)). Note that the θ-directed current includes factors of radius in the second derivative expressions, which are evaluated as follows:

$$\left[\frac{\partial^2}{\partial r^2}\left(v_\theta \frac{\langle f\rangle_s}{r}\right)\right]_{i,j,k,l,m,n} = \frac{(v_\theta)_m}{h_r^2}\left(\frac{\langle f_s\rangle_{i+1,j,k,l,m,n}}{r_{i+1}} - 2\frac{\langle f_s\rangle_{i,j,k,l,m,n}}{r_i} + \frac{\langle f_s\rangle_{i-1,j,k,l,m,n}}{r_{i-1}}\right) \tag{3.324}$$

$$\left[\frac{\partial^2}{\partial z^2}\left(v_\theta \frac{\langle f\rangle_s}{r}\right)\right]_{i,j,k,l,m,n} = \frac{(v_\theta)_m}{h_z^2 r_i}\left(\langle f_s\rangle_{i,j,k+1,l,m,n} - 2\langle f_s\rangle_{i,j,k,l,m,n} + \langle f_s\rangle_{i,j,k-1,l,m,n}\right) \tag{3.325}$$

$$\left[\frac{\partial^2}{\partial v_r^2}\left(v_\theta \frac{\langle f\rangle_s}{r}\right)\right]_{i,j,k,l,m,n} = \frac{(v_\theta)_m}{h_{v_r}^2 r_i}\left(\langle f_s\rangle_{i,j,k,l+1,m,n} - 2\langle f_s\rangle_{i,j,k,l,m,n} + \langle f_s\rangle_{i,j,k,l-1,m,n}\right) \tag{3.326}$$

$$\left[\frac{\partial^2}{\partial v_\theta^2}\left(v_\theta \frac{\langle f\rangle_s}{r}\right)\right]_{i,j,k,l,m,n} = \frac{1}{h_{v_\theta}^2 r_i}\Big((v_\theta)_{m+1}\langle f_s\rangle_{i,j,k,l,m+1,n} - 2(v_\theta)_m\langle f_s\rangle_{i,j,k,l,m,n} + (v_\theta)_{m-1}\langle f_s\rangle_{i,j,k,l,m-1,n}\Big) \tag{3.327}$$

$$\left[\frac{\partial^2}{\partial v_z^2}\left(v_\theta \frac{\langle f\rangle_s}{r}\right)\right]_{i,j,k,l,m,n} = \frac{(v_\theta)_m}{h_{v_z}^2 r_i}\left(\langle f_s\rangle_{i,j,k,l,m,n+1} - 2\langle f_s\rangle_{i,j,k,l,m,n} + \langle f_s\rangle_{i,j,k,l,m,n-1}\right). \tag{3.328}$$

From the local values given by Eqs. (3.321) – (3.323) the species currents can be computed, such that

$$\langle J_{sr}\rangle_{i,j,k} = Z_s \sum_{l=0}^{N_{v_r}-1}\sum_{m=0}^{N_{v_\theta}-1}\sum_{n=0}^{N_{v_z}-1}\langle v_r f_s\rangle_{i,j,k,l,m,n} \tag{3.329}$$

$$\langle J_{s\theta}\rangle_{i,j,k} = Z_s \sum_{l=0}^{N_{v_r}-1}\sum_{m=0}^{N_{v_\theta}-1}\sum_{n=0}^{N_{v_z}-1}\langle v_\theta f_s\rangle_{i,j,k,l,m,n} \tag{3.330}$$

$$\langle J_{sz}\rangle_{i,j,k} = Z_s \sum_{l=0}^{N_{v_r}-1}\sum_{m=0}^{N_{v_\theta}-1}\sum_{n=0}^{N_{v_z}-1}\langle v_z f_s\rangle_{i,j,k,l,m,n} \tag{3.331}$$

The total current along each direction is obtained by summing $\langle J_{sr}\rangle, \langle J_{s\theta}\rangle$, and $\langle J_{sz}\rangle$ over species. Note that the currents are defined at cross sections through the center of the cell, as shown in Fig. 3.9.

3.9.3 Poisson solve for electrostatic field in one dimension

For an electrostatic system in cylindrical coordinates, solving for the electric field requires first solving for the potential. Starting from the weak form of Poisson's equation (see Eq. (2.97)), a discrete relation between the electrostatic potential and charge density is derived, and solved for ϕ. The procedure is analogous to that described in Section 3.5.6.4, with a few aspects that are specific to cylindrical coordinates. These aspects include the fact that the differential area along the radial direction depends on the radial coordinate r, and the fact that cell-integrated and face-integrated values have a more complicated relationship in cylindrical coordinates, which calls for the use of point-values when solving for ϕ. Note that the radial coordinate precludes any use of discrete Fourier transforms.

Consider a one-dimensional system in which the electric field is a function of radius. Let $\langle\rho\rangle_i$ be the cell-integrated charge density, i.e. the total charge in a cell. The weak form of Poisson's equation evaluated for a single cell states that

$$-\left(\left[\frac{d\phi}{dr}\right]_{i+\frac{1}{2}} r_{i+\frac{1}{2}} - \left[\frac{d\phi}{dr}\right]_{i-\frac{1}{2}} r_{i-\frac{1}{2}}\right) = \langle\rho\rangle_i \tag{3.332}$$

where the area of a cell face (see integrand in Eq. (2.97)) depends on the radius. Note the distinction between this expression and the expression for Cartesian coordinates (see Eq. (3.205)), in which the cell face area is arbitrary.

The point value of the derivative of the potential, $\left[\frac{d\phi}{dr}\right]_{i+\frac{1}{2}}$, can be evaluated at a cell face using a fourth-order accurate finite-difference stencil, which can be derived using Taylor series expansions. A fourth-order accurate stencil for the derivative is needed so that ϕ can be computed to fifth-order accuracy, and by extension the electric field can be computed to fourth-order accuracy. Let D^h denote a centered difference stencil that uses values that are a distance h apart, and let D^{3h} denote a centered difference stencil that uses values that are a distance $3h$ apart. Applying these discrete centered differences to the arbitrary function g at a point x_0 and expressing the result in terms of Taylor series expansions yields

$$D^h g = \frac{1}{h}\left[g\left(x_0+\frac{h}{2}\right) - g\left(x_0-\frac{h}{2}\right)\right] = g'(x_0) + \frac{1}{24}g'''(x_0)h^2 + \mathcal{O}(h^4) \tag{3.333}$$

$$D^{3h} g = \frac{1}{h}\left[g\left(x_0+\frac{3h}{2}\right) - g\left(x_0-\frac{3h}{2}\right)\right] = g'(x_0) + \frac{1}{24}g'''(x_0)h^2 + \mathcal{O}(h^4). \tag{3.334}$$

The stencils D^h and D^{3h} are second-order accurate, but they can be linearly combined to derive a fourth-order stencil for $g'(x_0)$, such that

$$c_1 D^h + c_2 D^{3h} = g'(x_0) + \mathcal{O}(h^4), \tag{3.335}$$

where c_1 and c_2 are unknown constant coefficients. Setting up a linear system using Eqs. (3.333) –

(3.335) and solving for c_1 and c_2 yields

$$\begin{bmatrix} 1 & 1 \\ 1/24 & 3/8 \end{bmatrix} \begin{bmatrix} c_1 \\ c_2 \end{bmatrix} = \begin{bmatrix} 1 \\ 0 \end{bmatrix} \tag{3.336}$$

$$\begin{bmatrix} c_1 \\ c_2 \end{bmatrix} = \begin{bmatrix} 1 & 1 \\ 1/24 & 3/8 \end{bmatrix}^{-1} \begin{bmatrix} 1 \\ 0 \end{bmatrix} = \begin{bmatrix} 9/8 \\ -1/8 \end{bmatrix}. \tag{3.337}$$

Thus the stencil for a first derivative at a cell face using cell-centered values is

$$g'_{i+\frac{1}{2}} = \frac{9}{8h}\left(g_{i+1} - g_i\right) - \frac{1}{24h}\left(g_{i+2} - g_{i-1}\right). \tag{3.338}$$

Using the stencil in Eq. (3.338) to evaluate the derivative terms in Eq. (3.332) yields the following relation between the discrete volume-integrated charge density and the cell-centered values of the electrostatic potential

$$\langle\rho\rangle_i = -\frac{1}{h_r}\Bigg(\left[\frac{9}{8}\left(\phi_{i+1} - \phi_i\right) - \frac{1}{24}\left(\phi_{i+2} - \phi_{i-1}\right)\right] r_{i+\frac{1}{2}} - \left[\frac{9}{8}\left(\phi_i - \phi_{i-1}\right) - \frac{1}{24}\left(\phi_{i+1} - \phi_{i-2}\right)\right] r_{i-\frac{1}{2}} \Bigg) \tag{3.339}$$

$$\langle\rho\rangle_i = -\frac{1}{h_r}\Bigg(-\frac{1}{24} r_{i-\frac{1}{2}}\phi_{i-2} + \left(\frac{9}{8} r_{i-\frac{1}{2}} + \frac{1}{24} r_{i+\frac{1}{2}}\right)\phi_{i-1} - \left(\frac{9}{8} r_{i-\frac{1}{2}} + \frac{9}{8} r_{i+\frac{1}{2}}\right)\phi_i + \left(\frac{1}{24} r_{i-\frac{1}{2}} + \frac{9}{8} r_{i+\frac{1}{2}}\right)\phi_{i+1} - \frac{1}{24} r_{i+\frac{1}{2}}\phi_{i+2} \Bigg), \tag{3.340}$$

where Eq. (3.340) is an expanded version of Eq. (3.339). Using the local relation given by Eq. (3.340) for each cell in the domain, a global linear system of equations is constructed and solved (see Section 3.5.6.4). Note that the stencils for cells near boundaries must be modified to be one-sided. To derive one-sided stencils fifth-order accurate polynomial reconstructions of the cell-centered point values of the electrostatic potential are used. Fifth-order accuracy is needed since the sought after solution for the electric field needs to be fourth-order accurate everywhere in the domain, including at boundaries. From point values of the electrostatic potential, the point values of the electric field can be derived using a fifth-order polynomial reconstruction of ϕ, which can either be centered,

$$(E_r)_i = -\frac{1}{12h_r}\left(\phi_{i-2} - 8\phi_{i-1} + 8\phi_{i+1} - \phi_{i+2}\right), \tag{3.341}$$

or one-sided for cells near boundaries. The use of point values both for the potential and electric field circumvents the need to include the r Jacobian of integration in polynomial

reconstructions. A volume-integrated or area-integrated electric field can also be derived from point values of the electrostatic potential. Whether an integrated value or a point value of the field is sought is largely determined by the quadrature rule used to evaluate the fluxes in the Vlasov equation. For cylindrical coordinate calculations, the point value of the field is more useful because the Vlasov equation flux calculations rely on the quadrature rule in Eq. (3.30). For Cartesian coordinates, either the point value of the field in conjunction with the quadrature rule in Eq. (3.30) or the volume-integrated value of the field in conjunction with the quadrature rule in Eq. (3.31) can be used.

3.9.4 Boundary conditions for electromagnetic fields

3.9.4.1 Conducting wall field boundary conditions

For all of the cylindrical coordinate simulations carried out here the domain along the radial direction, with $r \in [0, r_{\max}]$ is assumed to have a perfectly conducting wall at $r = r_{\max}$. The fields at $r_{\max}$ are thus subject to the constraints given by Eqs. (2.100) – (2.102), such that

$$E_\theta|_{r=r_{\max}} = 0 \tag{3.342}$$

$$E_z|_{r=r_{\max}} = 0 \tag{3.343}$$

$$B_r|_{r=r_{\max}} = 0 \tag{3.344}$$

$$\left[\frac{1}{r}\frac{\partial}{\partial r}\left(rB_\theta\right) - \frac{1}{r}\frac{\partial B_r}{\partial \theta} - J_z\right]_{r=r_{\max}} = 0 \tag{3.345}$$

$$\left[\frac{\partial B_r}{\partial z} - \frac{\partial B_z}{\partial r} - J_\theta\right]_{r=r_{\max}} = 0. \tag{3.346}$$

Since Eq. (3.344) specifies the value of B_r, then Eq. (3.345) is simply a condition on B_θ with $\partial B_r/\partial\theta = 0$, and Eq. (3.346) is a condition on B_z with $\partial B_r/\partial z = 0$. In addition to these conducting wall boundary conditions, for a bounded system Gauss's law in Eq. (2.122) stipulates that

$$\left[E_r\right]_{r=r_{\max}} = 0. \tag{3.347}$$

Much like in the case of Cartesian coordinates, not all of the boundary conditions given by Eqs. (3.342) – (3.347) are necessary because not all of them are needed to perform the one-dimensional interpolations. Note that in the context of cylindrical coordinates, an explicit choice is made to implement boundary condition only in the interpolation step, and not the quadrature evaluation portion of the discretization. As a consequence, the boundary condition for B_r given by Eq. (3.344) is never used explicitly since for the purposes of line-integral calculations the r-component of the magnetic field need never be evaluated at the $x = r_{\max}$ boundary. Likewise, the condition given by Eq. (3.347) is never used in the interpolation stage of the discretization since E_r need never be evaluated at r-directed cell

faces. Thus for the chosen means of discretization, the necessary boundary conditions for the electromagnetic fields in cylindrical coordinates are

$$E_\theta|_{r=r_{\max}} = 0 \tag{3.348}$$

$$E_z|_{r=r_{\max}} = 0 \tag{3.349}$$

$$\left[\frac{1}{r}\frac{\partial}{\partial r}\left(rB_\theta\right) - J_z\right]_{r=r_{\max}} = 0 \tag{3.350}$$

$$\left[-\frac{\partial B_z}{\partial r} - J_\theta\right]_{r=r_{\max}} = 0. \tag{3.351}$$

In the one-dimensional interpolation portion of the algorithm, these boundary conditions are implemented through the use of one-sided fourth-order accurate polynomial reconstructions at $r = r_{\max}$ and $r = (r_{\max} - h_r)$. These amount to third-degree polynomial fits that use area-integrated values of the fields in three cells and a constraint given by one of the expressions in Eqs. (3.348) – (3.351). The resulting interpolated face values of the electric field components to fourth-order accuracy are

$$\lfloor E_\theta \rfloor|_{r_{\max}} = 0 \tag{3.352}$$

$$\lfloor E_\theta \rfloor|_{(r_{\max}-h_r)} = \frac{1}{18h_r}\left(-\lfloor E_\theta \rfloor_{N_r-3} + 8\langle E_\theta \rangle_{N_r-2} + 17\lfloor E_\theta \rfloor_{N_r-1}\right) \tag{3.353}$$

$$\lfloor E_z \rfloor|_{r_{\max}} = 0 \tag{3.354}$$

$$\begin{aligned}\lfloor E_z \rfloor|_{(r_{\max}-h_r)} = \frac{1}{18h_r^2(-12+33\ell-24\ell^2+5\ell^3)}\Big(& \\ (\ -4+\ 11\ell-\ 5\ell^2)\lfloor E_z \rfloor_{N_r-3} & \\ +(\ 50-\ 124\ell+\ 40\ell^2)\lfloor E_z \rfloor_{N_r-2} & \\ +(\ 374-\ 367\ell+\ 85\ell^2)\lfloor E_z \rfloor_{N_r-1}\Big), &\end{aligned} \tag{3.355}$$

where $\ell = (r_{\max} - h_r)/h_r$, $\lfloor E_\theta \rfloor$ is defined in Eq. (3.285), $\lfloor E_z \rfloor$ is defined in Eq. (3.286), and cells in domain $r \in [0, r_{\max}]$ are indexed by $i = \{0, 1, \cdots, N_r - 1\}$. The fourth-order accurate interpolated face values of the magnetic field components are

$$\begin{aligned}\lfloor B_\theta \rfloor|_{r_{\max}} = \frac{r_{\max}}{6h_r(5h_r - 7r_{\max})}\Big(& -17\lfloor B_\theta \rfloor_{N_r-3} + 67\lfloor B_\theta \rfloor_{N_r-2} \\ & - 92\lfloor B_\theta \rfloor_{N_r-1} + 30h_r^2 J_z(r_{\max})\Big)\end{aligned} \tag{3.356}$$

$$\begin{aligned}\lfloor B_\theta \rfloor|_{(r_{\max}-h_r)} = \frac{r_{\max}}{30h_r(5h_r - 7r_{\max})}\Big(& -197\lfloor B_\theta \rfloor_{N_r-3} + 712\lfloor B_\theta \rfloor_{N_r-2} - 827\lfloor B_\theta \rfloor_{N_r-1} \\ & + 7r_{\max}\big(2\lfloor B_\theta \rfloor_{N_r-3} + 5\lfloor B_\theta \rfloor_{N_r-2} - 37\lfloor B_\theta \rfloor_{N_r-1} + 66h_r^2 J_z(r_{\max})\big)\Big)\end{aligned} \tag{3.357}$$

$$\lfloor B_z \rfloor|_{r_{\max}} = \frac{1}{6h_r^2(99+327\ell-255\ell^2+55\ell^3)}\Big((24-48\ell+20\ell^2)\lfloor B_z \rfloor_{N_r-3} + (-219+384\ell-115\ell^2)\lfloor B_z \rfloor_{N_r-2} + (1725-1776\ell+425\ell^2)\lfloor B_z \rfloor_{N_r-1} + (216-594\ell+432\ell^2-90\ell^3)h_r^3 J_\theta(r_{\max})\Big) \quad (3.358)$$

$$\lfloor B_z \rfloor|_{(r_{\max}-h_r)} = \frac{1}{6h_r^2(99+327\ell-255\ell^2+55\ell^3)}\Big((-15+52\ell-25\ell^2)\lfloor B_z \rfloor_{N_r-3} + (174-551\ell+185\ell^2)\lfloor B_z \rfloor_{N_r-2} + (741-731\ell+170\ell^2)\lfloor B_z \rfloor_{N_r-1} + (-36+168\ell-138\ell^2+30\ell^3)h_r^3 J_\theta(r_{\max})\Big), \quad (3.359)$$

where $\lfloor B_\theta \rfloor$ is defined in Eq. (3.288), and $\lfloor B_z \rfloor$ is defined in Eq. (3.289). Note that ℓ is an integer index value that specifies the number of h_r distances away from the axis. Thus in Eq. (3.358) $\ell = r_{\max}/h_r$ and in Eq. (3.359) $\ell = (r_{\max}-h_r)/h_r$. Note that the current J_θ and J_z must be computed from the distribution function at the $r = r_{\max}$ domain boundary.

3.9.4.2 Axis boundary conditions for fields

For an axisymmetric system, the analytic expressions for the axis boundary conditions for the electromagnetic fields are given by Eqs. (2.116) – (2.121). These boundary conditions are implemented in the one-dimensional interpolation stage of the discretization method. The one-dimensional interpolation is modified to use a one-sided polynomial reconstruction of the primary area-integrated field variables. One-sided reconstructions are used instead of ghost cells so as to match the approach used for boundary conditions for the Vlasov equation. Moreover, ghost cell values can be ambiguous for variables that involve the Jacobian r (e.g. see definitions of $\lfloor E_z \rfloor$ and $\lfloor B_z \rfloor$ in Eqs. (3.286) and (3.289)) since the reconstruction stencil for these variables depends on the distance from the axis. The electric field components evaluated at $r = 0$ and $r = h_r$ to fourth-order accuracy are

$$\lfloor E_\theta \rfloor|_0 = 0 \quad (3.360)$$

$$\lfloor E_\theta \rfloor|_{h_r} = \frac{1}{18h_r}\left(-197\lfloor E_\theta \rfloor_0 + 82\lfloor E_\theta \rfloor_1 - 17\lfloor E_\theta \rfloor_2\right) \quad (3.361)$$

$$\lfloor E_z \rfloor|_0 = \frac{1}{198h_r^2}\left(575\lfloor E_z \rfloor_0 - 73\lfloor E_z \rfloor_1 + 8\lfloor E_z \rfloor_2\right) \quad (3.362)$$

$$\lfloor E_z \rfloor|_{h_r} = \frac{1}{198h_r^2}\left(247\lfloor E_z \rfloor_0 + 58\lfloor E_z \rfloor_1 - 5\lfloor E_z \rfloor_2\right) \quad (3.363)$$

and likewise the magnetic field components to fourth-order accuracy are

$$\lfloor B_\theta \rfloor|_{r=0} = 0 \tag{3.364}$$

$$\lfloor B_\theta \rfloor|_{r=h_r} = \frac{1}{18h_r}\left(-197\lfloor B_\theta \rfloor_0 + 82\lfloor B_\theta \rfloor_1 - 17\lfloor B_\theta \rfloor_2\right) \tag{3.365}$$

$$\lfloor B_z \rfloor|_{r=0} = \frac{1}{198h_r^2}\left(575\lfloor B_z \rfloor_0 - 73\lfloor B_z \rfloor_1 + 8\lfloor B_z \rfloor_2\right) \tag{3.366}$$

$$\lfloor B_z \rfloor|_{r=h_r} = \frac{1}{198h_r^2}\left(247\lfloor B_z \rfloor_0 + 58\lfloor B_z \rfloor_1 - 5\lfloor B_z \rfloor_2\right), \tag{3.367}$$

where the area-integrated fields are defined in Eqs. (3.284) – (3.289). Note that the boundary conditions $E_r(0) = B_r(0) = 0$ is not used since it is not needed in the evaluation of the line integrals in Maxwell's equations. Note that the interpolation stencils for the electric field and the magnetic field are identical since the symmetry conditions at the axis (see discussion in Section 2.5.2.2) are the same.

3.10 Cylindrical coordinates: fourth-order accurate diagnostics

Section 3.6 describes the fourth-order accurate calculation of diagnostic for Vlasov-Maxwell simulations in Cartesian coordinates. In cylindrical coordinates the same diagnostics are needed. In cylindrical coordinates the way in which density, charge density, and mass is computed is identical to the procedure described in Section 3.6.1. The calculation of momentum and energy, however, are slightly different on account of quadratures needing to account for cell volumes depending on the coordinate r. Thus the discussion of diagnostics here is restricted to momentum and energy, and the associated quadrature rules.

3.10.1 Momentum

Much like the calculation of current (see Section 3.9.2), calculating the momentum of a given species along a given direction requires taking the first velocity moment of the distribution function. Here the momentum is computed to fourth-order accuracy as volume-integrated quantity. To ensure fourth-order accuracy, the following steps are used to compute the species momentum:

1. The point value of the distribution function is computed at the center of a cell. See Eq. (3.317).

2. The local cell-volume-integrated product vf is computed to fourth-order accuracy using point values and the quadrature rule given by Eq. (3.30). Note that the quadrature rule in Eq. (3.30) is for area integrals, not volume integrals, but the extension to volume integrals is straightforward.

3. The local (in phase space) fourth-order accurate product $\langle vf \rangle_{i,j,k,l,m,n}$ is summed over velocity direction l, m, n to compute momentum.

For cylindrical coordinates, the local products of the velocity coordinate and the distribution function to fourth-order accuracy are

$$\langle v_r f_s \rangle_{i,j,k,l,m,n} = (v_r)_l r_i (f_s)_{i,j,k,l,m,n} h_r h_\theta h_z h_{v_r} h_{v_\theta} h_{v_z} + \frac{1}{24} \Bigg[h_r^2 \frac{\partial^2}{\partial r^2} (v_r \langle f_s \rangle) + h_\theta^2 \frac{\partial^2}{\partial \theta^2} (v_r \langle f_s \rangle) + h_z^2 \frac{\partial^2}{\partial z^2} (v_r \langle f_s \rangle) + h_{v_r}^2 \frac{\partial^2}{\partial v_r^2} (v_r \langle f_s \rangle) + h_{v_\theta}^2 \frac{\partial^2}{\partial v_\theta^2} (v_r \langle f_s \rangle) + h_{v_z}^2 \frac{\partial^2}{\partial v_z^2} (v_r \langle f_s \rangle) \Bigg]_{i,j,k,l,m,n} \tag{3.368}$$

$$\langle v_\theta f_s \rangle_{i,j,k,l,m,n} = (v_\theta)_m r_i (f_s)_{i,j,k,l,m,n} h_r h_\theta h_z h_{v_r} h_{v_\theta} h_{v_z} + \frac{1}{24} \Bigg[h_r^2 \frac{\partial^2}{\partial r^2} (v_\theta \langle f_s \rangle) + h_\theta^2 \frac{\partial^2}{\partial \theta^2} (v_\theta \langle f_s \rangle) + h_z^2 \frac{\partial^2}{\partial z^2} (v_\theta \langle f_s \rangle) + h_{v_r}^2 \frac{\partial^2}{\partial v_r^2} (v_\theta \langle f_s \rangle) + h_{v_\theta}^2 \frac{\partial^2}{\partial v_\theta^2} (v_\theta \langle f_s \rangle) + h_{v_z}^2 \frac{\partial^2}{\partial v_z^2} (v_\theta \langle f_s \rangle) \Bigg]_{i,j,k,l,m,n} \tag{3.369}$$

$$\langle v_z f_s \rangle_{i,j,k,l,m,n} = (v_z)_n r_i (f_s)_{i,j,k,l,m,n} h_r h_\theta h_z h_{v_r} h_{v_\theta} h_{v_z} + \frac{1}{24} \Bigg[h_r^2 \frac{\partial^2}{\partial r^2} (v_z \langle f_s \rangle) + h_\theta^2 \frac{\partial^2}{\partial \theta^2} (v_z \langle f_s \rangle) + h_z^2 \frac{\partial^2}{\partial z^2} (v_z \langle f_s \rangle) + h_{v_r}^2 \frac{\partial^2}{\partial v_r^2} (v_z \langle f_s \rangle) + h_{v_\theta}^2 \frac{\partial^2}{\partial v_\theta^2} (v_z \langle f_s \rangle) + h_{v_z}^2 \frac{\partial^2}{\partial v_z^2} (v_z \langle f_s \rangle) \Bigg]_{i,j,k,l,m,n} . \tag{3.370}$$

The associated discrete fourth-order accurate cell-volume-integrated momentum in cylindrical coordinates along each direction is

$$\langle p_{sr} \rangle_{i,j,k} = \sum_{l=0}^{N_{v_r}-1} \sum_{m=0}^{N_{v_\theta}-1} \sum_{n=0}^{N_{v_z}-1} \langle v_r f_s \rangle_{i,j,k,l,m,n} \tag{3.371}$$

$$\langle p_{s\theta} \rangle_{i,j,k} = \sum_{l=0}^{N_{v_r}-1} \sum_{m=0}^{N_{v_\theta}-1} \sum_{n=0}^{N_{v_z}-1} \langle v_\theta f_s \rangle_{i,j,k,l,m,n} \tag{3.372}$$

$$\langle p_{sz} \rangle_{i,j,k} = \sum_{l=0}^{N_{v_r}-1} \sum_{m=0}^{N_{v_\theta}-1} \sum_{n=0}^{N_{v_z}-1} \langle v_z f_s \rangle_{i,j,k,l,m,n} . \tag{3.373}$$

Summing over species s yields the discrete value of the total momentum in a given direction.

3.10.2 Energy

The procedure for computing momentum, as described above, can be used for computing the kinetic energy of the distribution function. First the distribution function is deconvolved to obtain a point value at the center of a phase space cell, then the local cell-volume-integrated product $\langle v^2 f \rangle$ is computed to fourth-order accuracy for each velocity component using the quadrature rule in Eq. (3.30). The local fourth-order accurate product is subsequently summed over velocity directions to obtain a value of kinetic energy associated with a given velocity direction.

For cylindrical coordinates the local products of the square of the velocity and the distribution function are

$$\begin{aligned}\left\langle v_r^2 f_s \right\rangle_{i,j,k,l,m,n} = (v_r)_l^2 r_i (f_s)_{i,j,k,l,m,n} h_r h_\theta h_z h_{v_r} h_{v_\theta} h_{v_z} + \frac{1}{24}\Bigg[& h_r^2 \frac{\partial^2}{\partial r^2}\left(v_r^2 \langle f_s \rangle\right) \\ & + h_\theta^2 \frac{\partial^2}{\partial \theta^2}\left(v_r \langle f_s \rangle\right) + h_z^2 \frac{\partial^2}{\partial z^2}\left(v_r^2 \langle f_s \rangle\right) + h_{v_r}^2 \frac{\partial^2}{\partial v_r^2}\left(v_r^2 \langle f_s \rangle\right) \\ & + h_{v_\theta}^2 \frac{\partial^2}{\partial v_\theta^2}\left(v_r^2 \langle f_s \rangle\right) + h_{v_z}^2 \frac{\partial^2}{\partial v_z^2}\left(v_r^2 \langle f_s \rangle\right) \Bigg]_{i,j,k,l,m,n}\end{aligned} \tag{3.374}$$

$$\begin{aligned}\left\langle v_\theta^2 f_s \right\rangle_{i,j,k,l,m,n} = (v_\theta)_m^2 r_i (f_s)_{i,j,k,l,m,n} h_r h_\theta h_z h_{v_r} h_{v_\theta} h_{v_z} + \frac{1}{24}\Bigg[& h_r^2 \frac{\partial^2}{\partial r^2}\left(v_\theta^2 \langle f_s \rangle\right) \\ & + h_\theta^2 \frac{\partial^2}{\partial \theta^2}\left(v_\theta^2 \langle f_s \rangle\right) + h_z^2 \frac{\partial^2}{\partial z^2}\left(v_\theta^2 \langle f_s \rangle\right) + h_{v_r}^2 \frac{\partial^2}{\partial v_r^2}\left(v_\theta^2 \langle f_s \rangle\right) \\ & + h_{v_\theta}^2 \frac{\partial^2}{\partial v_\theta^2}\left(v_\theta^2 \langle f_s \rangle\right) + h_{v_z}^2 \frac{\partial^2}{\partial v_z^2}\left(v_\theta^2 \langle f_s \rangle\right) \Bigg]_{i,j,k,l,m,n}\end{aligned} \tag{3.375}$$

$$\begin{aligned}\left\langle v_z^2 f_s \right\rangle_{i,j,k,l,m,n} = (v_z)_n r_i (f_s)_{i,j,k,l,m,n} h_r h_\theta h_z h_{v_r} h_{v_\theta} h_{v_z} + \frac{1}{24}\Bigg[& h_r^2 \frac{\partial^2}{\partial r^2}\left(v_z^2 \langle f_s \rangle\right) \\ & + h_\theta^2 \frac{\partial^2}{\partial \theta^2}\left(v_z^2 \langle f_s \rangle\right) + h_z^2 \frac{\partial^2}{\partial z^2}\left(v_z^2 \langle f_s \rangle\right) + h_{v_r}^2 \frac{\partial^2}{\partial v_r^2}\left(v_z^2 \langle f_s \rangle\right) \\ & + h_{v_\theta}^2 \frac{\partial^2}{\partial v_\theta^2}\left(v_z^2 \langle f_s \rangle\right) + h_{v_z}^2 \frac{\partial^2}{\partial v_z^2}\left(v_z^2 \langle f_s \rangle\right) \Bigg]_{i,j,k,l,m,n}\end{aligned}, \tag{3.376}$$

and the net kinetic energy for a species s in a physical volume in cylindrical coordinates is

$$\langle W_s \rangle_{i,j,k} = \frac{1}{2} \sum_{l=0}^{N_{v_r}-1} \sum_{m=0}^{N_{v_\theta}-1} \sum_{n=0}^{N_{v_z}-1} \left(\left\langle v_r^2 f_s \right\rangle_{i,j,k,l,m,n} + \left\langle v_\theta^2 f_s \right\rangle_{i,j,k,l,m,n} + \left\langle v_z^2 f_s \right\rangle_{i,j,k,l,m,n} \right). \quad (3.377)$$

The calculation of field energy in cylindrical coordinates requires more care on account of factors of radius that are associated with certain field directions and not others. See Section 3.9.1 for the definitions of the area-integrated fields for cylindrical coordinates. The fourth-order accurate point values of the magnetic field components in cylindrical coordinates are

$$(B_r)_{i,j,k} = \frac{1}{h_\theta h_z} \left(\lfloor B_r \rfloor_{i_0,j,k} - \frac{1}{24} \left[h_\theta^2 \frac{\partial^2}{\partial \theta^2} \lfloor B_r \rfloor + h_z^2 \frac{\partial^2}{\partial z^2} \lfloor B_r \rfloor \right]_{i_0,j,k} \right) \quad (3.378)$$

$$(B_\theta)_{i,j,k} = \frac{1}{h_r h_z} \left(\lfloor B_\theta \rfloor_{i,j_0,k} - \frac{1}{24} \left(h_r^2 \frac{\partial^2}{\partial r^2} \lfloor B_\theta \rfloor + h_z^2 \frac{\partial^2}{\partial z^2} \lfloor B_\theta \rfloor \right]_{i,j_0,k} \right) \quad (3.379)$$

$$(B_z)_{i,j,k} = \frac{1}{r_i h_r h_\theta} \left(\lfloor B_z \rfloor_{i,j,k_0} - \frac{1}{24} \left(h_r^2 \frac{\partial^2}{\partial r^2} \lfloor B_z \rfloor + h_\theta^2 \frac{\partial^2}{\partial \theta^2} \lfloor B_z \rfloor \right]_{i,j,k_0} \right). \quad (3.380)$$

Note that h_θ is assumed to have units of radians, not length. The cell-volume integrated fourth-order accurate squared values of each component of the magnetic field in cylindrical coordinates are

$$\left\langle B_r^2 \right\rangle_{i_0,j,k} = (B_r)_{i,j,k} r_i h_r h_\theta h_z + \frac{h_r r_i}{24 h_\theta h_z} \left[h_r^2 \frac{\partial^2}{\partial r^2} \lfloor B_r \rfloor^2 + h_\theta^2 \frac{\partial^2}{\partial \theta^2} \lfloor B_r \rfloor^2 + h_z^2 \frac{\partial^2}{\partial z^2} \lfloor B_r \rfloor^2 \right]_{i_0,j,k} \quad (3.381)$$

$$\left\langle B_\theta^2 \right\rangle_{i,j_0,k} = (B_\theta)_{i,j,k} r_i h_r h_\theta h_z + \frac{h_\theta r_i}{24 h_r h_z} \left[h_r^2 \frac{\partial^2}{\partial r^2} \lfloor B_\theta \rfloor^2 + h_\theta^2 \frac{\partial^2}{\partial \theta^2} \lfloor B_\theta \rfloor^2 + h_z^2 \frac{\partial^2}{\partial z^2} \lfloor B_\theta \rfloor^2 \right]_{i,j_0,k} \quad (3.382)$$

$$\left\langle B_z^2 \right\rangle_{i,j,k_0} = (B_z)_{i,j,k} r_i h_r h_\theta h_z + \frac{h_z}{24 r_i h_r h_z} \left[h_r^2 \frac{\partial^2}{\partial r^2} \lfloor B_z \rfloor^2 + h_\theta^2 \frac{\partial^2}{\partial \theta^2} \lfloor B_z \rfloor^2 + h_z^2 \frac{\partial^2}{\partial z^2} \lfloor B_z \rfloor^2 \right]_{i,j,k_0} \quad (3.383)$$

The electric field terms contributing the field energy can be computed in the same way. Thus the total fourth-order accurate volume-integrated field energy in cylindrical coordinates is the sum of all contributing field components:

$$\langle U \rangle_{i,j,k} = \frac{1}{2} \left(\left\langle B_r^2 \right\rangle_{i,j,k} + \left\langle B_\theta^2 \right\rangle_{i,j,k} + \left\langle B_z^2 \right\rangle_{i,j,k} + \left\langle E_r^2 \right\rangle_{i,j,k} + \left\langle E_\theta^2 \right\rangle_{i,j,k} + \left\langle E_z^2 \right\rangle_{i,j,k} \right). \quad (3.384)$$

The same quadrature rule used throughout the discretization, is thus applied to compute energy to fourth-order accuracy in cylindrical phase space coordinates.

3.11 Cylindrical coordinates: algorithm outline

Recall that the Vlasov-Maxwell system of equations can be expressed in the form

$$\frac{\partial \boldsymbol{q}}{\partial t} = \boldsymbol{L}\boldsymbol{q} + \boldsymbol{Y}. \tag{3.385}$$

The finite-volume discretization allows the righthand side to be evaluated in terms of arithmetic operations. In cylindrical coordinates the primary variable, source, and flux terms for the Vlasov-Maxwell equation system are

$$\boldsymbol{q} = \begin{bmatrix} \langle f_s \rangle_{i,j,k,l,m,n} \\ \lfloor E_r \rfloor_{i_0,j,k} \\ \lfloor E_\theta \rfloor_{i,j_0,k} \\ \lfloor E_z \rfloor_{i,j,k_0} \\ \lfloor B_r \rfloor_{i_0,j,k} \\ \lfloor B_\theta \rfloor_{i,j_0,k} \\ \lfloor B_z \rfloor_{i,j,k_0} \end{bmatrix}, \qquad \boldsymbol{Y} = \begin{bmatrix} 0 \\ -\lfloor J_r \rfloor_{i_0,j,k} \\ -\lfloor J_\theta \rfloor_{i,j_0,k} \\ -\lfloor J_z \rfloor_{i,j,k_0} \\ 0 \\ 0 \\ 0 \end{bmatrix}, \tag{3.386}$$

$$\boldsymbol{L}\boldsymbol{q} = \begin{bmatrix} L(F_r) + L(F_\theta) + L(F_z) + L(F_{v_r}) + L(F_{v_\theta}) + L(F_{v_z}) \\ \frac{\omega_{cp}}{\omega_{pp}} \left(-\lfloor B_\theta \rfloor \Big|_{i_0,j,k-\frac{1}{2}}^{i_0,j,k+\frac{1}{2}} + \lfloor B_z \rfloor \Big|_{i_0,j-\frac{1}{2},k}^{i_0,j+\frac{1}{2},k} \right) \\ \frac{\omega_{cp}}{\omega_{pp}} \left(\lfloor B_r \rfloor \Big|_{i,j_0,k-\frac{1}{2}}^{i,j_0,k+\frac{1}{2}} - \lfloor B_z \rfloor \Big|_{i-\frac{1}{2},j_0,k}^{i+\frac{1}{2},j_0,k} \right) \\ \frac{\omega_{cp}}{\omega_{pp}} \left(-\lfloor B_r \rfloor \Big|_{i,j-\frac{1}{2},k_0}^{i,j+\frac{1}{2},k_0} + \lfloor B_\theta \rfloor \Big|_{i-\frac{1}{2},j,k_0}^{i+\frac{1}{2},j,k_0} \right) \\ \frac{\omega_{pp}}{\omega_{cp}} \left(\lfloor E_r \rfloor \Big|_{i_0,j,k-\frac{1}{2}}^{i_0,j,k+\frac{1}{2}} - \lfloor E_z \rfloor \Big|_{i_0,j-\frac{1}{2},k}^{i_0,j+\frac{1}{2},k} \right) \\ \frac{\omega_{pp}}{\omega_{cp}} \left(-\lfloor E_r \rfloor \Big|_{i,j_0,k-\frac{1}{2}}^{i,j_0,k+\frac{1}{2}} + \lfloor E_z \rfloor \Big|_{i-\frac{1}{2},j_0,k}^{i+\frac{1}{2},j_0,k} \right) \\ \frac{\omega_{pp}}{\omega_{cp}} \left(\lfloor E_r \rfloor \Big|_{i,j-\frac{1}{2},k_0}^{i,j+\frac{1}{2},k_0} - \lfloor E_\theta \rfloor \Big|_{i-\frac{1}{2},j,k_0}^{i+\frac{1}{2},j,k_0} \right) \end{bmatrix}. \tag{3.387}$$

In cylindrical coordinates the flux terms associated with the distribution function are

$$L(F_r) = -\left\langle v_r f_s \right\rangle \Big|_{i-\frac{1}{2},j,k,l,m,n}^{i+\frac{1}{2},j,k,l,m,n} \tag{3.388}$$

$$L(F_\theta) = -\left\langle v_\theta f_s \right\rangle \Big|_{i,j-\frac{1}{2},k,l,m,n}^{i,j+\frac{1}{2},k,l,m,n} \tag{3.389}$$

$$L(F_z) = -\left\langle v_z f_s \right\rangle \Big|_{i,j,k-\frac{1}{2},l,m,n}^{i,j,k+\frac{1}{2},l,m,n} \tag{3.390}$$

$$L(F_{v_r}) = -\left\langle \frac{Z_s}{M_s}\left\{E_r + \frac{\omega_{cp}}{\omega_{pp}}\left[v_\theta B_z - v_z B_\theta\right]\right\} f_s + \frac{v_\theta^2}{r} f_s \right\rangle \Big|_{i,j,k,l-\frac{1}{2},m,n}^{i,j,k,l+\frac{1}{2},m,n} \tag{3.391}$$

$$L(F_{v_\theta}) = -\left\langle \frac{Z_s}{M_s}\left\{E_\theta + \frac{\omega_{cp}}{\omega_{pp}}\left[v_z B_r - v_r B_z\right]\right\} f_s - \frac{v_r v_\theta}{r} f_s \right\rangle \Big|_{i,j,k,l,m-\frac{1}{2},n}^{i,j,k,l,m+\frac{1}{2},n} \tag{3.392}$$

$$L(F_{v_z}) = -\left\langle \frac{Z_s}{M_s}\left\{E_z + \frac{\omega_{cp}}{\omega_{pp}}\left[v_r B_\theta - v_\theta B_r\right]\right\} f_s \right\rangle \Big|_{i,j,k,l,m,n-\frac{1}{2}}^{i,j,k,l,m,n+\frac{1}{2}} \tag{3.393}$$

Note that in cylindrical coordinates all of the integrals denoted by $\langle\cdot\rangle$ and some of the integrals denoted by $\lfloor\cdot\rfloor$ involve the Jacobian r. Note also that there can be multiple distribution functions, one for each species s. While the equation system has been written out for a full six-dimensional distribution function with three-dimensional fields, in practice, depending on the problem of interest and computational cost considerations, not all of the flux terms are included. For example, if B_z is known to be zero for all time, then the terms in $L(F_{v_r})$, and $L(F_{v_\theta})$ associated with this component of the magnetic field are set to zero. Likewise, if only one-dimensional dynamics along the radial direction are of interest, then $L(F_\theta) = L(F_z) = 0$. For phase space simulations it is important that there are at least as many velocity dimensions as physical space dimensions. And for cylindrical coordinates, in particular, it is important to model both the v_r and v_θ directions (and thereby include the fluxes $F(v_r)$ and $F(v_\theta)$) whenever radial dynamics are of interest.

The outline of the cylindrical coordinate Vlasov-Maxwell algorithm for solving the system of equations in Eq. (3.385) is as follows. First the primary variables are initialized to fourth-order accuracy, using either analytic definite integrals or quadrature rules. The distribution function is initialized as a fourth-order volume-integrated value in each phase space cell, and the electromagnetic fields are initialized as fourth-order area integrals through the mid-planes of each cell in physical space. For each time step the algorithm for advancing the primary variables performs the following steps.

1. For each stage in RK4

    a) Compute the distribution function flux terms in $\boldsymbol{Lq}$.

i. Deconvolve the electric and magnetic field so as to compute point values in the center of a cell to fourth-order accuracy.

ii. Interpolate the volume-integrated distribution function to cell faces using an upwinded stencil (see Section 3.8.2.2). Upwinding direction is based on advection speeds – either the velocity coordinates or the local point-value of the forces (Lorentz force, centrifugal force, and/or Coriolis force).

iii. Compute the distribution function fluxes given in Eqs. (3.388) – (3.393), using the fourth-order quadrature rule described in Section 3.8.2.3.

iv. Compute the divergence of fluxes, i.e. the sum of the terms in Eqs. (3.388) – (3.393) to obtain the distribution function increment associated with the k-th stage of RK4 (see Eqs. (3.15) – (3.18)).

b) Compute the line-integral and source terms in $\boldsymbol{Lq} + \boldsymbol{Y}$ associated with the electromagnetic fields.

i. Interpolate the area-integrated electromagnetic field variables to cell faces, using the centered stencil described in Section 3.9.1.1.

ii. Evaluate the local line integrals needed to update each field component as described in Section 3.9.1.2.

iii. Compute the area-integrated current density from the distribution function, as described in Section 3.9.2.

iv. Compute the closed-loop line-integrals given in the term $\boldsymbol{Lq}$ in Eq. (3.387) to obtain the electromagnetic field increment associated with the k-th stage of RK4.

2. Update distribution function and electromagnetic field solution using the k_1, k_2, k_3, k_4 increments obtained from each stage of RK4 (see Eq. (3.19)).

3. Compute diagnostics, as described in Section 3.10.

The outline of the Vlasov-Poisson algorithm for solving the system $\frac{\partial \boldsymbol{q}}{\partial t} = \boldsymbol{Lq}$ with electrostatic fields is simpler. The distribution function is initialized as a fourth-order volume-integrated value in each phase space cell, and the following steps are performed to update the solution.

1. For each stage in RK4

a) Compute the charge density from the distribution function (see Section 3.5.6.1).

b) Solve the Poisson equation for the discrete potential (see Section 3.9.3).

c) Compute the electric field from the discrete values of the potential using a fourth-order interpolation.

d) Interpolate the volume-integrated distribution function to cell faces using an upwinded stencil (see Section 3.8.2.2). Upwinding direction is based on advection speeds – either the velocity coordinates or the local point-value of the Lorentz force.

e) Compute the distribution function fluxes given in Eqs. (3.388) – (3.393), using the fourth-order quadrature rule described in Section 3.4.2.3.

f) Compute the divergence of fluxes, i.e. the sum of the terms in Eq. (3.388) through Eq. (3.393) to obtain the RK4 distribution function increment associated with the k-th stage of RK4 (see Eqs. (3.15) – (3.18)).

2. Update distribution function using the k_1, k_2, k_3, k_4 increments obtained from each stage of RK4. See Eq. (3.19).

3. Compute diagnostics, as described in Section 3.10.

Both algorithms rely on evaluating the terms $\boldsymbol{Lq} + \boldsymbol{Y}$ for each stage of the RK4 time integrator, using the interpolation and quadrature evaluation procedure detailed in this chapter.

Chapter 4

Numerical test problems in Cartesian coordinates

Before the finite-volume implementation can be used to shed light on new physics, its functionality and convergence properties must be verified. To facilitate this, each portion of the solver is tested for physical accuracy and for fourth-order convergence. As such, this chapter focuses on numerical test problems for Maxwell's equations, and simple test cases for the Vlasov-Poisson and Vlasov-Maxwell equation systems in Cartesian coordinates. The results are compared to theoretical predictions and the strengths and weaknesses of the discretization are assessed.

4.1 Vlasov-Poisson

4.1.1 Free-streaming recurrence time

Free-stream advection in the context of the 1D (x, v_x) Vlasov equation can be tested by zeroing out all velocity-directed fluxes, and allowing the distribution function to evolve in a periodic domain $x \in [0, L_x]$. The governing equation in this case is the Vlasov equation, with all force terms set to zero, resulting in a linear hyperbolic advection equation:

$$\frac{\partial f}{\partial t} + \frac{\partial}{\partial x}(v_x f) = 0. \tag{4.1}$$

The distribution function evolves along the x direction, and after a period of time, due to finite resolution in velocity space, reproduces the initial condition. The time at which the initial condition reappears is the recurrence time, which has a known theoretical value of

$$T_R^{\text{th}} = \frac{L_x}{h_{v_x}}, \tag{4.2}$$

where h_{v_x} is the cell width along the v_x-direction. This provides a metric to assess the free-stream advection in simulations by seeing how well the simulated recurrence time matches

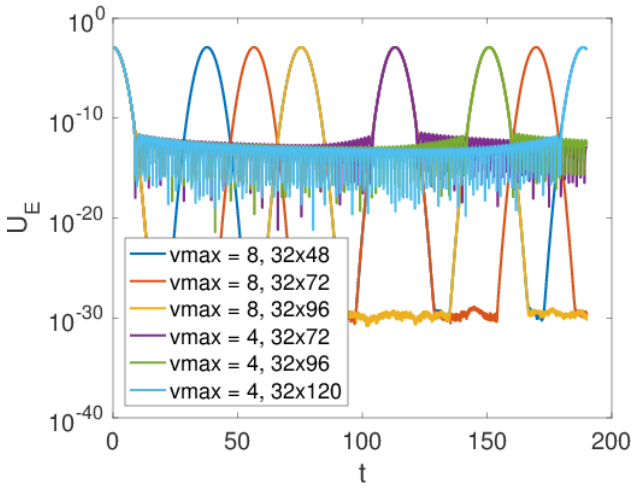

Figure 4.1: Electric field energy as a function of time, associated with a $f(x, v_x)$ distribution function that is allowed to advect only along the x-direction. The recurrence time is the time at which the initial condition is reproduced. As velocity space resolution is increased, the recurrence time increases as well.

the theoretical value. Notably recurrence in this case is a numerical, and not a physical phenomenon – see discussion in Refs. [15, 50]. Instead of tracking the recurrence of the distribution function, which is two-dimensional, it is easier to track the recurrence of the density, which is one-dimensional. An even simpler indicator of recurrence is the electric field energy associated with the given charge density, which is a scalar. Thus while the electric field does not play a role in the evolution of the distribution function in this case, it is used as an indicator of recurrence time. The initial condition for this test case is

$$f(x, v_x)|_{t=0} = \frac{1}{(2\pi)^{1/2}} \exp\left(-\frac{v_x^2}{2}\right)\left(1 + 0.01\cos(kx)\right) \tag{4.3}$$

$$k = 0.5 \tag{4.4}$$

$$x \in \left[0, \frac{2\pi}{k}\right] \tag{4.5}$$

The electric field energy as a function of time for different resolutions is shown in Fig. 4.1. The recurrence time from each simulation is shown in Table 4.1, which also shows the relative difference between the theoretical and numerical recurrence time as well as the relative difference between the initial value of field energy $U_E(0)$ and the value at recurrence time $U_E(T_R)$. These results show that the recurrence time from simulations agree well with the theoretical recurrence time, and likewise the initial value of field energy is reproduced with high fidelity. The values cannot match exactly on account of finite time step size, and amplitude and phase error associated with the discretization.

Table 4.1: Recurrence time for simulations with different velocity domain resolutions. The difference between the theoretical recurrence time (see Eq. (4.2)) and the recurrence time in simulations T_R^{num} is small, as is the relative change in the peak field energy U_E.

$v_{\max}$	N_x	N_{v_x}	h_v	T_R^{th}	T_R^{num}	$\frac{T_R^{\text{num}}-T_R^{\text{th}}}{T_R^{\text{th}}}$	$\frac{U_E(T_R)-U_E(0)}{U_E(0)}$
8	32	48	0.1667	37.699	37.749	-1.33e-03	-5.80e-04
8	32	72	0.1111	56.549	56.583	-6.12e-04	-2.54e-04
8	32	96	0.0833	75.398	75.417	-2.56e-04	-6.05e-05
4	32	72	0.0556	113.097	113.140	-3.77e-04	-3.40e-04
4	32	96	0.0417	150.796	150.815	-1.23e-04	-3.13e-05
4	32	120	0.0333	188.496	188.519	-1.24e-04	-5.47e-05

4.1.2 Landau Damping

Landau damping is a common benchmark (see for example Refs. [51, 22, 4, 52, 53]) in kinetic calculations because it can be simulated in one spatial and one velocity dimension. Landau damping is a mechanism by which electric field energy is converted into thermal energy in a collisionless plasma. The phenomenon occurs in a variety of contexts, but the simplest case involves a uniform infinite thermal-equilibrium plasma, whose electrons are displaced away from the ions. The ions can be assumed to be uniformly distributed and stationary, such that the dynamics can be modeled with a single electron distribution function and an electrostatic field. The electric field induced by the charge separation oscillates and damps in time, as the original potential energy is converted into thermal energy of the electrons. The frequency of oscillation and the decay rate of the electric field are given by a dispersion relation, which can be derived from the linearized or quasi-linearized Vlasov and Poisson equations. The linear-theory dispersion relation is discussed in Ref. [54] and tabulated frequencies and decay rates for different wave numbers of the perturbation can be found in Ref. [55]. Simplified dispersion relations can be obtained in certain asymptotic limits [5]. If the perturbation is large then a non-linear or "strong" form of Landau damping is observed, in which the original decay in the electric field is followed by growth later in time. Non-linear Landau damping offers one of very few test cases of non-linear kinetic physics for which a semi-analytic solution exists.

The governing equations in this case are the 1D Vlasov equation for the electron distribution function, and Gauss's law for the electric field

$$\frac{\partial f_e}{\partial t} + \frac{\partial}{\partial x}(v_x f_e) + \frac{\partial}{\partial v_x}(E_x f_e) = 0. \tag{4.6}$$

$$\frac{\partial E_x}{\partial x} = 1 - \int_{-\infty}^{\infty} f_e(x, v_x) dv_x. \tag{4.7}$$

The ions constitute a stationary neutralizing background, such that the system is charge neutral. Since ion dynamics are not involved, the ion plasma frequency can be assumed to

be equal to the electron plasma frequency, such that the time in this governing equation system is measured in units of inverse electron plasma frequency. The initial condition for the electron distribution is

$$f(x, v_x)|_{t=0} = \frac{1}{(2\pi)^{1/2}} \exp\left(-\frac{v_x^2}{2}\right)\left(1 + \alpha\cos(kx)\right) \tag{4.8}$$

$$k = 0.5. \tag{4.9}$$

This initial condition is consistent with the one used in Ref. [15]. The spatial domain is periodic with length $2\pi/k$, and the velocity domain is $v_x \in [-10, 10]$. For weak Landau damping the magnitude of the perturbation is $\alpha = 0.01$, and for strong Landau damping $\alpha = 0.5$.

The evolution of the distribution function for a 256×256 resolution linear Landau damping simulation is shown in Fig. 4.2. The shearing of the distribution function in phase space is accompanied by a net decay in the electric field energy as the electrostatic wave interacts with the plasma. The electric field energy evolution is plotted in Fig. 4.3. The damping rate in the simulation is obtained through a linear fit of the local maxima of $\log(U_E)$. The oscillation frequency is $\omega = \pi/T$, where T is the period of $U_E(t)$ oscillation in units of normalized time. For the 256×256 simulation, the damping rate is $\gamma^{\text{num}} = 0.3075$ and the oscillation frequency is $\omega^{\text{num}} = 1.4113$. These values compare well with the theoretically predicted values of $\omega^{\text{th}} = 1.4156$, and $\gamma^{\text{th}} = 0.3066$ [15]. Since electric field energy or a norm of the electric field are both used as measures of decay rate, it is worth noting that the theoretical decay rate of the electric field energy is twice the theoretical decay rate of the norm of the electric field. Due to the effects of finite resolution, the decay in the energy eventually stops, and a partial recurrence is observed close to the theoretical recurrence time of $T_R^{\text{th}} = 80.4$.

The electric field evolution for the case of strong Landau damping, with perturbation amplitude $\alpha = 0.5$, is shown in Fig. 4.4. The growth and decay rates agree well with the theoretical predictions presented in Ref. [15].

4.1.3 Two-stream instability

The two-stream instability is another common benchmark for Vlasov-Poisson simulations in (x, v_x) coordinates. In the simplest case the instability involves counter-streaming particles of the same species that, when spatially perturbed, interact through their electrostatic repulsive forces in a way that results in the amplification of the electric field. A neutralizing background of oppositely-charged particles is assumed. The initial condition for the electron distribution

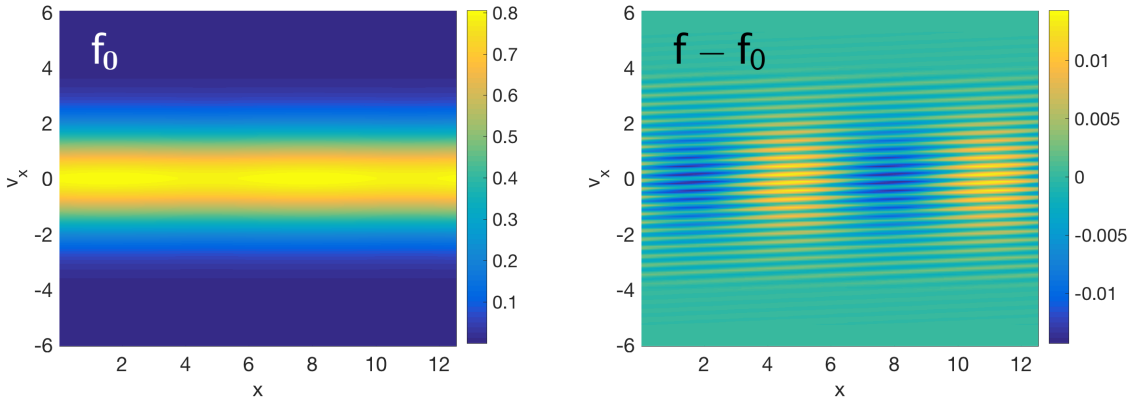

(a) Initial condition $f(x, v_x)$ **(b)** Net change in distribution

Figure 4.2: In 2D (x, v_x), linear Landau damping is (a) initialized in a periodic domain with an electron distribution function that is Maxwellian in velocity, with a small sinusoidal perturbation along the spatial coordinate. The distribution function shears in time, which causes the original perturbation to smear out in phase space, as shown in (b) at time $t = 50$.

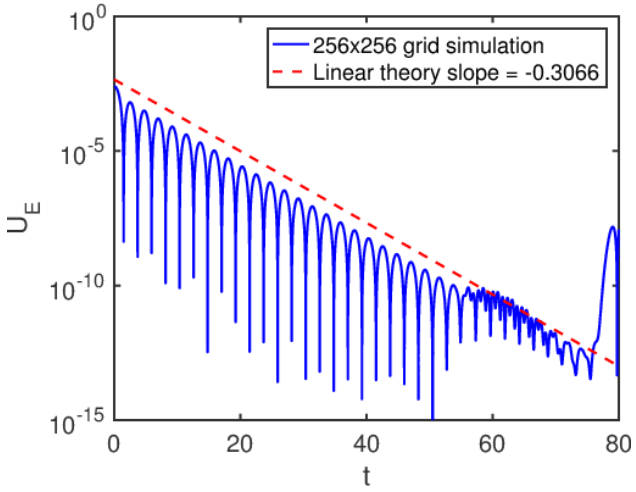

Figure 4.3: Evolution of electric field energy in a 2D (x, v_x) linear Landau damping simulation with 256×256 cells. The field energy, which is a measure of the electric field amplitude, oscillates and damps in time at frequency $\omega^{\text{num}} = 1.4113$ and rate of $\gamma^{\text{num}} = 0.3075$ obtained from the simulation. Theoretical values are $\omega^{\text{th}} = 1.4156$, and $\gamma^{\text{th}} = 0.3066$ [15]. In simulations the decay eventually stops due to finite resolution, and a partial recurrence is observed close to the theoretical recurrence time of $T_R^{\text{th}} = 80.4$.

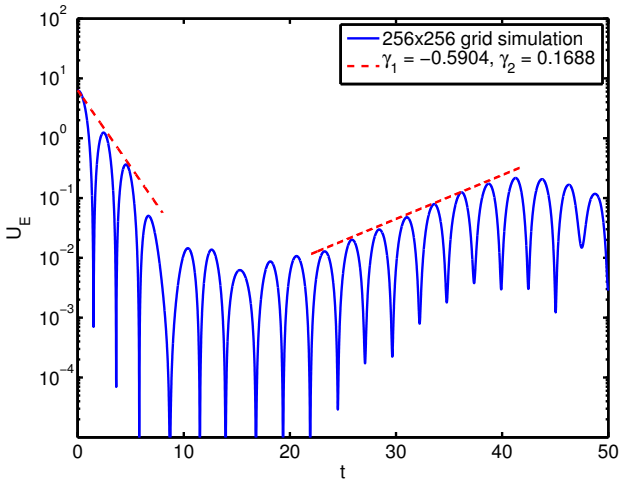

Figure 4.4: Evolution of electric field energy in a 1D (x, v_x) a non-linear Landau damping simulation with 256×256 cells. The simulated decay and growth rates are consistent with theoretical predictions.

function is

$$f(x, v_x)|_{t=0} = \frac{1}{(2\pi)^{1/2}} v_x^2 \exp\left(-\frac{v_x^2}{2}\right)\left(1 + \alpha\cos(kx)\right) \tag{4.10}$$

$$x \in \left[0, \frac{2\pi}{k}\right] \tag{4.11}$$

$$v_x \in [-v_{\max}, v_{\max}] \tag{4.12}$$

$$v_{\max} = 10 \tag{4.13}$$

$$k = 0.5 \tag{4.14}$$

$$\alpha = 0.01. \tag{4.15}$$

The boundary conditions are periodic along x. Since ions do not play a role in the physics, the time is in effect normalized by the electron plasma frequency. The velocity dependence for this initial condition has a double-peaked profile, shown in Fig. 4.5. While not all double-peaked distribution functions in velocity space result in instability, in the absence of magnetic fields they are often candidates for driving an instability [56, 57].

The evolution of the distribution function for the two-stream instability is shown in Fig. 4.6. As the instability evolves from linear to non-linear, a vortex-like structure forms in phase space indicating the one-dimensional trapping of particles, meaning that the dynamic species becomes concentrated in the center of the domain. As the distribution function evolves, it filaments, leading to the formation of fine structures. In the absence of collisions, these structures continue to get finer with time. Eventually, a finite-resolution grid cannot capture these features, such that the distribution function takes on negative values in regions

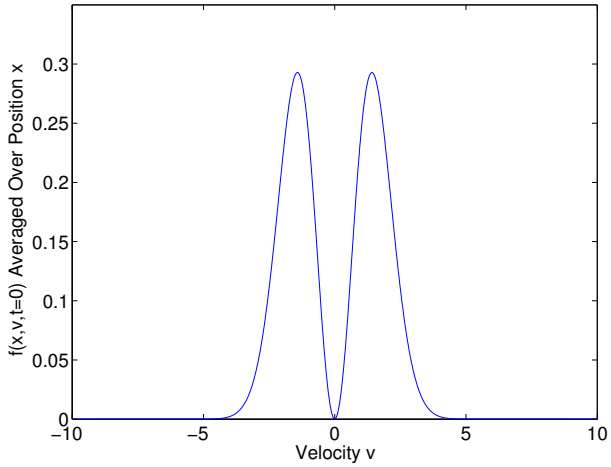

Figure 4.5: The distribution function initial condition for the two-stream instability is a double-peaked profile in velocity space.

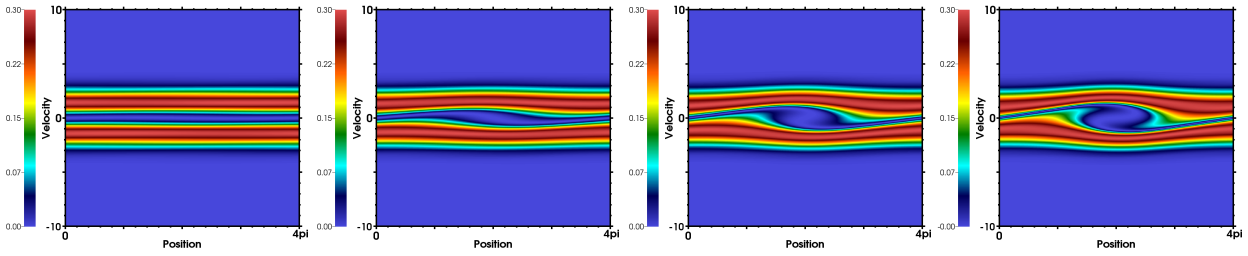

(a) t=0 **(b)** t=15.7 **(c)** t=18.8 **(d)** t=20.4

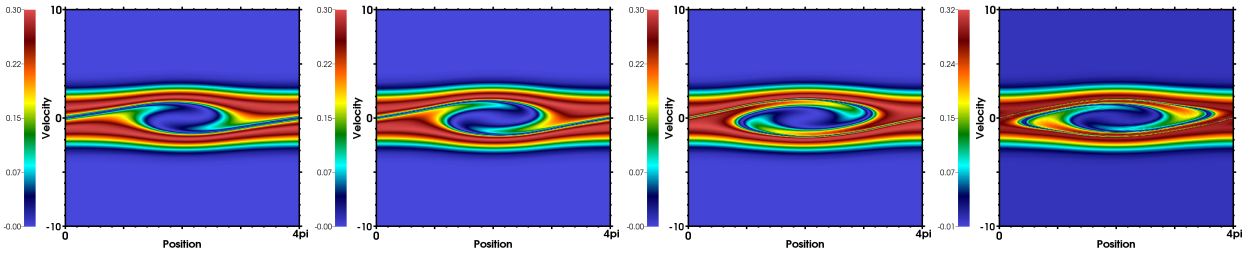

(e) t=21.2 **(f)** t=22.8 **(g)** t=25.9 **(h)** t=29.8

Figure 4.6: Evolution of the distribution function for a two-stream instability simulation using a 256×1024 grid and a CFL of 0.8. Note that the linear phase begins at approximately $t = 13$ and ends at approximately $t = 18$, after which the instability reaches the non-linear regime.

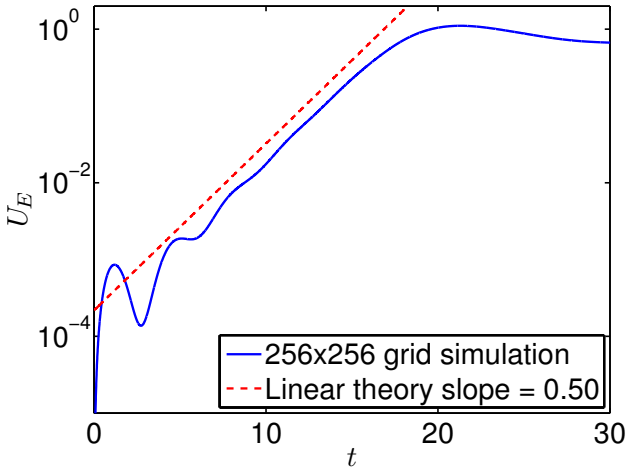

Figure 4.7: Evolution of the electric field energy in a 256×256 resolution simulation of the linear two-stream instability. The growth rate observed in the simulation agrees well with the theoretical growth rate predicted by linear theory.

where the gradient is not resolved (see last plot in Fig. 4.6). Features that are smaller than the grid size are subject to numerical dissipation.

The evolution of the electric field energy for the two-stream instability as a function of time is shown in Fig. 4.7. The growth rate agrees well with the linear-theory prediction.

4.2 Maxwell's equations

The Maxwell solver for the electromagnetic fields is tested using simple configurations with known analytic solutions. Divergence errors are assessed for Cartesian coordinates using a test problem involving an electromagnetic pulse propagating through a domain with a fixed charge density distribution. Testing a Maxwell solver on problems that involve currents is considerably more difficult since exact solutions require the use of the Biot-Savart law, and the evaluation of associated elliptic integrals. Discussion of approaches to solve for the magnetic field in the presence of simple current configurations is presented in Refs. [58, 59, 60, 61, 62, 63, 64, 65, 66].

4.2.1 Electromagnetic pulse

The Cartesian coordinate Maxwell solver is applied to simulate an electromagnetic pulse in a two-dimensional (x, y) domain that contains a charge density. In the absence of charges, the initial condition is zero for all fields except B_z, which at initial time is set to be

$$B_z\Big|_{t=0} = A_B \exp(-x^2 - y^2), \tag{4.16}$$

with $A_B = 0.1$. The domain is defined to be $x, y \in [-5, 5] \times [-5, 5]$. If charges are present then E_x and E_y components of the electric field have to be initialized in a way that is consistent with the charge, as dictated by Gauss's law. The governing equations for the electromagnetic pulse are Faraday's and Ampere's law without currents, which in their weak form are

$$\begin{bmatrix} \iint B_x dydz \\ \iint B_y dxdz \\ \iint B_z dxdy \end{bmatrix} = - \begin{bmatrix} \left(\int E_z(x_i, y)dz\right)_{y_{j-\frac{1}{2}}}^{y_{j+\frac{1}{2}}} \\ -\left(\int E_z(x, y_j)dz\right)_{x_{i-\frac{1}{2}}}^{x_{i+\frac{1}{2}}} \\ -\left(\int E_x(x, y)dx\right]_{y_{j-\frac{1}{2}}}^{y_{j+\frac{1}{2}}} + \left[\int E_y(x, y)dy\right)_{x_{i-\frac{1}{2}}}^{x_{i+\frac{1}{2}}} \end{bmatrix} + \lambda \begin{bmatrix} \iint \left(\frac{\partial^2}{\partial x^2}B_x + \frac{\partial^2}{\partial x \partial y}B_y + \frac{\partial^2}{\partial x \partial z}B_z\right) dydz \\ \iint \left(\frac{\partial^2}{\partial y \partial x}B_x + \frac{\partial^2}{\partial y^2}B_y + \frac{\partial^2}{\partial y \partial z}B_z\right) dxdz \\ \iint \left(\frac{\partial^2}{\partial z \partial x}B_x + \frac{\partial^2}{\partial z \partial y}B_y + \frac{\partial^2}{\partial z^2}B_z\right) dxdy \end{bmatrix} \quad (4.17)$$

$$\begin{bmatrix} \iint E_x dydz \\ \iint E_y dxdz \\ \iint E_z dxdy \end{bmatrix} = \begin{bmatrix} \left(\int B_z(x_i, y)dz\right)_{y_{j-\frac{1}{2}}}^{y_{j+\frac{1}{2}}} \\ -\left(\int B_z(x, y_j)dz\right)_{x_{i-\frac{1}{2}}}^{x_{i+\frac{1}{2}}} \\ -\left(\int B_x(x, y)dx\right]_{y_{j-\frac{1}{2}}}^{y_{j+\frac{1}{2}}} + \left[\int B_y(x, y)dy\right)_{x_{i-\frac{1}{2}}}^{x_{i+\frac{1}{2}}} \end{bmatrix} + \lambda \left(\begin{bmatrix} \iint \left(\frac{\partial^2}{\partial x^2}E_x + \frac{\partial^2}{\partial x \partial y}E_y + \frac{\partial^2}{\partial x \partial z}E_z\right) dydz \\ \iint \left(\frac{\partial^2}{\partial y \partial x}E_x + \frac{\partial^2}{\partial y^2}E_y + \frac{\partial^2}{\partial y \partial z}E_z\right) dxdz \\ \iint \left(\frac{\partial^2}{\partial z \partial x}E_x + \frac{\partial^2}{\partial z \partial y}E_y + \frac{\partial^2}{\partial z^2}E_z\right) dxdy \end{bmatrix} - \begin{bmatrix} \iint \frac{\partial \rho}{\partial x} dydz \\ \iint \frac{\partial \rho}{\partial y} dxdz \\ \iint \frac{\partial \rho}{\partial z} dxdy \end{bmatrix} \right) \quad (4.18)$$

Note that these are the modified forms of the equations that incorporate a parabolic divergence cleaning term with constant $\lambda = ah^2$, where $a \leq 0.35$ (see Section 3.5.5) and h is the cell spacing, which is assumed to be isotropic. Note also that integrals over the z direction and derivatives with respect to z are trivial since the fields and densities are assumed to be independent of z for this two-dimensional system. Since the initial condition magnetic field is chosen to be along the z direction, with other components set to zero, only the B_z, E_x, and E_y components of the electromagnetic field have a role in the evolution of the pulse.

To test the parabolic divergence cleaning portion of the algorithm, an initial condition with B_z defined as in Eq. (4.16), electric field set to zero, and a charge density set to

$$\rho = A_\rho \Big(\exp\left[-\big((x-1)^2 + (y-1)^2\big)\right] - \exp\left[-\big((x+1)^2 + (y+1)^2\big)\right] \Big) \quad (4.19)$$

$$A_\rho = 1 \times 10^{-6} \quad (4.20)$$

is used. Note that this charge density is not consistent with a zero-electric field, and does not satisfy Gauss's law, which means that a divergence error (see Eq. (2.89)) is present from the onset. The parabolic divergence cleaner should diminish the error as the electromagnetic pulse evolves. This effect is demonstrated in Fig. 4.8 for cleaning parameter $a = 0.1$. Figure 4.8a shows the fields close to initial time, Fig. 4.8b shows the fields later in time after the electromagnetic pulse has propagated outward. Figure 4.8c shows the divergence of the electric field near initial time, and Fig. 4.8d shows the divergence error at time $t = 0.052$ due to the electric field not satisfying Gauss's law. Figure 4.8e shows the divergence of the electric field later in time, and Fig. 4.8f shows the associated divergence error. Figure 4.8g shows the divergence error at different times along the $x = y$ diagonal of the domain. The divergence error is shown to diminish. The rate is consistent with the cleaning parameter a; as a is increased, the rate at which the error decreases to zero increases as well.

In practice, the initial conditions for simulations involving dynamic fields should be set so as to satisfy Gauss's law constraints. There are two ways of doing this. The first way is to manufacture a solution. For example, choosing

$$E_x = -Aye^{-x^4-y^4} \tag{4.21}$$

$$E_y = Axe^{-x^4-y^4} \tag{4.22}$$

one can compute the associated charge density by taking the divergence of the electric field. While simple, this approach can result in unphysical scenarios. For example, the electrostatic potential for the fields above involves a Gamma function, suggesting that this configuration is physically unlikely. The second way to initialize electric fields that are consistent with charge density is to solve a Poisson equation, and determine the electric field from the potential. With the aim of modeling electromagnetic pulse propagation in the presence of charges with self-consistent electric fields, the latter approach is used here.

Let the charge density be a smooth function with compact support, defined locally as a polynomial that is a function of $r = \sqrt{x^2 + y^2}$, subject to the constraints

$$\left.\frac{\partial \rho}{\partial r}\right|_{r=0} = 0 \tag{4.23}$$

$$\left.\frac{\partial \rho}{\partial r}\right|_{r=r_0} = 0 \tag{4.24}$$

$$\left.\frac{\partial^2 \rho}{\partial r^2}\right|_{r=r_0} = 0 \tag{4.25}$$

$$\rho|_{r=0} = A_\rho \tag{4.26}$$

$$\rho|_{r=r_0} = 0, \tag{4.27}$$

where for $r_0 > 0$ the charge density is zero. The constraint given by Eq. (4.25) is aimed to ensure smoothness, which is desirable when it comes to minimizing divergence error. A

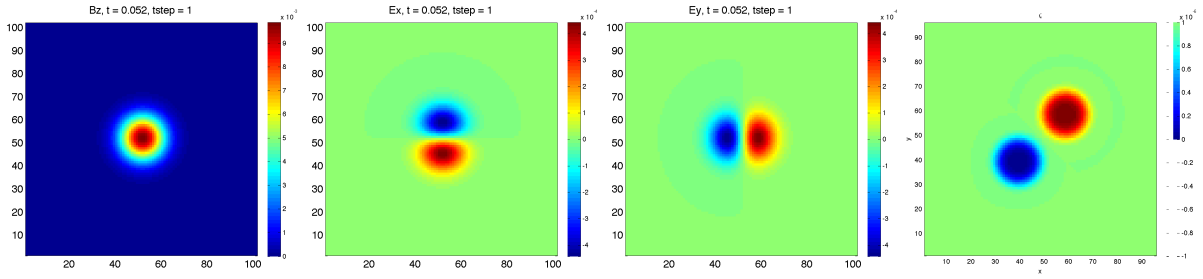

(a) B_z, E_x, E_y, and ρ at time $t = 0.052$

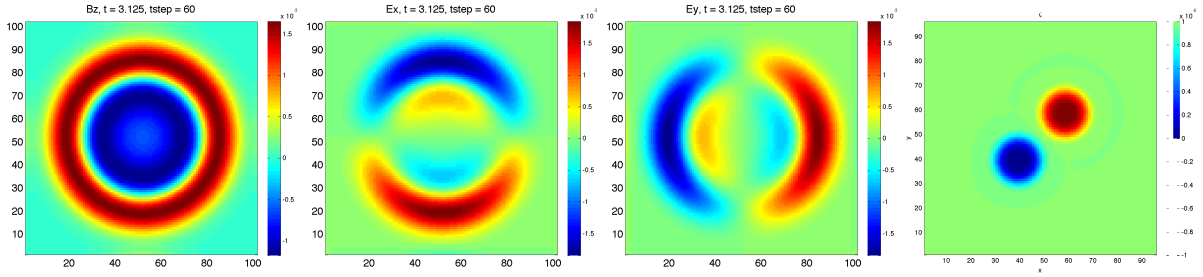

(b) B_z, E_x, E_y, and ρ at time $t = 3.125$

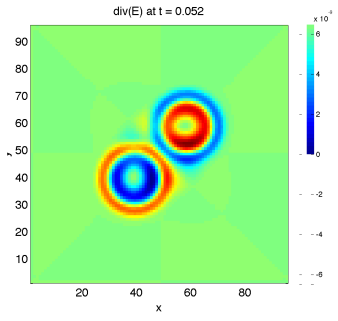

(c) $\nabla \cdot \boldsymbol{E}$, $t = 0.052$

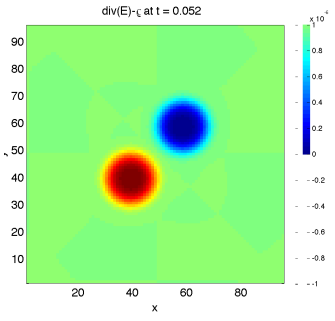

(d) $\nabla \cdot \boldsymbol{E} - \rho$, $t = 0.052$

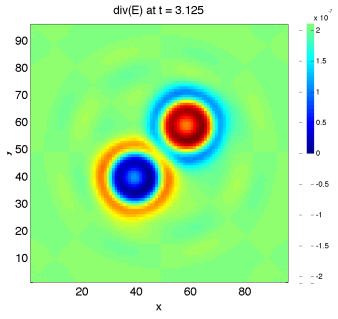

(e) $\nabla \cdot \boldsymbol{E}$, $t = 3.125$

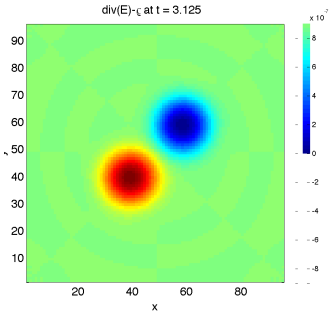

(f) $\nabla \cdot \boldsymbol{E} - \rho$, $t = 3.125$

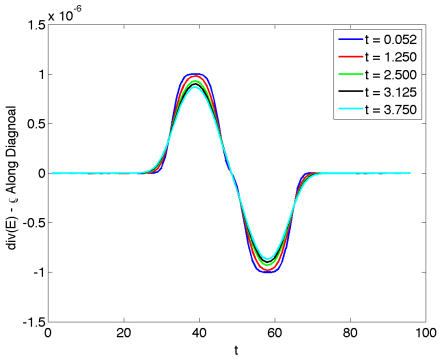

(g) $[\nabla \cdot \boldsymbol{E} - \rho]_{x=y}$

Figure 4.8: 96^2 resolution simulation of electromagnetic pulse propagating outward in a domain with a charge density. Divergence error is present at the onset. Divergence cleaning is applied with parameter $a = 0.1$. The divergence error $\nabla \cdot \boldsymbol{E} - \rho$ is shown to diminish in time. The (x, y) coordinates are designated by their index value in a domain of size $[-5, 5] \times [-5, 5]$.

charge density distribution that satisfies the above constraints is

$$\rho(r) = \begin{cases} \alpha\left(-\frac{3}{r_0^4}r^4 + \frac{8}{r_0^3}r^3 - \frac{6}{r_0^2}r^2 + 1\right) & r \in [0, r_0] \\ 0 & r > r_0 \end{cases} \tag{4.28}$$

For the charge density given by Eq. (4.28), solving the Poisson equation,

$$\frac{1}{r}\frac{\partial}{\partial r}\left(r\frac{\partial \phi}{\partial r}\right) = -\rho, \tag{4.29}$$

for the potential yields

$$\phi(r) = \begin{cases} \alpha\left(-\frac{r^2}{4} + \frac{3r^4}{8r_0^2} - \frac{8r^5}{25r_0^3} + \frac{x^6}{12r_0^4} + \frac{67r_0^2}{600} - \frac{r_0^2}{10}\log r_0\right) & r \in [0, r_0] \\ -\frac{\alpha r_0^2}{10}\log r & r > r_0 \end{cases} \tag{4.30}$$

Note that this expression for the potential is valid for an infinite domain. From the electrostatic potential, the electric field is readily derived,

$$E_x = -\frac{\partial \phi}{\partial x} = \begin{cases} -\alpha\left(-\frac{x}{2} + \frac{3x(x^2+y^2)}{2r_0^2} - \frac{8x(x^2+y^2)^{3/2}}{5r_0^3} + \frac{x(x^2+y^2)^2}{2r_0^4}\right) & r \in [0, r_0] \\ \frac{\alpha r_0^2 x}{10(x^2+y^2)} & r > r_0 \end{cases} \tag{4.31}$$

$$E_y = -\frac{\partial \phi}{\partial y} = \begin{cases} -\alpha\left(-\frac{y}{2} + \frac{3y(x^2+y^2)}{2r_0^2} - \frac{8y(x^2+y^2)^{3/2}}{5r_0^3} + \frac{y(x^2+y^2)^2}{2r_0^4}\right) & r \in [0, r_0] \\ \frac{\alpha r_0^2 y}{10(x^2+y^2)} & r > r_0 \end{cases} \tag{4.32}$$

With initial charge density given by Eq. (4.28), initial electric field components given by Eqs. (4.31) and (4.32), and magnetic field given by Eq. (4.16), the electromagnetic pulse is modeled in a domain $x, y \in [-10, 10]$. A larger domain is used for this case in order to avoid discrepancies at boundaries due to the fact that the electrostatic potential (and associated electric field) is defined over an infinite domain, whereas the simulation domain is bounded. The field and charge density configuration are shown for $t = 0.013$ in Fig. 4.9a and for $t = 3.125$ in Fig. 4.9b. The speed at which the pulse propagates outward is consistent with the normalized speed of light in the system, which has a value of one. The max norm of the associated divergence error for the electric field is plotted in Fig. 4.10 for simulations executed with resolutions 192^2, 384^2, and 768^2. As the resolution is doubled, the error decreases by a factor of about sixteen, which is expected for a fourth-order simulation.

4.3 Vlasov-Maxwell

4.3.1 Harris equilibrium

The Harris current sheet [67] is a well-known one-dimensional plasma equilibrium in which pressure forces are exactly balanced by electromagnetic forces, and the net charge density is

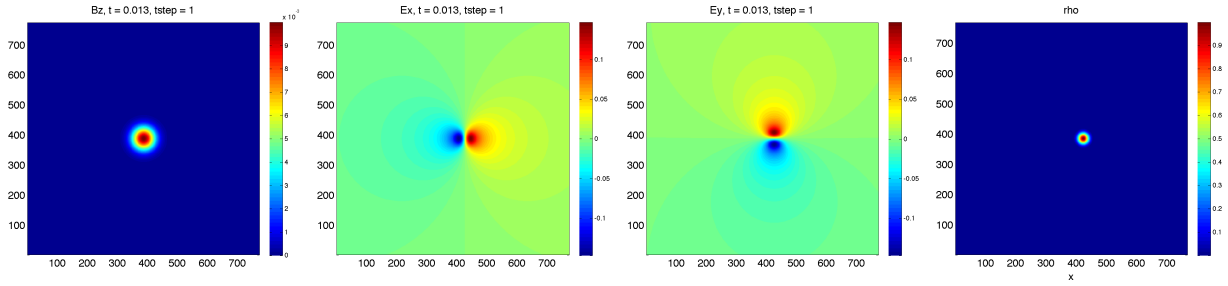

(a) B_z, E_x, E_y, and ρ at time $t = 0.013$

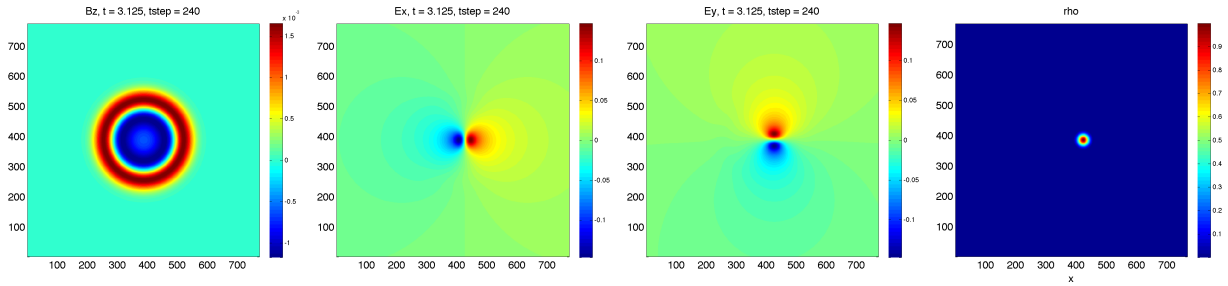

(b) B_z, E_x, E_y, and ρ at time $t = 3.125$

Figure 4.9: 768^2 simulation of electromagnetic pulse propagating outward in a domain with a charge density distribution given by Eq. (4.28) that is offset from the center. The (x, y) coordinates are designated by their index value in a domain of size $[-10, 10]\times[-10, 10]$. Divergence cleaning parameter a is set to be 0.35. The electric field due to the charge is large compared to the electric field due to the electromagnetic pulse.

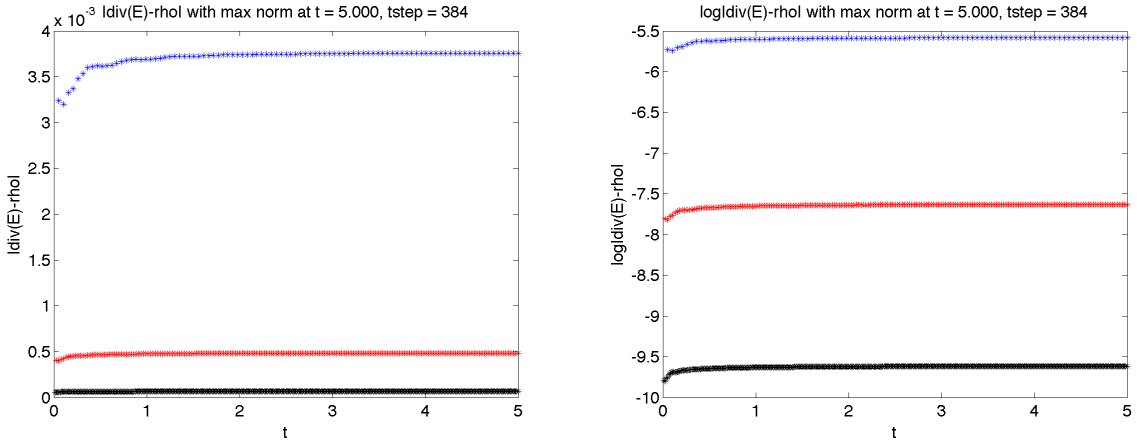

Figure 4.10: Evolution of the max-norm of the divergence error for the electromagnetic pulse propagating outward, $\nabla \cdot \boldsymbol{E} - \rho$ for different resolutions: 192^2 resolution is in blue, 384^2 resolution is in red, and 768^2 resolution is in black. The divergence error converges at third order accuracy as evidenced by error decreasing by a factor of about nine each time resolution is doubled.

zero. This configuration and its various adaptations form the basis for the study of plasma phenomena such as the lower-hybrid drift instability [68, 69] and magnetic reconnection [70]. Here the unperturbed Harris current sheet is used to test the convergence of the (x, v_x, v_y) Vlasov-Maxwell solver when applied to a configuration involving current and particle species of different mass. Numerical errors will result in a departure away from equilibrium, but this deviation should converge to zero as the grid is refined.

4.3.1.1 Normalization-consistent initialization

Simulation initial conditions for a Harris current sheet depend on the choice of normalization for the governing differential equations and the choice of parameters like thermal speed. To ensure parameters are self-consistent, the equilibrium profiles of the fields are derived directly from the ion and electron distribution functions, using the normalized Vlasov-Maxwell equation system presented in Section 2.2.1. The electron and ion distribution functions associated with the Harris current sheet are drifting Maxwellians, such that

$$f_e = \frac{1}{2\pi v_{Te}^2} \exp\left(-\frac{v_x^2 + (v_y - u_e)^2}{2v_{Te}^2}\right) n_0 \text{sech}^2\left(\frac{x}{\ell}\right) \tag{4.33}$$

$$f_i = \frac{1}{2\pi v_{Ti}^2} \exp\left(-\frac{v_x^2 + (v_y - u_i)^2}{2v_{Ti}^2}\right) n_0 \text{sech}^2\left(\frac{x}{\ell}\right), \tag{4.34}$$

where v_{Te} and v_{Ti} are the electron and ion thermal speeds, u_e and u_i are the electron and ion drift speeds, n_0 is a nominal number density, and ℓ is the width of the current sheet. From these distribution functions, the species currents J_{ye} and J_{yi}, and net current J_y can be derived, such that

$$J_{ye} = Z_e \int_{-\infty}^{\infty}\int_{-\infty}^{\infty} v_y f_e dv_x dv_y = -u_e n_0 \text{sech}^2\left(\frac{x}{\ell}\right) \tag{4.35}$$

$$J_{yi} = Z_i \int_{-\infty}^{\infty}\int_{-\infty}^{\infty} v_y f_i dv_x dv_y = u_i n_0 \text{sech}^2\left(\frac{x}{\ell}\right) \tag{4.36}$$

$$J_y = (u_i - u_e) n_0 \text{sech}^2\left(\frac{x}{\ell}\right). \tag{4.37}$$

If the equilibrium Ampere's law is to be satisfied then $\partial \boldsymbol{E}/\partial t$ must be zero. Noting that the equilibrium is in one spatial dimension (x), a relationship between the net current and the magnetic field is obtained

$$\frac{\omega_{cp}}{\omega_{pp}} \frac{\partial}{\partial \boldsymbol{x}} \times \boldsymbol{B} = \sum_s Z_s \int \boldsymbol{v}' f_s(\boldsymbol{v}') d\boldsymbol{v}' \tag{4.38}$$

$$\frac{\omega_{cp}}{\omega_{pp}} \frac{\partial B_z}{\partial x} = J_y \tag{4.39}$$

Substituting Eq. (4.37) into Eq. (4.39), integrating both sides, and assuming the constant of integration (i.e. the background magnetic field) is zero yields an expression for the magnetic

field in terms of known parameters,

$$B_z = -\frac{\omega_{pp}}{\omega_{cp}}(u_i - u_e)n_0\ell \tanh\left(\frac{x}{\ell}\right). \tag{4.40}$$

The normalized Vlasov equation for each species s in this one-dimensional configuration with zero electric field is

$$0 = \frac{\partial f_s}{\partial t} + v_x\frac{\partial f}{\partial x} + \frac{Z_s}{M_s}\frac{\omega_{cp}}{\omega_{pp}}(v_y B_z)\frac{\partial f_s}{\partial v_x} + \frac{Z_s}{M_s}\frac{\omega_{cp}}{\omega_{pp}}(-v_x B_z)\frac{\partial f_s}{\partial v_x}. \tag{4.41}$$

For equilibrium $\partial f_e/\partial t$ and $\partial f_i/\partial t$ must be zero. Substituting Eqs. (4.33) and (4.40) into Eq. (4.41) and evaluating each term, it is found that for electrons to be in equilibrium the following relation must hold

$$0 = \left(-\ell^2\frac{M_i}{M_e}u_e\left(u_i - u_e\right) - 2v_{Te}^2\right)\frac{v_x}{\ell v_{Te}^2}\tanh\left(\frac{x}{\ell}\right). \tag{4.42}$$

Substituting Eqs. (4.34) and (4.40) into Eq. (4.41), it is found that for ions to be in equilibrium the following relation must hold

$$0 = \left(\ell^2 u_i(u_i - u_e) - 2v_{Ti}^2\right)\frac{v_x}{\ell v_{Ti}^2}\tanh\left(\frac{x}{\ell}\right). \tag{4.43}$$

For these relations to be satisfied for all x, the equalities

$$-\ell^2\frac{M_i}{M_e}u_e\left(u_i - u_e\right) = 2v_{Te}^2 \tag{4.44}$$

$$\ell^2 u_i(u_i - u_e) = 2v_{Ti}^2 \tag{4.45}$$

must be satisfied for both the electrons and ions to be in equilibrium. Taking the ratio of Eq. (4.45) to Eq. (4.44) yields a relationship between drift speed and thermal speed parameters, such that

$$-\frac{u_i}{u_e} = \frac{M_i}{M_e}\frac{v_{Ti}^2}{v_{Te}^2}. \tag{4.46}$$

Since temperature in terms of thermal speed is $T_s = \frac{1}{2}M_s v_{Ts}^2$ then Eq. (4.46) is equivalent to

$$-\frac{u_i}{u_e} = \frac{T_i}{T_e}. \tag{4.47}$$

Substituting Eq. (4.47) into Eq. (4.45) yields a relationship between the ion drift speed, thermal speed, and sheet width, such that

$$\frac{u_i^2}{v_{Ti}^2} = \frac{2}{\left(1 + \frac{T_e}{T_i}\right)\ell^2}. \tag{4.48}$$

Note that since the speed of light is chosen to be the characteristic speed, the characteristic length in this system is the ion skin depth $\delta_i = c/\omega_{pi}$. Hence the value of sheet width ℓ is relative to the characteristic length in the system, and speeds are relative to the speed of light. The expression for the magnetic field in Eq. (4.40) can be written using the parameter relations derived above, such that

$$B_z = -B_0 \tanh\left(\frac{x}{\ell}\right) \tag{4.49}$$

$$B_0 = \omega_{pi}\frac{r_{Li}}{\ell}\left(2\frac{v_{Ti}}{u_i}\right)n_0, \tag{4.50}$$

where r_{Li} is the characteristic ion Larmor radius associated with the characteristic ion cyclotron frequency.

With a specified form of electron distribution function (Eq. (4.33)), ion distribution function (Eq. (4.34)), magnetic field (Eq. (4.49)), and the relations given by Eq. (4.47) and Eq. (4.48) the initial condition for the Harris sheet can be fully specified by setting the mass ratio M_i/M_e, the temperature ratio T_i/T_e, the ratio of ion drift speed to ion thermal speed u_i/v_{Ti}, the ratio of Larmor radius to sheet width r_{Li}/ℓ, and finally by specifying the ion thermal speed v_{Ti}. For the simulations conducted here the values of the ratios are set to be the same as in Ref. [68], such that

$$\frac{M_i}{M_e} = 180 \tag{4.51}$$

$$\frac{T_i}{T_e} = 4 \tag{4.52}$$

$$\frac{u_i}{v_{Ti}} = 1 \tag{4.53}$$

$$\frac{r_L}{\ell} = 1. \tag{4.54}$$

Note that an artificial mass ratio is used, which is consistent with Ref. [68] and also convenient in that the time step size restriction associated with the electron distribution function is less severe for an artificial mass ratio than for a realistic mass ratio (see discussion of CFL condition in Section 3.3.1). Using the ratio specifications in Eq. (4.51) through Eq. (4.54), and different choices of ion thermal speed, Table 4.2 shows the values of all the parameters used to initialize the distribution functions and the magnetic field for a self-consistent Harris equilibrium. The distribution functions for parameters given by the second row of Table 4.2, corresponding to $v_{Ti} = 0.01$, are shown in Fig. 4.11 – these are the initial conditions used for the simulation results presented here. Note that the frequencies in the system only depend on the mass ratio and the magnitude of the magnetic field set by B_0, such that

$$\omega_{pe} = (M_i/M_e)^{1/2}\omega_{pi} \tag{4.55}$$

$$\omega_{ce} = \frac{M_i}{M_e}\frac{Z_e}{Z_i}\omega_{ci} \tag{4.56}$$

$$\omega_{ci} = B_0, \tag{4.57}$$

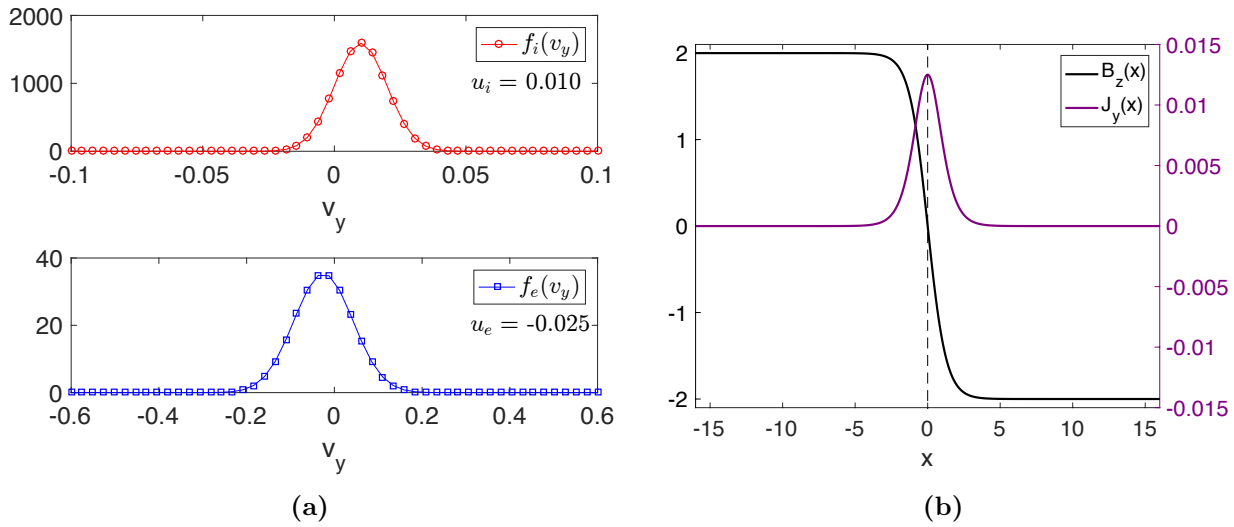

Figure 4.11: (a) Electron and ion distribution functions plotted as a function of v_y for the Harris current sheet equilibrium assuming $M_i/M_e = 180$, $\frac{T_i}{T_e} = 4$, $\frac{u_i}{v_{Ti}} = 1$, and $v_{Ti} = 1/100$. Note that the horizontal and vertical axes are different for f_i and f_e, since the thermal speed of electrons is much larger than that of the ions. (b) Associated current $J_y(x)$ and magnetic field $B_z(x)$ profiles.

with $Z_i/Z_e = -1$ and $\omega_{pi} = 1$. In effect, the fastest frequency in this system is the electron cyclotron frequency, and the fastest speed is the speed of light. These parameters set the time scale that needs to be resolved in the simulations.

The governing equations are the Vlasov equation for each species, and Faraday's law and Ampere's law in one dimension:

$$0 = \frac{\partial f_s}{\partial t} + v_x \frac{\partial f}{\partial x} + \frac{Z_s}{M_s}\left(E_x + \frac{\omega_{cp}}{\omega_{pp}}(v_y B_z)\right)\frac{\partial f_s}{\partial v_x} + \frac{Z_s}{M_s}\left(E_y + \frac{\omega_{cp}}{\omega_{pp}}(-v_x B_z)\right)\frac{\partial f_s}{\partial v_x} \quad (4.58)$$

$$\frac{\partial B_z}{\partial t} = -\frac{\omega_{pp}}{\omega_{cp}}\left(\frac{\partial E_y}{\partial x} - \frac{\partial E_x}{\partial y}\right) \quad (4.59)$$

$$\frac{\partial E_x}{\partial t} = -J_x \quad (4.60)$$

$$\frac{\partial E_y}{\partial t} = -\frac{\omega_{cp}}{\omega_{pp}}\frac{\partial B_z}{\partial x} - J_y. \quad (4.61)$$

The domain used for simulations is $x \in [-16, 16]$. To account for the large difference in thermal speeds, for electrons the velocity boundaries are set at $|v_{\max,e}| = 0.6$, and for ions the velocity boundaries are set at $|v_{\max,i}| = 0.1$. Since in the absence of collisions the two distribution functions only interact through the electromagnetic fields, the difference in velocity domain size does not affect the mechanics of the computation. The initialization described by Eqs. (4.33), (4.34), and (4.49), and the parameters in Table 4.2 for $v_{Ti} =$

Table 4.2: The parameters for initializing a self-consistent Harris current sheet equilibrium depend on different choices of ion thermal speed v_{Ti}, presented in fraction form and decimal form, and on the specified ratios $M_i/M_e = 180$, $T_i/T_e = 4$, $u_i/v_{Ti} = 1$, and $r_L/\ell = 1$.

v_{Ti}	u_i	ℓ	u_e	v_{Te}	B_0
1/10	1/10	$2\sqrt{2/5}$	$-1/40$	$3/(2\sqrt{5})$	2
1e-1	1e-1	1.26	2.5e-2	6.7e-1	2
1/100	1/100	$2\sqrt{2/5}$	$-1/400$	$3/(20\sqrt{5})$	2
1e-2	1e-2	1.26	-2.5e-3	6.7e-2	2
1/1000	1/1000	$2\sqrt{2/5}$	$-1/4000$	$3/(200\sqrt{5})$	2
1e-3	1e-3	1.26	-2.5e-4	6.7e-3	2

0.01 and $n_0 = 1$ is coupled with conducting wall boundary conditions, consistent with PIC simulations of the Harris current sheet [68, 69]. Note that the conducting wall boundaries are handled through ghost cells, which results in the additional constraint that $\partial n_s/\partial x = 0$. Since the values of the distribution functions and their gradient are very small at $x = \pm 16$ with values on the order of 10^{-11} this additional constraint is expected to alter the equilibrium slightly near the boundaries, but not have a noticeable effect overall.

4.3.1.2 Simulation results

Simulations of the one-dimensional Harris current sheet equilibrium in (x, v_x, v_y) phase space are conducted using grid resolutions $288 \times 64 \times 64$ and $576 \times 128 \times 128$. The evolution of the fields and currents from the simulation are shown in Fig. 4.12. The y-directed electric field, the net change in the y-directed current, and the net change in the z-directed magnetic field, all converge to zero at the expected rate for a fourth-order calculation. The x-directed current is non-zero on account of Langmuir oscillations, associated with the electrons oscillating about the ions. These Langmuir oscillations are evident in that the x-directed current oscillates about zero in localized regions near the center of the domain. Spatial oscillations are observed in the plot of E_y, and are the result of electromagnetic waves, which are generated in the middle of the domain, propagate to the boundaries, reflect off the conducting walls, and interfere with counterpropagating waves. The net change in the y-directed current, and the z-directed field are on the order of truncation error.

The evolution of the x-directed electric field, charge density, and divergence error are shown in Fig. 4.13 for two different resolutions. All of these quantities should converge to zero as the grid is refined, such that the solution approaches the initialized Harris equilibrium. Figure 4.13 shows that as the resolution is doubled, the magnitude of each quantity decreases by at least a factor of twenty in the middle of the domain, indicating fourth-order convergence. At boundaries, the solution does not converge and exhibits spurious oscillations in the electric field, which suggests that the solution is sensitive to the implementation of the conducting wall boundary conditions.

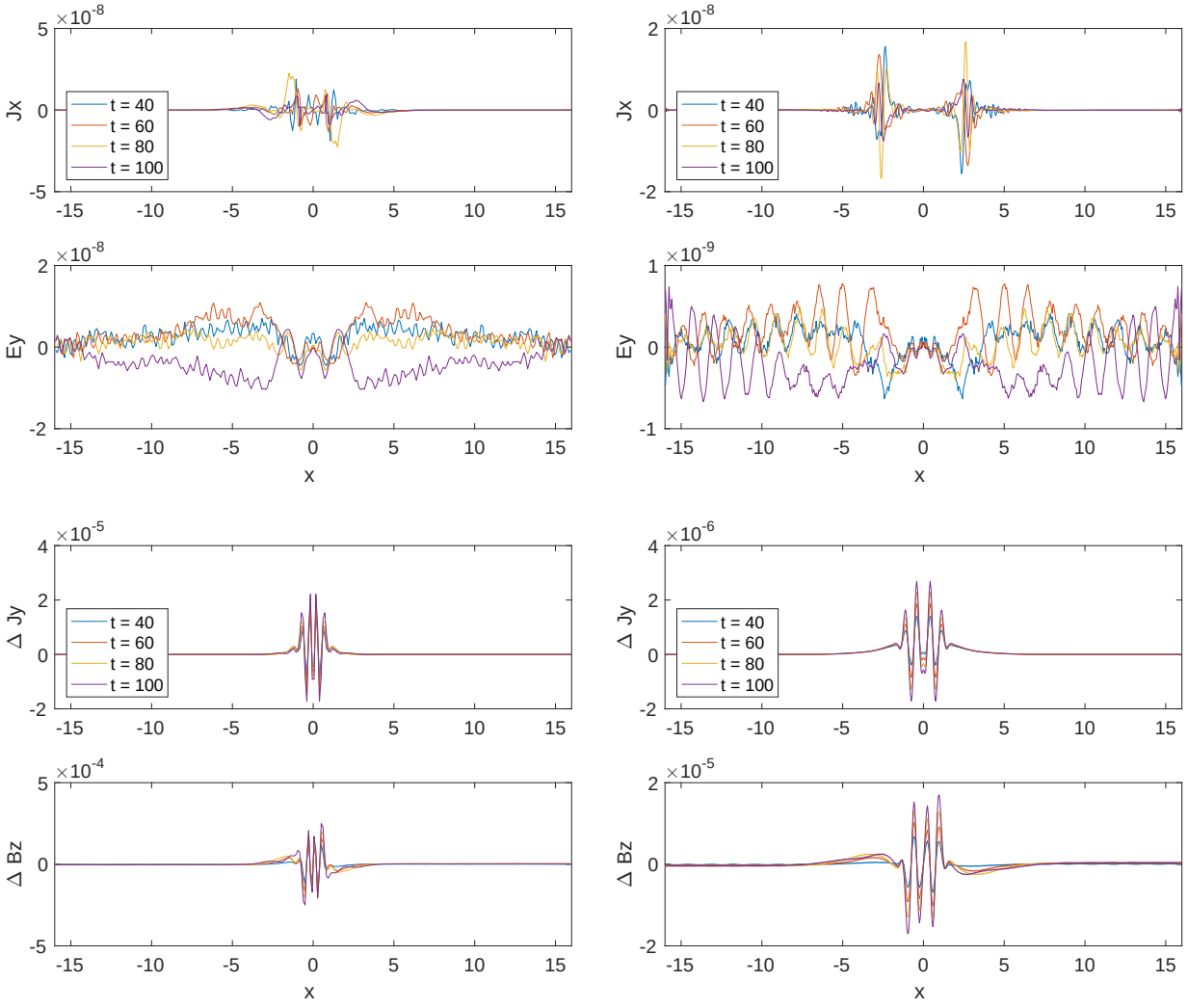

(a) $288 \times 64 \times 64$ resolution **(b)** $576 \times 128 \times 128$ resolution

Figure 4.12: The net x-directed current, the y-directed electric field, the net change in the y-directed current, and the net change in the z-directed magnetic field are plotted as a function of x for a simulation of the Harris equilibrium at two different resolutions. For a fourth-order discretization, all values are expected to decrease by a factor of sixteen as the resolution is doubled, which is what is observed for each quantity except for J_x. Time is normalized by ion plasma frequency.

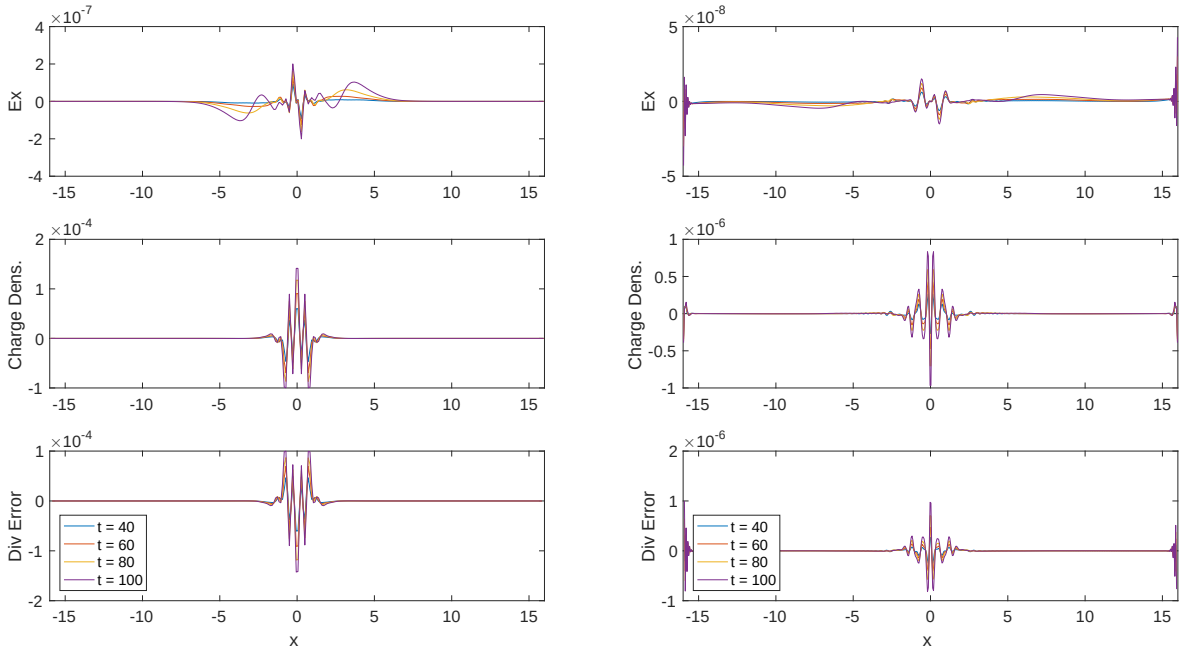

(a) 288 × 64 × 64 resolution **(b)** 576 × 128 × 128 resolution

Figure 4.13: The x-directed electric field, net charge density, and divergence error plotted for a simulation of the Harris equilibrium at two different resolutions. All values are expected to converge to zero as resolution is increased. Convergence is observed near the middle of the domain, but not at boundaries. Time is normalized by ion plasma frequency.

Notably the features near boundaries are only evident at high resolution, and only when the evolving species have disparate masses. Having species of different mass means that one species is likely to evolve to be displaced relative to the other, creating localized regions of non-zero charge density, as seen in the second row of plots in Fig. 4.13. The last row of plots in Fig. 4.13 shows that divergence errors are evident, as there is no divergence cleaning applied in this simulation. The numerical features at boundaries can be the result of the zero-gradient density constraint imposed in the implementation of specular reflection boundary conditions (see discussion in Section 3.4.3.3). As such, they can be mitigated in several ways. One way is by extending the domain size to ensure that the initial condition density gradients are zero to machine precision at the boundaries. This would ensure that the density gradient constraint imposed through the use of ghost cells is not violated. The oscillations can potentially be eliminated by implementing specular reflection through the extrapolation-and-copy procedure described in Section 3.8.3.1, in which case there would be no constraint on the density gradient at boundaries. Another approach would be to use characteristics-compatible boundary conditions instead of conducting-wall boundary conditions, so as to eliminate inconsistencies between the boundary condition and the initialized profiles. It is

worth pointing out that the boundary features are very small in magnitude, and in the context of PIC simulations such features would be obfuscated by noise. Since the study of non-periodic boundary conditions for distribution functions in continuum kinetic simulations is still in its nascent stages and since modeling of the Harris current sheet has been restricted to PIC methods, the investigation of boundary conditions in the context of this application is left for future research.

While a time-dependent simulation is not expected to be able to retain an equilibrium solution exactly on account of numerical errors, the solution is expected to converge to equilibrium as resolution is increased. With the exception of anomalous features at boundaries, the results of the simulations show that the Harris equilibrium is maintained over the course of 100 ion plasma frequencies, and that the solution converges at the expected rate to the initialized equilibrium. This verifies that the Vlasov-Maxwell solver is effectively able to capture the Harris current sheet configuration, and is able to model multiple distribution functions. The solver can be improved with further investigation of boundary conditions, which are left for future work.

Chapter 5

Development of the warm-temperature Dory-Guest-Harris instability benchmark [1]

Kinetic model algorithms in general, and continuum methods in particular, lack an arsenal of standardized benchmark problems. This is in part due to the comparatively recent development of continuum methods, but more fundamentally because PIC and continuum methods have different limitations. Whereas PIC accuracy is limited by both the number of particles and grid resolution in up to three spatial dimensions, continuum method accuracy is limited by grid resolution in up to six phase space dimensions. A consequence of this is that PIC methods most effectively model cold plasmas and beams, whereas continuum methods are more conducive to modeling finite or high temperature phenomena with smooth initial conditions. Thus standard benchmarks for PIC involving cold plasma assumptions with delta function initial conditions in velocity space [5] do not in general carry over to continuum methods.

Existing standardized benchmarks for continuum methods are largely limited to electrostatic phenomena that can be simulated in 2D (x, v_x) phase space. These standardized test problems include: weak Landau damping [51, 22, 52, 53, 71, 15, 72], strong Landau damping [22, 4, 52, 53, 71, 15], two-stream instability [22, 4, 52, 53, 71, 15], bump-on-tail instability [51, 22], and Langmuir waves [18, 73]. In addition, ion-acoustic turbulence has been used as a qualitative benchmark [51]. Plasma in the presence of magnetic fields have been simulated with continuum methods using the following much less developed test problems: particle gyration [74, 18], high-frequency electromagnetic waves [18], Raman scattering in 2D (x, v_x) [75] and in 4D (x, y, v_x, v_y) [18], Weibel instability [74, 76, 77, 78], Bernstein waves [72], relativistic wakefield acceleration [74, 79], and the Kelvin-Helmholtz instability [19, 80, 16].

To address the paucity of benchmark problems for continuum methods, this chapter investigates the Dory-Guest-Harris instability [81], which is a type of cyclotron harmonic instability [82, 83, 84] that is closely related to Bernstein modes [85], as a means of validating continuum kinetic simulations. In particular, the instability provides a straightforward

means by which to benchmark simulations of magnetized plasmas in a limited number of dimensions: one spatial dimension and two velocity dimensions (1D2V). The chapter is organized such that Section 5.1 draws on the theory of perpendicularly-propagating electrostatic waves in a warm magnetized plasma and provides a derivation of a closed-form dispersion relation for multiple species with arbitrary equilibrium distribution functions. Section 5.2 explores the dispersion relation characteristics for a Dory-Guest-Harris distribution and presents benchmarks against which continuum kinetic methods can be tested. Section 5.3 outlines a continuum fourth-order accurate 3D (x, v_x, v_y) Vlasov-Poisson solver that is used to simulate the instability. Sections 5.4 and 5.5 present simulation results and discuss the utility of the theoretical benchmarks as a validation platform.

5.1 Linear analysis of electrostatic $k_{\parallel} = 0$ waves in uniformly magnetized plasma

In kinetic theory constituent particle species in a plasma are described by probability distribution functions in phase space. The probability distribution function $f_s(\boldsymbol{x}, \boldsymbol{v}, t)$ for species s depends on the position coordinate $\boldsymbol{x}$, velocity coordinate $\boldsymbol{v}$, and time t. The evolution of the distribution function in the case of electrostatic fields is described by the Vlasov equation and Gauss's law. The non-dimensional form of this system of governing equations is

$$0 = \frac{\partial f_s}{\partial t} + \boldsymbol{v} \cdot \frac{\partial f_s}{\partial \boldsymbol{x}} + \frac{Z_s}{M_s}\left(\boldsymbol{E} \cdot \frac{\partial f_s}{\partial \boldsymbol{v}} + \frac{\omega_c}{\omega_p}\boldsymbol{v} \times \hat{\boldsymbol{b}} \cdot \frac{\partial f_s}{\partial \boldsymbol{v}}\right) \tag{5.1}$$

$$\nabla \cdot \boldsymbol{E} = \sum_s Z_s \int f_s d\boldsymbol{v}, \tag{5.2}$$

where f is the non-dimensional distribution function normalized by a nominal electron density n_0; $\hat{\boldsymbol{b}}$ is the direction of the magnetic field $\boldsymbol{B} = B\hat{\boldsymbol{b}}$; $M_s = m_s/m_e$ is the ratio of the mass of species s to the electron mass; and $Z_s = q_s/|e|$ is ionization state i.e. the ratio of the charge of species s to the electron charge. Note that t is the non-dimensional time, i.e. the physical time normalized by the electron plasma frequency. The factor in front of the cross product term is the ratio of electron cyclotron frequency $\omega_c = eB/m_e$ to electron plasma frequency $\omega_p = (n_0 e^2/\varepsilon_0 m_e)^{1/2}$, where $-e$ is the electron charge and ε_0 is the permittivity of free space. For electrostatic waves the electric field can be defined in terms of the electric potential ϕ and thus Gauss's law can be expressed as Poisson's equation – see Eq. (2.44).

The properties of small-amplitude waves depend on the equilibrium fields ($\boldsymbol{E}_0$, $\boldsymbol{B}_0$) and the equilibrium probability distribution function $f_{s0}(\boldsymbol{x}, \boldsymbol{v})$. The response of equilibria to perturbations can be analyzed using the linearized governing equations. In the linearization procedure the fields and the distribution function $f_s(\boldsymbol{x}, \boldsymbol{v}, t)$ are expressed as a sum of an equilibrium part and a perturbation about that equilibrium [2]: $\boldsymbol{E} = \boldsymbol{E}_0 + \boldsymbol{E}_1$, $\boldsymbol{B} = \boldsymbol{B}_0 + \boldsymbol{B}_1$, $f_s = f_{s0} + f_{s1}$. It is assumed that the perturbation values are much smaller in magnitude

than the equilibrium values, e.g. $f_{s1} \ll f_{s0}$, such that nonlinear products of the perturbation terms can be neglected.

For an electrostatic system with a time-invariant equilibrium magnetic field ($\boldsymbol{B} = \boldsymbol{B}_0$) and no equilibrium electric field ($\boldsymbol{E} = \boldsymbol{E}_1$), the departure away from equilibrium is described by the linearized Vlasov equation and Gauss's law. These are expressed in their non-dimensional form as

$$0 = \frac{\partial f_{s1}}{\partial t} + \boldsymbol{v} \cdot \frac{\partial f_{s1}}{\partial \boldsymbol{x}} + \frac{Z_s}{M_s}\left(\boldsymbol{E}_1 \cdot \frac{\partial f_{s0}}{\partial \boldsymbol{v}} + \frac{\omega_c}{\omega_p}\boldsymbol{v} \times \hat{\boldsymbol{b}}_0 \cdot \frac{\partial f_{s1}}{\partial \boldsymbol{v}}\right) \tag{5.3}$$

$$\nabla \cdot \boldsymbol{E}_1 = \sum_s Z_s \int f_{s1} d\boldsymbol{v}, \tag{5.4}$$

where $f_{s0}(v_\perp, v_\parallel)$ is the equilibrium velocity distribution for species s, $v_\perp$ and $v_\parallel$ are the non-dimensional components of electron velocity that are perpendicular and parallel to the equilibrium magnetic field $\boldsymbol{B}_0 = B_0\hat{\boldsymbol{b}}_0$, and f_{s1} is the first order perturbation of the probability distribution function away from equilibrium.

Equations (5.3) and (5.4) can be used to derive a dispersion relation for small-amplitude waves. For the purposes of this study, consideration is limited to electrostatic waves propagating perpendicular to the equilibrium magnetic field with wave vector components $k_\perp \neq 0$ and $k_\parallel = 0$. Such waves are not subject to the effects of collisionless cyclotron or Landau damping [81, 84]. Without loss of generality, let $\boldsymbol{B}_0 = B_0\hat{\boldsymbol{z}}$ and $\boldsymbol{k} = k_\perp\hat{\boldsymbol{x}}$ to simplify the analysis. Taking advantage of the azimuthal symmetry associated with the equilibrium magnetic field, and following the procedure detailed in Ref. [86, pp. 341–351], a cylindrical coordinate system is introduced in which velocity is defined as

$$\boldsymbol{v} = v_\perp \cos\theta\hat{\boldsymbol{x}} + v_\perp \sin\theta\hat{\boldsymbol{y}} + v_\parallel\hat{\boldsymbol{z}}. \tag{5.5}$$

Fourier transforms in space and time are applied to both f_1 and $\boldsymbol{E}_1$, such that the transformed versions are $\hat{f}_1$ and $\hat{\boldsymbol{E}}_1$, respectively. To analyze a single fixed wave number Fourier mode, $f_1 = \hat{f}_1 e^{i(\boldsymbol{k}\cdot\boldsymbol{x}-\omega t)}$ and $\boldsymbol{E}_1 = \hat{\boldsymbol{E}}_1 e^{i(\boldsymbol{k}\cdot\boldsymbol{x}-\omega t)}$ are substituted into Eq. (5.3), which yields

$$0 = -i\omega\hat{f}_{s1} + i\boldsymbol{v}\cdot\boldsymbol{k}\hat{f}_{s1} + \frac{Z_s}{M_s}\hat{\boldsymbol{E}}_1 \cdot \frac{\partial f_{s0}}{\partial \boldsymbol{v}} - \frac{Z_s\omega_c}{M_s\omega_p}\frac{\partial \hat{f}_{s1}}{\partial\theta}. \tag{5.6}$$

Note that $\boldsymbol{v}\cdot\boldsymbol{k} = k_\perp v_\perp\cos\theta$ and let the non-dimensionalized species-dependent cyclotron frequency be defined as $\Omega_{cs} = Z_s\omega_c/(M_s\omega_p)$, then the transformed linearized Vlasov equation is

$$0 = i\left(\frac{\omega}{\Omega_{cs}} - \frac{k_\perp v_\perp}{\Omega_{cs}}\cos\theta\right)\hat{f}_{s1} - \frac{\omega_p}{\omega_c}\hat{\boldsymbol{E}}_1 \cdot \frac{\partial f_{s0}}{\partial \boldsymbol{v}} + \frac{\partial \hat{f}_{s1}}{\partial\theta}. \tag{5.7}$$

Equation (5.7) is an ordinary differential equation that can be analytically solved for $\hat{f}_{s1}$. The solution is then substituted into the transformed Poisson equation

$$k_\perp^2\hat{\Phi}_1 = \sum_s Z_s \int \hat{f}_{s1} d\boldsymbol{v}, \tag{5.8}$$

such that the variables $\hat{\boldsymbol{E}}_1$, $\hat{\Phi}_1$, and f_{s1} are eliminated. See Appendix B.1 for details. The resulting dispersion relation, given by $D(\omega, k_\perp) = 0$, where $D(\omega, k_\perp)$ is an implicit function that can be expressed as

$$D(\omega, k_\perp) = 1 + \sum_s M_s \frac{\omega_p^2}{\omega_c^2} \int_0^\pi \frac{\sin\left(\frac{\omega}{\Omega_{cs}}\tau\right)}{\sin\left(\frac{\omega}{\Omega_{cs}}\pi\right)} \sin(\tau)\, F_0(\tau + \pi) d\tau = 0 \tag{5.9}$$

$$F_0(\tau) = \int_0^\infty f_{s0}(v_\perp) J_0\left(2\frac{k_\perp v_\perp}{\Omega_{cs}} \sin\frac{\tau}{2}\right) 2\pi v_\perp dv_\perp, \tag{5.10}$$

where J_0 is the zeroth order Bessel function of the first kind. Note that $v_\parallel$ dependence has been eliminated since it does not play a role for $k_\parallel = 0$ waves. Note also that the dispersion relation is independent of the sign of Ω_{cs} because J_0 is an even function. Thus, for convenience, Ω_{cs} is henceforth defined to be positive such that $\Omega_{cs} = |Z_s|\omega_c/(M_s\omega_p)$. Equation (5.9) is the non-dimensional multi-species closed-form dispersion relation and is a generalization of the dimensional single-species closed-form expression presented without proof in Ref. [84]. The closed-form representation (see Appendix B.1 for a complete derivation) does not involve infinite sums, and thus a solution $\omega(k_\perp)$ can be computed numerically with great accuracy for any arbitrary equilibrium distribution function.

The dispersion relation describes the propagation of waves of the form $e^{i(k_\perp x - \omega t)}$. To obtain an explicit relation for frequency as a function of wavenumber, i.e. $\omega(k_\perp)$, the roots of Eq. (5.9) are evaluated numerically for real values of $k_\perp$. In general frequency ω is complex-valued, such that $\omega = \omega_r + i\omega_i$. The real and imaginary components of frequency indicate the temporal evolution of the perturbation: ω_r provides the oscillation frequency and ω_i, depending on the sign, provides the growth ($\omega_i > 0$) or decay ($\omega_i < 0$) rate. For a given mixed-complex frequency solution of the dispersion relation, its complex conjugate is also a solution; however, because exponential growth $e^{|\omega_i|t}$ dominates over an exponential rate of decay $e^{-|\omega_i|t}$, only the exponentially growing solution is of consequence.

5.2 Dory-Guest-Harris instability in warm plasmas

The dispersion relation in Eq. (5.9) describes the properties of electrostatic waves propagating perpendicular to a uniform externally applied magnetic field in a spatially uniform infinite plasma. The properties of these waves over small and large time scales are relevant to a number of applications [87] including neutral beam heating in tokamaks [88, 89], electrostatic cyclotron harmonic emissions in the magnetosphere [90, 91], auroral precipitation [92, 93], magnetic mirror loss cones [94], and electron cyclotron resonance heating [95]. Notably, the exact dispersion relation properties are determined by the equilibrium distribution function in velocity space, $f_0(v_\perp)$.

Different probability distribution functions and their associated stability properties have been investigated theoretically [81, 83, 84, 85, 96] and computationally [82, 97, 98]. In

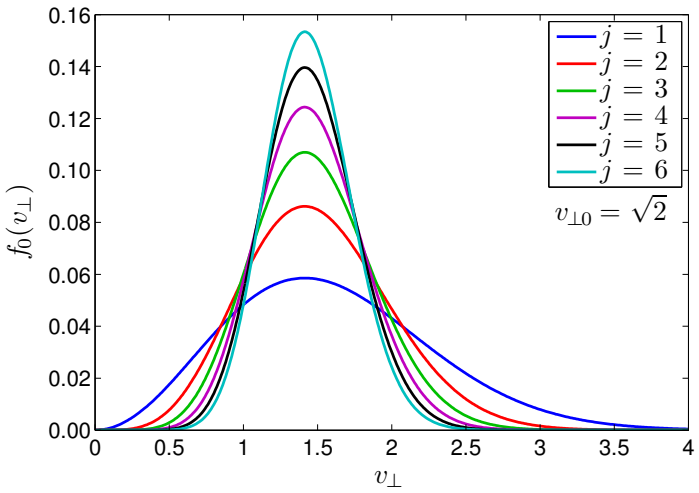

Figure 5.1: Dory-Guest-Harris equilibrium probability distribution function in velocity space for different values of j. See Eq. (5.11). The larger the value of non-negative integer j, the more peaked the distribution. When superimposed with a spatially-dependent perturbation, the distribution function is unconditionally stable for $j = \{0, 1, 2\}$ and conditionally stable for $j \geq 3$.

particular, Dory et al. [81] identified that such waves are unstable for a warm ring velocity distribution provided that (a) the distribution $f_0(v_\perp)$ is sufficiently peaked, (b) the ratio of plasma frequency to cyclotron frequency is above a specified threshold value, and (c) the wave number falls in a specific range. The class of single-species velocity distribution functions investigated by Dory et al. [81] can be expressed as:

$$f_0(v_\perp) = \frac{1}{\pi \alpha_\perp^2 j!} \left(\frac{v_\perp}{\alpha_\perp} \right)^{2j} \exp\left(-\frac{v_\perp^2}{\alpha_\perp^2} \right), \tag{5.11}$$

where $f_0(v_\perp)$ is the normalized equilibrium distribution function whose integral over the velocity domain has a value of one. Parameter $\alpha_\perp$ and non-negative integer j control the velocity spread of the distribution and the location of the peak. The distribution is peaked at $v_{\perp 0} = j^{1/2}\alpha_\perp$ and has a half-width at half-maximum that is approximated by $\alpha_\perp / j^{1/2}$. The half-width approximation is incorrectly presented in Ref. [81].

Note the dependence of the velocity distribution function on j: $j = 0$ corresponds to a Maxwellian, $j > 0$ corresponds to a ring, and in the limit of $j \to \infty$ the distribution is a delta function ring with infinitesimal velocity spread. Figure 5.1 shows the velocity distribution function for different values of j. Dory et al. [81] identified that for $j = \{0, 1, 2\}$ the equilibrium distribution function is unconditionally stable; for $j = \{3, 4, 5\}$ it is conditionally stable and supports wave frequencies that are either purely real or purely imaginary; for $j \geq 6$ the distribution is conditionally stable and supports wave frequencies that have purely real, purely imaginary, or mixed complex frequencies.

While the dispersion relation of Eq. (5.9) applies more generally, the evolution of the Dory-Guest-Harris instability concerns particles of a single species. It is assumed that the plasma is composed of particle species that have disparate masses, e.g. ions and electrons, and thereby the interactions between species are not important [81]. Thus on time scales over which ion motion can be neglected, the only evolving distribution function is that of the electrons. Similarly, on time scales much greater than the electron plasma frequency, the only evolving distribution function is that of the ions. In effort to avoid ambiguity, f is henceforth the electron distribution function and a fixed uniform ion background is assumed.

The dispersion relation for the Dory-Guest-Harris distribution can be solved numerically for frequency as a function of wave number. It is convenient to solve for the normalized frequency $\tilde{\omega} = \tilde{\omega}_r + i\tilde{\omega}_i$ as a function of the normalized wave number $\tilde{k}$, defined respectively as

$$\tilde{\omega} = \omega/\Omega_c \tag{5.12}$$

$$\tilde{k} = k_\perp v_{\perp 0}/\Omega_c, \tag{5.13}$$

where $\Omega_c = \omega_c/\omega_p$. As described in Section 5.1, time is normalized by ω_p. Solutions to the dispersion relation are found by selecting a particular real wave number value, $\tilde{k}^*$, and finding the value of frequency $\tilde{\omega}$ for which the equality $D(\tilde{\omega}, \tilde{k}^*) = 0$ is satisfied. In cases where $\tilde{\omega}$ is purely real, or purely imaginary, the bisection method can be used to find the frequency. When frequency is mixed complex, a minimization of $(D(\tilde{\omega}, \tilde{k}^*))^2$ is performed to solve for the real and imaginary components of frequency. In the minimization method, an initial guess is informed by first evaluating $D(\tilde{\omega}_r, \tilde{\omega}_i, \tilde{k}^*)$ for a range of real and imaginary frequency values and then finding the intersection of the $\mathrm{Re}(D(\tilde{\omega}_r, \tilde{\omega}_i, \tilde{k}^*)) = 0$ contours with the $\mathrm{Im}(D(\tilde{\omega}_r, \tilde{\omega}_i, \tilde{k}^*)) = 0$ contours in the $\tilde{\omega}_r$-$\tilde{\omega}_i$ plane. Note that $\tilde{\omega}(\tilde{k})$ is multivalued, so that for each value of $\tilde{k}$, there are multiple values of $\tilde{\omega}$ that satisfy the dispersion relation of Eq. (5.9). These multiple values correspond to different harmonics. Thus, when numerically solving for frequency as a function of wavenumber, it is helpful to limit the range of $\tilde{\omega}$ over which solutions are sought.

The resulting dispersion diagram for the case of a Maxwellian distribution ($j = 0$, $\alpha_\perp = 2^{1/2}$) is shown in Fig. 5.2, and is consistent with the results presented in Refs. [83, 84]. Because frequency is real-valued for all values of wave number independent of the ratio ω_p/ω_c, the Maxwellian distribution is unconditionally stable. The dispersion diagrams for the unconditionally stable case of $j = 2$ are shown in Fig. 5.3 for different values of ω_p/ω_c. As is consistent with [84], the cutoff frequencies (for which $\tilde{k} = 0$) are: at integer multiples of the non-dimensional cyclotron frequency, $n\Omega_c$ with $|n| > 1$; and at the non-dimensional upper hybrid frequency, $(1 + \Omega_c^2)^{1/2}$. Likewise, the resonance frequencies (for which $\tilde{k}$ is infinite), are at $n\Omega_c$ with $|n| > 0$.

For conditionally stable cases of $j = 4$ and $j = 6$ dispersion diagrams are shown in Fig. 5.4 and Fig. 5.5, respectively. Instability for the $j = 4$ equilibrium distribution function is evidenced when $\tilde{\omega}_i > 0$, which occurs for a finite range of wave numbers provided that the ratio of electron plasma frequency to cyclotron frequency exceeds the threshold value

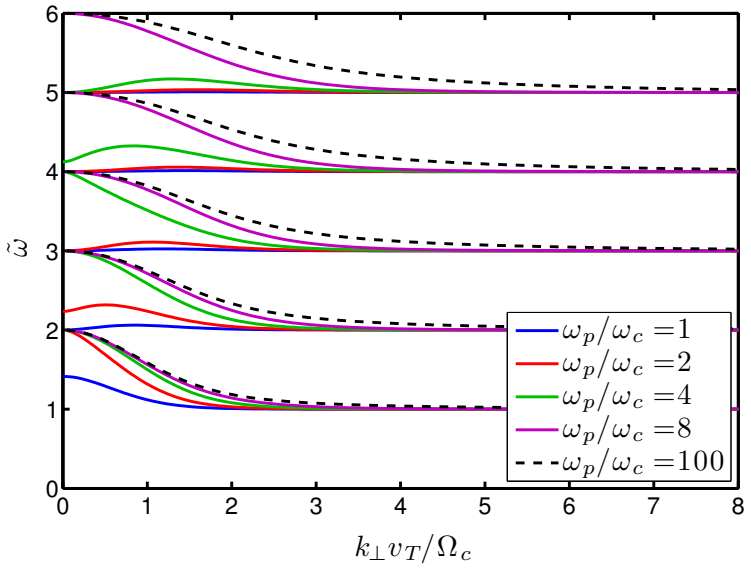

Figure 5.2: Dispersion diagram for a Maxwellian distribution function in velocity space, with $j = 0$ and $\alpha_\perp = 2^{1/2}$ in Eq. (5.11). The Maxwellian distribution is unconditionally stable such that frequency is real-valued, independent of ω_p/ω_c and of $k_\perp v_T/\Omega_c$. Note that the wave number (see Eq. (5.13)) is normalized using thermal velocity defined by $v_T^2 = \alpha_\perp^2/2$ since $v_{\perp 0}$ is zero for a Maxwellian distribution.

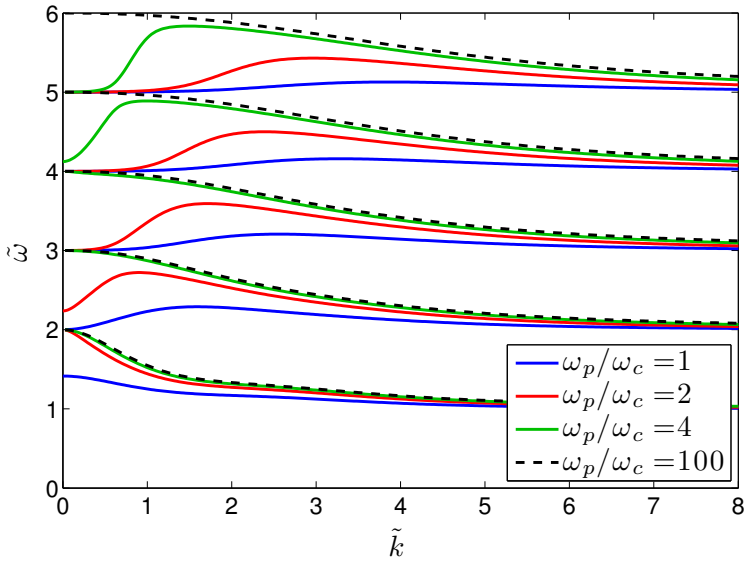

Figure 5.3: Dispersion diagram for an unconditionally stable warm ring velocity distribution function with $j = 2$ and $v_{\perp 0} = \sqrt{2}$, namely $\tilde{\omega}_i = 0$. Stability is evidenced by a real-valued frequency $\tilde{\omega}$ for each $\tilde{k}$, independent of the value of ω_p/ω_c.

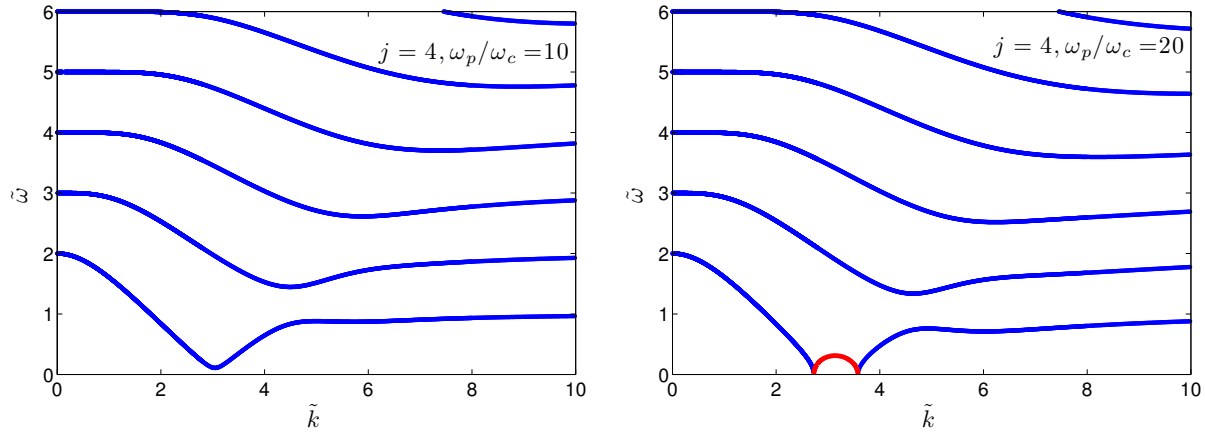

Figure 5.4: Dispersion diagrams for a conditionally stable velocity distribution function with $j = 4$ and $v_{\perp 0} = \sqrt{2}$. For these parameters frequency is either purely real (blue) or purely imaginary (red). Instability can occur when $\omega_p/\omega_c \gtrsim 10.5$. For $\omega_p/\omega_c = 20$, instability occurs when $\tilde{k} \in [2.73, 3.58]$.

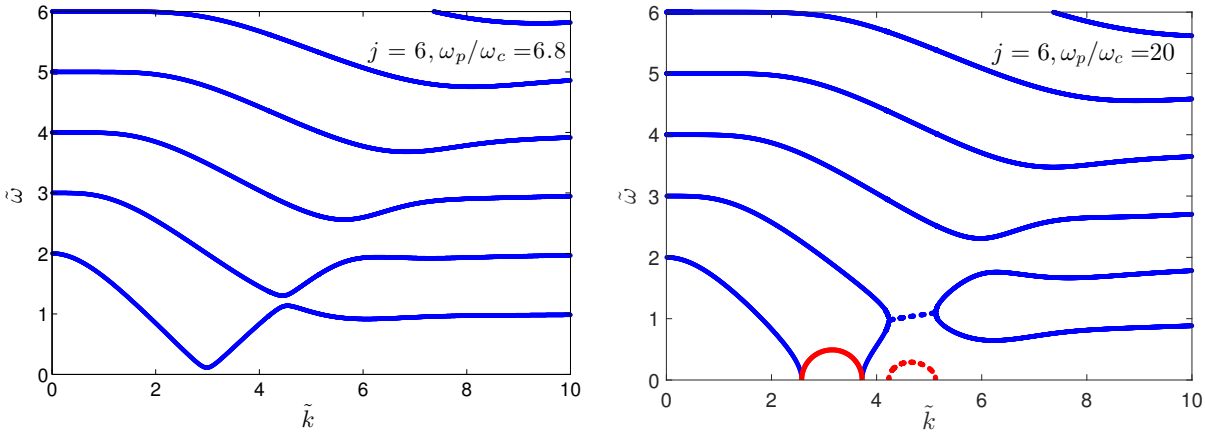

Figure 5.5: Dispersion diagrams for a conditionally stable velocity distribution function with $j = 6$ and $v_{\perp 0} = \sqrt{2}$. Instability can occur when $\omega_p/\omega_c \gtrsim 7.0$. Purely real frequencies ($\omega_r \neq 0, \omega_i = 0$) are solid blue, purely imaginary frequencies ($\omega_r = 0, \omega_i \neq 0$) are solid red, real components of mixed complex frequencies ($\omega_r \neq 0, \omega_i \neq 0$) are shown by dashed blue, imaginary components of mixed complex frequencies are shown in dashed red. For $\omega_p/\omega_c = 20$ an electrostatic wave exhibits pure growth when $\tilde{k} \in [2.57, 3.73]$, and growth with propagation when $\tilde{k} \in [4.23, 5.13]$.

of ≈ 10.5. In this case there are no mixed-complex frequency solutions to the dispersion relation. For $j = 6$ the distribution function is unstable for certain ranges of $\tilde{k}$ provided that $\omega_p/\omega_c \gtrsim 7.0$. Above this threshold value, instabilities with purely imaginary or mixed

complex frequencies can occur. Note that the threshold value of ω_p/ω_c above which instability can occur is smaller for larger values of j. These instability properties are consistent with the thresholds presented in Ref. [81]. As j is increased, the $\tilde{\omega}(\tilde{k})$ for the warm ring smoothly approaches the dispersion relation for the delta function ring [81]. Dispersion diagrams for delta function distributions are presented in Refs. [5, 84].

5.3 Vlasov-Poisson model and continuum algorithm

5.3.1 Non-dimensional 3D (x, v_x, v_y) Vlasov-Poisson system and domain specifications

The evolution of the Dory-Guest-Harris probability distribution function in response to electrostatic waves propagating perpendicular to an equilibrium magnetic field can be simulated in three-dimensional phase space: position coordinate x and velocity coordinates v_x and v_y, with magnetic field in the $\hat{z}$ direction and electric field of the wave in the $\hat{x}$ direction. This evolution is described by the non-relativistic Vlasov-Poisson equation system. In non-dimensional conservation law form the 3D (x, v_x, v_y) Vlasov-Poisson system of governing equations is:

$$0 = \frac{\partial f}{\partial t} + \frac{\partial}{\partial x}\left(v_x f\right) + \frac{Z_e}{M_e}\frac{\partial}{\partial v_x}\left(\left[E_x + v_y\frac{\omega_c}{\omega_p}\right] f\right) + \frac{Z_e}{M_e}\frac{\partial}{\partial v_y}\left(-v_x\frac{\omega_c}{\omega_p} f\right) \tag{5.14}$$

$$-\frac{\partial^2\phi}{\partial x^2} = 1 - \int_{-\infty}^{\infty}\int_{-\infty}^{\infty} f dv_x dv_y \tag{5.15}$$

where Eq. (5.14) is the reduced dimension version of Eq. (5.1), f is the electron distribution function, and $Z_e/M_e = -1$. The spatial domain has length L, such that $x \in [0, L]$. To minimize computational cost, the velocity domain is truncated such that $v_x, v_y \in [-v_{\max}, v_{\max}]$ with finite $v_{\max}$. Note that the Poisson equation contains number density contributions from the electrons and from the ions, which are assumed to be fixed and uniformly distributed in space. The system is quasineutral such that the righthand side of Eq. (5.15) integrated over the spatial domain has a value of zero.

The domain is divided into $N_x \times N_{v_x} \times N_{v_y}$ cells where N_x, N_{v_x}, and N_{v_y} are the number of cells in each of the three phase space directions. Boundary conditions are imposed using ghost cells that are appended to the domain to allow for finite-volume calculations at boundaries. Because the plasma is assumed to be spatially infinite, periodic boundary conditions are applied in the $\hat{x}$ direction. Solid-wall boundary conditions are applied at $|v_x|, |v_y| = v_{\max}$ by: setting the value of the distribution function to zero in the velocity-boundary ghost cells i.e. enforcing $f = 0$ for $|v| > v_{\max}$; and setting the values of fluxes at velocity boundaries to zero. The latter stipulation ensures that the integral of the distribution function over the entire phase space domain is conserved. The solid-wall boundary condition is valid provided that $f(v_{\max})$ is sufficiently close to zero.

5.3.2 Fourth-order finite-volume discretization

The non-dimensional Vlasov-Poisson equation system is solved using the finite-volume discretization described in Chapter 3, except in this case the primary variable is a volume average such that the quadrature rule in Eq. (3.31) is used instead of the quadrature rule in Eq. (3.30). The algorithm outline is included here to illustrate the mechanics of the discretization with these modifications.

The probability distribution function is initialized by a fourth-order cell-average of the analytic $f(x, v_x, v_y)|_{t=0}$, such that the cell-average value is computed as the sum of the cell-center value and second derivative corrections:

$$\langle f \rangle_{i,j,k} = f_{i,j,k} + \frac{h_x^2}{24}\left(\frac{f_{i+1,j,k} - 2f_{i,j,k} + f_{i-1,j,k}}{h_x^2}\right) + \frac{h_{v_x}^2}{24}\left(\frac{f_{i,j+1,k} - 2f_{i,j,k} + f_{i,j-1,k}}{h_{v_x}^2}\right) + \frac{h_{v_y}^2}{24}\left(\frac{f_{i,j,k+1} - 2f_{i,j,k+1} + f_{i,j,k-1}}{h_{v_y}^2}\right) \quad (5.16)$$

where $\langle \cdot \rangle$ denotes the cell-average value, subscripts i, j, k denote discretized domain cell indices, and h_x, h_{v_x} and h_{v_y} are the grid spacings in the $\hat{x}$, $\hat{v}_x$, and $\hat{v}_y$ directions, respectively. Note that the implementation of this algorithm relies on the quadrature rule given in Eq. (3.31), and on the fact that cell-average and cell-integrated values in Cartesian coordinates are equivalent to within a constant factor.

For each time step, the algorithm for advancing the cell-average distribution function is:

1. The Poisson equation is solved for the cell-average potential $\langle \phi \rangle_i$ using a fourth-order finite-volume stencil:

$$-\left(-\frac{1}{12}\langle \phi \rangle_{i+2} + \frac{4}{3}\langle \phi \rangle_{i+1} - \frac{5}{2}\langle \phi \rangle_i + \frac{4}{3}\langle \phi \rangle_{i-1} - \frac{1}{12}\langle \phi \rangle_{i-2}\right) = 1 - \sum_j \sum_k \langle f \rangle_{i,j,k} h_{v_x} h_{v_y}, \quad (5.17)$$

   with the constraint $\sum_i \langle \phi \rangle_i = 0$, which is used as a means to ensure that the net electric field in the domain is zero.

2. The cell-average electric field $\langle E \rangle_i$ is computed using the cell-average potential:

$$\langle E \rangle_i = -\frac{8}{12h_x}\Big(\langle \phi \rangle_{i+1} - \langle \phi \rangle_{i-1}\Big) + \frac{1}{12h_x}\Big(\langle \phi \rangle_{i+2} - \langle \phi \rangle_{i-2}\Big). \quad (5.18)$$

3. The cell-average values of the distribution function are interpolated to cell-faces, using

a one-point upstream-centered stencil:

$$f^{x\text{-face}}_{i+\frac{1}{2},j,k} = \begin{cases} \frac{1}{60}\Big(\quad 2f_{i-2,j,k} - 13f_{i-1,j,k} + 47f_{i,j,k} \\ \qquad\qquad + 27f_{i+1,j,k} - 3f_{i+2,j,k} \Big) & \text{for } v_x > 0 \\ \frac{1}{60}\Big(-3f_{i-1,j,k} + 27f_{i,j,k} + 47f_{i+1,j,k} \\ \qquad\qquad - 13f_{i+2,j,k} + 2f_{i+3,j,k} \Big) & \text{for } v_x \leq 0 \end{cases} \tag{5.19}$$

$$f^{v_x\text{-face}}_{i,j+\frac{1}{2},k} = \begin{cases} \frac{1}{60}\Big(\quad 2f_{i,j-2,k} - 13f_{i,j-1,k} + 47f_{i,j,k} \\ \qquad\qquad + 27f_{i,j+1,k} - 3f_{i,j+2,k} \Big) & \text{for } Z_e\left(E_x + v_y\frac{\omega_c}{\omega_p}\right) > 0 \\ \frac{1}{60}\Big(-3f_{i,j-1,k} + 27f_{i,j,k} + 47f_{i,j+1,k} \\ \qquad\qquad - 13f_{i,j+2,k} + 2f_{i,j+3,k} \Big) & \text{for } Z_e\left(E_x + v_y\frac{\omega_c}{\omega_p}\right) \leq 0 \end{cases} \tag{5.20}$$

$$f^{v_y\text{-face}}_{i,j,k+\frac{1}{2}} = \begin{cases} \frac{1}{60}\Big(\quad 2f_{i,j,k-2} - 13f_{i,j,k-1} + 47f_{i,j,k} \\ \qquad\qquad + 27f_{i,j,k+1} - 3f_{i,j,k+2} \Big) & \text{for } v_x\frac{\omega_c}{\omega_p} > 0 \\ \frac{1}{60}\Big(-3f_{i,j,k-1} + 27f_{i,j,k} + 47f_{i,j,k+1} \\ \qquad\qquad - 13f_{i,j,k+2} + 2f_{i,j,k+3} \Big) & \text{for } v_x\frac{\omega_c}{\omega_p} \leq 0 \end{cases} \tag{5.21}$$

4. Flux terms on the righthand side of Eq. (5.14) are evaluated using cell-face values of E, v_x, v_y, f, and B_z and associated fourth-order corrections [31]:

$$F^{x\text{-face}}_{i+\frac{1}{2},j,k} = f^{x\text{-face}}_{i+\frac{1}{2},j,k}\left\langle v_x\right\rangle_j + \frac{h_{v_x}}{24}\left(f^{x\text{-face}}_{i+\frac{1}{2},j+1,k} - f^{x\text{-face}}_{i+\frac{1}{2},j-1,k}\right) \tag{5.22}$$

$$\begin{aligned} F^{v_x\text{-face}}_{i,j+\frac{1}{2},k} = {} & f^{v_x\text{-face}}_{i,j+\frac{1}{2},k}\left\langle E\right\rangle_i + \frac{1}{48}\left(f^{v_x\text{-face}}_{i+1,j+\frac{1}{2},k} - f^{v_x\text{-face}}_{i-1,j+\frac{1}{2},k}\right)\left(\left\langle E\right\rangle_{i+1} - \left\langle E\right\rangle_{i-1}\right) \\ & + \frac{\omega_c}{\omega_p}\left[f^{v_x\text{-face}}_{i,j+\frac{1}{2},k}\left\langle v_y\right\rangle_k + \frac{h_{v_y}}{24}\left(f^{v_x\text{-face}}_{i,j+\frac{1}{2},k+1} - f^{v_x\text{-face}}_{i,j+\frac{1}{2},k-1}\right)\right] \end{aligned} \tag{5.23}$$

$$F^{v_y\text{-face}}_{i,j,k+\frac{1}{2}} = \frac{\omega_c}{\omega_p}\left[f^{v_y\text{-face}}_{i,j,k+\frac{1}{2}}\left\langle v_x\right\rangle_j + \frac{h_{v_x}}{24}\left(f^{v_y\text{-face}}_{i,j+1,k+\frac{1}{2}} - f^{v_y\text{-face}}_{i,j-1,k+\frac{1}{2}}\right)\right]. \tag{5.24}$$

Note that x, v_x, and v_y are independent coordinates, electric field depends only on position, and the magnetic field is constant.

5. Eq. (5.14) is expressed in terms of a time derivative and divergence of fluxes:

$$\begin{aligned} \frac{\partial}{\partial t}\left\langle f\right\rangle_{i,j,k} = {} & -\frac{1}{h_x}\left(F^{x\text{-face}}_{i+\frac{1}{2},j,k} - F^{x\text{-face}}_{i-\frac{1}{2},j,k}\right) + \frac{1}{h_{v_x}}\left(F^{v_x\text{-face}}_{i,j+\frac{1}{2},k} - F^{v_x\text{-face}}_{i,j-\frac{1}{2},k}\right) \\ & - \frac{1}{h_{v_y}}\left(F^{v_y\text{-face}}_{i,j,k+\frac{1}{2}} - F^{v_y\text{-face}}_{i,j,k-\frac{1}{2}}\right). \end{aligned} \tag{5.25}$$

6. $\langle f \rangle_{i,j,k}$ is advanced in time using a fourth-order explicit Runge-Kutta method.

The one-point upstream-centered stencil used to interpolate $\langle f \rangle$ to cell faces is an upwind-biased method [42] that takes into account the direction of hyperbolic advection. Thus upwind-biasing provides dissipation to damp out numerical errors with wavelengths $2h_x, 2h_{v_x}$, and $2h_{v_y}$, which are inherent to high-order centered-difference stencils.

For explicit methods the time step is limited by the CFL condition, which depends on grid spacing in each direction (h_x, h_{v_x}, h_{v_y}) and the fastest advection speed in the system. In this case, the advection speeds that control the distribution function evolution in the $\hat{x}$, $\hat{v}_x$, and $\hat{v}_y$ directions are: $|v_x|$, $|E_x + v_y \frac{\omega_p}{\omega_c}|$, and $|v_x \frac{\omega_p}{\omega_c}|$, respectively. In phase space calculations, velocity is a coordinate and therefore the extent of the domain in the velocity direction imposes a limit on the time step. The limit on the time step size is

$$\Delta t \leq \sigma \cdot \min \left\{ \frac{h_x}{v_{\max}}, \frac{h_{v_x}}{|E|_{\max} + \frac{\omega_c}{\omega_p} v_{\max}}, \frac{h_{v_y}}{\frac{\omega_c}{\omega_p} v_{\max}} \right\}, \tag{5.26}$$

where $|E|_{\max}$ is the maximum of the absolute value of the electric field at any given time and σ is the CFL number. The described high-order upwind-biased spatial discretization sets a constraint on the CFL, such that σ must be less than ≈ 0.6 to ensure that the method is numerically stable.

5.3.3 Initial condition and its influence on the dominant mode

The initial condition for the Dory-Guest-Harris instability involves an equilibrium velocity distribution function specified in Eq. (5.11), and a position-dependent sinusoidal perturbation which constitutes the electrostatic wave. It is important to note that the dependence of the perturbation on v_x and v_y is arbitrary; however, this dependence dictates how strongly the dominant, fastest-growing mode is excited. This is related to the fact that $\tilde{\omega}_i > 0$ solutions to the dispersion relation identify the growth rate of the fastest growing mode, whereas other modes will exhibit smaller growth rates. A perturbation with an arbitrary velocity dependence leads to a growth of many different modes, only one of which, over a long period of time, emerges as the dominant mode with the largest growth rate.

In order to determine the velocity dependence of a perturbation that more strongly excites the fastest-growing mode, a perturbation that is symmetric in velocity is first investigated,

such that the initial condition is

$$f(x,v_x,v_y)|_{t=0} = \frac{1}{\pi\alpha_\perp^2 j!}\left(\frac{v_x^2+v_y^2}{\alpha_\perp^2}\right)^j \exp\left(-\frac{v_x^2+v_y^2}{\alpha_\perp^2}\right)\left(1+\epsilon\sin\left(\frac{\tilde{k}\,\Omega_c}{v_{\perp 0}}x\right)\right) \tag{5.27}$$

$$x \in [0, L]$$
$$v_x \in [-v_{\max}, v_{\max}]$$
$$v_y \in [-v_{\max}, v_{\max}]$$
$$\tilde{k} = \frac{2\pi}{L}\frac{v_{\perp 0}}{\Omega_c}$$

where $\epsilon \ll 1$ is the amplitude of the perturbation. This distribution, with $\tilde{k}$ and ω_p/ω_c for which the dispersion relation predicts a non-zero imaginary component of frequency, is evolved for a time period of several hundred plasma frequencies. Isosurfaces of the peak values of $f(x,v_x,v_y)$ at the final time gives an indication of the dominant mode topology. Informed by this qualitative analysis, an initial condition with a perturbation of the following form is found to most effectively excite the dominant mode:

$$f(x,v_x,v_y)|_{t=0} = \frac{1}{\pi\alpha_\perp^2 j!}\left(\frac{v_x^2+v_y^2}{\alpha_\perp^2}\right)^j \exp\left(-\frac{v_x^2+v_y^2}{\alpha_\perp^2}\right)\left(1+\epsilon\sin\left(4\theta-\frac{\tilde{k}\,\Omega_c}{v_{\perp 0}}x\right)\right) \tag{5.28}$$

$$\theta = \arctan\left(\frac{v_y}{v_x}\right). \tag{5.29}$$

This perturbation is peaked along a four-stranded helix in phase space coordinates (x, v_x, v_y), with a position-dependent sinusoidal wave with wavelength L and a velocity-dependent component that excites the fastest growing mode for cases of $\tilde{\omega}_i > 0$. See Fig. 5.7 for a depiction of the peaks of this perturbation. Figure 5.6 shows the electric field energy evolution resulting from using Eq. (5.27) as the initial condition and Eq. (5.28) as the initial condition. A simple sinusoidal perturbation excites many modes, whereas the helical perturbation is able to strongly excite the fastest growing mode.

For all simulation results presented here, the perturbation amplitude is chosen to be $\epsilon = 1\times10^{-4}$ and parameter $\alpha_\perp$ is selected to have a value of $(2/j)^{1/2}$ so that $v_{\perp 0} = \sqrt{2}$. The perturbation amplitude determines how quickly the instability saturates, and thus for smaller ϵ the linear phase of the instability lasts longer. In general $\alpha_\perp$ and j should be selected subject to constraints associated with resolution limits (due to computational cost) and the CFL condition.

Another aspect of the initial condition that deserves particular attention is the normalization. The integral of Eq. (5.27) and Eq. (5.28) over the infinite velocity domain is one, which ensures that the system being modeled is globally charge neutral. However, for computational cost purposes associated with resolution and the CFL stability limit on the time step size (see Eq. (5.26)), the velocity domain is truncated such that in simulations $v_x, v_y \in [-v_{\max}, v_{\max}]$. In the simulations discussed in this chapter, $v_{\max} = 4$. Using a higher

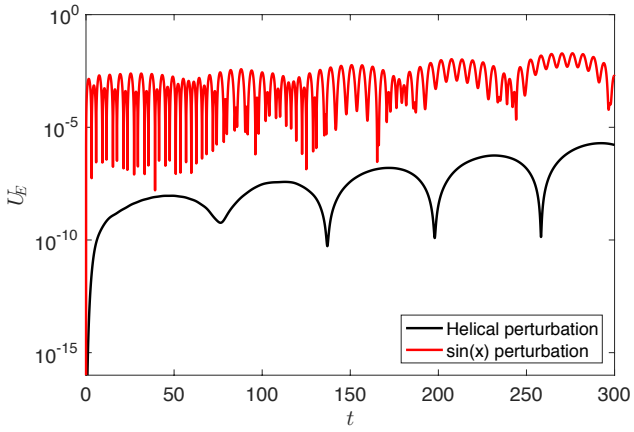

Figure 5.6: The evolution of electric field energy for two different types of perturbations: a simple sinusoidal perturbation given by Eq. (5.27) and the helical perturbation given by Eq. (5.28). The latter perturbation is able to strongly excite the fastest growing mode.

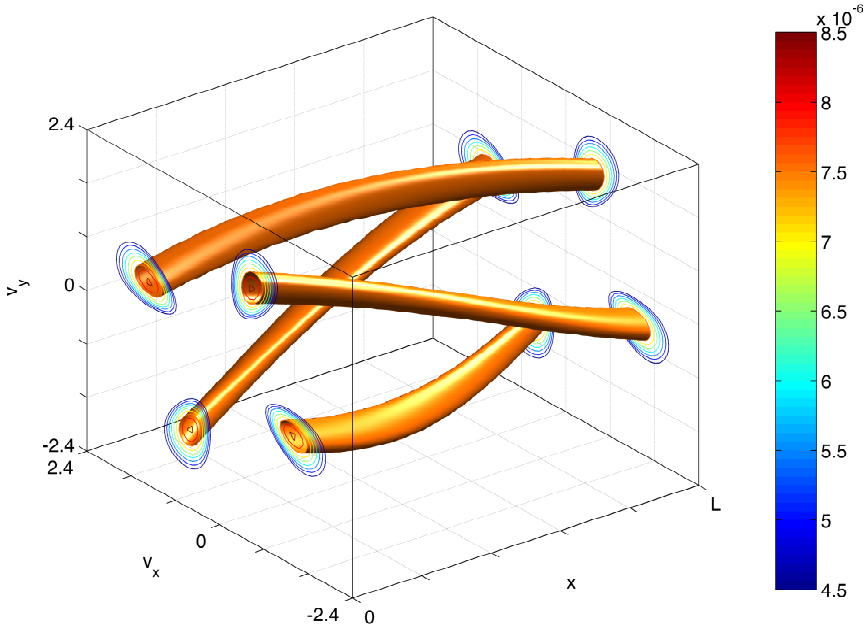

Figure 5.7: Isosurface $(f - f_0) = 7.5 \times 10^{-6}$ in phase space at initial time, depicting the helical structure of the initial perturbation that strongly excites the dominant mode. Contours at $x = 0$ and $x = L$ show that the perturbation is periodic along the $\hat{x}$ direction.

$v_{\max}$ would introduce a prohibitive computational expense by (a) further limiting the time step size required for numerical stability and (b) requiring more grid cells to properly resolve the distribution function. Thus the integral over the truncated domain, depending on the choice of $v_{\max}$ and the distribution function parameters, may not be normalized to numerical precision.

To address the effects of a truncated velocity domain and to ensure charge neutrality in the system, the initial condition is scaled by a constant factor $\mathcal{A}$ such that the following expression is satisfied to 10^{-15} precision:

$$\mathcal{A}\int_{-v_{\max}}^{v_{\max}}\int_{-v_{\max}}^{v_{\max}}\frac{1}{\pi\alpha_\perp^2 j!}\left(\frac{v_x^2+v_y^2}{\alpha_\perp^2}\right)^j\exp\left(-\frac{v_x^2+v_y^2}{\alpha_\perp^2}\right)dv_xdv_y=1, \tag{5.30}$$

where the value of $\mathcal{A}$ depends on the value of $v_{\max}$, j, and $\alpha_\perp$. Ideally $v_{\max}$ would be chosen to be sufficiently high that the scale factor $\mathcal{A}$ would not be necessary, i.e. the scale factor would equal one to numerical precision. For the parameters of interest with $j=\{2,4,6\}$, the scale factor value is one to within a precision of 10^{-6}, 10^{-10}, and 10^{-15}, respectively.

5.4 Simulation of the Dory-Guest-Harris instability

5.4.1 Quantifying instability growth rate from electric field energy evolution

In order to compare simulation results to the theoretical predictions from the dispersion relations for the Dory-Guest-Harris probability distribution function, potential energy is tracked as a function of time. The nondimensional electrostatic potential energy, i.e. the electric field energy U_E, is defined analytically as

$$U_E=\frac{1}{2}\int_0^L E^2(x)dx \tag{5.31}$$

and in fourth-order accurate discrete form as

$$U_E=\frac{1}{2}\sum_i\langle E\rangle_i^2+\frac{h_x^2}{12}\left(\frac{\langle E\rangle_{i+1}-\langle E\rangle_{i-1}}{2h_x}\right)^2. \tag{5.32}$$

In simulations the Dory-Guest-Harris instability is evidenced by net exponential growth of electrostatic potential energy as a function of time. According to the dispersion relation in Eq. (5.9), this occurs for waves whose normalized wave numbers yield a positive imaginary frequency, i.e. $\tilde{\omega}_i(\tilde{k})>0$. The growth rate of electric field energy in a simulation is determined by fitting an exponential to $U_E(t)$, or equivalently finding the slope S of the line that fits $\log(U_E)$ versus time during the linear stage of evolution. In the non-dimensional system of equations being solved, time t is also non-dimensional and is defined to be the product of

physical time and the electron plasma frequency. Note that it is the growth rate of the electric field, not electric field energy, that is compared against the value of $\tilde{\omega}_i^{\text{th}}$ predicted by the linear theory dispersion relation. The growth rate of the electric field is a factor of two smaller than the growth rate of the electric field energy. From the numerical simulations, the electric field growth rate $\tilde{\omega}_i^{\text{num}}$ is calculated as

$$\tilde{\omega}_i^{\text{num}} = \frac{1}{2}\frac{\omega_p}{\omega_c}S \tag{5.33}$$

where the ω_p/ω_c factor is necessary for proper normalization. When $\tilde{\omega}_i > 0, \tilde{\omega}_r = 0$, pure exponential growth of the electric field is observed, until the instability enters the nonlinear regime and saturates. When $\tilde{\omega}_i > 0, \tilde{\omega}_r > 0$, the electric field energy oscillates at a frequency $2\tilde{\omega}_r$ and grows at a rate of $2\tilde{\omega}_i$, which means the electrostatic wave propagates and amplifies until it saturates. From the simulations, the oscillation frequency $\tilde{\omega}_r^{\text{num}}$ of the electric field is determined from $U_E(t)$

$$\tilde{\omega}_r^{\text{num}} = \frac{\pi}{T}\frac{\omega_p}{\omega_c}, \tag{5.34}$$

where T is the period of $U_E(t)$ oscillation in units of normalized time, and the ratio of plasma frequency to cyclotron frequency is necessary to be consistent with Eq. (5.12).

When potential energy oscillates without net growth or decay ($\tilde{\omega}_i = 0$), the electrostatic wave is stable and propagates unchanged through the infinite plasma. In this case $\tilde{\omega}_r^{\text{num}}$ is difficult to determine from the simulation, since many different modes are excited by the initial perturbation, none of which grow in time. Exciting a single mode would require solving for the eigenfunction associated with the linearized Vlasov-Poisson system. Such analysis is beyond the scope of this dissertation and is not necessary to determine stability properties and characterize the behavior of the instability. Cases of stability are therefore verified not by comparing $\tilde{\omega}_r^{\text{num}}$ to the theoretically predicted $\tilde{\omega}_r^{\text{th}}$, but by verifying that there is no net growth of potential energy as a function of time. Figure 5.8 shows the electric field energy evolution for the three different cases discussed.

5.4.2 Discussion of fourth-order simulation results

Cases of stability allow for a qualitative comparison between simulation results and theoretical predictions. The Maxwellian equilibrium distribution function is verified to be stable for different values of $\alpha_\perp$ and $\tilde{k}$. This result is consistent with those presented in Ref. [84]. Other parameter values for which linear theory predicts stability are listed in Table 5.1 and are verified to be stable in simulations. Note that these parameters correspond to cases for which frequency is real-valued — see Fig. 5.3, Fig. 5.4, and Fig. 5.5 for the dispersion diagrams. For each set of stable parameters, the electric field energy exhibits no net change in magnitude. Figure 5.8 shows the electric field energy evolution for the stable case of $j = 2$, $\tilde{k} = 2.12$, and $\omega_p/\omega_c = 10$ as compared to unstable cases, for which field energy grows by many orders of magnitude.

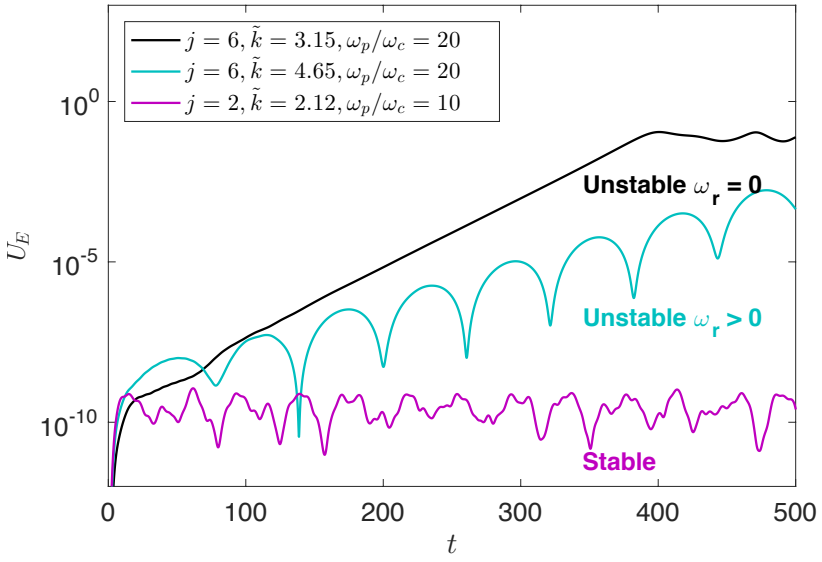

Figure 5.8: Comparison of electric field energy evolution for cases in which perturbation: amplifies only (black), amplifies and propagates (cyan), and propagates only (purple). Time is normalized by the electron plasma frequency.

Table 5.1: Sets of parameters $j, \omega_p/\omega_c$, and $\tilde{k}$ for which simulations show stability of the Dory-Guest-Harris distribution in response to perturbation.

j	2	2	2	2	2	2	4	4	4	4	4	6	6	6	6
ω_p/ω_c	20	20	20	10	10	10	20	20	10	10	10	20	6	6	6
$\tilde{k}$	1.41	2.12	2.83	1.41	2.12	2.83	2.00	4.00	2.00	3.00	4.00	0.50	0.50	3.15	4.65

For parameter values that result in growth of the instability, simulation results can be quantitatively compared against theoretical predictions. See Table 5.2 for a comparison of frequency values obtained from simulation against dispersion relation predictions. For the case of pure growth with $j = 4, \tilde{k} = 3.00$, and $\omega_p/\omega_c = 20$ the simulation-derived growth rate is 0.3003, which is 2.2% larger than the theoretical value. Simulated electric field energy evolution as a function of time for $j = 6$ is shown in Fig. 5.9a for the case of pure growth, with $\tilde{k} = 3.15$ and $\omega_p/\omega_c = 20$. For these parameters, the electrostatic wave does not propagate and its amplitude grows exponentially in time at a rate of $\tilde{\omega}_i^{\text{num}} = 0.4958$. This growth rate value is within one percent of the theoretical value $\tilde{\omega}_i^{\text{th}} = 0.4912$ predicted by the dispersion relation. Figure 5.10a shows electric field energy evolution for the case of growth with propagation, with $j = 6$, $\tilde{k} = 4.65$ and $\omega_p/\omega_c = 20$. For this set of parameters the perturbation grows at a rate of $\tilde{\omega}_i^{\text{num}} = 0.2903$ and oscillates at a frequency of $\tilde{\omega}_r^{\text{num}} = 1.0310$. These values are within one percent of the theoretical predictions (see Table 5.2).

All values of simulation-derived frequencies presented in this study are converged from simulation outputs for three different grid resolutions. Thus for a given set of simulation

Table 5.2: Converged values of frequencies from simulations compared to theoretical values predicted by the dispersion relation for parameters that result in instability. Error is defined as the relative difference between the theoretical value and the converged value from fourth-order simulations, e.g. $|\tilde{\omega}_i^{\text{th}} - \tilde{\omega}_i^{\text{num}}|/\tilde{\omega}_i$.

j	ω_p/ω_c	$\tilde{k}$	$\tilde{\omega}_i^{\text{th}}$	$\tilde{\omega}_i^{\text{num}}$	Error	$\tilde{\omega}_r^{\text{th}}$	$\tilde{\omega}_r^{\text{num}}$	Error
4	20	3.00	0.2938	0.3003	2.2%	-	-	-
6	20	3.15	0.4912	0.4958	0.9%	-	-	-
6	20	4.65	0.2899	0.2903	0.1%	1.0361	1.0310	0.5%

parameters, the fourth-order electric field energy outputs are generated using grids of size $N_x \times N_{v_x} \times N_{v_y}$: $32 \times 64 \times 64$, $40 \times 80 \times 80$, and $48 \times 96 \times 96$. The number of cells N_{v_x} in the $\hat{v}_x$ direction and N_{v_y} in the $\hat{v}_y$ directions are equal such that the velocity grid spacings are uniform, $h_{v_x} = h_{v_y} = h_v$. As the grid is refined, $h_v \to 0$ and $\tilde{\omega}^{\text{num}}$ approaches a limiting value. The value h_v^c is the lowest resolution grid cell spacing, corresponding to the $32 \times 64 \times 64$ grid. Converged fourth-order simulation results for cases of instability growth are presented in Figs. 5.9b, 5.10b, and 5.10c.

Representative convergence study results are shown in Fig. 5.9b for a purely imaginary frequency, and in Figs. 5.10b and 5.10c for a mixed complex frequency. The convergence study enables one to find values of $\tilde{\omega}_r^{\text{num}}$ and $\tilde{\omega}_i^{\text{num}}$ in the limit of infinite resolution and to verify the accuracy of the numerical method. Since the discrete numerical representation of the Vlasov-Poisson partial differential equation system is an approximation with order accuracy p, the error is expected to scale as $(h_v)^p$. For the finite-volume method described in Section 5.3.2, $p = 4$. Thus, simulation-derived frequency values as a function of $(h_v)^4$ should be a linear relation such that the y-intercept is the converged value of frequency. The data in Figs. 5.9b, 5.10b, and 5.10c are well represented by line fits, which verifies that the numerical method is fourth-order accurate.

One of the metrics for finite-volume calculations is the degree to which a simulation is able to conserve certain physical invariants. In simulations of the Dory-Guest-Harris instability, the total integral of the distribution function is conserved to machine precision. This is guaranteed by the finite-volume discretization and the use of solid wall velocity boundaries, which do not allow any portion of the distribution function to leave the domain. Unlike the conservation of the distribution function, conservation of momentum and energy is not guaranteed by the discretization. The degree to which momentum and energy are conserved for the $j = 6$, $\omega_c/\omega_p = 20$, and $\tilde{k} = 4.65$ test case is shown in Fig. 5.11. Momentum is only conserved at high resolution, but remains close to zero throughout the simulation. Total energy, that is the sum of kinetic energy and electric field energy changes over the course of the instability evolution. Total energy starts at a value of 65.82, and increases as a function of time. As the resolution is doubled, the net change in the total energy decreases by a factor of twenty – a rate that is consistent with fourth-order convergence.

Figures 5.9a and 5.10a show that the instability evolution enters a nonlinear regime and

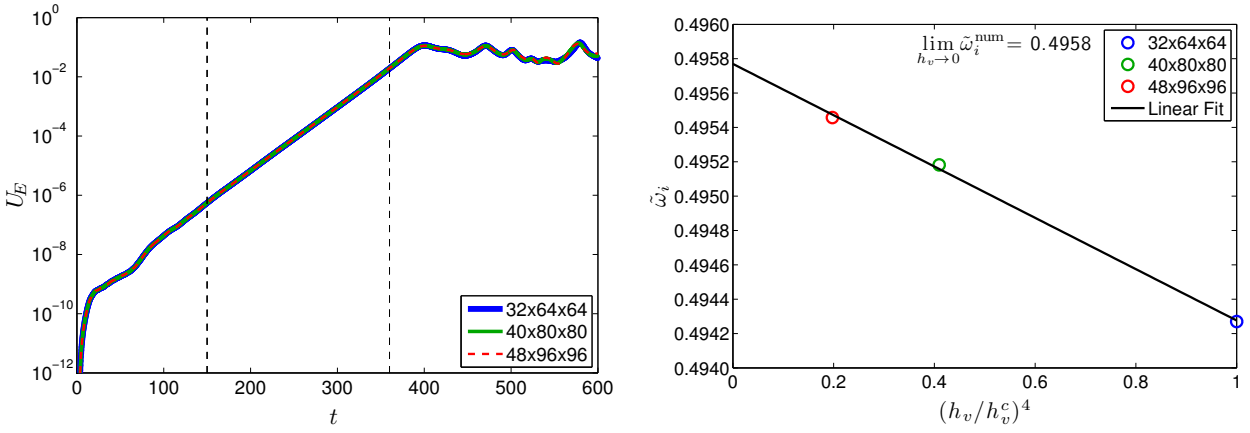

(a) **(b)**

Figure 5.9: Fourth-order simulation results with $j = 6$, $\omega_p/\omega_c = 20$, and $\tilde{k} = 3.15$. (a) Electric field energy grows exponentially in time. Linear phase is observed for time $t \in [150, 360]$, denoted by the vertical dashed lines. Time is normalized by the electron plasma frequency. (b) As the simulation grid is refined from $32 \times 64 \times 64$ to $48 \times 96 \times 96$, the growth rate converges at fourth-order to a value of 0.4958.

saturates. Saturation occurs when the electric field energy reaches a value on the order of 10^{-2}. This saturation threshold is consistent with PIC simulations for a delta function ring initial condition [82]. Figure 5.12 shows contour slices of the electron probability distribution function in phase space during the nonlinear phase of the evolution for parameters $j = 6, \tilde{k} = 4.65, \omega_p/\omega_c = 20$. The figure shows that the Dory-Guest-Harris instability is characterized by a complicated 3D structure in phase space with evidence of phase mixing due to the combined effects of shearing and Larmor motion. The probability distribution function, averaged over position x, exhibits increased velocity spread over time. For the warm ring initial conditions presented here, this effect is subtle during the linear stage of evolution, but becomes more pronounced during the nonlinear regime. As a point of comparison, delta-function ring distributions simulated using a PIC method also exhibit increased velocity spread, leading up to and following saturation [82].

5.4.3 Order of accuracy considerations

To assess the effect of numerical method accuracy on the simulation results, a second-order variant of the fourth-order finite-volume method discussed in Section 5.3.2 is implemented. The second-order method uses second-order explicit Runge Kutta time advance and smaller stencils for the spatial finite-volume discretization. Thereby it takes less numerical operations and achieves lower computational cost at the expense of spatial and temporal accuracy.

Second-order simulations with $j = 6, \tilde{k} = 3.15$, and $\omega_p/\omega_c = 20$ exhibit electric field energy evolution that is similar to the fourth-order results presented in Fig. 5.9a. The linear

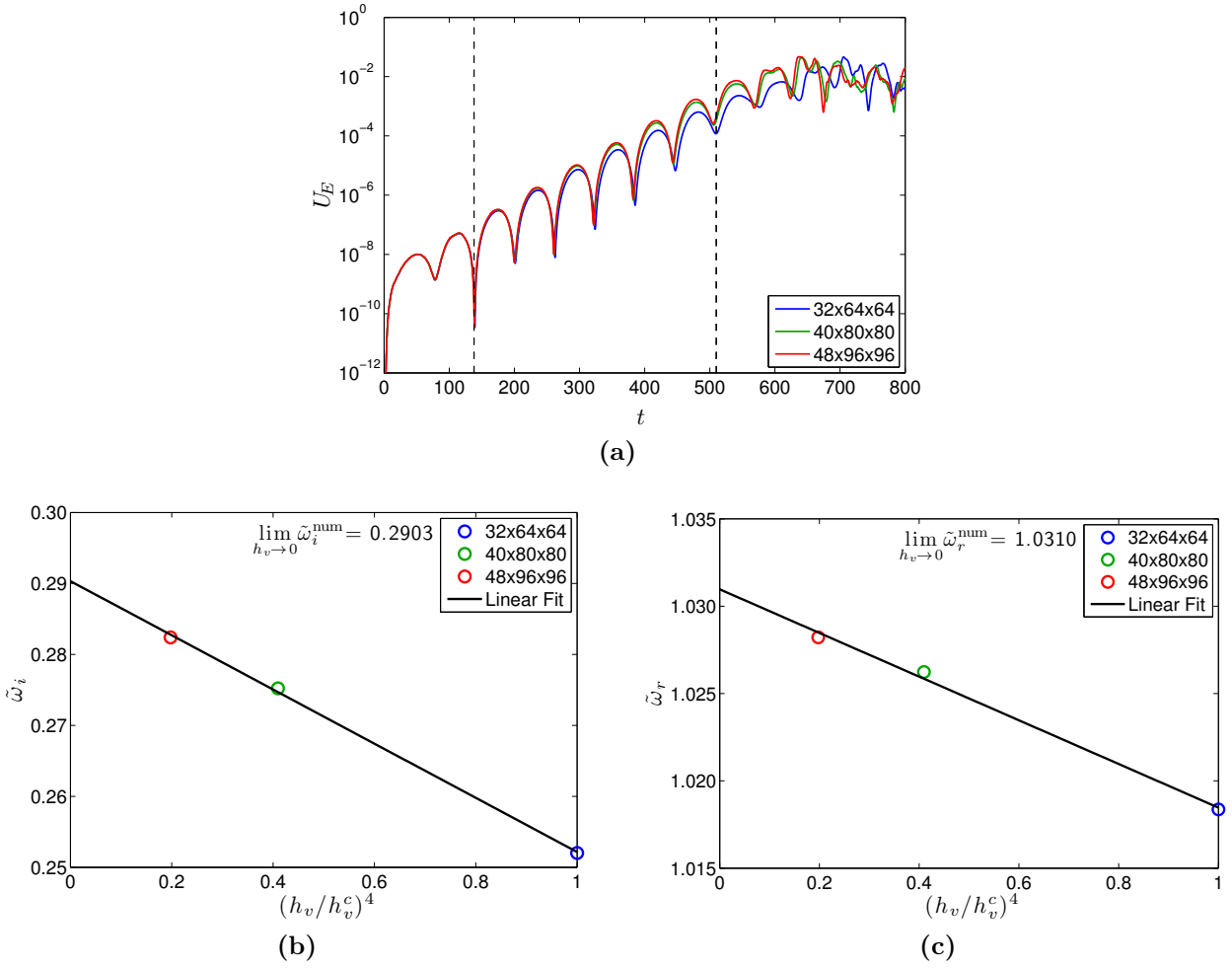

Figure 5.10: Fourth-order simulation results with $j = 6$, $\omega_c/\omega_p = 20$, and $\tilde{k} = 4.65$ using different grid resolutions.(a) The Dory-Guest-Harris equilibrium distribution function is unstable and the initial small-amplitude wave grows and propagates in time. Propagation is evidenced by the periodic oscillations in the electric field energy. The linear phase of the instability is observed for $t \in [138, 510]$ and is denoted by vertical black dashed lines. Time is normalized by the electron plasma frequency. (b) As the simulation grid is refined instability growth rate converges at fourth-order to a value of 0.2903. (c) Real frequency converges at fourth-order to a value of 1.0310.

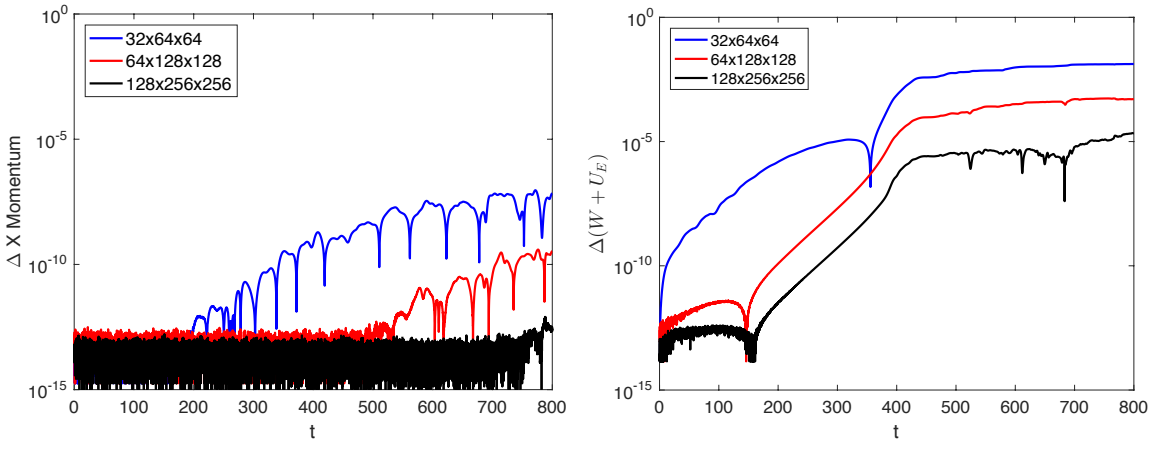

Figure 5.11: Fourth-order simulation results with $j = 6$, $\omega_c/\omega_p = 20$, and $\tilde{k} = 4.65$ using different grid resolutions. (a) The evolution of the x-directed momentum, associated with the first velocity moment of the distribution function, remains close to zero for all time, but is not conserved. The evolution of the y-directed momentum (not shown) has nearly identical evolution profiles. (b) The total energy is also not conserved, but as the grid resolution is increased the net change in total energy decreases to zero at a rate that is consistent with fourth-order convergence.

phase of the instability visibly depends on the grid resolution, but otherwise exhibits the same features: the linear phase starts at time $t = 150$ and saturation occurs when electric field energy reaches 10^{-2}. Figure 5.13 shows the instability growth rates as derived from the second-order simulations using different grid resolutions. The value of the growth rate is a linear function of $(h_v)^2$, verifying that the rate of convergence is second-order. The converged value of the instability growth rate in this case is 0.5413, which is 10% off from the theoretically-predicted value shown in Table 5.2. The large error is due to the lower accuracy of the method and can be improved with higher resolution.

Second-order simulations of instability growth and propagation with $j = 6, \tilde{k} = 4.65$, and $\omega_p/\omega_c = 20$ are shown in Fig. 5.14. In this case grid resolutions $32 \times 64 \times 64$ and $40 \times 80 \times 80$ are insufficient and fail to capture the growth and propagation of the initial electric field perturbation. Higher resolution is required in order to reach the asymptotic regime and demonstrate convergence of the second-order method. Even when using a resolution of $64 \times 128 \times 128$, the second-order method is unable to capture the transition between the linear and non-linear phases of instability evolution. Consequently the evolution of the electric field energy starts to exhibit nonlinear behavior long before the instability is expected to saturate. As the grid is refined from $48 \times 96 \times 96$ to $64 \times 128 \times 128$, the imaginary component of frequency converges to a value of 0.3693 which is 27% off from the theoretically predicted value (see Table 5.2). The converged value of the oscillation frequency, $\tilde{\omega}_r^{\text{num}} = 1.0445$ is 0.8% off from the theoretically predicted value. As in the case of pure growth, large error in the growth

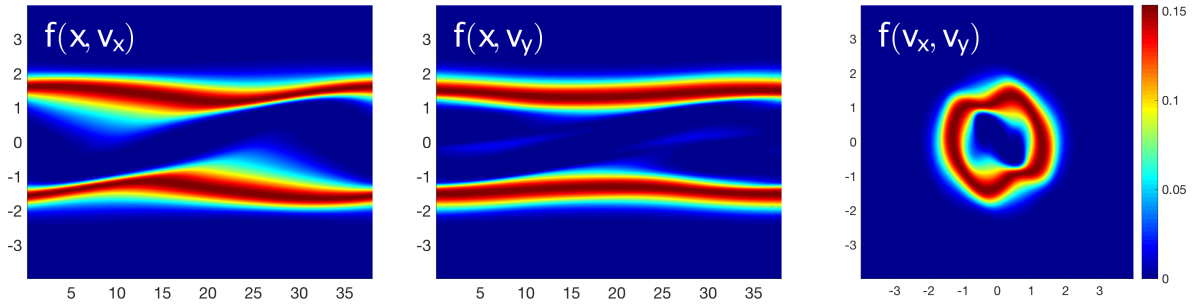

(a) $t = 538$

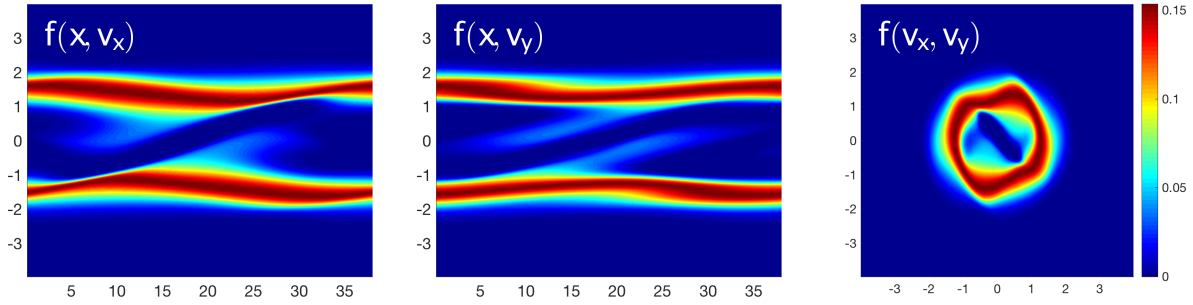

(b) $t = 554$

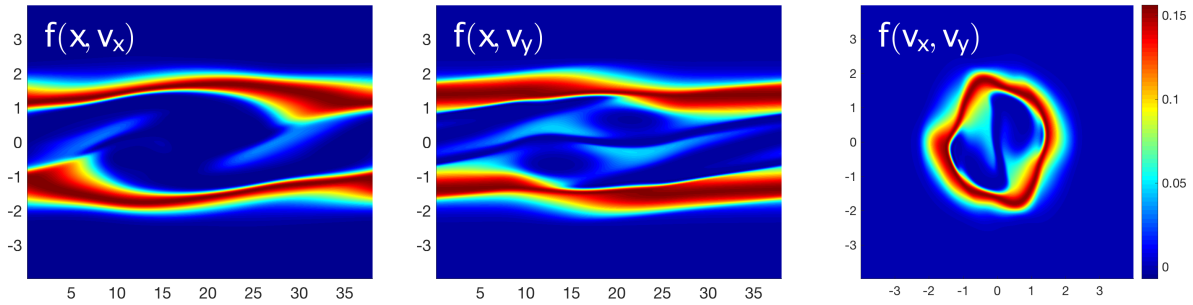

(c) $t = 586$

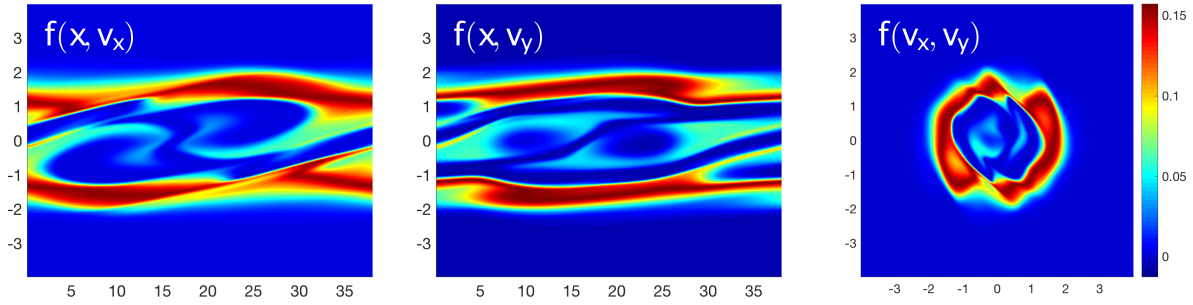

(d) $t = 618$

Figure 5.12: Contours showing the fourth-order accurate nonlinear evolution of the distribution function on a $128 \times 256 \times 256$ grid with $j = 6, \tilde{k} = 4.65, \omega_p/\omega_c = 20$ with slices at $v_y = 0$, $v_x = 0$, and $x = L/2$. Negative values of the distribution function are an unphysical numerical artifact. Time is normalized by the electron plasma frequency.

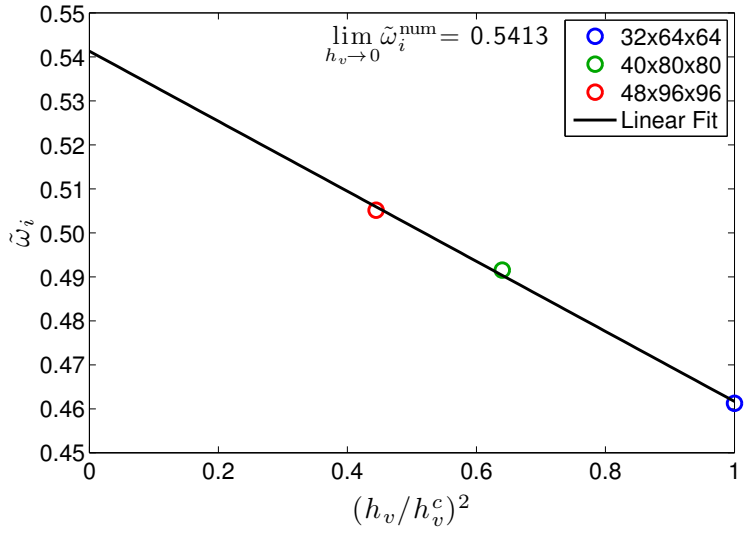

Figure 5.13: Second-order simulation results for the case of pure growth with $j = 6$, $\omega_p/\omega_c = 20$, and $\tilde{k} = 3.15$. As the simulation grid is refined from $32 \times 64 \times 64$ to $48 \times 96 \times 96$, the growth rate converges at second-order to a value of 0.5413.

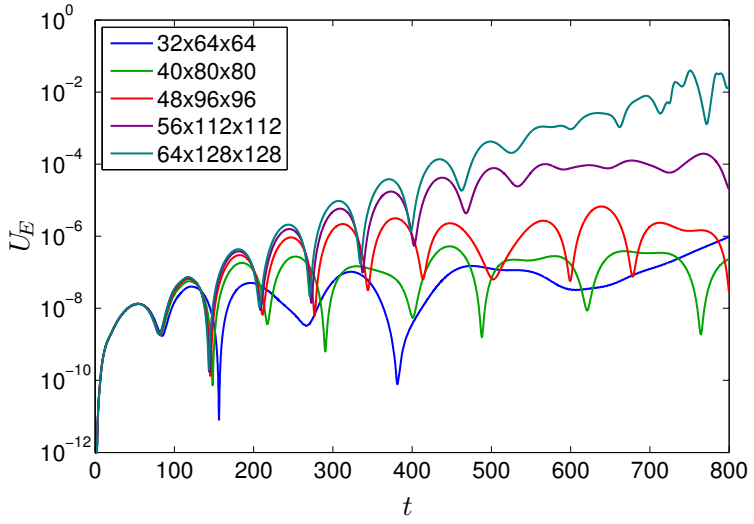

Figure 5.14: Second-order simulation results with $j = 6$, $\omega_p/\omega_c = 20$, and $\tilde{k} = 4.65$. In order to adequately capture the electric field energy growth and oscillation associated with the linear phase of the Dory-Guest-Harris instability, the second-order method requires higher resolution.

rate can be mitigated by using higher resolution.

As expected, second-order simulation results are consistent with fourth-order results, but require higher resolution to achieve adequate convergence for the value of the growth rate. Cases in which the instability amplifies and propagates are particularly sensitive to the order of accuracy. Thus low order methods can successfully be benchmarked against the Dory-Guest-Harris instability, provided the resolution is high enough to ensure that a given simulation is in the asymptotic regime.

5.4.4 Sources of error

While converged values of fourth-order simulation-derived frequencies closely agree with theoretical values predicted by the dispersion relation, an assessment of simulation limitations and sources of error is warranted. One source of error in the simulations is the truncation of velocity boundaries. Truncation is necessitated by the CFL condition, which limits time step size based on the value of $v_{\max}$ — a unique feature of phase space calculations (see Eq. (5.26)). When the velocity domain is truncated, the value of the distribution function at the velocity boundary can be appreciably greater than zero, which affects the validity of the imposed velocity boundary conditions. Note that j, $\alpha_\perp$ and the re-normalization of the distribution function after velocity boundary truncation (see Eq. (5.30)) affect the value of $f(v_{\max})$. Since solid wall boundary conditions at $|v_x|, |v_y| = v_{\max}$ are imposed by setting ghost cell values and fluxes to zero, truncation does not affect conservation. Thus, in the finite-volume simulation results presented, mass (i.e. the zeroth velocity moment of the distribution function) is conserved to numerical precision. Truncation does, however, introduce an unphysical barrier that can impact the solution. This may explain why the $j = 4$ test case, which has a higher value of $f(v_{\max})$, exhibits the worst agreement with theoretical predictions. Using a higher value of $v_{\max}$ would resolve discrepancies due to boundary effects at the expense of increased computational cost. Equilibrium distribution function parameters j and $\alpha_\perp$ can also be modified to decrease the value of $f(v_{\max})$ without increasing the value of $v_{\max}$, and thereby improve agreement between theoretical and numerical values of frequency. It is important, however, to ensure that the distribution function features are adequately resolved by the simulation grid.

Numerical errors are another source of discrepancy. These cause the probability distribution function to become negative in regions far away from the distribution function peaks (as evidenced in the minimum values of f shown in Fig. 5.12). These negative values are unphysical and are the result of under-resolved gradients associated with the spatial discretization. Consequently the errors can be diminished by increasing the resolution. Since fine-scale phase space features develop progressively throughout a simulation, increased resolution would also extend the duration over which the instability can be modeled. Positivity preserving methods involving limiters can also be used to mitigate the effects of these numerical errors.

Low resolution also limits the accuracy of the convergence study – both for high-order and low-order numerical methods. Second-order simulations in particular require higher

resolution in order to converge to a theoretically predicted solution. The grid resolution is limited by the computational cost of advancing the distribution function in three dimensions. Higher resolution simulations, facilitated by optimization of algorithm performance, would likely improve the accuracy of the convergence fits (see Figs. 5.9b, 5.10b, and 5.10c), and thereby reduce the error in the converged values of $\tilde{\omega}_i^{\text{num}}$ and $\tilde{\omega}_r^{\text{num}}$. Even with limited resolution, however, fourth-order simulation results demonstrate good convergence, implying that higher resolution calculations may not yield any additional physical insight.

Finally, it is important to note that a nonlinear equation system and nonlinear discretization are being used to simulate a linear problem. Thus discrepancies between the simulation results and dispersion relation predictions are expected as the assumptions used in the linearization process become invalid. Despite the limitations of the algorithm with regard to resolution, truncation, and numerical error, it is shown to successfully model the Dory-Guest-Harris instability, as validated against linear theory.

5.5 Concluding remarks

The Dory-Guest-Harris instability is demonstrated to be a well-suited benchmark for continuum kinetic Vlasov-Poisson algorithms in 3D (x, v_x, v_y) phase space. It has a closed-form linear theory dispersion relation that can be used to identify thresholds for instability, against which continuum method simulations can be quantitatively compared. This is done by initializing a warm ring velocity distribution function with a position-dependent sinusoidal wave perturbation. The velocity spread of the distribution function, the wave number of the perturbation, and the ratio of electron plasma frequency to electron cyclotron frequency determine whether an instability occurs. In cases of instability, the electric field energy grows exponentially in time, and the associated growth rate and oscillation frequency can be deduced and compared against linear theory predictions.

A fourth-order accurate finite-volume continuum Vlasov-Poisson algorithm is successfully benchmarked using the presented analysis of the Dory-Guest-Harris distribution function. In cases of stability, the simulation results exhibit no net change in electric field energy. For parameter values that yield an instability, convergence studies are performed to compute real and imaginary frequency components in the limit of infinite resolution. The same convergence studies are used to verify the order of accuracy of the algorithm. The resulting real and imaginary values of frequency are shown to closely agree with theoretical predictions. A specialized form of the initial condition is shown to strongly excite the fastest growing mode, which greatly simplifies the process by which frequency values are obtained from the simulation. Discrepancies between simulation outputs and theory are attributed to a number of factors including computational cost limitations, truncation of velocity boundaries, and numerical error. In spite of these factors, growth rates and oscillation frequencies obtained from fourth-order simulations fall within three percent of the values predicted by the dispersion relation.

Results from second-order accurate finite-volume simulations indicate that the Dory-Guest-Harris instability can be modeled with low-order numerical methods, provided that the resolution is sufficiently high. Since low-order methods involve less floating point operations, increasing grid resolution as means of improving the level of agreement between simulation results and theoretical predictions is common practice.

As evidenced by the evolution of the Dory-Guest-Harris distribution function, the instability necessitates simulating three dimensions (x, v_x, v_y) of phase space. Thus the instability provides a means to go beyond the present scope of 2D (x, v_x) standardized benchmark problems, and provides a robust test for extending continuum kinetic algorithms to more phase space dimensions. The described Dory-Guest-Harris benchmark is particularly valuable in that it involves a warm magnetized plasma in which the magnetic field has an important role in the distribution function evolution. The benchmark facilitates a quantitative means by which to evaluate continuum kinetic algorithms, as they become more developed, more robust, and include more generalized physics.

Chapter 6

Numerical results in cylindrical coordinates

The fourth-order finite-volume discretization for cylindrical coordinates is first applied to test the field solvers. The discretization of the Poisson equation is tested using a prescribed charge density distribution with a known analytic solution for the potential. To test the implementation of Ampere's law and Faraday's law, a cylindrical waveguide problem is used. Parabolic divergence cleaning is not implemented in this case. The testing of the discretization of the cylindrical coordinate Vlasov equation is approached with care since the singularity at the axis has not been explored in the context of continuum kinetic calculations. As such, the Vlasov solver is first applied to a zero-field test case involving a spatially uniform collisionless neutral gas. The departure away from equilibrium is assessed and the convergence of the algorithm is verified. The Vlasov-Maxwell solver is then applied to a Z-pinch calculation involving nonlinear ion oscillations about a fixed distribution of electrons.

6.1 Maxwell's equations

6.1.1 1D cylindrical Poisson solve

The finite-volume approach for solving the Poisson equation to fourth-order accuracy is presented in Section 3.9.3. The convergence properties of the method are evaluated using a test problem with an analytic solution. Such a test problem can be formulated by choosing an analytic function for the electrostatic potential ϕ, and computing the analytic Laplacian of ϕ to obtain the self-consistent charge density. Using the discrete version of the analytic charge density, and the discrete operator acting on ϕ, one can obtain the numerical solution for the electrostatic potential and compare it to the exact solution.

The electrostatic potential is chosen to be

$$\phi = J_0(r), \tag{6.1}$$

where J_0 is the zeroth-order Bessel function of the first kind. This constitutes the exact solution. The charge density associated with this electrostatic potential is

$$\rho(r) = -J_0(r). \tag{6.2}$$

Formulating this as a discrete problem, the charge i.e. the volume-integrated charge density $\langle\rho\rangle_i$ in cell i , is defined to be

$$\langle\rho\rangle_i = -\int_{r_{i-\frac{1}{2}}}^{r_{i+\frac{1}{2}}} J_0(r) r dr \tag{6.3}$$

$$= -\left[rJ_1(r)\right]_{r_{i-\frac{1}{2}}}^{r_{i+\frac{1}{2}}}. \tag{6.4}$$

The discrete Laplacian operator, described in Section 3.9.3, requires boundary conditions. For this test case the boundary conditions on the electrostatic potential are a homogeneous Neumann boundary condition at the axis, and a homogeneous Dirichlet boundary condition at the righthand bound of the domain, such that

$$\left.\frac{d\phi}{dr}\right|_{r=0} = 0 \tag{6.5}$$

$$\phi|_{r=r_{\max}} = 0, \tag{6.6}$$

where the length of the domain, $r_{\max}$, is chosen to be a zero of J_0. The stencils for first two cells $i = \{0, 1\}$ and last two cells $i = \{N_r - 2, N_r - 1\}$ in the domain must be modified to be consistent with these boundary conditions, such that

$$\langle\rho\rangle_0 = -\left(-\frac{13}{12}\phi_0 + \frac{9}{8}\phi_1 - \frac{1}{24}\phi_2\right) r_{\frac{1}{2}} \tag{6.7}$$

$$\langle\rho\rangle_1 = -\left(\left[\frac{13}{12}r_{\frac{1}{2}} + \frac{1}{24}r_{\frac{3}{2}}\right]\phi_1 - \left[\frac{9}{8}r_{\frac{1}{2}} + \frac{9}{8}r_{\frac{3}{2}}\right]\phi_2 + \left[\frac{1}{24}r_{\frac{1}{2}} + \frac{9}{8}r_{\frac{3}{2}}\right]\phi_3 - \frac{1}{24}r_{\frac{3}{2}}\phi_4\right) \tag{6.8}$$

$$\begin{aligned}\langle\rho\rangle_{N_r-1} = -\Bigg(&- \left[\frac{1}{126}(r_{\max} - h_r) + \frac{1}{18}r_{\max}\right]\phi_{N_r-5} \\ &+ \left[\frac{5}{168}(r_{\max} - h_r) + \frac{3}{8}r_{\max}\right]\phi_{N_r-4} - \left[\frac{1}{8}(r_{\max} - h_r) + \frac{9}{8}r_{\max}\right]\phi_{N_r-3} \\ &+ \left[\frac{91}{72}(r_{\max} - h_r) + \frac{17}{8}r_{\max}\right]\phi_{N_r-2} - \left[\frac{4}{3}(r_{\max} - h_r) + \frac{39}{8}r_{\max}\right]\phi_{N_r-1}\Bigg)\end{aligned} \tag{6.9}$$

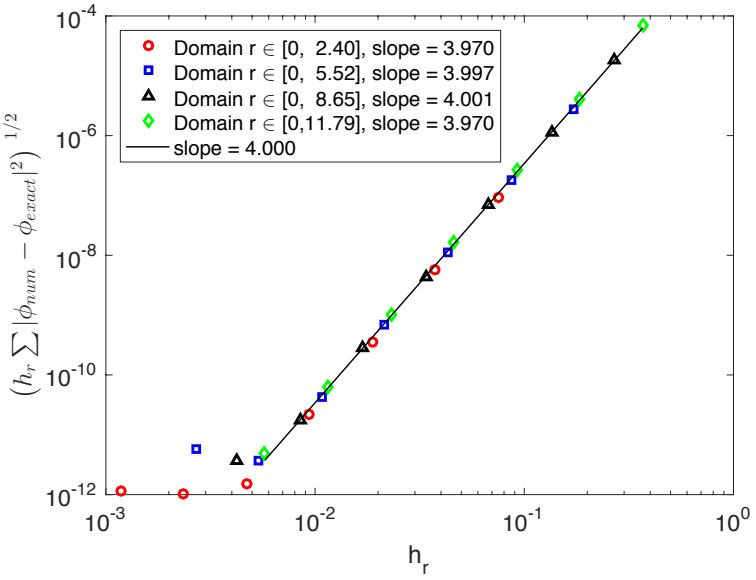

Figure 6.1: L2-norm of the difference between the exact analytic solution ϕ and the discrete ϕ_i for different resolutions and different values of $r_{\max}$. The error converges at fourth-order accuracy. For small domain sizes at high resolution, for which the spacing $h_r \lesssim 8 \times 10^{-3}$, numerical round off error prevents reduction of the error below 10^{-12}.

$$\begin{aligned}\langle\rho\rangle_{N_r-2} = -\Bigg(&\left[\frac{1}{216}(r_{\max}-h_r)\right]\phi_{N_r-5} - \left[\frac{1}{24}(r_{\max}-2h_r)+\frac{5}{168}(r_{\max}-h_r)\right]\phi_{N_r-4} \\ &+\left[\frac{9}{8}(r_{\max}-2h_r)+\frac{1}{8}(r_{\max}-h_r)\right]\phi_{N_r-3} \\ &-\left[\frac{9}{8}(r_{\max}-2h_r)+\frac{91}{72}(r_{\max}-h_r)\right]\phi_{N_r-2} \\ &+\left[\frac{1}{24}(r_{\max}-2h_r)+\frac{4}{3}(r_{\max}-h_r)\right]\phi_{N_r-1}\Bigg). \end{aligned} \tag{6.10}$$

These stencils come from fifth-order accurate one-sided polynomial reconstructions of the derivative $[d\phi/dr]_{i+\frac{1}{2}}$ (see Eq. (3.332)) from discrete cell-centered values of ϕ near the boundaries. Using these stencils at the boundary, and the stencil in Eq. (3.340) for the domain interior, a global linear operator can be constructed. The resulting linear system is solved for cell-centered values of the electrostatic potential at different resolutions and for different values of $r_{\max}$. The L2-norm of the difference between the numerical solution and the exact solution is plotted in Fig. 6.1, and the error is shown to converge at fourth-order. This demonstrates that the discretization method for solving the Poisson equation is indeed fourth-order accurate. Beyond a certain resolution, i.e. for cell spacing less than about 8×10^{-3}, the error does not decrease below 10^{-12} due to round-off error.

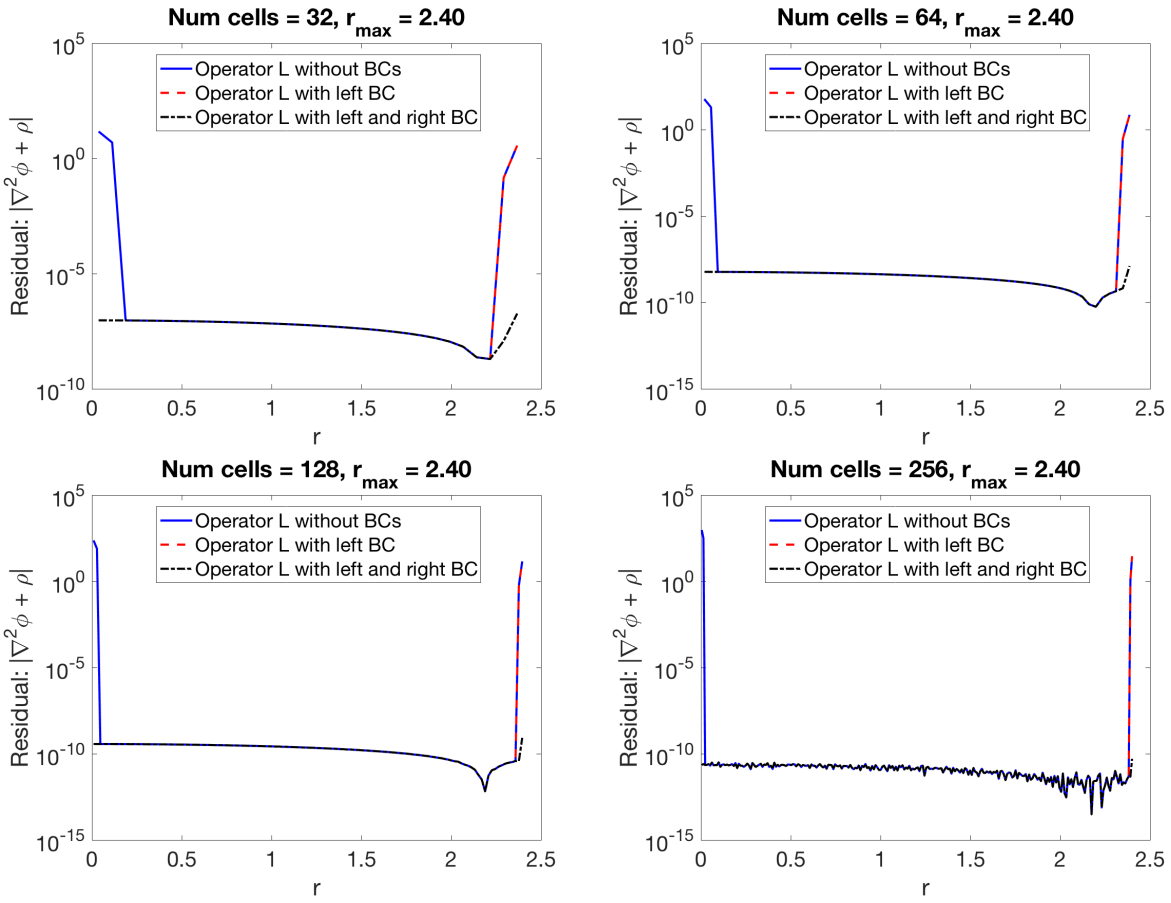

Figure 6.2: The residual for Poisson's equation, defined in Eq. (6.12), evaluated using the analytic charge within a cell and the fourth-order finite-volume discrete operator acting on the analytic ϕ. The residual is evaluated for three different versions of the discrete Laplacian operator: without boundary conditions (using only the stencil in Eq. (3.340)), with only the left-hand boundary condition (using the additional stencils in Eq. (6.7) and Eq. (6.8)), and one with boundary conditions. When both boundaries are properly set, the residual has the same magnitude throughout the domain.

The importance of implementing boundary conditions at the appropriate order of accuracy cannot be overstated. Boundary conditions that are not implemented appropriately can be identified by computing the residual, defined analytically as

$$R = \nabla^2 \phi + \rho \tag{6.11}$$

and discretely as

$$R_i = L\phi + \langle \rho \rangle_i \tag{6.12}$$

where L is the linear discretization operator for the Laplacian, acting on the analytic cell-centered values of ϕ. Note that the signs are consistent with the original Poisson equation,

see for example Eq. (2.97). The residual is plotted in Fig. 6.2 for different resolutions for three different version of the discrete Laplacian: one that does not involve any boundary conditions, another that only sets the lefthand boundary condition, and the case where both the lefthand and righthand boundaries are set to be fourth-order accurate. For correct implementation of boundary conditions, the value of the residual should have the same magnitude throughout the domain. For example, for second-order accurate boundary conditions, large spikes in the residual would be observed, much like the in the absence of boundary conditions (see blue traces in Fig. 6.2). The residual thus gives an indication of how well the discrete Laplacian operator approximates the analytic Laplacian. The residual plots also show that as resolution is doubled, the residual decreases by about a factor of about 10 to 20, which is expected since the error for the discretization is proportional to h_r^4.

6.1.2 Electromagnetic fields in a circular waveguide

The cylindrical coordinate Maxwell solver is applied to simulate a standing electromagnetic wave in the (r, z) plane, guided along the axis of a cylindrical waveguide with a circular cross section. This problem has an analytic solution, against which simulation results can be compared. The solution is derived as follows.

In the absence of a plasma the ratio ω_{pp}/ω_{cp} in the normalized form of Maxwell's equation can be set to one and current is zero. For convenience the characteristic speed is assumed to be the speed of light, such that all of the constant ratios in Eq. (2.21) and Eq. (2.22) are unity. The fields in Faraday's and Ampere's law can be separated into transverse and longitudinal components, such that

$$-\frac{\partial}{\partial t}\left(\boldsymbol{B}_\perp + B_z\right) = \left(\nabla_\perp + \hat{z}\frac{\partial}{\partial z}\right) \times \left(\boldsymbol{E}_\perp + E_z\right) \tag{6.13}$$

$$\frac{\partial}{\partial t}\left(\boldsymbol{E}_\perp + E_z\right) = \left(\nabla_\perp + \hat{z}\frac{\partial}{\partial z}\right) \times \left(\boldsymbol{B}_\perp + B_z\right) \tag{6.14}$$

Assuming that the z dependence and time dependence of each field vector can be expressed as $e^{i(k_z z - \omega t)}$, meaning the wave is periodic along the z direction and oscillates at frequency ω, the time derivative can be eliminated, such that the resulting Faraday's law and Ampere's law is

$$i\omega\left(\boldsymbol{B}_\perp + B_z\right) = \left(\nabla_\perp + \hat{z}\frac{\partial}{\partial z}\right) \times \left(\boldsymbol{E}_\perp + E_z\right) \tag{6.15}$$

$$-i\omega\left(\boldsymbol{E}_\perp + E_z\right) = \left(\nabla_\perp + \hat{z}\frac{\partial}{\partial z}\right) \times \left(\boldsymbol{B}_\perp + B_z\right) \tag{6.16}$$

Separating the expressions into transverse and longitudinal directions yields

$$i\omega \boldsymbol{B}_\perp = \nabla_\perp \times E_z + \hat{z} \times \frac{\partial \boldsymbol{E}_\perp}{\partial z} \tag{6.17}$$

$$-i\omega \boldsymbol{E}_\perp = \nabla_\perp \times B_z + \hat{z} \times \frac{\partial \boldsymbol{B}_\perp}{\partial z} \tag{6.18}$$

$$i\omega B_z = \nabla_\perp \times \boldsymbol{E}_\perp \tag{6.19}$$

$$-i\omega E_z = \nabla_\perp \times \boldsymbol{B}_\perp \tag{6.20}$$

Following the steps outlined in Ref. [99], $\hat{z}$ is crossed with Eqs. (6.17) and (6.18), and the identities $\hat{z} \times (\nabla_\perp \times E_z) = \nabla_\perp E_z$ and $\hat{z} \times (\hat{z} \times \boldsymbol{E}_\perp) = -\boldsymbol{E}_\perp$ are applied to yield the following forms of Faraday's and Ampere's law for the transverse components

$$\hat{z} \times (i\omega \boldsymbol{B}_\perp) = \nabla_\perp E_z - \frac{\partial \boldsymbol{E}_\perp}{\partial z} \tag{6.21}$$

$$\hat{z} \times (-i\omega \boldsymbol{E}_\perp) = \nabla_\perp B_z - \frac{\partial \boldsymbol{B}_\perp}{\partial z}. \tag{6.22}$$

Differentiating Eqs. (6.21) and (6.22) with respect to z, and noting that $\partial^2/\partial z^2 = -k_z^2$ allows Eq. (6.21) to be substituted into Eq. (6.18) and Eq. (6.22) to be substituted into Eq. (6.17) to eliminate the $\hat{z}\times$ terms. This yields expressions for the transverse components of the fields in terms of the longitudinal components, such that

$$\boldsymbol{E}_\perp = \frac{1}{\omega^2 - k_z^2} \left(\nabla_\perp \frac{\partial E_z}{\partial z} + i\omega \nabla_\perp \times B_z \right) \tag{6.23}$$

$$\boldsymbol{B}_\perp = \frac{1}{\omega^2 - k_z^2} \left(\nabla_\perp \frac{\partial B_z}{\partial z} - i\omega \nabla_\perp \times E_z \right) \tag{6.24}$$

Substituting Eq. (6.23) into Eq. (6.19) and Eq. (6.24) into Eq. (6.20) yields the homogeneous Helmholtz equation for the longitudinal components of the fields,

$$\left(\nabla_\perp^2 + \omega^2 - k_z^2\right) \begin{bmatrix} E_z \\ B_z \end{bmatrix} = 0. \tag{6.25}$$

Thus given a solution to Eq. (6.25) for the longitudinal field components, the transverse components are readily obtained from Eq. (6.23) and Eq. (6.24). For the purpose of ultimately modeling axisymmetric plasma configurations, the fields are assumed to be independent of the azimuthal angle.

For an axisymmetric TM_{01} wave that has no variation with θ and a single half-wave along the radial direction, the longitudinal magnetic field is zero and the longitudinal electric field that satisfies the Helmholtz equation has the form

$$E_z = J_0(k_r r) e^{ik_z z} e^{-i\omega t}. \tag{6.26}$$

From Eq. (6.23) and Eq. (6.24) the transverse components are then

$$E_r = -\frac{1}{\omega^2 - k_z^2}\frac{\partial}{\partial z}\frac{\partial E_z}{\partial r}e^{-i\omega t} = -\frac{ik_z k_r}{\omega^2 - k_z^2}J_1(k_r r)e^{ik_z z}e^{-i\omega t} \tag{6.27}$$

$$E_\theta = \frac{1}{\omega^2 - k_z^2}\frac{1}{r}\frac{\partial}{\partial \theta}\frac{\partial E_z}{\partial z}e^{-i\omega t} = 0 \tag{6.28}$$

$$B_r = -\frac{i\omega}{\omega^2 - k_z^2}\frac{1}{r}\frac{\partial E_z}{\partial \theta}e^{-i\omega t} = 0 \tag{6.29}$$

$$B_\theta = -\frac{i\omega}{\omega^2 - k_z^2}\left(-\frac{\partial E_z}{\partial r}\right)e^{-i\omega t} = -\frac{i\omega k_r}{\omega^2 - k_z^2}J_1(k_r r)e^{ikz}e^{-i\omega t}, \tag{6.30}$$

where $\omega^2 = k_r^2 + k_z^2$ in this non-dimensionalized system. Similarly, the TE_{01} wave has the analytic solution

$$B_z = J_0(k_r r)e^{ik_z z}e^{-i\omega t} \tag{6.31}$$

$$B_r = -\frac{ik_z k_r}{\omega^2 - k_z^2}J_1(k_r r)e^{ik_z z}e^{-i\omega t} \tag{6.32}$$

$$B_\theta = 0 \tag{6.33}$$

$$E_r = 0 \tag{6.34}$$

$$E_\theta = \frac{i\omega k_r}{\omega^2 - k_z^2}J_1(k_r r)e^{ik_z z}e^{-i\omega t}. \tag{6.35}$$

The weak-form governing equations for the circular waveguide problem are

$$\begin{bmatrix} \iint E_r r d\theta dz \\ \iint E_\theta dr dz \\ \iint E_z r dr d\theta \end{bmatrix} = \begin{bmatrix} -\left[r_i \int B_\theta(r_i,\theta,z)d\theta\right]_{z_{k-\frac{1}{2}}}^{z_{k+\frac{1}{2}}} \\ \left[\int B_r(r,\theta_j,z)dr\right]_{z_{k-\frac{1}{2}}}^{z_{k+\frac{1}{2}}} - \left[\int B_z(r,\theta_j,z)dz\right]_{r_{i-\frac{1}{2}}}^{r_{i+\frac{1}{2}}} \\ \left[r \int B_\theta(r,\theta,z_k)d\theta\right]_{r_{i-\frac{1}{2}}}^{r_{i+\frac{1}{2}}} \end{bmatrix} \tag{6.36}$$

$$\begin{bmatrix} \iint B_r r d\theta dz \\ \iint B_\theta dr dz \\ \iint B_z r dr d\theta \end{bmatrix} = -\begin{bmatrix} -\left[r_i \int E_\theta(r_i,\theta,z)d\theta\right]_{z_{k-\frac{1}{2}}}^{z_{k+\frac{1}{2}}} \\ \left[\int E_r(r,\theta_j,z)dr\right]_{z_{k-\frac{1}{2}}}^{z_{k+\frac{1}{2}}} - \left[\int E_z(r,\theta_j,z)dz\right]_{r_{i-\frac{1}{2}}}^{r_{i+\frac{1}{2}}} \\ \left[r \int E_\theta(r,\theta,z_k)d\theta\right]_{r_{i-\frac{1}{2}}}^{r_{i+\frac{1}{2}}} \end{bmatrix} \tag{6.37}$$

Note that integrals over the θ direction are trivial since axisymmetry is assumed. For a

simulation of the TM_{01} mode the initial condition is set to be

$$E_r = \texttt{Real}\left[-\frac{ik_z k_r}{\omega^2 - k_z^2} J_1(k_r r) e^{ik_z z}\right] \tag{6.38}$$

$$E_\theta = 0 \tag{6.39}$$

$$E_z = \texttt{Real}\left[J_0(k_r r) e^{ik_z z}\right] \tag{6.40}$$

$$B_r = 0 \tag{6.41}$$

$$B_\theta = \texttt{Real}\left[-\frac{i\omega k_r}{\omega^2 - k_z^2} J_1(k_r r) e^{ikz}\right] \tag{6.42}$$

$$B_z = 0 \tag{6.43}$$

$$k_r = \xi_0 \tag{6.44}$$

$$k_z = \pi \tag{6.45}$$

where $\xi_0 = 2.40482555769577$ is the first zero of the Bessel function J_0. The domain is defined to be $r, z \in [0, \xi_0/k_r] \times [0, 2\pi/k_z]$. The $r_{\max} = 1$ boundary is a conducting wall. Note that the values of k_r and k_z given in Eqs. (6.44) and (6.45) set the temporal frequency of oscillation such that the period of one oscillation is $T = 2\pi/(k_z^2 + k_r^2)^{1/2}$. The evolution of the primary variable electromagnetic field components from a 128×64 resolution simulation are shown in Fig. 6.3. The electromagnetic wave propagates through the periodic domain at the speed of light, which in this normalized system is one. Thus the circular waveguide, with a perfectly conducting wall and axisymmetric fields, is successfully modeled. Fig. 6.4 shows that the numerical solution from the (r, z) Maxwell solver converges at fourth order to the exact analytic solution given by Eqs. (6.27) – (6.30) for E_r, E_z, and B_θ.

A known issue with high-order schemes for Maxwell's equations is the potential for instabilities to develop over the course of long-time integration [100] even for discretization schemes that are classically stable [101]. For the fourth-order finite-volume discretization used here, it is found that after many (on the order of one hundred) periods of oscillation, the numerical solution becomes unstable – first long wavelength instability features develop, followed by short wavelength features. The analysis of such instabilities typically calls for Gustafsson-Kreiss-Sundstrom (GKS) theory [102, 103, 104], which is a means to assess stability properties for systems involving non-periodic boundaries. However, GKS stability is not enough to guarantee long-time stability [101]. The analysis of the long-time instability is beyond the scope of this dissertation. It is hypothesized that the numerical instability is mitigated when the Maxwell solver includes sources, as it does when coupled to the Vlasov discretization. The presence of a current density source term, computed from the distribution function, introduces non-linearity to the Maxwell solver and thereby affects the stability properties.

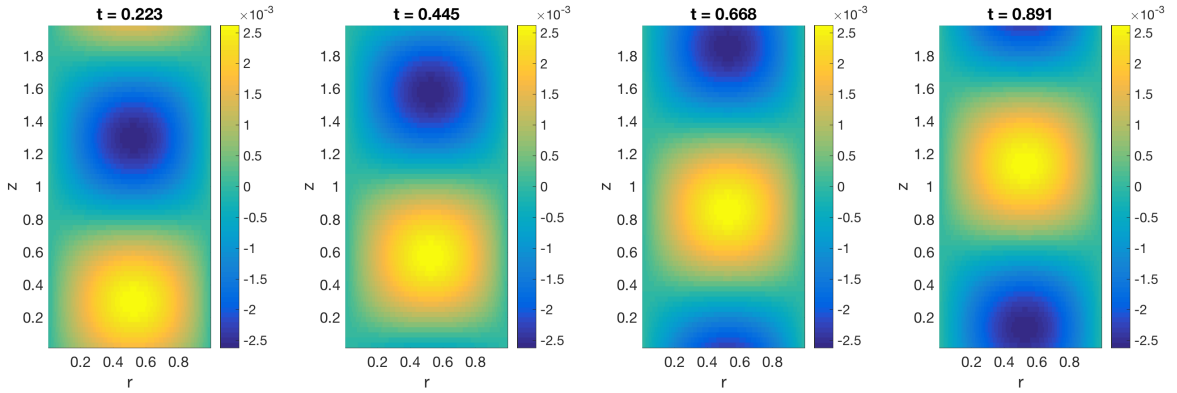

(a) $\iint E_z(r,z)rdrd\theta$

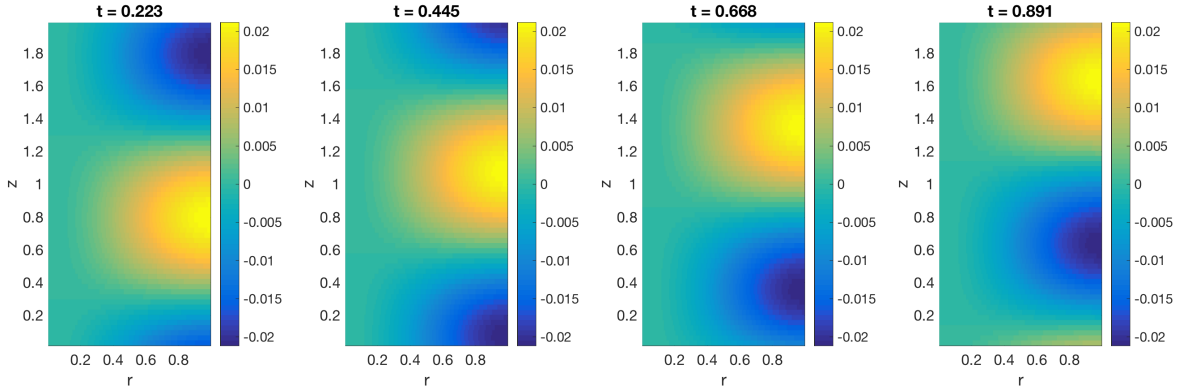

(b) $\iint E_r(r,z)rd\theta dz$

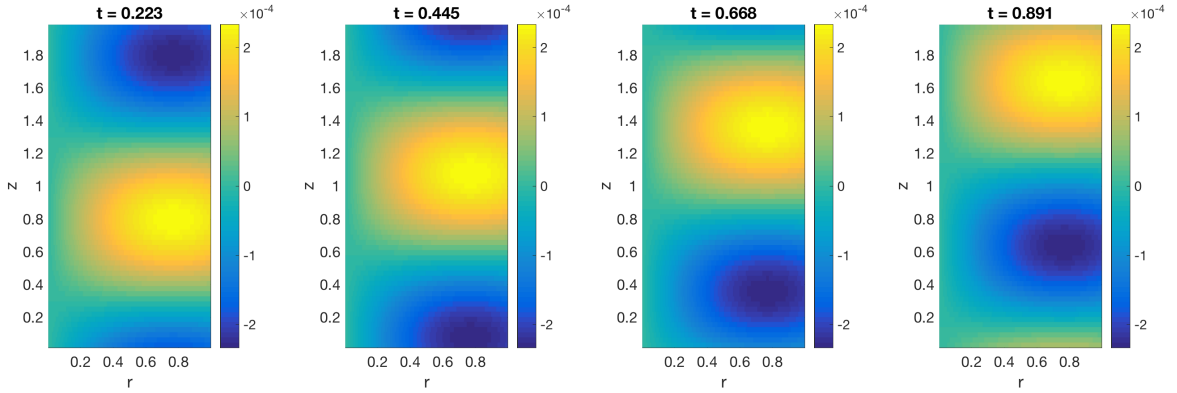

(c) $\iint B_\theta(r,z)drdz$

Figure 6.3: Contour plots of the fields from a 128×64 simulation of a propagating TM_{01} mode in a cylindrical waveguide. The fields are local area-integrated quantities and are shown at time $t = \{0.223, 0.445, 0.668, 0.891\}$. The initial condition is given in Eq. (6.38) through Eq. (6.45). One complete oscillation cycle is approximately 1.59 units of time.

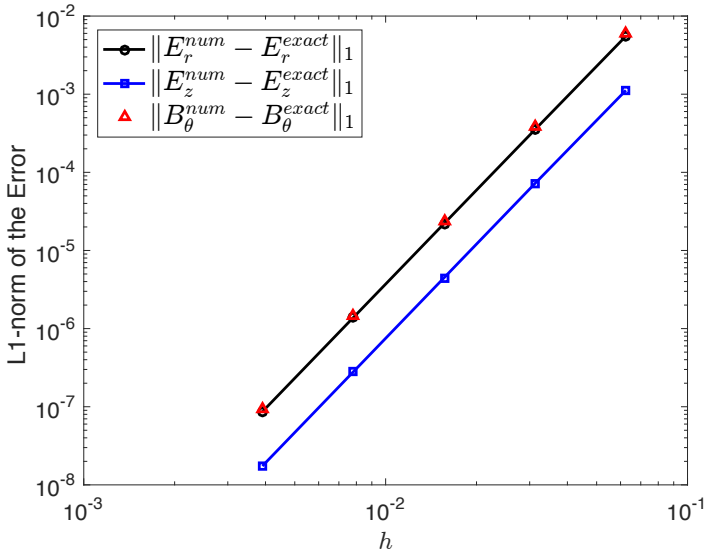

Figure 6.4: The L1-norm of the error, defined as the difference between the numerical solution from the (r, z) Maxwell solver and the exact solution for the TM_{01} mode for a cylindrical waveguide, plotted on a log-log scale as a function of cell spacing h. The error is evaluated at time $t = 1.4$. Fourth order convergence is evident in that the error drops by four orders of magnitude for one magnitude decrease in cell spacing.

6.2 Simulation of axisymmetric plasmas in cylindrical phase space coordinates

Plasmas often exhibit some form of symmetry, and simple axisymmetry is inherent in a number of plasma devices including field-reversed configurations, Z-pinches, Hall thrusters, spheromaks, and particle beams. When it comes to kinetic simulations, modeling an axisymmetric plasma in Cartesian phase space coordinates would require discretizing a six-dimensional phase space, which currently presents a prohibitive computational expense. The purpose of developing the mathematical and numerical formulation for modeling distribution functions in cylindrical phase space coordinates is ultimately to exploit axisymmetry, and reduce the required number of dimensions from six to five, while retaining high accuracy. With this vision, much of the focus here is on proof-of-concept, with the aim of demonstrating that conservative high-order accurate continuum kinetic simulations of distribution functions in cylindrical phase space coordinates are viable.

Computational investigation of the kinetic physics of axisymmetric plasmas is most often carried out using PIC methods. A number of techniques have been developed for PIC methods to handle particles traversing cells with non-uniform volumes, including specialized weighting and interpolation [6], as well as procedures involving mapping from a unit square logical domain [105], and advancing particles in three dimensions for axisymmetric configu-

rations to circumvent problems at the axis [106]. Research literature on continuum kinetic methods for discretizing cylindrical phase space coordinates is extremely sparse. In Ref. [29] Filbet et al. demonstrated a semi-Lagrangian method applied to axisymmetric charge dominated beam plasmas. The authors used a modified form the cylindrical coordinate Vlasov equation based on the invariance of the canonical angular momentum, and applied their numerical method to an RMS-matched semi-Gaussian beam and a perturbed thermal equilibrium. While there have been extensive developments in the finite-volume discretization of the Euler and Navier-Stokes equations in axisymmetric geometries [107, 108], the features of the axis singularity are distinctly different in these equation systems compared to the Vlasov equation. In particular, since velocities are coordinates in the Vlasov equation, the regularity condition often applied in fluid calculations (i.e. the condition that radial velocity is linearly dependent on radius as $r \to 0$) does not apply. Conservative discretization of the continuum kinetic cylindrical coordinate Vlasov equation thereby constitutes largely unchartered territory.

6.2.1 Preservation of a spatially uniform distribution function

A unique aspect of cylindrical phase space coordinates is that the distribution function always advects in velocity space. Even in the absence of electromagnetic fields and with zero drift (i.e. distribution functions centered at the velocity origin) there is advection in velocity space due to Coriolis and centrifugal force terms (see Fig. 6.5), which are present in the cylindrical form of the Vlasov equation whenever the radial direction is involved. This feature, combined with the fact that in the absence of collisions a perturbed Vlasov equilibrium cannot return to the original state, has important implications.

Consider the case of a one-dimensional spatially-uniform thermal-equilibrium plasma, in which all species are uniformly distributed, and all electromagnetic fields are zero. In Cartesian phase space coordinates, the associated advection equation is simply

$$\frac{\partial f}{\partial t} + v_x \frac{\partial f}{\partial x} = 0. \tag{6.46}$$

For periodic or specular-reflection boundary conditions, the distribution function associated with this equilibrium state cannot evolve away from the initial condition due to the fact that there are no forces and the spatial gradient is zero. In cylindrical coordinates, the associated advection equation for the equilibrium state is

$$0 = \frac{\partial f}{\partial t} + v_r \frac{\partial f}{\partial r} + \frac{v_\theta^2}{r} \frac{\partial f}{\partial v_r} - \frac{v_\theta v_r}{r} \frac{\partial f}{\partial v_\theta}, \tag{6.47}$$

and necessarily includes the terms associated with the Coriolis and centrifugal force. For a spatially-uniform equilibrium state to be preserved in cylindrical coordinates (i.e. for $\partial f/\partial t$ in Eq. (6.47) to be zero), the last two terms have to cancel each other exactly. For example, setting f to be a Maxwellian distribution function that is spatially uniform, one can show

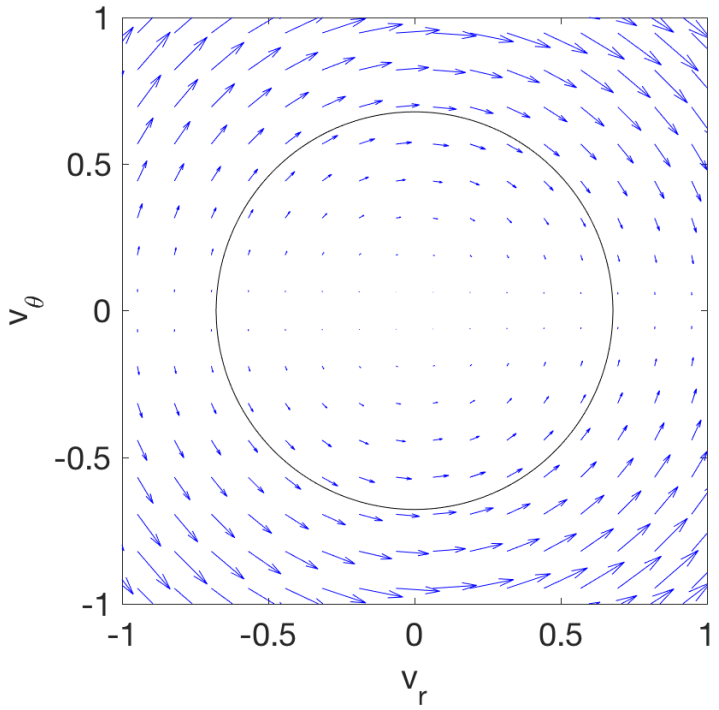

Figure 6.5: The circulation pattern in (v_r, v_θ) plane due to the Coriolis $(-v_r v_\theta / r)$ and centrifugal (v_θ^2/r) terms in the cylindrical coordinate Vlasov equation. The arrows indicate the direction of advection for the distribution function. The black circle is drawn for reference to better show the circular nature of the flow pattern.

that the Coriolis and centrifugal terms cancel each other. Note that while this cancellation is analytically exact, it is not necessarily exact in the discrete form of the Vlasov equation. Further complications arise when using the conservation-law form of the Vlasov equation,

$$0 = \frac{\partial f}{\partial t} + \frac{1}{r}\frac{\partial}{\partial r}\left(r v_r f\right) + \frac{\partial}{\partial v_r}\left(\frac{v_\theta^2}{r} f\right) + \frac{\partial}{\partial v_\theta}\left(-\frac{v_r v_\theta}{r} f\right), \tag{6.48}$$

Ensuring that $\partial f/\partial t$ is zero in Eq. (6.48) relies on the cancellation of three terms — a cancellation that is not guaranteed in the context of a numerical discretization. This means that in cylindrical phase space coordinates numerical error alone can cause a spatially-uniform distribution function to evolve away from equilibrium. If a numerical method cannot exactly preserve a spatially-uniform equilibrium state, then it should at least converge to the equilibrium as the grid is refined. Thus the goal is to initialize an equilibrium and demonstrate that $\partial f/\partial t$ converges to zero as the grid is refined.

To assess how well an equilibrium can be preserved in cylindrical phase space coordinates, a Maxwellian velocity dependence is considered. Let f_0 be defined in (r, v_r, v_θ) coordinates

as a spatially-uniform Maxwellian distribution function, such that

$$f_0 = \frac{1}{\pi v_T^2} \exp\left(-\frac{v_r^2 + v_\theta^2}{v_T^2}\right), \tag{6.49}$$

where v_T is the thermal speed. In the absence of electromagnetic fields, this distribution function satisfies the equilibrium form of the Vlasov equation, as can be shown by evaluating each of the terms in the Liouville form of the equation (Eq. (6.47)),

$$v_r \frac{\partial f_0}{\partial r} = 0 \tag{6.50}$$

$$\frac{v_\theta^2}{r} \frac{\partial f_0}{\partial v_r} = -\frac{2 v_r v_\theta^2}{r v_T^2} f_0 \tag{6.51}$$

$$-\frac{v_\theta v_r}{r} \frac{\partial f_0}{\partial v_\theta} = \frac{2 v_r v_\theta^2}{r v_T^2} f_0, \tag{6.52}$$

and noting that they sum to zero. In the conservation law form of the Vlasov equation (Eq. (6.48)), the terms are

$$\frac{1}{r} \frac{\partial}{\partial r} \left(r v_r f_0\right) = \frac{v_r}{r} f_0 \tag{6.53}$$

$$\frac{\partial}{\partial v_r} \left(\frac{v_\theta^2}{r} f_0\right) = -\frac{2 v_r v_\theta^2}{r v_T^2} f_0 \tag{6.54}$$

$$\frac{\partial}{\partial v_\theta} \left(-\frac{v_r v_\theta}{r} f_0\right) = -\frac{v_r}{r} f_0 + \frac{2 v_r v_\theta^2}{v_T^2} f_0 \tag{6.55}$$

and likewise sum to zero. Using Eq. (6.49) as the initial condition with $v_T = 0.12$, $v_r, v_\theta \in [-1, 1] \times [-1, 1]$, and $r \in [0, 4]$, the distribution function is advanced in time using the zero-field governing equation given by Eq. (6.48) and the finite-volume discretization described in Chapter 3. The results are presented in Fig. 6.6 through Fig. 6.9 for two different grid resolutions. A time step size of $\Delta t = 2 \times 10^{-4}$ is used in both cases.

Figure 6.6 shows the net change in mass, the total volume-integrated momentum in the v_r and v_θ directions, and the evolution of kinetic energy in the system. The net change in mass is zero to numerical precision, independent of the resolution. This is guaranteed by the finite volume discretization provided that the system boundaries are closed. Since a specular reflection boundary condition is used for the axis at the lefthand side as well as for the conducting wall at the righthand side, and zero-flux boundaries are set at $v_r, v_\theta = \pm v_{\max}$, no portion of the distribution function can leave the simulation domain. The volume-integrated value of the radial momentum decreases with time, indicating that the original Maxwellian distribution function develops a drift. As the grid is refined, the magnitude of the drift decreases toward zero. The value of the azimuthal momentum stays fixed at zero. The kinetic energy decreases with time, and the net change in the kinetic energy shrinks as grid resolution is increased. These reduced variables indicate that increasing resolution leads

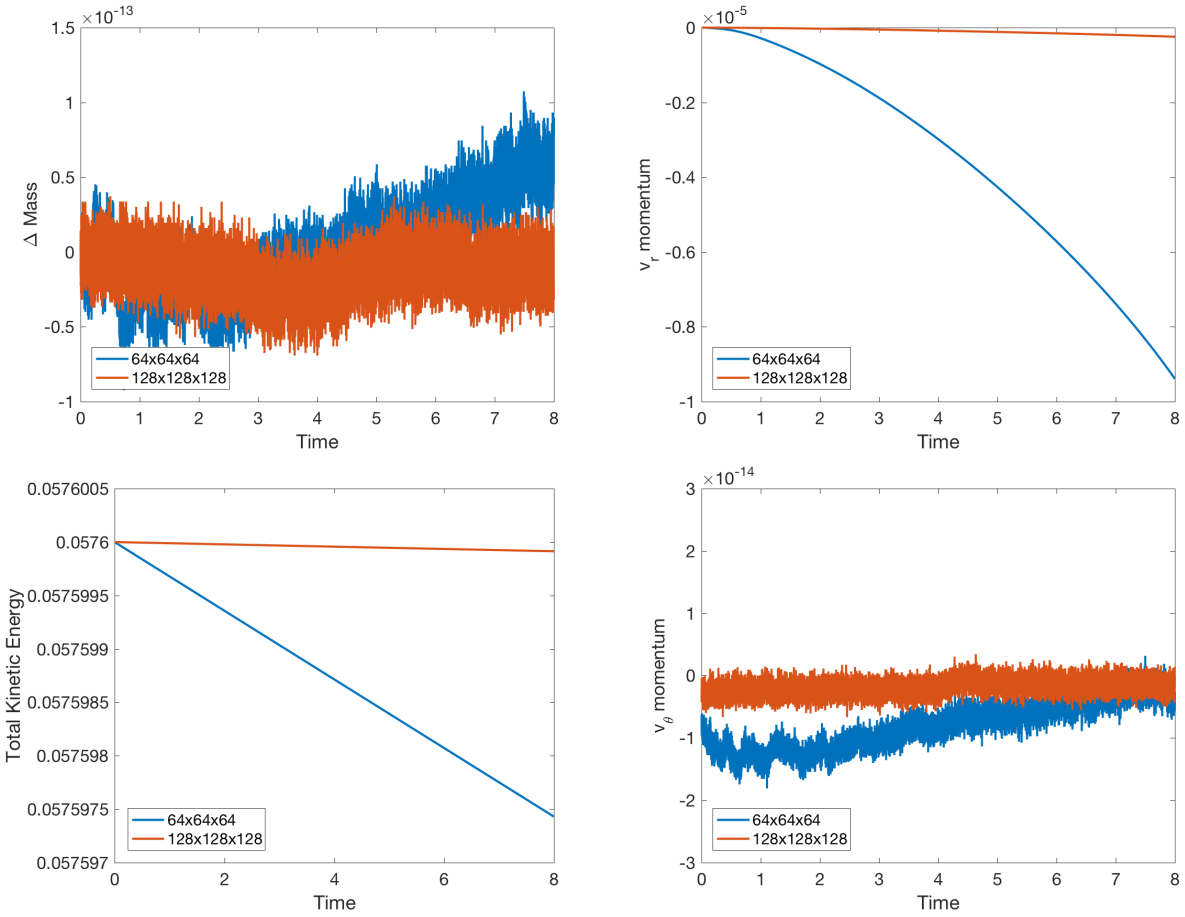

Figure 6.6: The net change in mass, net momentum, and net kinetic energy for a spatially-uniform Maxwellian initial condition in (r, v_r, v_θ) coordinates using 64^3 and 128^3 grid resolution. Mass is conserved to numerical precision, whereas momentum and energy are not conserved. As resolution is increased, however, momentum and energy converge to initial-condition values.

to smaller departures away from equilibrium, which is what is expected for a converging algorithm.

Figure 6.7 shows the evolution of the net change in density as function of radius and time. For an equilibrium system, the net change should be zero, but due to numerical errors spatial variations in the density develop immediately near the axis as well as at the outer boundary. These arise due to the fact that the numerical method cannot exactly preserve the isotropic velocity dependence of the Maxwellian distribution function. The departure from a Maxwellian in turn leads to a lack of cancellation of the terms in Eq. (6.48) resulting in advection along the radial direction. The most significant departure from the initial condition occurs at the axis where the advection speeds are the largest. These start off as localized spikes and then propagate into the domain, amplifying in time. The features amplify until they become on the order of the truncation error, at which point they are subject to numerical dissipation from the upwind spatial discretization, which smooths out these variations. It is important to note that the fields in the evolution equation are explicitly set to zero, which means that the distribution function is in effect that of a collisionless neutral gas. In the context of a plasma, density features would lead to the generation of electric fields, which would result in more complicated dynamics.

Since the analytic solution stipulates that $\Delta n = 0$, the convergence rate can be computed from the density data from the 64^3 and 128^3 resolution simulations. The convergence rate p can be computed from Eq. (3.10) using the L1-norm, such that

$$p = \frac{1}{\log 2} \log \left(\frac{\frac{1}{N_r} \sum_{i=1}^{N_r} |\Delta n_i^{2h}|}{\frac{1}{2N_r} \sum_{i=1}^{2N_r} |\Delta n_i^{h}|} \right) \tag{6.56}$$

where the change in density in cell i for radial grid spacing h is defined in terms of the phase-space-volume-integrated distribution function as

$$\Delta n_i^h = \frac{1}{r_i h} \left[\sum_j \sum_k \left(\langle f \rangle_{i,j,k} - \langle f_0 \rangle_{i,j,k} \right) \right] \tag{6.57}$$

Evaluating the convergence rate at the final time (time 8, time step 40,000) yields $p = 4.3690$, indicating slightly better than fourth order convergence. This verifies that the discretization is fourth-order accurate. The accuracy is slightly higher than fourth order likely due to the fact that the fluxes in this case only depend on the distribution function (which is interpolated to cell faces using a fifth-order reconstruction) and on coordinate values (r, v_r, v_θ), which are linear and hence known exactly at any given cell face.

Figure 6.8 shows the evolution of the radial momentum as a function of radius and time as the Maxwellian distribution is advanced forward in time. Much like the density, the radial momentum develops spatial features at the axis and conducting wall boundaries due to numerical errors. These features start off as spikes, that then amplify in time and propagate into the domain, until they reach a value that is on the order of the truncation error, at which point they are smoothed out by the numerical dissipation built into the algorithm.

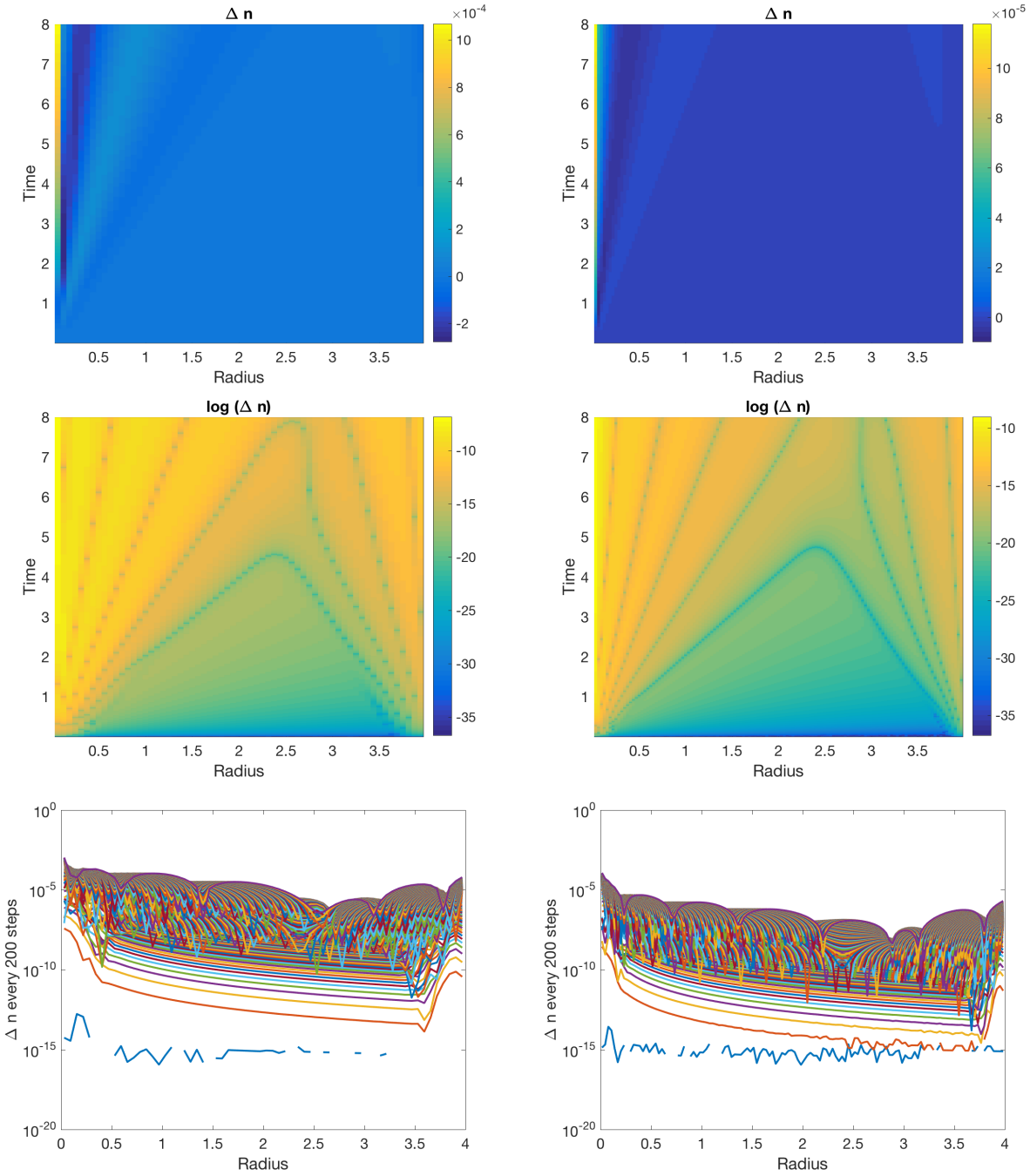

(a) 64^3 **(b)** 128^3

Figure 6.7: Evolution of the change in number density for a spatially-uniform Maxwellian initial condition in (r, v_r, v_θ) coordinates using (a) 64^3 resolution and (b) 128^3 resolution grids. Spatial variations arise at domain boundaries, and propagate into the domain. These variations are a result of numerical errors, and as the resolution is doubled they diminish by about a factor of ten. The time step size is $\Delta t = 2 \times 10^{-4}$ for both resolutions.

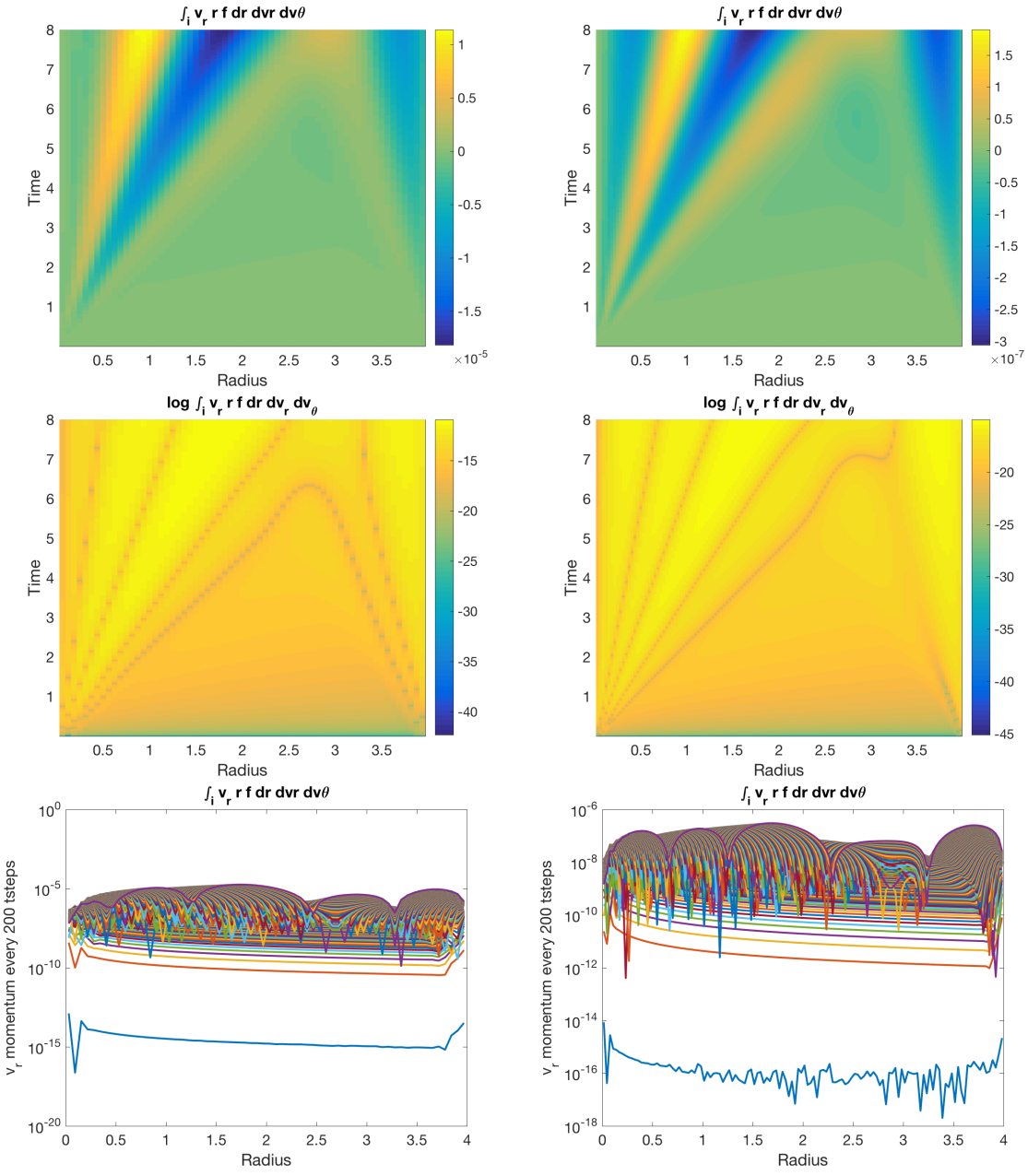

(a) 64^3 **(b)** 128^3

Figure 6.8: Evolution of the volume-integrated v_r momentum for a spatially-uniform Maxwellian initial condition in (r, v_r, v_θ) coordinates using 64^3 resolution (left) and 128^3 resolution (right) grids. Much like in the case of density, spatial variations in momentum arise at domain boundaries, and propagate into the domain. These variations are a result of numerical errors, and as the resolution is doubled they diminish by about a factor of ten. The time step size is $\Delta t = 2 \times 10^{-4}$ for both resolutions.

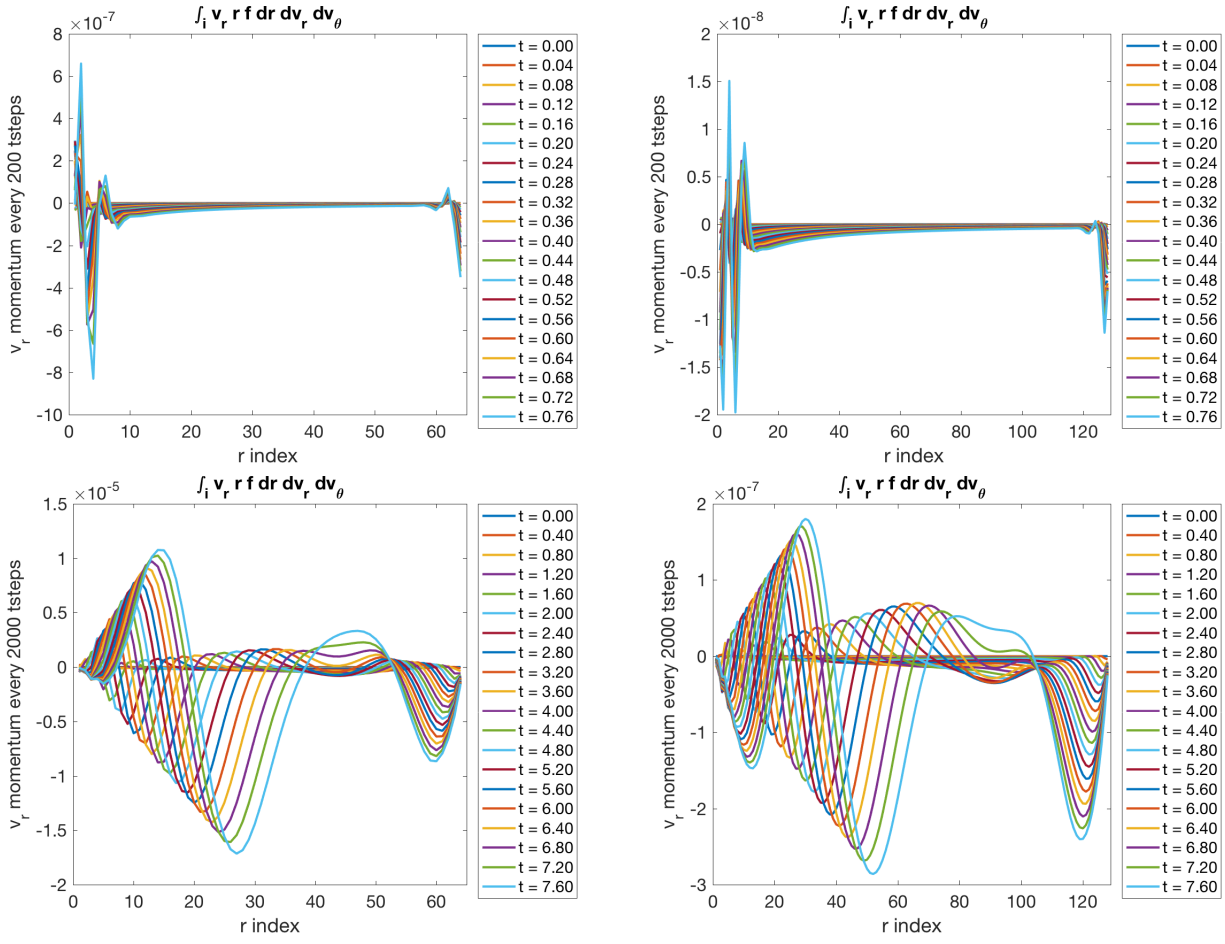

(a) 64^3 **(b)** 128^3

Figure 6.9: Short-term and long-term evolution of the volume-integrated v_r momentum for a spatially-uniform Maxwellian initial condition in (r, v_r, v_θ) coordinates using (a) 64^3 resolution and (b) 128^3 resolution grids. Spikes in the momentum develop near boundaries in the first few time steps and amplify in time until they reach a value on the order of the truncation error, at which point they are subject to dissipation by the upwind discretization, which causes them to smooth out into larger-wavelength numerical features. The time step size is $\Delta t = 2 \times 10^{-4}$ for both resolutions.

The formation of the spikes and their subsequent smoothing is shown in Fig. 6.9. As the grid resolution is increased, the radial momentum converges to zero at the expected rate for a fourth-order discretization.

Figures 6.10 and 6.11 show contour plots of the distribution function, relative to the initial condition given in Eq. (6.49). The distribution function becomes asymmetric along the v_r-direction, which leads to advection along the radial direction. Note that this asymmetry

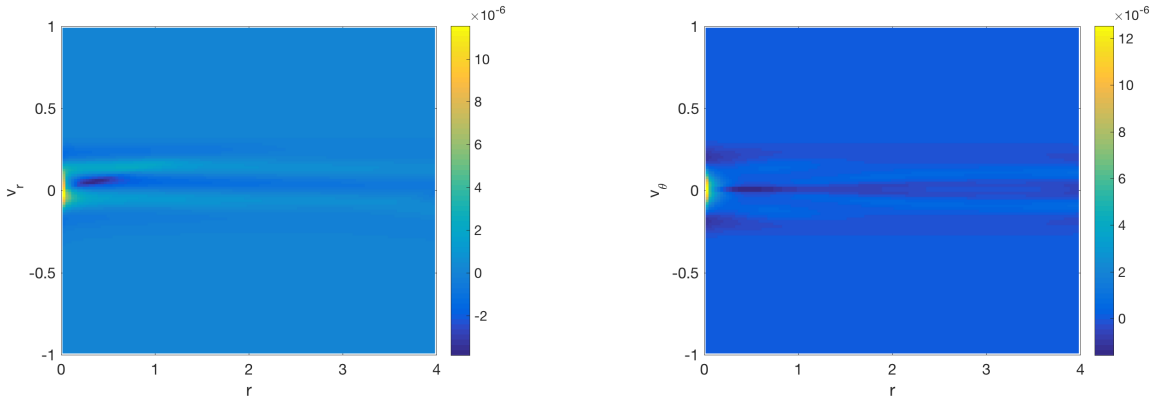

(a) $\sum_{k=0}^{N_{v_\theta}-1}\left(\langle f\rangle_{i,j,k}-\langle f_0\rangle_{i,j,k}\right)/(r_i h_r)$ **(b)** $\sum_{j=01}^{N_{v_r}-1}\left(\langle f\rangle_{i,j,k}-\langle f_0\rangle_{i,j,k}\right)/(r_i h_r)$

Figure 6.10: The net change in the volume-average distribution function for a 128^3 resolution calculation, between $t = 0$ and time $t = 7.8$. The spatially-uniform Maxwellian initial condition given in Eq. (6.49) is not maintained. The net change in the distribution function is shown in (a) the (r, v_r) plane and (b) the (r, v_θ) plane, integrated over the orthogonal direction. The distribution function stays symmetric in v_θ, and develops a drift in v_r.

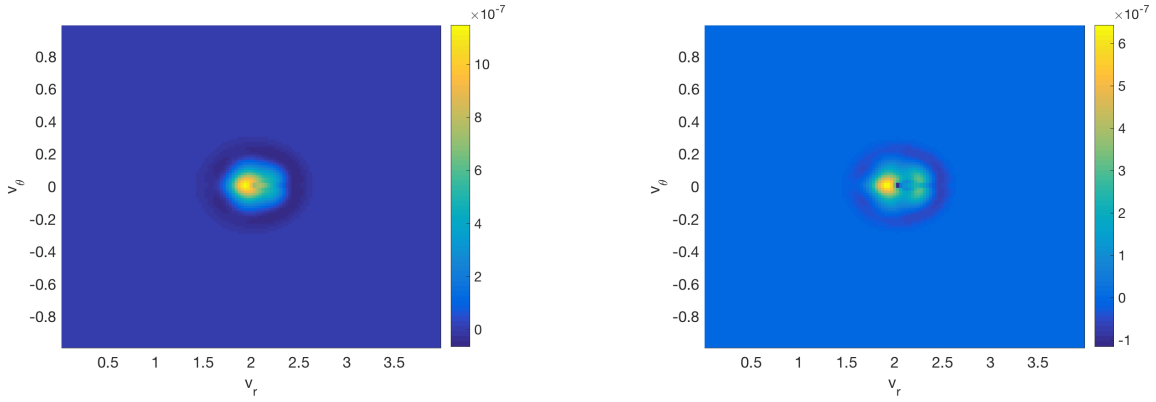

(a) $\delta f(v_r, v_\theta) = \left(\langle f\rangle_{0,j,k}-\langle f_0\rangle_{0,j,k}\right)/(r_0 h_r)$ **(b)** $\delta f(v_r, v_\theta) = \left(\langle f\rangle_{1,j,k}-\langle f_0\rangle_{1,j,k}\right)/(r_1 h_r)$

Figure 6.11: The net change in the volume-average distribution function for a 128^3 resolution calculation, between $t = 0$ and time $t = 7.8$. The spatially-uniform Maxwellian initial condition given in Eq. (6.49) is not maintained. Two difference slices are shown: (a) the $(r = h_r/2, v_r, v_\theta)$ plane and (b) the $(r = 3h_r/2, v_r, v_\theta)$ plane. Due to expected numerical errors, the distribution becomes asymmetric in v_r, which leads to advection along the radial direction. Consequently equilibrium is not maintained. The distribution function does remain symmetric along the v_θ direction, which means that despite numerical artifacts, there is no net rotation imparted on the particles in the system.

is consistent with the circulation pattern presented in Fig. 6.5. The departure away from equilibrium is most pronounced near the axis, which is where the Coriolis and centrifugal term advection speeds are highest.

In practice a time-integrated finite-volume discretization is not designed to model steady-state solutions – the algorithm used here is aimed at modeling dynamics. Investigating the behavior of the solution in a steady-state configuration, however, yields insights into the numerical solutions obtained for dynamic problems. It is also important that the finite-volume solution (a) converges to the expected steady-state value and (b) converges at the expected rate when applied to model an equilibrium, as is demonstrated here. Verified convergence yields confidence that in the limit of infinite resolution the approximate numerical solution approaches the true solution to the governing partial differential equation.

6.2.2 Ion confinement in one-dimensional Z-pinch

The cylindrical coordinate Vlasov-Maxwell solver described in this dissertation is designed to study kinetic effects in axisymmetric plasmas. A one-dimensional plasma configuration is considered – that of the Z-pinch. Z-pinches feature a simple cylindrical geometry (see Fig. 6.12) and rapid onset of instabilities, meaning they have fast dynamics that are accessible to kinetic simulations. Computational investigation of Z-pinch dynamics are typically carried out using fluid models; however, kinetic effects are believed to be important, particularly near the axis where the mean fee path can be large relative to the system size [109] and also in regions of large density gradients, which can lead to drift wave turbulence [110].

In a Z-pinch, electrons carry the bulk of the current, and are thereby electromagnetically confined; whereas ions, which carry little to no current, are electrostatically confined. The objective here is to model this collisionless configuration along the radial direction, with ion dynamics modeled in (r, v_r, v_θ) phase space coordinates, and electron distribution assumed to be fixed for all time. This system can be described by the two-fluid model, such that in equilibrium ion pressure is balanced by the electrostatic field

$$\frac{\partial P_i}{\partial r} = q_i n_i E_r \tag{6.58}$$

and electron pressure is balanced by the electric and magnetic field,

$$\frac{\partial P_e}{\partial r} = q_e n_e \left(E_r - u_{ze} B_\theta\right). \tag{6.59}$$

Assuming that electrons are stationary means that the pressure gradient is constant for all time, which implies that any change in E_r is exactly balanced by a change in the $u_{ze}B_\theta$ term.

To study ion dynamics the equilibrium is perturbed, such that the ions are initialized to be radially displaced from the electrons – see Fig. 6.13. The resulting electric field accelerates the ions toward the stationary electrons, and thereby the original potential energy is converted into kinetic energy. The ions will move toward the axis until they overshoot the electrons, causing the electric field to change sign and accelerate them radially outward, and the process

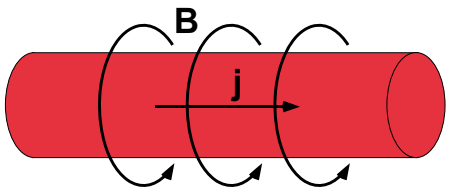

Figure 6.12: A Z-pinch is a simple plasma configuration characterized by a column of current-carry plasma that is confined by a self-generated magnetic field.

repeats. This type of electrostatic oscillation is known as a Langmuir wave, and is well-characterized in the context of a spatially-uniform plasma, such that the dispersion relation is given by

$$\omega^2 = \omega_p^2 + 3k^2 v_T^2, \tag{6.60}$$

where ω_p is the plasma frequency (in this case the ion plasma frequency), v_T is the ion thermal speed, and k is the wave number of the perturbation. This dispersion relation, however, does not apply for the case of an axisymmetric Z-pinch because the wave number is not well defined along the radial direction and the plasma density in general is not uniform, which means that the plasma frequency varies spatially. Moreover, in the kinetic model description, phase mixing also plays a role, such that the oscillation is nonlinear and can damp in time.

For the computational investigation of this problem, the ions and electrons are initialized to have a smooth radial profile with compact support, such that the densities are

$$n_i(r) = \frac{8}{3}\left(1 - \frac{8}{9}r^2 + \frac{16}{81}r^4\right) \qquad r \in [0, r_{0,i}] \tag{6.61}$$

$$n_e(r) = \frac{250}{77}\left(\frac{11}{10} - \frac{1375}{343}r^3 + \frac{20625}{4802}r^4 - \frac{20625}{16807}r^5\right) \qquad r \in [0, r_{0,e}] \tag{6.62}$$

where $r_{0,i} = 1.5$ and $r_{0,e} = 1.4$. These are simply polynomials subject to certain constraints to ensure smoothness. For the electrons the constraints are $\int_0^{r_{0,e}} n_e r dr = 1, n_e'(0) = 0, n_e(r_{0,e}) = 0, n_e'(r_{0,e}) = 0$, and for ions the constraints are $\int_0^{r_{0,i}} n_i r dr = 1, n_i'(0) = 0, n_i'(r_{0,i}) = 0, n_i(|r_{0,i}|) = 0$. The last condition is intended to ensure the ion density distribution is symmetric about $r = 0$. Note that the density profiles are scaled so that the total ion charge in the system is one and the total electron charge in the system is negative one. The ion velocity dependence is an isotropic Maxwellian with thermal speed $v_T = 0.12$, such that the temperature is spatially uniform. Since the electrons are assumed to be stationary their velocity dependence is irrelevant. The mean radius for each species can be evaluated using the expression

$$\bar{r}_s = \frac{\int n_s r^2 dr}{\int n_s r dr}, \tag{6.63}$$

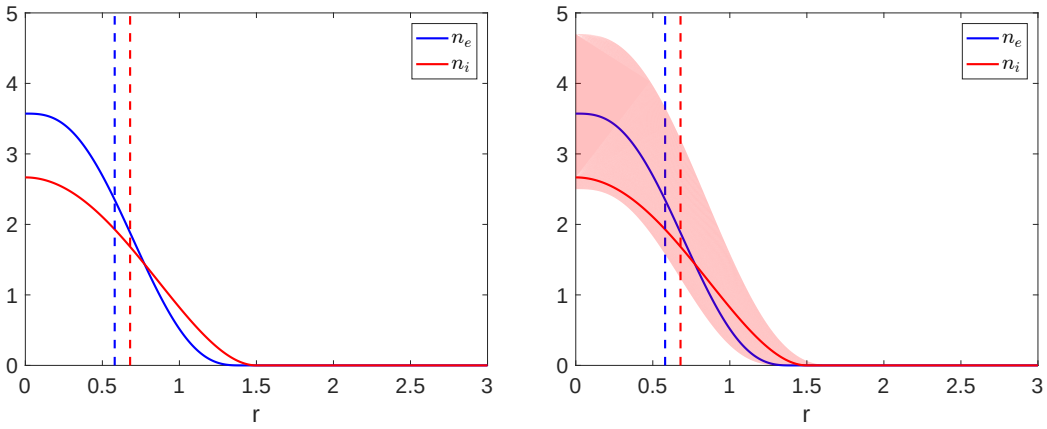

Figure 6.13: A heuristic diagram of ion oscillations in an axisymmetric configuration. The y-axis is in arbitrary units. (a) To model the electrostatic ion confinement in a Z-pinch, ions (red) are initialized to be displaced away from electrons (blue). Electrons are assumed to be stationary. Vertical dashed lines show the mean radius of the ions and the electrons. (b) The ions are expected to oscillate nonlinearly, within the shaded region.

such that $\bar{r}_e \approx 0.58$ and $\bar{r}_i \approx 0.68$. The mean radius indicates the average radial location of each species, and thereby provides a metric for evaluating the distance between the ion and electron distributions. The initial condition number densities, total charge density, and associated radial electric field, which can be derived from Gauss's law, is plotted in Fig. 6.14.

This initial condition is evolved forward in time using a Vlasov-Maxwell solver, which allows for dynamic magnetic fields. The governing equations for the ions are

$$0 = \frac{\partial f}{\partial t} + \frac{1}{r}\frac{\partial}{\partial r}\left(r v_r f\right) + \frac{\partial}{\partial v_r}\left(\left[E_r + \frac{v_\theta^2}{r}\right] f\right) + \frac{\partial}{\partial v_\theta}\left(\left[E_\theta - \frac{v_r v_\theta}{r} f\right]\right) \tag{6.64}$$

$$\frac{\partial E_r}{\partial t} = -\int_{-\infty}^{\infty} v_r f \, dv_r dv_\theta, \tag{6.65}$$

where it has been assumed that the relative charge is $Z_i = 1$ and relative mass is $M_i = 1$. The domain is $r, v_r, v_\theta \in [0, 4] \times [-1, 1] \times [-1, 1]$.

The evolution of the distribution function $f(r, v_r, v_\theta)$, averaged over a cell, is shown in Fig. 6.15. The distribution function starts off having zero drift, such that the velocity centroid is at $(v_r, v_\theta) = (0, 0)$. As the ions are accelerated toward the axis, the bulk of the distribution function shifts toward negative v_r, such that the magnitude of the shift is radius-dependent, which can be seen in the (r, v_r) plane. As the ions move toward the axis, they are compressed and heated, as evidenced by the distribution function widening in the (v_r, v_θ) plane, which corresponds to an increase in thermal speed. When the ions overshoot the electrons they are accelerated in the positive radial direction, such that the bulk of the

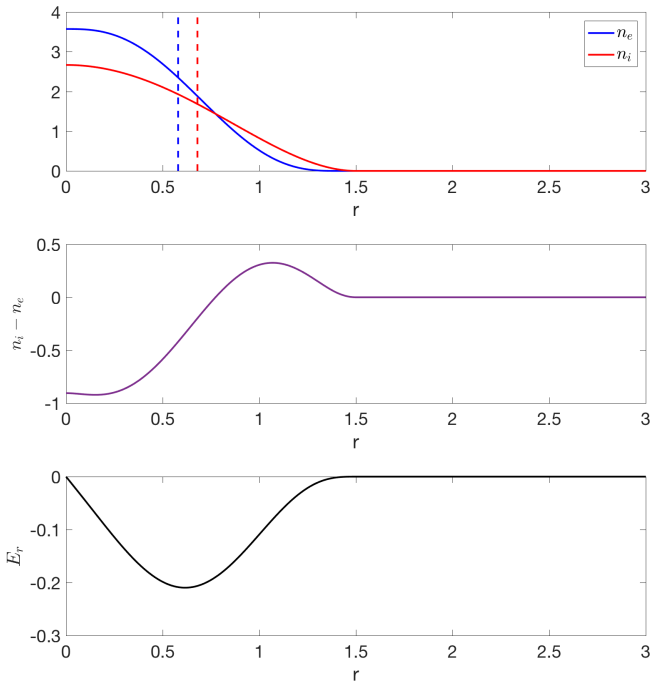

Figure 6.14: Initial conditions for ion confinement simulation in cylindrical phase space coordinates. The plots show ion density and electron density (top) with centroids plotted in dashed lines, charge density (middle), and the associated electric field (bottom).

distribution function shifts toward positive v_r. As the ions move away from the axis, they cool, resulting in a decrease in thermal energy seen by the shrinking of the Maxwellian in the (v_r, v_θ) plane. Since the density depends on radius, the amount of time that a portion of the distribution function moves from negative to positive v_r is also radius dependent. This results in a non-linear oscillation. Since the distribution function also moves along the radial direction, the oscillation is accompanied by phase mixing, and the development of substructures. With time the magnitude of the shifts in the v_r direction decreases, and ultimately the distribution function reaches a new equilibrium.

The net mass in the system is conserved to round-off error, as is guaranteed by the discretization. The evolution of the net ion momentum in the system is shown in Fig. 6.16. The net momentum along the radial direction oscillates in time about zero, and the magnitude of the momentum damps. This behavior is consistent with the dynamics seen in the distribution function (see Fig. 6.15) from which the momentum is derived. The net azimuthal momentum in the system is zero to round-off error, as there are no forces that could induce rotation. The evolution of the net temperature is shown in Fig. 6.17. A temperature anisotropy develops, such that the thermal energy associated with motion along the

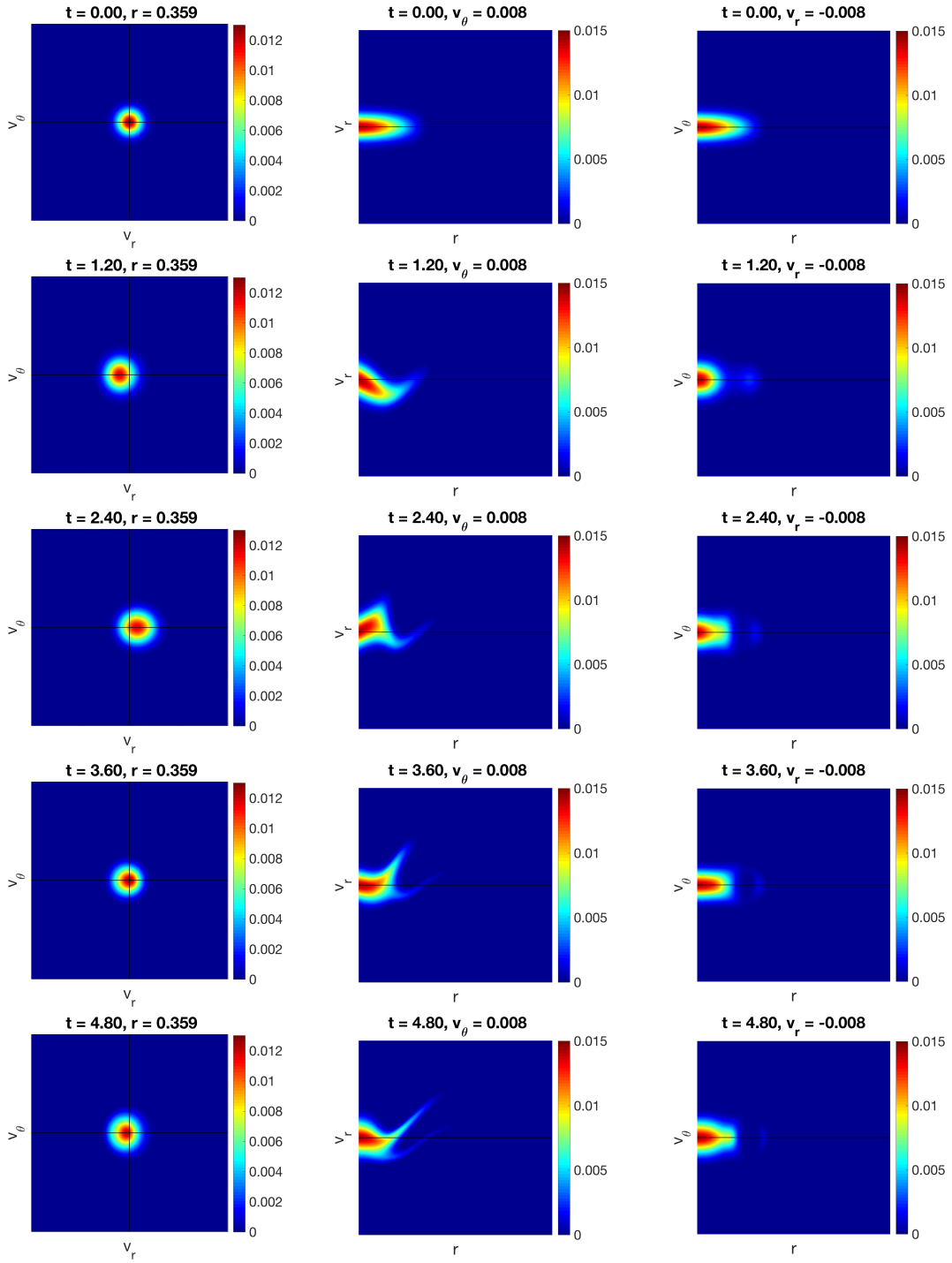

(a) $f(v_r, v_\theta, r = 0.359)$ **(b)** $f(r, v_r, v_\theta = 0.008)$ **(c)** $f(r, v_r = -0.008, v_\theta)$

Figure 6.15: Distribution function evolution in different slices for 128^2 simulation of axisymmetric ion confinement in a Z-inch.

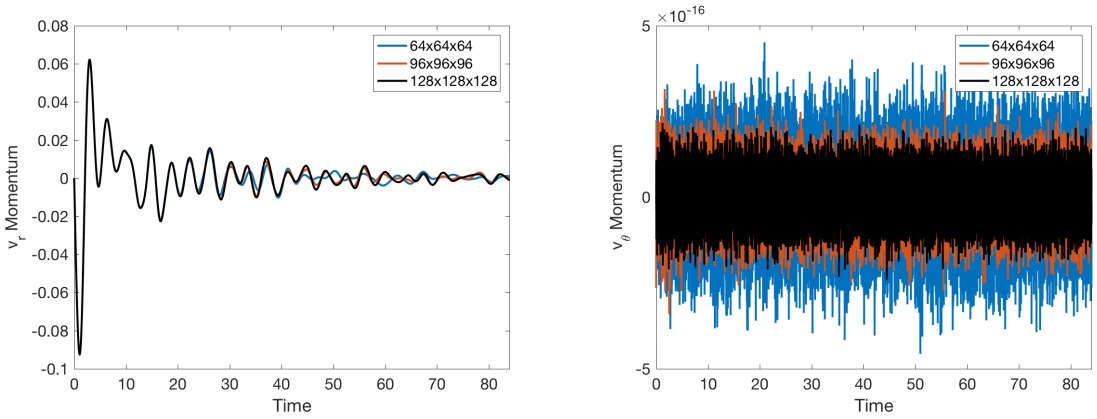

(a) Net radial momentum **(b)** Net azimuthal momentum

Figure 6.16: Evolution of the net (a) radial and (b) azimuthal momentum in simulations of axisymmetric ion confinement in a Z-pinch. The radial momentum oscillates about zero as the ions move toward and away from the axis. The azimuthal momentum remains zero to round-off error.

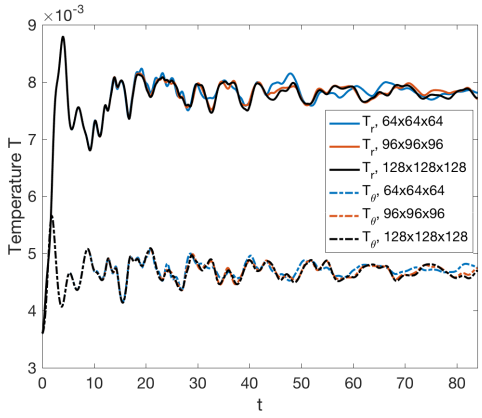

Figure 6.17: Evolution of the ion temperature associated with random motion along the radial direction (T_r) and random motion along the azimuthal direction (T_θ) in simulations of axisymmetric ion confinement in a Z-pinch. A temperature anisotropy develops such that $T_r > T_\theta$, and the temperatures oscillate in time, consistent with the compression and expansion dynamics of the ions.

radial direction becomes greater than the thermal energy associated with motion along the azimuthal direction. Such anisotropy is expected in a system where there are no collisions to drive the ions toward an isotropic distribution. The net gain in thermal energy comes at the expense of the potential energy, associated with the electric field.

The spatiotemporal evolution of ion number density is shown in Fig. 6.18. The final mean

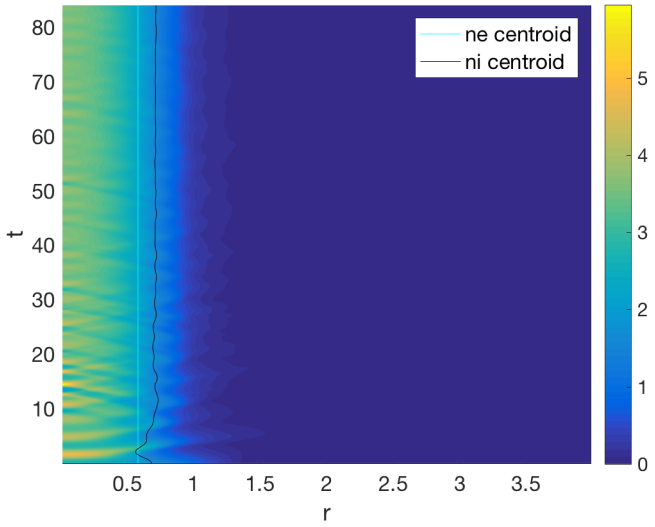

Figure 6.18: Evolution of the ion number density as a function of space and time in a 128^3 resolution simulation of axisymmetric ion confinement in a Z-pinch. The final mean radius of the ions is 0.719, such that the separation between the ions and electrons is 0.136, which is on the order of a Debye length – the distance at which the charge from the electrons is shielded by the dynamic ions.

radius of the ions is 0.719, such that the separation between the ions and electrons is 0.136. This separation distance is on the order of a Debye length, which is the distance at which the dynamic species (in this case the ions) screens out the electric field of the stationary electrons. Notably the Debye length (see Eq. (2.25)) does not have a well-defined value in this system since plasma frequency is spatially dependent. As a point of comparison, the initial Debye length, using the initial condition thermal speed $v_T = 0.12$ and plasma frequency defined in terms of the net ion number density in the system, is 0.339. Note that the azimuthal direction is assumed to occupy one radian.

The electric field evolution for the ion confinement simulation is shown in Fig. 6.19. The electric field starts off negative (directed toward the axis) for $r \in [0, 1.5]$, and changes sign whenever ions overshoot the electrons as they move toward and away from the axis. The electric field magnitude decreases as a function of time, indicating that some of the original the electric field energy is converted to kinetic energy. Unlike the initial condition (see Fig. 6.14), in which the electric field is localized, by the end of the simulation the electric field is non-zero throughout the domain. This means that a small portion of ions have reached the $r = r_{\max}$ boundary. A negative electric field develops at the periphery of the bulk ion density distribution, confining the ions to the stationary electrons.

Figure 6.20 shows the evolution of the radial momentum for the ions as a function of position and time. The frequency at which momentum changes sign varies depending on the radial location and time, providing further evidence of the nonlinear nature of the os-

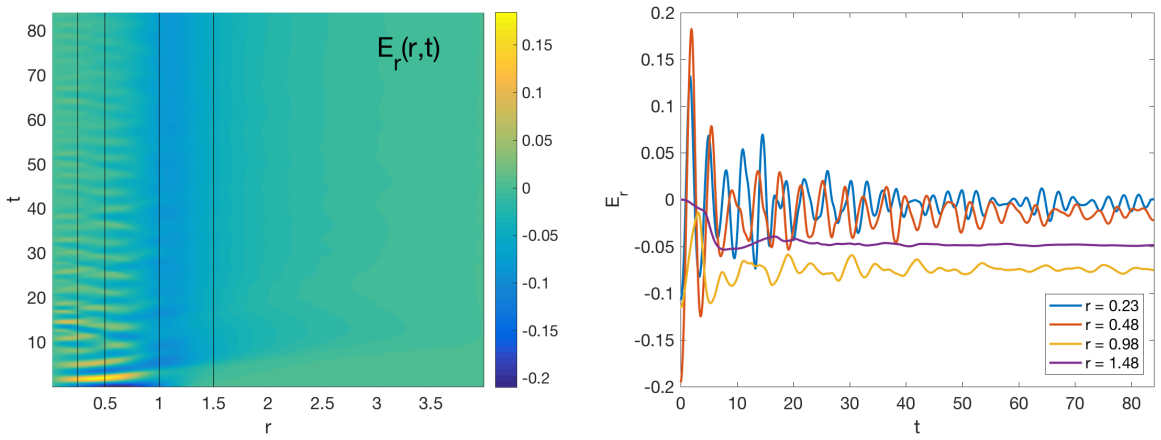

Figure 6.19: Evolution of the radial electric field as a function of space and time in a 128^3 resolution simulation of axisymmetric ion confinement in a Z-pinch. The contour plot of the electric field as a function of radius and time (left) shows how the electric field damps nonlinearly as a function of time. The electric field at four different radii, shown as black lines on the left, is plotted as a function of time (right). A negative electric field, directed toward the axis, develops at the periphery of the ion density distribution and confines the ions to the stationary electrons.

cillation. The highest frequency is observed closest to the axis, although the magnitude of the momentum is also small in this region. Independent of the radial location, over time the magnitude of the momentum approaches zero, indicating a transition to an equilibrium. Thus the bulk of the energy originally in the electric field is transferred into thermal energy, as opposed to directed kinetic energy.

Figure 6.21 shows the evolution of the number density, electric field, and momentum for time $t \in [0, 15]$. These plots show that the original monotonically-decreasing density profile later develops local minima and maxima, depending on the local motion of the ions. These profiles are consistent with the multi-mode structures in the electric field and momentum. Thus in this simple closed axisymmetric system with one mobile species, the dynamics are rather complicated.

These simulation results show that the ion dynamics and fields in this Z-pinch system evolve in a way that is qualitatively consistent with the physically expected behavior. At the same time, the simulations yield a vast amount of information regarding the details of ion dynamics in an axisymmetric system. It is worth noting that our ability to analytically predict the behavior of axisymmetric systems in a quantitative way is rather limited, particularly in instances where the plasma is non-uniform and nonlinear effects are important [111]. This is why simulation capabilities such as these are important to the development of a more complete understanding of plasma phenomena.

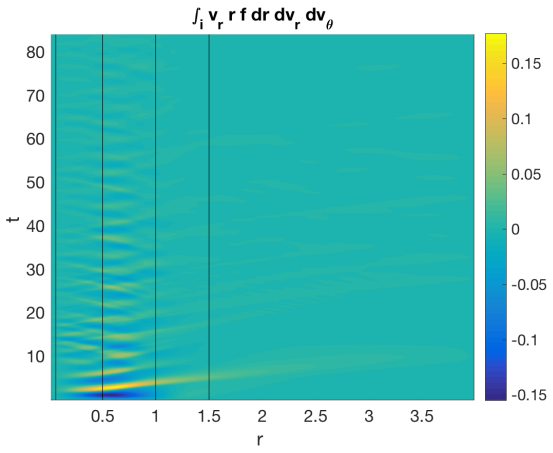

(a) $p_r(r,t)$

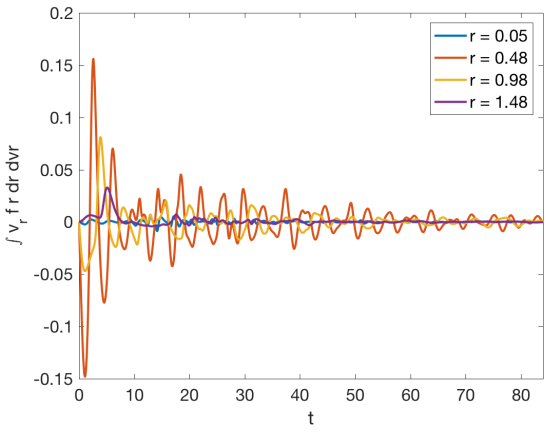

(b) $p_r(t)$ at fixed radius

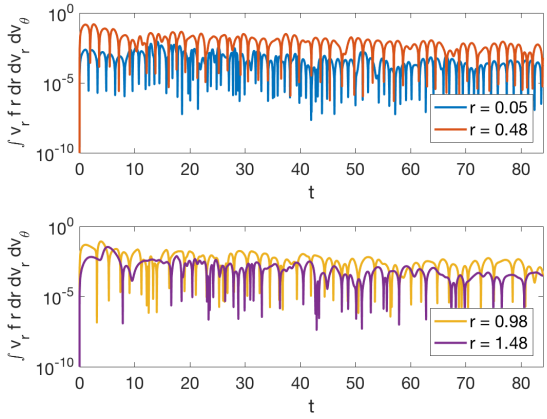

(c) $p_r(t)$ at fixed radius, log scale

Figure 6.20: (a) Volume-integrated radial momentum p_r as a function of position and time from a 128^3 resolution simulation of axisymmetric ion confinement in a Z-pinch. The vertical black lines in the contour plot indicate the slices plotted on the right both on (b) a linear scale and (c) a log scale. The momentum damps in time indicating a transition to an equilibrium state.

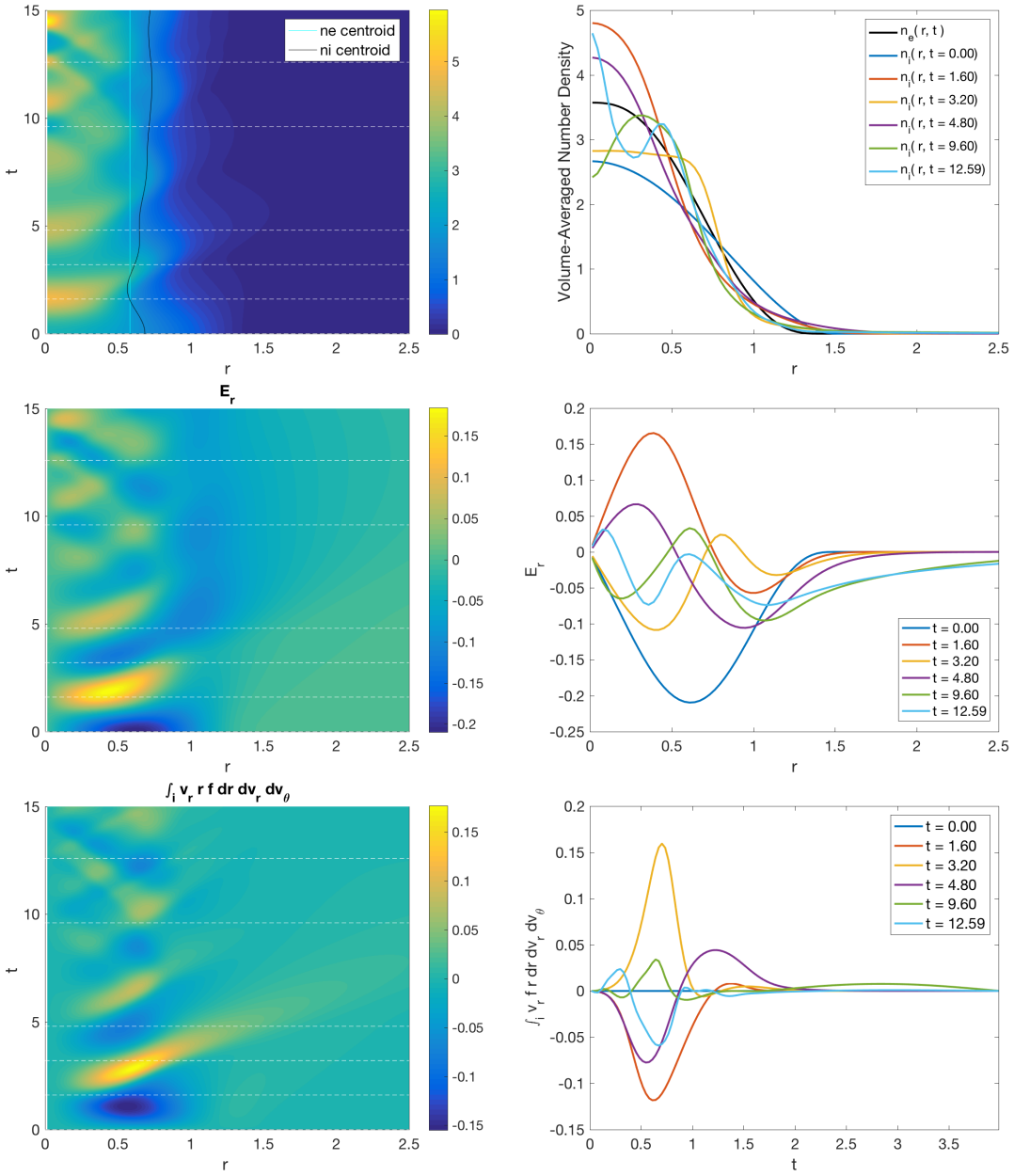

Figure 6.21: Evolution of number density, radial electric field, and volume-integrated radial momentum for $t \in [0, 15]$ from a 128^3 resolution simulation of axisymmetric ion confinement in a Z-pinch. These plots show the multi-mode structures that develop as the ions oscillate nonlinearly about the electron distribution. The white dashed lines in the contour plots on the left indicate the radial profiles plotted on the right.

Chapter 7

Computational framework

The Vlasov-Maxwell solver thus far has only been described in terms of its mathematical algorithm aspects. For efficient implementation of these algorithms, software and programming also play an important role. The primary way in which hyperbolic equation solvers are made efficient is through parallelization based on domain decomposition, which allows the computational work to be distributed among many processors. Parallelization is needed in order to efficiently execute three-dimensional simulations, and is indispensable when it comes to four- and five-dimensional phase space calculations. Parallelization also introduces complexity, and efficient implementation requires weighing computational cost against the cost of communication between processors.

The parallel implementation for the algorithms described in this dissertation made use of the Chombo library [112]. Chombo is a framework for solving partial differential equations on structured grids, and facilitates a parallel data infrastructure for fixed-mesh and adaptively-refined-mesh calculations. The framework has abstractions for defining data on patches that are distributed among processors, and abstractions for operations like specified-direction integration over data on many processors. Another feature is that it allows data to be defined in up to six dimensions, which makes it applicable to phase space discretization. These features are encapsulated in C++ classes that are a part of the Chombo library, but they require the user to program the discretization and solvers. The phase space simulations described in this dissertation have unique properties that make their software implementation different from that of other hyperbolic equation solvers. In addition to standard domain decomposition features, aspects of the customized software developed for the parallel implementation of the Vlasov-Maxwell solver are described here.

7.1 Parallelization features in Chombo

The finite-volume calculations described in this dissertation require careful indexing of multidimensional data. For a parallel implementation of the algorithm there has to be a protocol for dividing the data into subsets, distributing these subsets among processors so that each

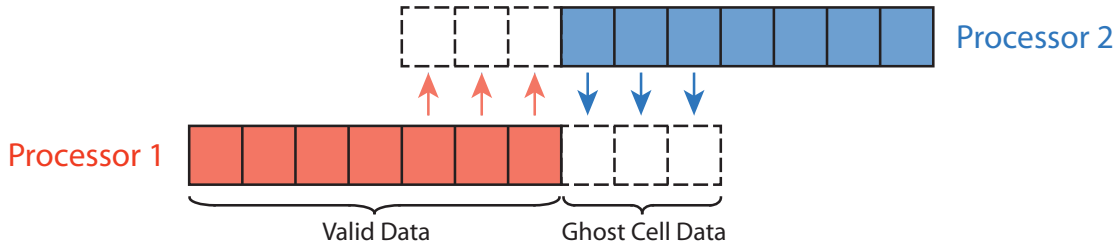

Figure 7.1: Processors that own neighboring data exchange information through ghost cells. Ghost cells of Processor 1 are filled with valid data from Processor 2, and vice versa.

processor can index and perform calculations on the data it owns, and for communicating data between processors whenever neighboring data are needed. In Chombo this is achieved through abstractions that allow data to be defined on unions of rectangles. Each rectangle occupies a D-dimensional integer lattice that represents a region of the D-dimensional domain. Chombo also provides abstractions for assigning each rectangle and its associated data to a processor. As a result each processor indexes and performs operations on the data it owns, while all processors execute the same code.

Since flux calculations require data from neighboring cells, processors have to exchange information with other processors that own neighboring data. In Chombo the mechanism of doing this is through ghost cells. Each rectangle of data thus has associated "valid" data, corresponding to a valid region in the domain, and local "ghost cell" data which consists of replicas of valid data from other processors. These local ghost cells are not to be confused with the global domain boundary ghost cells. Thus for two processors that own neighboring data, communication between the two processors involves copying data from valid regions of one processor to ghost cell regions of another processor. This process is illustrated in Fig. 7.1 for one-dimensional data and in Fig. 7.2 for two-dimensional data. Notably for fourth-order calculations involving the evaluation of transverse derivatives, corner ghost cells also need to be filled. The exchange of ghost cell data is abstracted away in Chombo such that the copy operations illustrated in Fig. 7.1 and Fig. 7.2 are handled through a simple function call that invokes message passing interface (MPI) commands. Thus while a user of Chombo is not tasked with explicitly writing message-passing code, they have to (a) be aware of when information needs to be communicated between processors and (b) write code that can be executed simultaneously on any number of processors using the provided data-holder and indexing classes. Since data communication is slow relative to floating point operations, the number of times ghost cell information is exchanged should be kept to a minimum.

The variables in the Vlasov-Maxwell equation system are unusual because the distribution function occupies a high-dimensional space, whereas electromagnetic fields, charge densities, and currents occupy a lower-dimensional space. Updating variables in the high-dimensional space requires information from the lower-dimensional space, and vice versa. For example, updating the electric field requires integrating the distribution function over

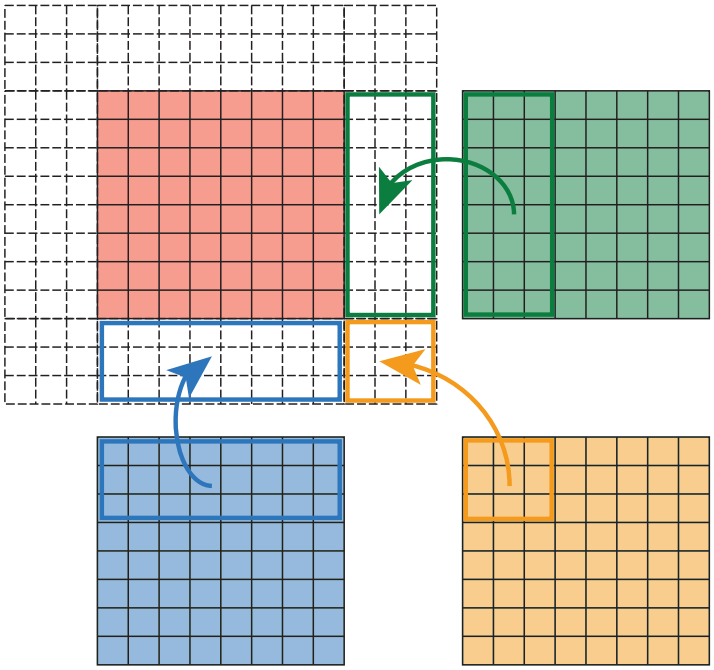

Figure 7.2: Communication associated with filling one processor's ghost cells in two dimensions. Different-color grids denote valid data owned by different processors. Dashed lines indicate the ghost cells, which need to be filled using neighboring valid data, owned by other processors. Corner ghost cells are needed in order to evaluate fourth-order quadratures.

velocity space. This constitutes a reduction operation, in that the number of dimensions is reduced. Inversely, velocity-direction fluxes for updating the distribution function require electromagnetic field data, such that the field variable has to be dispersed from the lower-dimensional subspace to the high-dimensional space. For a parallel implementation both the reduction and dispersal operations call for additional instances of processor communication. Chombo facilitates communication associated with these operations through C++ class objects. Through these constructs, the direction of integration or dispersal can be specified, without writing MPI message-passing code to interface the appropriate processors.

Table 7.1 lists the Chombo classes used for the parallel implementation of the Vlasov-Maxwell solver, and identifies their main feature. These consist of data holders, indexing classes, and constructs for performing integration and dispersal operations. More detailed descriptions can be found in Ref. [112].

Table 7.1: Summary of the Chombo constructs used in the parallel implementation of the Vlasov-Maxwell algorithm.

C++ **Class**	**Description**
`ProblemDomain`	Specifies the indices on an integer lattice on which a physical domain is defined, and identifies periodic directions.
`Box`	Represents a D-dimensional rectangular region on an integer lattice, used to identify a block of data in the domain. Incorporates functions to check indices, intersections, bounds, etc.
`DisjointBoxLayout`	Represents a disjoint union of rectangles corresponding to regions of the domain. Encapsulates the mapping of these rectangles to different processors.
`LevelData`	Represents data built on a DisjointBoxLayout. The data within this data holder is distributed among processors. Incorporates functions that are called to communicate data between processors that own neighboring data.
FArrayBox	An array for storing floating-point data. Incorporates operations for performing aggregate floating-point arithmetic, such as point-by-point summation, multiplication, etc.
`ReductionCopier`	Abstraction for performing specific-direction integration over data owned by multiple processors
`SpreadingCopier`	Abstraction for spreading data from a subset of processors, to a larger set of processors.
`DataIterator`	Means of indexing a `Box` within a `DisjointBoxLayout`
`BoxIterator`	Means of indexing data within a `Box`.

7.2 C++ classes for Vlasov-Maxwell implementation

Using the Chombo data constructs described above, implementing the Vlasov-Maxwell solver requires writing customized code using the object-oriented programming paradigm. The main classes are centered around an Runge-Kutta time-advance object, and are summarized below:

- `RK4`, which is used to advance all primary variables forward in time
- Primary variables
  - `DistFunc`, which encapsulates all distribution function data, and associated operations such as initialization, computing fluxes for the distribution function, computing moments to evaluate number density and current, etc
  - `EMField`, which encapsulates all electromagnetic field data, and associated operations such as initialization, computing line-integrals, etc
- Increments to primary variables
  - `DeltaDistFunc`, which is used to store the distribution function increments associated with each stage of the fourth-order time advance (i.e. the k values in Eq. (3.19))
  - `DeltaEMField`, which is used to store the electromagnetic field increments associated with each stage of the fourth-order time advance
- Wrapper classes
  - `VMVariableWrapper`, which is a container class used to store all primary variables
  - `DeltaVMVariableWrapper`, which is a container class used to store all increment data
- Auxiliary functions
  - `DivFlux`, used to perform all operations associated with evaluating the right-hand side spatial discretization operator and includes calls to computing number densities, currents, divergence of fluxes for the distribution functions, and divergence of fluxes for the fields
  - `FillDistFuncGhostCells`, used to set boundary conditions for the distribution function
  - `FillFieldGhostCells`, used to set boundary conditions for the fields

In the context of Vlasov-Poisson calculations, open-source C++ libraries were used, including the Eigen library for linear algebra, as well as the FFTW library for performing discrete Fourier transforms.

7.3 Specular reflection boundary conditions in parallel

The implementation of most boundary conditions does not involve communication beyond the usual ghost cell exchange between processors that own neighboring data. This is because most boundary conditions involve operations on local data. One exception is periodic boundary conditions, which require data communication. Since periodic boundary conditions are ubiquitous, in Chombo the data communication for them is handled with a simple function call. Another boundary condition that requires communication between processors is the specular reflection boundary condition for the Vlasov equation (see Section 3.8.3.1 for a description, and see Fig. 3.8 and Fig. 3.2 for diagrams). The parallel implementation of this boundary condition necessitates special treatment.

Consider the (r, v_r) plane at the $r = 0$ boundary (see Fig. 3.8). Before data can be communicated from one half-plane to another, each processor that owns data in the $v_r < 0$ half plane at $r = 0$ has to be mapped to a processor that owns a symmetric piece of data in the $v_r > 0$ half plane. This mapping is established by identifying the global velocity index j^* at which $v_r = 0$, and identifying the location of each processor's data relative to j^*. Once the mapping is known, data can be copied from the source processors to the destination processors, and thereby enabling the implementation of the boundary condition.

7.4 Effect of dimensionality on computation and communication

A unique facet of phase space simulations is that the distribution function can occupy more than three dimensions. This has important implications for the computational workload and communication between processors.

In terms of computational workload, the vast majority of time is spent updating the distribution function, such that the duration of a field update is negligible in comparison. This is due to the fact that computational cost scales as N^D, where N is the number of cells along each direction and D is the number of dimensions occupied by a given variable. Suppose a simulation calls for one hundred cells along each direction, then the computational cost for different numbers of dimensions is shown in Table 7.2. The table shows that the computational cost of a one-dimensional data set is trivial compared to a three-dimensional data set. Consequently advancing $f(r, v_r, v_\theta, t)$ constitutes a much more significant workload than updating $E_r(r, t)$, independent of whether the calculation is performed in serial or in parallel. Table 7.2 further illustrates that high resolution is a heavy price for accuracy, especially when the number of dimensions exceeds three. This bolsters the argument for using high-order methods, which achieve high accuracy with less degrees of freedom.

For distribution functions that occupy four or more phase space dimensions, communication costs of high-dimensional data also have to be considered. If a domain with N^D

Table 7.2: Computational cost of having 100 cells along each direction of a D dimensional domain is N^D.

Number of dimensions D	1	2	3	4	5	6
Computational cost N^D	10^2	10^4	10^6	10^8	10^{10}	10^{12}

Table 7.3: Relative cost of communication as the number of dimensions is increased and the block width is kept fixed. The value n^D is the number of cells assigned to a given processor.

Block Width n	Dimensions D	Computational Cost n^D	Relative Cost of Communication D/n
32	3	3.3×10^4	0.094
32	4	1.0×10^6	0.125
32	5	3.3×10^7	0.156
32	6	1.1×10^9	0.189

number of cells is divided into blocks of width n and volume n^D, and each block is assigned to its own processor, then the amount of computation on a single processor is n^D. The cost of communication scales roughly as the surface area of each block, $2Dn^{D-1}$ (note that this approximation does not account for communication required to fill corner ghost cells – see Fig. 7.1). The ratio of communication cost to computational cost is thereby proportional to D/n. For efficient parallel simulations, this ratio should be small, such that the bulk of the execution time should be spent doing floating point operations, as opposed to passing messages between processors. Table 7.3 shows the relative cost of communication for block width $n = 32$ for calculations in three, four, five, and six dimensions. For a fixed block width, as the number of dimensions increases, the computational cost becomes exceedingly high, which calls for smaller blocks. However, if the block width is halved, then the relative cost of communication is doubled. In effect, with more dimensions it becomes more difficult to increase the computational efficiency of the algorithm through parallelization based on domain decomposition alone.

Increasing the efficiency of calculations involving 4D and 5D distribution functions calls for modifications to the standard domain-decomposition paradigm used in Chombo. At the expense of further complexity, using multiple levels of parallelism, e.g. by combining MPI with an application programming interface such as OpenMP, would enable processors to operate on large blocks of data quickly without increasing the cost of communication. The cost of communication can also be curbed by cutting the amount of data that is communicated to fill corner ghost cells during every exchange operation since much of this corner data

is not needed for high-order flux calculations. This would require changing the standard message passing protocol that works well in 2D and 3D. Independent of dimensionality, additional gains in efficiency can be made through judicious implementation of asynchronous algorithms, wherein unrelated portions of the numerical algorithm are executed simultaneously.

Chapter 8

Conclusions

The research described in this dissertation develops and extends advanced computational tools to enable more complete investigation of plasma physics phenomena. High-accuracy robust numerical solvers are successfully applied to the high-fidelity kinetic model description of a plasma. A new benchmark for kinetic calculations is developed and deployed. The benchmark, one very few to involve warm magnetized plasmas, offers a quantitative means of assessing numerical simulations in three phase space dimensions, thereby extending the scope of standard benchmark problems. Furthermore, a conservative method for simulating axisymmetric kinetic physics in plasmas is demonstrated for the first time. This capability offers a means to exploit symmetry and mitigate the computational cost of continuum kinetic simulations. The methods, results, and computational aspects are summarized here.

8.1 Discussion of methods and results

A fourth-order finite-volume discretization is implemented to solve the Vlasov-Maxwell partial differential equation system in Cartesian (x, v_x, v_y) and cylindrical (r, v_r, v_θ) phase space coordinates. The discretization relies on one-dimensional polynomial reconstructions for the primary variables, and utilizes a quadrature rule based on Taylor series expansion to achieve high-order accuracy. A mathematical formulation for the conservation-law form of the cylindrical coordinate Vlasov equation is derived, and the numerical method is extended to apply to this form. The numerical method is designed to handle some of the unique aspects of phase space coordinates, including specular reflection boundary conditions that involve half-plane reflection of the primary variable distribution function. Aside from periodic boundaries, this constitutes one of the few instances in hyperbolic differential equations where non-local information is needed to set local boundary conditions.

Some of the challenges associated with the discretization of Maxwell's equations are managed through the incorporation of parabolic cleaning to satisfy divergence constraints and through high-order dissipation to mitigate the effects of dispersive errors. Stability analysis is carried out for both of these aspects in Cartesian coordinates; however, the

analysis does not extend to cylindrical geometry. Thus further exploration of long-time numerical stability for the Maxwell solver is warranted, but lies beyond the scope of this dissertation.

The discretization uses explicit fourth-order Runge-Kutta to advance the primary variables forward in time, thereby achieving fourth-order temporal and spatial accuracy. The choice of an explicit time integration scheme can be quite restrictive for cylindrical phase space coordinates, in which local advection speeds depend in part on the resolution along the radial coordinate. This demonstrates one of the advantages of using high-order methods, as opposed to high-resolution, to achieve desired accuracy – i.e. a smaller penalty on time step size for cylindrical coordinate calculations.

The fourth-order finite-volume method is applied to simulate well-known phenomena in plasma physics including linear and nonlinear Landau damping, the two-stream instability, and the Harris equilibrium. The results agree closely with theoretical predictions. In an effort to extend the scope of quantitative benchmark problems for kinetic calculations, a new benchmark based on the Dory-Guest-Harris instability is developed. The development extends the linear analysis of electrostatic waves in uniform magnetized plasmas to arrive at a closed-form dispersion relation that applies to warm-temperature plasmas. The approach is thereby not restricted to delta function initial conditions that are often used to benchmark particle-in-cell methods. The closed-form dispersion relation is applied to the warm-temperature Dory-Guest-Harris distribution function, and solved to obtain electric field energy growth rate and frequency as a function of perturbation wave number. The quantitative metrics are used to assess the convergence rate of a fourth-order and a second-order discretization. A specific form of the initial condition is shown to strongly excite the fastest growing mode, which presents an initial value problem that can be used to test various methods. The fourth-order simulation results are shown to be in agreement with theoretical predictions. The benchmark is thus demonstrated to be well-suited for continuum kinetic Vlasov-Poisson algorithms in 3D (x, v_x, v_y) phase space coordinates, and is shown to be a valuable means of demonstrating that simulations are true to the physics.

The fourth-order algorithm is applied to the Vlasov equation in cylindrical (r, v_r, v_θ) phase space coordinates. The ability of the algorithm to preserve an equilibrium distribution function is assessed. It is noted that in cylindrical phase space coordinates, even a spatially-uniform Maxwellian distribution function will experience advection. Analytically, equilibrium is satisfied by the cancellation of multiple terms in the Vlasov equation – a cancellation that is not guaranteed in the context of a numerical algorithm on account of truncation error. As a result equilibrium is not maintained by the numerical method, but the simulation results are shown to converge to equilibrium at a rate that is consistent with a fourth-order accurate discretization. The algorithm is then applied to simulate electrostatic ion confinement in a Z-pinch, a problem in which ions are dynamic and electrons are assumed to be stationary. The simulation results are consistent with expected behavior, and demonstrate the rich kinetic physics that in many respects can only be accessed through simulations. To the author's knowledge this is the first demonstration of a conservative finite-volume implementation for the solution of the cylindrical coordinate Vlasov equation.

Fundamental to the efficient use of the numerical algorithms described in this dissertation is their parallel implementation. Much of the parallelization used here relies on the abstractions provided by the Chombo library, which is a collection of C++ objects that are designed to simplify the domain-decomposition of structured grid calculations so that the workload can be distributed on many processors. One of the unique aspects of phase space simulations is the fact that the main variable, the distribution function, can occupy a space of dimension greater than three. In the context of parallelism based strictly on domain decomposition, communication constitutes a much more significant fraction of the overall computational cost in four dimensions, as compared to three dimensions. This presents a challenge when it comes to the development of algorithms in more than three dimensions, since using more processors does not result in speedup. Approaches to decreasing the communication cost and thereby the overall computational cost are well-known, and involve optimizations associated with data communication as well as employing multiple levels of parallelism.

8.2 Future work

The research presented here lies at the intersection of plasma physics, numerical methods, and scientific computing. Thus the extension of this work relies on further development in each of these areas.

To study more interesting physics, the Vlasov-Maxwell solver needs to be extended to four and five phase space dimensions. This requires combatting the computational costs associated with high-dimensional calculations, and constitutes ongoing work. Further extensions of the physics capability of the algorithm would involve the implementation of a collision operator. This would offer a generalization of the collisionless kinetic model description that has been explored here, and would allow for the investigation of a large variety of plasma phenomena. The finite-volume method described here is especially well suited for collision operators, such as the Fokker-Planck operator, that can be expressed in divergence form. It is important to note that collision-dominated physics can also introduce additional constraints on time step size in simulations. Thus the details of the physics of interest and their impact on the numerics need to be carefully considered. Alternate means of temporal discretization are also important to consider when simulating multiple species of particles with disparate masses. The use of multi-rate or implicit methods can help address the issues associated with capturing multiscale phenomena.

The numerical discretization employed here is not designed to handle steep gradients. This causes the distribution function to take on negative values whenever gradients are not well-resolved. This can be combatted through the use of limiters to preserve positivity — a technique that is well-known and well-developed for finite-volume methods. Implementation of adaptive mesh refinement (AMR) so as to better capture fine features in the solution to the governing equations can also help address this issue. The optimal approach to adaptivity in the context of phase space simulations needs to be carefully explored since high-dimensionality affects the computational performance of these techniques. Moreover

the need to constantly compute moments of the distribution function presents additional AMR algorithm design challenges that would need to be addressed.

Parallel implementation of the fourth-order Vlasov-Maxwell solver relied on the use of Chombo library features. In parallel calculations using Chombo high performance is generally achieved through mixed-language programming, with abstractions written in C++ and arithmetic stencil operations written in Fortran. In effort to avoid complexity and at the expense of improved performance, the algorithm implementations described in this dissertation were written entirely in C++. Significant gains in computational performance can be made by invoking Fortan for stencil arithmetic, by abstracting stencil operations into optimized library calls written in C++, and/or by using multiple levels of parallelism. The latter two approaches are the subject of current and future research.

Bibliography

[1] G. V. Vogman, P. Colella, and U. Shumlak, "Dory–Guest–Harris instability as a benchmark for continuum kinetic Vlasov–Poisson simulations of magnetized plasmas," *Journal of Computational Physics*, vol. 277, pp. 101 – 120, 2014.

[2] N. Krall and A. Trivelpiece, *Principles of Plasma Physics*. McGraw-Hill, New York, NY, 1973.

[3] F. Filbet and E. Sonnendrücker, *Numerical methods for the Vlasov equation*, pp. 459–468. Milano: Springer Milan, 2003.

[4] F. Filbet and E. Sonnendrücker, "Comparison of Eulerian Vlasov solvers," *Computer Physics Communications*, vol. 150, no. 3, pp. 247 – 266, 2003.

[5] C. Birdsall and A. Langdon, *Plasma physics via computer simulation*. McGraw-Hill, New York, NY, 1985.

[6] J. P. Verboncoeur, "Particle simulation of plasmas: review and advances," *Plasma Physics and Controlled Fusion*, vol. 47, no. 5A, p. A231, 2005.

[7] D. Tskhakaya, K. Matyash, R. Schneider, and F. Taccogna, "The particle-in-cell method," *Contributions to Plasma Physics*, vol. 47, no. 8-9, pp. 563–594, 2007.

[8] A. B. Langdon, "Evolution of particle-in-cell plasma simulation," *IEEE Transactions on Plasma Science*, vol. 42, pp. 1317–1320, May 2014.

[9] B. Wang, *A particle-in-cell method with adaptive phase-space remapping for kinetic lasmas*. PhD thesis, University of California Davis, 2011.

[10] G.-H. Cottet and P.-A. Raviart, "Particle methods for the one-dimensional vlasov–poisson equations," *SIAM Journal on Numerical Analysis*, vol. 21, no. 1, pp. 52–76, 1984.

[11] A. B. Langdon, "Kinetic theory for fluctuations and noise in computer simulation of plasma," *Physics of Fluids*, vol. 22, no. 1, pp. 163–171, 1979.

[12] W. Nevins, A. Dimits, G. Hammett, W. Dorland, and D. E. Shumaker, "Discrete particle noise in particle-in-cell simulations of plasma microturbulence," *Physics of Plasmas*, vol. 12, no. 12, pp. –, 2005.

[13] I. Holod and Z. Lin, "Statistical analysis of fluctuations and noise-driven transport in particle-in-cell simulations of plasma turbulence," *Physics of Plasmas*, vol. 14, no. 3, 2007.

[14] A. Klimas and W. Farrell, "A splitting algorithm for vlasov simulation with filamentation filtration," *Journal of Computational Physics*, vol. 110, no. 1, pp. 150 – 163, 1994.

[15] C. Cheng and G. Knorr, "The integration of the Vlasov equation in configuration space," *Journal of Computational Physics*, vol. 22, no. 3, pp. 330 – 351, 1976.

[16] E. Sonnendrücker, J. Roche, P. Bertrand, and A. Ghizzo, "The semi-Lagrangian method for the numerical resolution of the Vlasov equation," *Journal of Computational Physics*, vol. 149, no. 2, pp. 201–220, 1999.

[17] F. Filbet, E. Sonnendrcker, and P. Bertrand, "Conservative numerical schemes for the Vlasov equation," *Journal of Computational Physics*, vol. 172, no. 1, pp. 166 – 187, 2001.

[18] N. Sircombe and T. Arber, "VALIS: A split-conservative scheme for the relativistic 2D Vlasov–Maxwell system," *Journal of Computational Physics*, vol. 228, no. 13, pp. 4773 – 4788, 2009.

[19] T. Umeda, J.-I. Miwa, Y. Matsumoto, T. K. M. Nakamura, K. Togano, K. Fukazawa, and I. Shinohara, "Full electromagnetic Vlasov code simulation of the Kelvin-Helmholtz instability," *Physics of Plasmas*, vol. 17, no. 5, 2010.

[20] J. Candy and R. E. Waltz, "Velocity-space resolution, entropy production, and upwind dissipation in Eulerian gyrokinetic simulations," *Physics of Plasmas (1994-present)*, vol. 13, no. 3, pp. –, 2006.

[21] R. Numata, G. G. Howes, T. Tatsuno, M. Barnes, and W. Dorland, "AstroGK: Astrophysical gyrokinetics code," *Journal of Computational Physics*, vol. 229, no. 24, pp. 9347 – 9372, 2010.

[22] J. Banks and J. Hittinger, "A new class of nonlinear finite-volume methods for Vlasov simulation," *Plasma Science, IEEE Transactions on*, vol. 38, no. 9, pp. 2198–2207, 2010.

[23] Y. Cheng, I. Gamba, F. Li, and P. Morrison, "Discontinuous galerkin methods for the vlasov–maxwell equations," *SIAM Journal on Numerical Analysis*, vol. 52, no. 2, pp. 1017–1049, 2014.

[24] T. H. Stix, *Waves in plasmas*. Springer Science & Business Media, 1992.

[25] L. Mieussens, "Discrete-velocity models and numerical schemes for the boltzmann-bgk equation in plane and axisymmetric geometries," *Journal of Computational Physics*, vol. 162, no. 2, pp. 429 – 466, 2000.

[26] E. Epperlein, "Fokker–planck modeling of electron transport in laser-produced plasmas," *Laser and Particle Beams*, vol. 12, pp. 257–272, 6 1994.

[27] M. Kogan, *Rarefied gas dynamics: Dinamika razrezennogo gaza. Transl. from Russian*. Plenum Press, 1969.

[28] A. A. Vlasov, *Statistical Distribution Functions*. Nauka, Moscow, 1966.

[29] F. Filbet, J.-L. Lemaire, and E. Sonnendrücker, *Direct Axisymmetric Vlasov Simulations of Space Charge Dominated Beams*, pp. 305–314. Berlin, Heidelberg: Springer Berlin Heidelberg, 2002.

[30] Y. Sone, *Kinetic theory and fluid dynamics*. Springer Science & Business Media, 2012.

[31] P. Colella, M. Dorr, J. Hittinger, and D. Martin, "High-order, finite-volume methods in mapped coordinates," *Journal of Computational Physics*, vol. 230, no. 8, pp. 2952 – 2976, 2011.

[32] M. Vinokur, "Conservation equations of gasdynamics in curvilinear coordinate systems," *Journal of Computational Physics*, vol. 14, no. 2, pp. 105–125, 1974.

[33] E. M. Shakhov, "Boltzmann equation and moment equations in curvilinear coordinates," *Fluid Dynamics*, vol. 2, no. 2, pp. 107–109, 1967.

[34] C.-D. Munz, P. Omnes, R. Schneider, E. Sonnendrücker, and U. Voß, "Divergence correction techniques for Maxwell solvers based on a hyperbolic model," *Journal of Computational Physics*, vol. 161, no. 2, pp. 484 – 511, 2000.

[35] B. Marder, "A method for incorporating Gauss' law into electromagnetic PIC codes," *Journal of Computational Physics*, vol. 68, no. 1, pp. 48 – 55, 1987.

[36] J. Cooper and A. Klimas, "Boundary value problems for the Vlasov-Maxwell equation in one dimension," *Journal of Mathematical Analysis and Applications*, vol. 75, no. 2, pp. 306 – 329, 1980.

[37] Y. Guo, "Global weak solutions of the Vlasov-Maxwell system with boundary conditions," *Communications in Mathematical Physics*, vol. 154, no. 2, pp. 245–263, 1993.

[38] T. T. Nguyen and W. A. Strauss, "Stability analysis of collisionless plasmas with specularly reflecting boundary," *SIAM Journal on Mathematical Analysis*, vol. 45, no. 2, pp. 777–808, 2013.

[39] C. Cercignani, "The Boltzmann Equation," in *The Boltzmann Equation and Its Applications*, pp. 40–103, Springer, 1988.

[40] W. G. Pilipp, H. Miggenrieder, M. D. Montgomery, K. H. Mühlhäuser, H. Rosenbauer, and R. Schwenn, "Characteristics of electron velocity distribution functions in the solar wind derived from the helios plasma experiment," *Journal of Geophysical Research: Space Physics*, vol. 92, no. A2, pp. 1075–1092, 1987.

[41] J. P. McFadden, C. W. Carlson, D. Larson, M. Ludlam, R. Abiad, B. Elliott, P. Turin, M. Marckwordt, and V. Angelopoulos, "The THEMIS ESA plasma instrument and in-flight calibration," *Space Science Reviews*, vol. 141, no. 1, pp. 277–302, 2008.

[42] C.-W. Shu, "Essentially non-oscillatory and weighted essentially non-oscillatory schemes for hyperbolic conservation laws," in *Advanced Numerical Approximation of Nonlinear Hyperbolic Equations* (A. Quarteroni, ed.), vol. 1697 of *Lecture Notes in Mathematics*, pp. 325–432, Springer Berlin Heidelberg, 1998.

[43] C.-W. Shu, "High-order finite difference and finite volume weno schemes and discontinuous Galerkin methods for CFD," *International Journal of Computational Fluid Dynamics*, vol. 17, no. 2, pp. 107–118, 2003.

[44] E. F. Toro, R. C. Millington, and L. A. M. Nejad, *Towards Very High Order Godunov Schemes*, pp. 907–940. Boston, MA: Springer US, 2001.

[45] V. Titarev and E. Toro, "ADER schemes for three-dimensional non-linear hyperbolic systems," *Journal of Computational Physics*, vol. 204, no. 2, pp. 715 – 736, 2005.

[46] P. McCorquodale and P. Colella, "A high-order finite-volume method for conservation laws on locally refined grids," *Communications in Applied Mathematics and Computational Science*, vol. 6, no. 1, pp. 1–25, 2011.

[47] P. DuChateau and D. Zachmann, *Applied partial differential equations*. Courier Corporation, 2012.

[48] J. D. Hoffman and S. Frankel, *Numerical methods for engineers and scientists*. CRC press, 2001.

[49] Q. Zhang, H. Johansen, and P. Colella, "A fourth-order accurate finite-volume method with structured adaptive mesh refinement for solving the advection-diffusion equation," *SIAM Journal on Scientific Computing*, vol. 34, no. 2, pp. B179–B201, 2012.

[50] J. Canosa, J. Gazdag, and J. Fromm, "The recurrence of the initial state in the numerical solution of the Vlasov equation," *Journal of Computational Physics*, vol. 15, no. 1, pp. 34–45, 1974.

[51] T. Arber and R. Vann, "A critical comparison of Eulerian-grid-based Vlasov solvers," *Journal of Computational Physics*, vol. 180, no. 1, pp. 339 – 357, 2002.

[52] W. Guo and J.-M. Qiu, "Hybrid semi-Lagrangian finite element-finite difference methods for the Vlasov equation," *Journal of Computational Physics*, vol. 234, no. 0, pp. 108 – 132, 2013.

[53] J.-M. Qiu and A. Christlieb, "A conservative high order semi-lagrangian WENO method for the Vlasov equation," *Journal of Computational Physics*, vol. 229, no. 4, pp. 1130 – 1149, 2010.

[54] J. Jackson, "Longitudinal plasma oscillations," *Journal of Nuclear Energy. Part C, Plasma Physics, Accelerators, Thermonuclear Research*, vol. 1, no. 4, p. 171, 1960.

[55] J. Canosa, "Numerical solution of Landau's dispersion equation," *Journal of Computational Physics*, vol. 13, no. 1, pp. 158 – 160, 1973.

[56] O. Penrose, "Electrostatic instabilities of a uniform non-Maxwellian plasma," *Physics of Fluids*, vol. 3, no. 2, pp. 258–265, 1960.

[57] N. Lindgren, A. B. Langdon, and C. Birdsall, "Electrostatic waves in an inhomogeneous collisionless plasma," *Physics of Fluids (1958-1988)*, vol. 19, no. 7, pp. 1026–1034, 1976.

[58] L. Urankar, "Vector potential and magnetic field of current-carrying finite arc segment in analytical form, part iii: Exact computation for rectangular cross section," *IEEE Transactions on Magnetics*, vol. 18, pp. 1860–1867, Nov 1982.

[59] L. Urankar, "Vector potential and magnetic field of current-carrying circular finite arc segment in analytical form. v. polygon cross section," *IEEE Transactions on Magnetics*, vol. 26, pp. 1171–1180, May 1990.

[60] M. Gyimesi, D. Lavers, T. Pawlak, and D. Ostergaard, "Biot-Savart integration for bars and arcs," *IEEE Transactions on Magnetics*, vol. 29, no. 6, pp. 2389–2391, 1993.

[61] C. Snow, *Magnetic fields of cylindrical coils and annular coils*. No. 38, US Govt. Print. Off., 1953.

[62] B. Azzerboni, E. Cardelli, M. Raugi, A. Tellini, and G. Tina, "Analytic expressions for magnetic field from finite curved conductors," *IEEE Transactions on Magnetics*, vol. 27, pp. 750–757, Mar 1991.

[63] B. Azzerboni, E. Cardelli, M. Raugi, A. Tellini, and G. Tina, "Magnetic field evaluation for thick annular conductors," *IEEE Transactions on Magnetics*, vol. 29, pp. 2090–2094, May 1993.

[64] J. T. Conway, "Exact solutions for the magnetic fields of axisymmetric solenoids and current distributions," *Magnetics, IEEE Transactions on*, vol. 37, no. 4, pp. 2977–2988, 2001.

[65] J. T. Conway, "Trigonometric integrals for the magnetic field of the coil of rectangular cross section," *IEEE Transactions on Magnetics*, vol. 42, pp. 1538–1548, May 2006.

[66] D. Zhang and C. S. Koh, "An efficient semianalytic computation method of magnetic field for a circular coil with rectangular cross section," *IEEE Transactions on Magnetics*, vol. 48, no. 1, pp. 62–68, 2012.

[67] E. Harris, "On a plasma sheath separating regions of oppositely directed magnetic field," *Il Nuovo Cimento Series 10*, vol. 23, no. 1, pp. 115–121, 1962.

[68] G. Lapenta and J. U. Brackbill, "Nonlinear evolution of the lower hybrid drift instability: Current sheet thinning and kinking," *Physics of Plasmas*, vol. 9, no. 5, pp. 1544–1554, 2002.

[69] W. Daughton, G. Lapenta, and P. Ricci, "Nonlinear evolution of the lower-hybrid drift instability in a current sheet," *Physical Review Letters*, vol. 93, p. 105004, Sep 2004.

[70] J. Birn, J. F. Drake, M. A. Shay, B. N. Rogers, R. E. Denton, M. Hesse, M. Kuznetsova, Z. W. Ma, A. Bhattacharjee, A. Otto, and P. L. Pritchett, "Geospace environmental modeling (gem) magnetic reconnection challenge," *Journal of Geophysical Research: Space Physics*, vol. 106, no. A3, pp. 3715–3719, 2001.

[71] J. A. Rossmanith and D. C. Seal, "A positivity-preserving high-order semi-Lagrangian discontinuous Galerkin scheme for the Vlasov–Poisson equations," *Journal of Computational Physics*, vol. 230, no. 16, pp. 6203 – 6232, 2011.

[72] F. Valentini, P. Veltri, and A. Mangeney, "A numerical scheme for the integration of the Vlasov–Poisson system of equations, in the magnetized case," *Journal of Computational Physics*, vol. 210, no. 2, pp. 730 – 751, 2005.

[73] T. Umeda, Y. Omura, P. Yoon, R. Gaelzer, and H. Matsumoto, "Harmonic Langmuir waves. iii. Vlasov simulation," *Physics of Plasmas*, vol. 10, no. 2, pp. 382–391, 2003.

[74] A. Suzuki and T. Shigeyama, "A conservative scheme for the relativistic Vlasov–Maxwell system," *Journal of Computational Physics*, vol. 229, no. 5, pp. 1643 – 1660, 2010.

[75] A. Ghizzo, P. Bertrand, M. Shoucri, T. Johnston, E. Fualkow, and M. Feix, "A Vlasov code for the numerical simulation of stimulated Raman scattering," *Journal of Computational Physics*, vol. 90, no. 2, pp. 431 – 457, 1990.

[76] F. Califano, T. Cecchi, and C. Chiuderi, "Nonlinear kinetic regime of the Weibel instability in an electron–ion plasma," *Physics of Plasmas*, vol. 9, no. 2, pp. 451–457, 2002.

[77] A. Mangeney, F. Califano, C. Cavazzoni, and P. Travnicek, "A numerical scheme for the integration of the Vlasov–Maxwell system of equations," *Journal of Computational Physics*, vol. 179, no. 2, pp. 495 – 538, 2002.

[78] A. Suzuki and T. Shigeyama, "Detailed analysis of filamentary structure in the Weibel instability," *The Astrophysical Journal*, vol. 695, no. 2, p. 1550, 2009.

[79] N. Besse, G. Latu, A. Ghizzo, E. Sonnendrücker, and P. Bertrand, "A wavelet-MRA-based adaptive semi-Lagrangian method for the relativistic Vlasov–Maxwell system," *Journal of Computational Physics*, vol. 227, no. 16, pp. 7889 – 7916, 2008.

[80] A. Ghizzo, P. Bertrand, M. Shoucri, E. Fijalkow, and M. Feix, "An Eulerian code for the study of the drift-kinetic Vlasov equation," *Journal of Computational Physics*, vol. 108, no. 1, pp. 105 – 121, 1993.

[81] R. A. Dory, G. E. Guest, and E. G. Harris, "Unstable electrostatic plasma waves propagating perpendicular to a magnetic field," *Physical Review Letters*, vol. 14, pp. 131–133, Feb 1965.

[82] J. A. Byers and M. Grewal, "Perpendicularly propagating plasma cyclotron instabilities simulated with a one-dimensional computer model," *Physics of Fluids*, vol. 13, no. 7, pp. 1819–1830, 1970.

[83] F. Crawford and J. Tataronis, "Absolute instabilities of perpendicularly propagating cyclotron harmonic plasma waves," *Journal of Applied Physics*, vol. 36, no. 9, pp. 2930–2934, 1965.

[84] J. Tataronis and F. Crawford, "Cyclotron harmonic wave propagation and instabilities: I. perpendicular propagation," *Journal of Plasma Physics*, vol. 4, pp. 231–248, 5 1970.

[85] I. B. Bernstein, "Waves in a plasma in a magnetic field," *Physical Review*, vol. 109, pp. 10–21, Jan 1958.

[86] D. A. Gurnett and A. Bhattacharjee, *Introduction to plasma physics: with space and laboratory applications*. Cambridge University Press, 2005.

[87] F. Crawford, "A review of cyclotron harmonic phenomena in plasmas," *Nuclear Fusion*, vol. 5, no. 1, p. 73, 1965.

[88] G. Cottrell and R. Dendy, "Superthermal radiation from fusion products in JET," *Physical Review Letters*, vol. 60, pp. 33–36, Jan 1988.

[89] A. Goede, P. Massmann, H. Hopman, and J. Kistemaker, "Ion Bernstein waves excited by an energeticion beam ion a plasma," *Nuclear Fusion*, vol. 16, no. 1, p. 85, 1976.

[90] R. F. Hubbard and T. J. Birmingham, "Electrostatic emissions between electron gyroharmonics in the outer magnetosphere," *Journal of Geophysical Research: Space Physics*, vol. 83, no. A10, pp. 4837–4850, 1978.

[91] S. Perraut, A. Roux, P. Robert, R. Gendrin, J.-A. Sauvaud, J.-M. Bosqued, G. Kremser, and A. Korth, "A systematic study of ULF waves above FH+ from GEOS 1 and 2 measurements and their relationships with proton ring distributions," *Journal of Geophysical Research: Space Physics*, vol. 87, no. A8, pp. 6219–6236, 1982.

[92] M. Ashour-Abdalla and C. Kennel, "Nonconvective and convective electron cyclotron harmonic instabilities," *Journal of Geophysical Research: Space Physics*, vol. 83, no. A4, pp. 1531–1543, 1978.

[93] R. L. Kaufmann, P. B. Dusenbery, and B. J. Thomas, "Stability of the auroral plasma: parallel and perpendicular propagation of electrostatic waves," *Journal of Geophysical Research: Space Physics*, vol. 83, no. A12, pp. 5663–5669, 1978.

[94] R. F. Post and M. Rosenbluth, "Electrostatic instabilities in finite mirror-confined plasmas," *Physics of Fluids*, vol. 9, no. 4, pp. 730–749, 1966.

[95] G. Guest, *Electron Cyclotron Heating of Plasmas*. John Wiley and Sons, 2009.

[96] E. Harris, "Plasma instabilities associated with anisotropic velocity distributions," *Journal of Nuclear Energy. Part C, Plasma Physics, Accelerators, Thermonuclear Research*, vol. 2, no. 1, p. 138, 1961.

[97] J. K. Lee and C. K. Birdsall, "Velocity space ring-plasma instability, magnetized, part ii: Simulation," *Physics of Fluids*, vol. 22, no. 7, pp. 1315–1322, 1979.

[98] T. Umeda, M. Ashour-Abdalla, D. Schriver, R. L. Richard, and F. V. Coroniti, "Particle-in-cell simulation of Maxwellian ring velocity distribution," *Journal of Geophysical Research: Space Physics*, vol. 112, no. A4, 2007.

[99] J. Kong, *Electromagnetic Wave Theory*. A Wiley-Interscience publication, Wiley, 1986.

[100] J. Shang, "High-order compact-difference schemes for time-dependent Maxwell equations," *Journal of Computational Physics*, vol. 153, no. 2, pp. 312 – 333, 1999.

[101] M. H. Carpenter, D. Gottlieb, and S. Abarbanel, "Time-stable boundary conditions for finite-difference schemes solving hyperbolic systems: Methodology and application to high-order compact schemes," *Journal of Computational Physics*, vol. 111, no. 2, pp. 220 – 236, 1994.

[102] M. H. Carpenter, D. Gottlieb, and S. Abarbanel, "The stability of numerical boundary treatments for compact high-order finite-difference schemes," *NASA-CR-187628*, 1991.

[103] L. N. Trefethen, "Stability of finite-difference models containing two boundaries or interfaces," *Mathematics of Computation*, vol. 45, no. 172, pp. 279–300, 1985.

[104] R. F. Warming and R. M. Beam, "Stability of semidiscrete approximations for hyperbolic initial-boundary-value problems: an eigenvalue analysis," in *Tenth International Conference on Numerical Methods in Fluid Dynamics*, pp. 647–653, Springer, 1986.

[105] C. A. Fichtl, J. M. Finn, and K. L. Cartwright, "An arbitrary curvilinear-coordinate method for particle-in-cell modeling," *Computational Science & Discovery*, vol. 5, no. 1, p. 014011, 2012.

[106] J.-L. Vay, D. Grote, R. Cohen, and A. Friedman, "Novel methods in the particle-in-cell accelerator code-framework warp," *Computational Science & Discovery*, vol. 5, no. 1, p. 014019, 2012.

[107] J. M. Blondin and E. A. Lufkin, "The piecewise-parabolic method in curvilinear coordinates," *Astrophysical Journal Supplement Series*, vol. 88, pp. 589–594, Oct. 1993.

[108] A. Mignone, "High-order conservative reconstruction schemes for finite volume methods in cylindrical and spherical coordinates," *Journal of Computational Physics*, vol. 270, pp. 784 – 814, 2014.

[109] M. G. Haines, "A review of the dense Z-pinch," *Plasma Physics and Controlled Fusion*, vol. 53, no. 9, p. 093001, 2011.

[110] D. D. Ryutov, "Characterizing the plasmas of dense z -pinches," *IEEE Transactions on Plasma Science*, vol. 43, pp. 2363–2384, Aug 2015.

[111] R. C. Davidson, *Physics of nonneutral plasmas*. Imperial College Press London, 2001.

[112] P. Colella, D. Graves, J. Johnson, H. Johansen, N. Keen, T. Ligocki, D. Martin, P. McCorquodale, D. Modiano, P. Schwartz, T. Sternberg, and B. Van Straalen, "Chombo software package for AMR applications – design document," tech. rep., Lawrence Berkeley National Laboratory, 2013.

[113] E. G. Harris, "Unstable plasma oscillations in a magnetic field," *Physical Review Letters*, vol. 2, pp. 34–36, Jan 1959.

[114] A. Erdélyi, W. Magnus, F. Oberhettinger, F. G. Tricomi, and H. Bateman, *Higher transcendental functions (California Institute of Technology H. Bateman MS Project)*, vol. 2. McGraw-Hill, New York, NY, 1953.

[115] F. Crawford, "Cyclotron harmonic waves in warm plasmas," *Journal of Research of the National Bureau of Standards*, vol. 69D, no. 6, p. 789, 1965.

Appendix A

Solving Poisson equation using fast Fourier transforms

A.1 Matlab code for 2D Poisson solve using FFTs

```
% Solving 2D Poisson's equation using ffts
close all;
clear all;


nx     = 32;                          % number of points in X
ny     = 64;                          % number of points in Y
Lx     = 2*pi;                        % physical domain length
Ly     = 4*pi;                        % physical domain length
dx    = Lx/nx;                        % X size of each cell in the domain
dy    = Ly/ny;                        % Y size of each cell in the domain
x     = (dx/2):dx:Lx;       % X domain
y     = (dy/2):dy:Ly;       % Y domain


% righthand side of poisson eqn, -\nabla^2 \phi = RHS
rhs=zeros(nx,ny);
for ix=1:nx
    for iy=1:ny
        X=x(ix);
        Y=y(iy);
        rhs(ix,iy)  = -(-2*sin(X)*cos(Y));
        exactSol(ix,iy)= sin(X)*cos(Y);
    end
end

rhsT = fft2(rhs);                    % take discrete FFT
break
kx     = (2*pi/Lx)*[0:nx/2-1, -nx/2:-1];    % vector of wave numbers, e.g. for
                                            % n=8, k= [0,1,2,3,-4,-3,-2,-1]
ky     = (2*pi/Ly)*[0:ny/2-1, -ny/2:-1];

% divide transformed RHS by k^2
rhsNew = zeros(nx,ny);
for ix=1:nx
```

```
    for iy=1:ny
        rhsNew(ix,iy)=rhsT(ix,iy)./(kx(ix)^2+ky(iy)^2);
    end
end
rhsNew(1,1)=0;
% inverse Fourier transform to obtain solution \phi(x)
sol=ifft2((rhsNew));

% plot
figure
pcolor(sol)
colorbar
title('num sol')
figure
pcolor(exactSol);
colorbar
title('exact sol')
figure
pcolor(sol-exactSol)
colorbar
title('diff')
```

A.2 C++ code for 2D Poisson solve using FFTW library

```
// testing FFTs (from fftw library) for solving Poisson equation
// -\nabla^2 \phi = \rho
#include <vector>
#include <cmath>
#include <iostream>
#include <fftw3.h>

using namespace std;

int main()
{
  // discretization variables
  int Nx = 32;
  int Ny = 64;
  double Lx = 2*M_PI;
  double Ly = 4*M_PI;
  double dx = (double) Lx/Nx;
  double dy = (double) Ly/Ny;
  double x;
  double y;

  // fft variables
  fftw_complex *in, *out, *outINV;
  fftw_plan pFFT, pINV;

  in = (fftw_complex*) fftw_malloc(sizeof(fftw_complex) * Nx*Ny);
  out = (fftw_complex*) fftw_malloc(sizeof(fftw_complex) * Nx*Ny);
  outINV = (fftw_complex*) fftw_malloc(sizeof(fftw_complex) * Nx*Ny);


  // fft plans using input and output array variables
  // last argument:
```

```
33    // FFTW_ESTIMATE - no optimization
34    // FFTW_MEASURE  - runs optimization, measuring execution time of several
          ffts
35    pFFT = fftw_plan_dft_2d(Nx,Ny,  in, out, FFTW_FORWARD, FFTW_ESTIMATE);
36    pINV = fftw_plan_dft_2d(Nx,Ny, out, outINV, FFTW_BACKWARD, FFTW_ESTIMATE);
37
38    // generate data that is to be transformed (the righthand side of Poisson
          eqn)
39    for (int i = 0; i < Nx; i++)
40      {
41        for (int j = 0; j < Ny; j++)
42         {
43           x = 0.5*dx + dx*i;
44           y = 0.5*dy + dy*j;
45           in[j+Ny*i][0] = 2.0*sin(x)*cos(y);  //real part
46           in[j+Ny*i][1] = 0.0;      //imaginary part
47         }
48      }
49
50    // perform forward fft on the data
51    fftw_execute(pFFT);
52
53    // wave number k = (2*pi/L)*[ 0:(N/2) -N/2:-1 ] starts at k=0
54    // for example if N=8 then k = [0, 1, 2, 3,-4,-3,-2,-1]
55    vector<double> kx(Nx,0.0);         // kx[0]=0.0;
56    for (int i = 1; i < Nx/2; i++)
57      {
58        kx[i] = kx[i-1]+1;
59      }
60      kx[Nx/2]= -Nx/2;
61    for (int i = Nx/2+1; i < Nx; i++)
62      {
63        kx[i] = kx[i-1]+1;
64      }
65    for (int i = 0; i < Nx; i++)
66      {
67        double kscaleX = 2.0*M_PI/Lx;
68        kx[i] *= kscaleX;
69      }
70
71    vector<double> ky(Ny,0.0);         // ky[0]=0.0;
72    for (int j = 1; j < Ny/2; j++)     // first half of ky vector
73      {
74        ky[j] = ky[j-1]+1;
75      }
76      ky[Ny/2]= -Ny/2;
77    for (int j = Ny/2+1; j < Ny; j++) // 2nd half of ky vector
78      {
79        ky[j] = ky[j-1]+1;
80      }
81    for (int j = 0; j < Ny; j++)       // scale by 2pi/L
82      {
83        double kscaleY = 2.0*M_PI/Ly;
84        ky[j] *= kscaleY;
85      }
86
87    // divide fft(rhs) by k^2 to bring del^2 operator to righthand side
88    out[0][0] = 0.0;
89    out[0][1] = 0.0;
90    for (int i= 0; i < Nx; i++)
```

```
91      {
92        for (int j= 0; j < Ny; j++)
93         {
94           double kxval = kx[i];
95           double kyval = ky[j];
96           out[j+Ny*i][0] = out[j+Ny*i][0]/(pow(kxval,2.0)+pow(kyval,2.0));
97           out[j+Ny*i][1] = out[j+Ny*i][1]/(pow(kxval,2.0)+pow(kyval,2.0));
98         }
99      }
100   // handle kx=ky=0 case
101   out[0][0] = 0.0;
102   out[0][1] = 0.0;
103
104   // perform inverse fast fourier transform to solve for phi
105   fftw_execute(pINV);
106
107         printf("\n");
108   for (int i= 0; i < Nx; i++)
109     {
110       for (int j= 0; j < Ny; j++)
111         {
112           outINV[j+Ny*i][0] /= double(Nx*Ny); //scale by (1/N), note: Matlab
                  does this automatically in ifft operation
113           outINV[j+Ny*i][1] /= double(Nx*Ny);
114           printf("%2.18f \t ", outINV[j+Ny*i][0]);
115         }
116         printf("\n");
117     }
118
119   // free up memory
120   fftw_destroy_plan(pFFT);
121   fftw_destroy_plan(pINV);
122   fftw_free(in);
123   fftw_free(out);
124   fftw_free(outINV);
125
126 return 0;
127 }
```

Appendix B

Dory-Guest-Harris dispersion relation [1]

B.1 Derivation of the closed-form dispersion relation for $k_{\|} = 0$ electrostatic waves

The dispersion relation for $k_{\|} = 0$ kinetic electrostatic waves is most often derived and expressed in a form that involves infinite sums [81, 86, 113, 96]. Tataronis et al. [84] present without proof an equivalent closed-form expression, a version of which can also be found in Ref. [83]. The closed-form dispersion relation allows for accurate computation of explicit numerical solutions (i.e. frequency as a function of wavenumber) for arbitrary probability distribution functions. In effort to fill in the missing details, a complete derivation of the dispersion relation is presented here, including the derivation of the closed-form expression (see Eqs. (5.9) and (5.10)) for a plasma with multiple species s.

From Eqs. (5.7) and (5.8) it is possible to obtain the analytic form of the dispersion relation by applying the procedure discussed in Ref. [86, pp. 341–352] to the non-dimensionalized system of equations that is used in this paper. Starting with the transformed non-dimensionalized Vlasov equation (see Eq. (5.7)), let $\alpha = -\omega/\Omega_{cs}$ and $\beta = k_{\perp} v_{\perp}/\Omega_{cs}$. Recall that $\Omega_{cs} = Z_s \omega_c/(M_s \omega_p)$. The result is an ordinary differential equation that can be analytically solved for $\hat{f}_{s1}$:

$$0 = -i\left(\alpha + \beta\cos\theta\right)\hat{f}_{s1} - \frac{\omega_p}{\omega_c}\hat{\boldsymbol{E}}_1 \cdot \frac{\partial f_{s0}}{\partial \boldsymbol{v}} + \frac{\partial \hat{f}_{s1}}{\partial \theta}. \tag{B.1}$$

Solving for $\hat{f}_{s1}$ using an integrating factor yields

$$\hat{f}_{s1} = e^{i(\alpha\theta + \beta\sin\theta)} \int_{\theta_0}^{\theta} \frac{\omega_p}{\omega_c}\hat{\boldsymbol{E}}_1 \cdot \frac{\partial f_{s0}}{\partial \boldsymbol{v}} e^{-i(\alpha\theta' + \beta\sin\theta')} d\theta'. \tag{B.2}$$

Substituting Eq. (B.2) into Poisson's equation (see Eq. (5.8)) and noting that $\boldsymbol{E} = -\nabla\Phi$ and consequently $\hat{\boldsymbol{E}}_1 = -i\boldsymbol{k}\hat{\Phi}_1$ yields

$$0 = 1 + \sum_s \frac{Z_s\omega_p}{k_\perp^2\omega_c}\int\left[e^{i(\alpha\theta+\beta\sin\theta)}\int_{\theta_0}^{\theta} i\boldsymbol{k}\cdot\frac{\partial f_{s0}}{\partial\boldsymbol{v}}e^{-i(\alpha\theta'+\beta\sin\theta')}d\theta'\right]d\boldsymbol{v}. \tag{B.3}$$

Recall that f_{s0} is the equilibrium distribution function and that it is azimuthally symmetric such that $\partial f_{s0}/\partial\theta = 0$. Also note that waves that propagate perpendicular to the magnetic field have $k_\parallel = 0$. Consequently the dot product term can be expressed as

$$i\boldsymbol{k}\cdot\frac{\partial f_0}{\partial\boldsymbol{v}} = ik_\perp\frac{\partial f_0}{\partial v_\perp}\cos\theta' = ik_\perp\frac{\partial f_0}{\partial v_\perp}\frac{e^{i\theta'}+e^{-i\theta'}}{2}. \tag{B.4}$$

Substituting Eq. (B.4) into Eq. (B.3) yields

$$0 = 1 + \sum_s \frac{Z_s\omega_p}{2k_\perp\omega_c}\int\left[e^{i(\alpha\theta+\beta\sin\theta)}i\frac{\partial f_{s0}}{\partial v_\perp}\int_{\theta_0}^{\theta}\left(e^{i\theta'}+e^{-i\theta'}\right)e^{-i(\alpha\theta'+\beta\sin\theta')}d\theta'\right]d\boldsymbol{v}. \tag{B.5}$$

The integral with respect to θ' is evaluated with the lower limit θ_0 selected so that the antiderivative is zero at $\theta' = \theta_0$. In order to simplify Eq. (B.5), special properties of the Bessel function of the first kind are invoked. These properties are [114, pp. 7,12]

$$e^{-i\beta\sin\theta} = \sum_{n=-\infty}^{\infty} J_n(\beta)e^{-in\theta} \tag{B.6}$$

$$J_{n+1}(\beta) + J_{n-1}(\beta) = \frac{2n}{\beta}J_n(\beta). \tag{B.7}$$

The resulting dispersion relation is

$$0 = 1 - \sum_s \frac{Z_s\omega_p}{k_\perp\omega_c}\int_{-\infty}^{\infty}\int_0^{\infty}\int_0^{2\pi}\left[\frac{1}{\beta}\frac{\partial f_{s0}}{\partial v_\perp}\sum_{m,n=-\infty}^{\infty} nJ_m(\beta)J_n(\beta)\frac{e^{i\theta(m-n)}}{(\alpha+n)}\right]v_\perp d\theta dv_\perp dv_\parallel. \tag{B.8}$$

Note that for the purposes of this paper, all physics of interest is independent of $v_\parallel$. Also note that by the orthogonality properties of Bessel functions and the Fourier basis functions, the terms in the summation Eq. (B.8) are zero for all $m \neq n$. The resulting dispersion relation is

$$0 = 1 + \sum_s \frac{Z_s^2}{M_s k_\perp^2}\int_0^{\infty}\frac{\partial f_0}{\partial v_\perp}\sum_{n=-\infty}^{\infty} J_n^2\left(\frac{k_\perp v_\perp}{\Omega_{cs}}\right)\frac{n}{\frac{\omega}{\Omega_{cs}}-n}2\pi dv_\perp. \tag{B.9}$$

This result is consistent with [81, 84]. Let $w_s = \omega/\Omega_{cs}$. It is noted by identity that $J_n^2 = J_{-n}^2$ (see Eq. (B.18)) and therefore

$$\sum_{n=-\infty}^{\infty}\frac{n}{w_s-n}J_n^2 = \sum_{n=-\infty}^{-1}\frac{n}{w_s-n}J_n^2 + \sum_{n=1}^{\infty}\frac{n}{w_s-n}J_n^2 \tag{B.10}$$

$$= \sum_{n=1}^{\infty}\left[\frac{2n^2}{w_s^2-n^2}\right]J_n^2. \tag{B.11}$$

Consequently the summation indices in Eq. (B.9) can be changed as follows

$$0 = 1 + \sum_s \frac{Z_s^2}{M_s k_\perp^2} \sum_{n=1}^{\infty} \frac{2n^2}{w_s^2 - n^2} \int_0^\infty \frac{\partial f_{s0}}{\partial v_\perp} J_n^2 \left(\frac{k_\perp v_\perp}{\Omega_{cs}} \right) 2\pi dv_\perp. \tag{B.12}$$

Applying integration by parts and noting that $J_n(0) = 0$ if $n \neq 0$ and that the equilibrium distribution function has compact support such that $f_{s0}|_{v_\perp = \infty} = 0$ yields

$$0 = 1 - \sum_s \frac{Z_s^2}{M_s k_\perp^2} \sum_{n=1}^{\infty} \frac{2n^2}{w_s^2 - n^2} \int_0^\infty f_{s0} \frac{\partial}{\partial v_\perp} \left[J_n^2 \left(\frac{k_\perp v_\perp}{\Omega_{cs}} \right) \right] 2\pi dv_\perp. \tag{B.13}$$

It can be readily shown that the following equality is satisfied

$$\frac{w_s \sin(w_s \pi)}{w_s^2 - n^2} = \int_0^\pi \cos(n(\tau + \pi)) \cos(w_s \tau) d\tau. \tag{B.14}$$

Substituting Eq. (B.14) into Eq. (B.13) yields

$$0 = 1 - \sum_s \frac{Z_s^2}{M_s k_\perp^2} \int_0^\infty f_{s0} \sum_{n=1}^{\infty} \left[2n^2 \int_0^\pi \frac{\cos(n(\tau + \pi)) \cos(w_s \tau)}{w_s \sin(w_s \pi)} d\tau \right] \frac{\partial}{\partial v_\perp} \left[J_n^2 \left(\frac{k_\perp v_\perp}{\Omega_{cs}} \right) \right] 2\pi dv_\perp. \tag{B.15}$$

The infinite sum in the dispersion relation of Eq. (B.15) can be reduced to an integral representation [83, 84, 115] using an auxiliary Bessel function identity:

$$\int_0^\pi w_s \sin(w_s \tau) \sin \tau J_0 \left(2z \cos \frac{\tau}{2} \right) d\tau = - \int_0^\pi \frac{1}{z} \sum_{n=1}^{\infty} 2n^2 \frac{\partial}{\partial z} \Big[J_n^2(z) \Big] \cos \Big(n(\tau + \pi) \Big) \cos(w_s \tau) d\tau. \tag{B.16}$$

See Appendix B.2 for a complete derivation of this identity. The result is a closed-form integral representation of the dispersion relation that is equivalent to Eq. (B.9):

$$0 = 1 + \sum_s \frac{Z_s^2}{M_s \Omega_{cs}^2} \int_0^\infty f_{s0} \int_0^\pi \frac{\sin(w_s \tau)}{\sin(w_s \pi)} \sin(\tau) J_0 \left(2 \frac{k_\perp v_\perp}{\Omega_{cs}} \sin \frac{\tau + \pi}{2} \right) d\tau 2\pi v_\perp dv_\perp, \tag{B.17}$$

which is consistent with the expressions presented in Refs. [83, 84].

B.2 Auxiliary Bessel function identity

For integer n, the following standard identities apply to Bessel functions of the first kind [114, pp. 6,12,102]

$$J_{-n}(z) = (-1)^n J_n(z) \tag{B.18}$$

$$J_{n-1}(z) - J_{n+1}(z) = 2 \frac{\partial}{\partial z} \Big[J_n(z) \Big] \tag{B.19}$$

$$J_0 \left(2z \sin \frac{\tau}{2} \right) = \sum_{n=0}^{\infty} \Delta_n J_n(z)^2 \cos(n\tau). \tag{B.20}$$

where Δ_n is defined as

$$\Delta_n = \begin{cases} 1 & \text{if } n = 0 \\ 2 & \text{if } n \neq 0 \end{cases}. \tag{B.21}$$

An additional auxiliary Bessel function identity is derived by manipulating Eq. (B.20). References [83] and [115] allude to these types of manipulations.

Starting with Eq. (B.20), the identity can be modified as follows

$$J_0\left(2z\sin\frac{\tau+\pi}{2}\right) = \sum_{n=0}^{\infty} \Delta_n J_n(z)^2 \cos\big(n(\tau+\pi)\big) \tag{B.22}$$

$$J_0\left(2z\cos\frac{\tau}{2}\right) = \sum_{n=0}^{\infty} \Delta_n J_n(z)^2 \cos\big(n(\tau+\pi)\big). \tag{B.23}$$

Taking the derivative of Eq. (B.23) with respect to τ and using identities in Eq. (B.18) and Eq. (B.19) yields

$$\sin\frac{\tau}{2} J_1\left(2z\cos\frac{\tau}{2}\right) = -\frac{2}{z}\sum_{n=1}^{\infty} n J_n^2(z)\sin\big(n(\tau+\pi)\big). \tag{B.24}$$

Taking derivative of Eq. (B.24) with respect to z and using Eq. (B.19) again yields

$$\begin{aligned}\cos\frac{\tau}{2}\sin\frac{\tau}{2}&\left[J_0\left(2z\cos\frac{\tau}{2}\right) - J_2\left(2z\cos\frac{\tau}{2}\right)\right] \\ &= \frac{2}{z^2}\sum_{n=1}^{\infty} n J_n^2 \sin\Big(n(\tau+\pi)\Big) - \frac{2}{z}\sum_{n=1}^{\infty} n\frac{\partial}{\partial z}\Big[J_n^2(z)\Big]\sin\Big(n(\tau+\pi)\Big).\end{aligned} \tag{B.25}$$

Using Bessel function identity of Eq. (B.7) and noting that $J_2\left(2z\cos\frac{\tau}{2}\right) = \frac{J_1\left(2z\cos\frac{\tau}{2}\right)}{z\cos\frac{\tau}{2}} - J_0\left(2z\cos\frac{\tau}{2}\right)$, Eq. (B.25) can be expressed as

$$\begin{aligned}2\cos\frac{\tau}{2}\sin\frac{\tau}{2}&J_0\left(2z\cos\frac{\tau}{2}\right) - \frac{\sin\frac{\tau}{2}}{z} J_1\left(2z\cos\frac{\tau}{2}\right) \\ &= \frac{2}{z^2}\sum_{n=1}^{\infty} n J_n^2 \sin\Big(n(\tau+\pi)\Big) - \frac{2}{z}\sum_{n=1}^{\infty} n\frac{\partial}{\partial z}\Big[J_n^2(z)\Big]\sin\Big(n(\tau+\pi)\Big).\end{aligned} \tag{B.26}$$

Multiplying equation Eq. (B.24) by z^{-1} and substituting into Eq. (B.26) results in the cancelation of two of the terms, thus the manipulated identity is now

$$2\cos\frac{\tau}{2}\sin\frac{\tau}{2} J_0\left(2z\cos\frac{\tau}{2}\right) = -\frac{2}{z}\sum_{n=1}^{\infty} n\frac{\partial}{\partial z}\Big[J_n^2(z)\Big]\sin\Big(n(\tau+\pi)\Big) \tag{B.27}$$

$$\sin\tau J_0\left(2z\cos\frac{\tau}{2}\right) = -\frac{2}{z}\sum_{n=1}^{\infty} n\frac{\partial}{\partial z}\Big[J_n^2(z)\Big]\sin\Big(n(\tau+\pi)\Big). \tag{B.28}$$

Taking the derivative of Eq. (B.28) with respect to τ, multiplying both sides by $\cos(w_s\tau)$, and using the product rule of differentiation yields

$$\frac{\partial}{\partial\tau}\left[\sin\tau J_0\left(2z\cos\frac{\tau}{2}\right)\cos(w_s\tau)\right] + w_s\sin(w_s\tau)\sin\tau J_0\left(2z\cos\frac{\tau}{2}\right) = -\frac{2}{z}\sum_{n=1}^{\infty} n^2\frac{\partial}{\partial z}\left[J_n^2(z)\right]\cos\Big(n(\tau+\pi)\Big)\cos(w_s\tau). \quad \text{(B.29)}$$

Integrating both sides with respect to τ on the interval $[0,\pi]$ yields the modified Bessel function identity

$$\int_0^{\pi} w_s\sin(w_s\tau)\sin\tau J_0\left(2z\cos\frac{\tau}{2}\right)d\tau = -\int_0^{\pi}\frac{1}{z}\sum_{n=1}^{\infty}2n^2\frac{\partial}{\partial z}\left[J_n^2(z)\right]\cos\Big(n(\tau+\pi)\Big)\cos(w_s\tau)d\tau, \quad \text{(B.30)}$$

which is used in the derivation of the $k_{\|}=0$ dispersion relation.